Quelques modèles mathématiques homogénéisés appliqués à la modélisation du parenchyme pulmonaire

Paul Cazeaux

Université Pierre et Marie Curie
Paris 6

Brown University

Quelques modèles mathématiques homogénéisés appliqués à la modélisation du parenchyme pulmonaire

THÈSE DE DOCTORAT

présentée par

Paul Cazeaux

pour obtenir le grade de

Docteur de l'Université Pierre et Marie Curie

Spécialité

Mathématiques Appliquées

sous la direction de Céline Grandmont et Yvon Maday

Soutenue publiquement le 12/12/2012 devant le jury composé de

M. Eric Bonnetier	Université Joseph Fourier	Rapporteur
Mme Catherine Choquet	Université de La Rochelle	Examinatrice
Mme Céline Grandmont	Inria	Directrice de thèse
M. Frédéric Hecht	Université Pierre et Marie Curie	Examinateur
M. Jan Hesthaven	Brown University	Membre invité
M. Yvon Maday	Université Pierre et Marie Curie	Directeur de thèse
M. Bertrand Maury	Université Paris–Sud	Examinateur

Et s'appuyant sur le rapport de M. Yves Capdeboscq (University of Oxford), Rapporteur

Laboratoire Jacques-Louis Lions
UMR 7598

Thèse effectuée aux :

Laboratoire Jacques-Louis Lions, UMR 7598

Division of Applied Mathematics
at Brown University

Adresse géographique :
Laboratoire Jacques Louis Lions
Bâtiments : 3ème étage – 15-16, 15-25, 16-26,
4 place Jussieu
75005 Paris, France
+33 1 44 27 42 98 (Tél.)
+33 1 44 27 72 00 (Fax)

Adresse postale :
Laboratoire Jacques-Louis Lions
Université Pierre et Marie Curie
Boîte courrier 187
75252 Paris Cedex 05 France

Adresse :
Divison of Applied Mathematics
Brown University
182 George Street
Providence, RI 02912, USA
+1 (401) 863-2115 (Tél.)
+1 (401) 863-1355 (Fax)

Résumé

Nous présentons des modèles macroscopiques du comportement mécanique du parenchyme pulmonaire humain obtenus par la méthode de l'homogénéisation double–échelle. Le parenchyme est un matériau poreux formé d'une multitude d'alvéoles remplies d'air, et connectées à l'air extérieur par l'arbre bronchique. Cette structure microscopique complexe est responsable du comportement macroscopique. Nous nous intéressons en particulier à deux problèmes : la modélisation de la déformation du parenchyme en prenant en compte sa ventilation par l'arbre bronchique, et la propagation du son ou de l'ultrason à travers le parenchyme.

Dans une première partie consacrée au couplage entre parenchyme et arbre bronchique, nous commençons par proposer un modèle de la déformation du parenchyme. Nous modélisons (i) le parenchyme par un matériau élastique linéaire, (ii) les alvéoles comme des cavités réparties périodiquement dans le domaine macroscopique occupé par le parenchyme et (iii) l'arbre bronchique par un arbre dyadique résistif. La loi de Poiseuille est supposée valide pour chaque voie aérienne du poumon. Cette modélisation nous permet d'écrire un système fluide–structure modélisant le déplacement du parenchyme et dépendant d'un paramètre ε qui correspond à la taille de la cellule de périodicité. Nous étudions la convergence double–échelle des solutions de ce système sous une hypothèse abstraite qui décrit la convergence de l'action de l'arbre sur le parenchyme. Nous obtenons une description macroscopique du parenchyme comme un matériau viscoélastique où l'arbre induit une dissipation non–locale en espace. Dans cette partie, nous étudions aussi la condition abstraite que nous avons introduite. Nous proposons deux modèles de l'irrigation du domaine par l'arbre inspirées par la structure du poumon et pour lesquelles cette condition abstraite est vérifiée. Finalement, nous décrivons une méthode numérique pour le problème macroscopique et nous illustrons le travail précédent par des résultats numériques en deux dimensions.

Dans une deuxième partie consacrée à la propagation d'ondes sonores dans le parenchyme, nous ne prenons pas en compte l'effet de l'arbre bronchique. Nous homogénéisons dans le domaine fréquentiel un premier modèle couplant l'élasticité linéarisée dans le parenchyme avec l'équation acoustique dans l'air. Nous retrouvons ainsi rigoureusement le modèle de Rice qui décrit la propagation du son à basses fréquences. Cette étude est compliquée par le fait que le problème considéré, de type Helmholtz, n'est pas bien posé pour toutes les valeurs de la fréquence. Pour montrer le résultat, nous utilisons un argument par contradiction basé sur l'alternative de Fredholm. Ensuite, nous homogénéisons un deuxième modèle qui prend en compte le caractère viscoélastique et inhomogène du parenchyme au niveau microscopique. Les coefficients viscoélastiques macroscopiques obtenus dépendent de la fréquence. Le matériau présente de nouveaux effets de mémoire par rapport à ses composants individuels. Nous proposons une méthode numérique basée sur des éléments finis Galerkin discontinus pour résoudre le problème homogénéisé que nous obtenons. Les résultats numériques obtenus dans un cas test 2D montrent que ce modèle permet de retrouver certaines observations physiologiques sur la propagation d'ultrasons de basse fréquence.

Abstract

We present macroscopic models of the mechanical behavior of the human lung's parenchyma obtained by the two–scale homogenization method. The parenchyma is a porous material, with a huge number of air–filled alveoli connected to the exterior air by the bronchial tree. This complex microscopic structure defines the macroscopic behavior. We propose to study two problems in particular : modeling the deformation of the parenchyma while taking into account the ventilation by the bronchial tree, and the sound or ultrasound propagation through the parenchyma.

The first part focuses on the coupling between parenchyma and bronchial tree. We begin by describing a model for the parenchyma deformation. We model (i) the parenchyma as a linear elastic material, (ii) the alveoli as periodically distributed cavities in the macroscopic parenchyma domain and (iii) the bronchial tree as a dyadic resistive tree. We write the equations of the model as a coupled fluid–structure system modeling the three–dimensional parenchyma's displacement and depending on a parameter ε which corresponds to the size of the periodicity cell. We study the two–scale convergence of the solutions of this system under an abstract hypothesis that describes the convergence of the action of the tree on the parenchyma. We obtain a macroscopic description of the parenchyma as a viscoelastic material where the tree induces a spatially non–local dissipation. In this part, we also study the abstract condition we have introduced. We propose two models for the irrigation of the domain by the tree inspired by the lung's structure and for which the abstract condition can be verified. Finally, we describe a numerical method for the macroscopic problem and we illustrate the previous work by numerical simulations in two dimensions.

The second part focuses on the sound wave propagation in the parenchyma. We do not take into account the effect of the bronchial tree in this case. We homogenize in the frequency domain a first model coupling the linearized elasticity equations in the parenchyma and the acoustic equation in the air. We rigorously obtain the Rice model which describes sound propagation at low frequencies. We encounter a difficulty because the problem we investigate, of Helmholtz type, is not well–posed for all values of the frequency. To show the result, we use an argument by contradiction based on the Fredholm alternative. Then, we homogenize a second model which takes into account the viscoelastic and heterogeneous nature of the parenchyma at the microscopic level. The macroscopic viscoelastic coefficients depend on frequency. The material exhibits some new memory effects compared to its individual components. We propose a numerical method based on discontinuous Galerkin finite elements to solve the homogenized problem we have obtained. The numerical results obtained in a two–dimensional test case show that this model enables us to recover some physiological observations on the propagation of low–frequency ultrasound.

Remerciements

Nombreux sont ceux que je veux remercier pour m'avoir aidé à l'accomplissement de ce mémoire. Mes remerciements vont tout d'abord à mes directeurs de thèse, Céline Grandmont et Yvon Maday, qui m'ont soutenu et aidé durant cette thèse. J'ai beaucoup appris de vous en ce qui concerne le travail scientifique. Merci pour votre patience, votre sérieux, vos encouragements mais aussi vos critiques, et pour la grande liberté que vous m'avez laissé pour mener ces travaux. Ce fut un honneur d'être votre élève pendant ces années. Je remercie ici aussi Jan Hesthaven, qui m'a accueilli et encadré à Brown University. Un grand merci pour ton écoute, ton enthousiasme, pour la confiance et les précieux conseils que tu m'as prodigués.

Je suis également extrêmement reconnaissant à Yves Capdeboscq et Eric Bonnetier qui ont accepté de rapporter ma thèse durant un automne chargé. Je remercie chaleureusement Catherine Choquet, Bertrand Maury et Evariste Sanchez-Palencia qui me font l'honneur d'être dans le jury de ma soutenance.

J'ai eu la grande chance de réaliser ce travail dans deux environnements stimulants et conviviaux, chacun à leur façon. J'en remercie collectivement tous les membres du Laboratoire Jacques Louis Lions et de la Division of Applied Mathematics de Brown. Je remercie également toute l'équipe du projet REO pour leur accueil. J'adresse en particulier mes remerciements à toutes les équipes administratives : Maryse pour avoir organisé mes missions à Brown depuis l'Inria ; Liliane, Danielle, Florence, Salima, Nadine et Isabelle qui contribuent tant à la vie et à la bonne humeur au LJLL ; Jean, Laura, Stephanie et tout le staff du DAM qui m'ont accueilli si simplement et chaleureusement dans cette grande maison. Je remercie également Christian, qui a imprimé ces manuscrits, Antoine et Kashayar pour leur indispensables coups de main informatiques.

Je tiens également à remercier tous mes compagnons de route doctorants, *grad students*, jeunes docteurs, qu'il ne m'est hélas pas possible de citer tous ici. Merci d'abord aux membres du bureau 315 : merci à Anne–Claire, Luna, Ange et Justine pour l'ambiance détendue et sérieuse qui m'a réconcilié avec Jussieu à mes retours. Merci à Marie pour tous nos échanges, merci à Jean–Paul, Magali, Benjamin, Olga, Pierre, Anne–Céline, Yannick, Juliette et Nicole pour l'organisation du GTT, Mamadou, Evelyne, Rachida, Alexis, Alexandra, et les habitants du sous–sol au DAM : Andréas et nos aventures, Scott et ses trous noirs, Zhu, Dan, Chia et son piano, Kenny, Dahlia, Nat, Kelly, Laura... Merci aux amis probabilistes chez qui j'ai parfois fugué : merci à Sophie L. pour nos moments, Sophie D., Reda, Pascal.

Je remercie également tous les mordus de mathématiques qui m'ont accompagné durant ma scolarité et m'ont transmis leur passion. Je remercie en particulier Antoine Marchal, mon professeur de terminale, M. Guezou et Mme Feuillet, mes chers professeurs des Lazos. Je remercie également mes professeurs de l'ENS et de l'UPMC qui m'ont guidé vers ce qui allait devenir mon sujet.

Tout ne se résumant pas aux mathématiques, je remercie également tous les amis que j'ai eu la chance de rencontrer ou de retrouver durant ces trois années. Sans pouvoir être exhaustif, j'adresse en particulier de grands remerciements à l'ex-quatuor cachanais, Olivier, Cyrille, Gilles et Ivan pour les années de souvenirs depuis le B2, les bons moments et le couch-surfing lors de mes retours à

Paris. Merci à Benjamin pour les soirs au Café Noir, Andréas pour les glaces chez Grom, Gersende pour les pancakes chez Julian's, Dan pour le barbecue dans le Far West, et Nathalie pour tes oursins et tes étoiles de mer. Merci aux anciens des Lazos pour leur soutien et leur chocolat, à Paris ou ailleurs.

At the start of each of my stays at Brown, I landed twice in the cold winter of Providence. I have to thank Rebecca McLaughlin for her support, her kindness, and the warm rooms in her home. Good luck to you and Oliver. Thanks also to Marco and all my roommates for many exotic conversations.

Merci enfin de tout coeur à ma famille qui m'a toujours supporté, soutenu et encouragé, et qui est là aujourd'hui. Merci Soeurette de me montrer la voie, parfois. Merci à Papa Moumine et à la Petite Mu d'être mon phare dans la tempête.

À mes parents

À Fanfan

Table des matières

Introduction Générale **1**

I Mechanical Behavior of the Lungs during the Respiration Process **23**

Introduction and Motivation **25**

1 A Multiscale Viscoelastic Model with Nonlocal Damping **29**
1.1 Presentation of the model . . . 30
1.1.1 Geometric setting . . . 30
1.1.2 Description of the parenchyma model . . . 32
1.1.3 Poiseuille flow through a finite resistive dyadic tree . . . 33
1.1.4 Coupling the elastic structure and the resistive dyadic tree . . . 35
1.1.5 A multiscale kernel describing the action of the resistive dyadic tree . . . 36
1.1.6 Two–scale convergence . . . 37
1.2 Study in the compressible case: homogenization limit . . . 38
1.2.1 Variational formulation and *a priori* estimates . . . 39
1.2.2 Two–scale convergence result . . . 43
1.2.3 Cell problems, correctors and the homogenized problem . . . 52
1.3 Study in the incompressible case . . . 57
1.3.1 Mixed variational formulation . . . 57
1.3.2 Pressure extension and *a priori* estimates . . . 58
1.3.3 Two–scale convergence . . . 59

2 Multi–scale Decompositions and the Tree Operator **67**
2.1 Multi–scale domain decompositions . . . 67
2.2 Letting a square breathe . . . 70
2.2.1 Geometry . . . 70
2.2.2 Convergence of the resistance operators and geometric resistive trees . . . 73
2.3 An algorithmic approach . . . 76
2.3.1 Geometry: approximation of a multi–scale decomposition . . . 76
2.3.2 Convergence of the resistance operators . . . 80
2.A Annex . . . 89
2.A.1 A geometric Lemma . . . 89
2.A.2 Proof of Proposition 2.3.3 (alias Proposition 2.A.1) . . . 91

3 Numerical Applications **95**
3.1 Discretization of the homogenized problem . . . 95
3.2 Numerical scheme . . . 96
3.3 A word on the computation of the homogenized parameters. . . . 98

3.4 Numerical results . . . 99
3.5 Numerical study of the energy dissipation . . . 100

II Modelling the Sound Propagation through the Parenchyma 105

4 Sound Modelling in the Parenchyma 107
4.1 Introduction and motivation . . . 107
4.2 Description of the coupling of the elastic and acoustic equations in a perforated domain 109
4.2.1 Geometric setting . . . 109
4.2.2 Acoustic–Elastic interaction . . . 111
4.2.3 A few useful definitions and results . . . 115
4.2.4 Gårding's inequality and well–posedness . . . 118
4.2.5 Energy estimates . . . 120
4.3 Two–scale homogenization of the coupled model . . . 121
4.3.1 Two–scale problem identification . . . 122
4.3.2 Proof of the *a priori* bounds and Theorem 4.3.1 . . . 131
4.3.3 Convergence Theorem and homogenized problem . . . 133
4.4 Conclusion . . . 133
4.5 Annex . . . 134

5 Sound and Ultrasound Propagation in a Viscoelastic Model of the Lungs' Parenchyma: Theory, Numerical Simulations 137
5.1 Motivation and introduction . . . 137
5.2 The viscoelastic homogenized model . . . 139
5.2.1 The microscale model . . . 139
5.2.2 The mathematical homogenization method . . . 142
5.2.3 The microcell problem . . . 145
5.2.4 Effective equation and effective relaxation modulus . . . 147
5.2.5 Effective equations in the time domain . . . 148
5.3 Numerical offline/online strategy for the global dispersive problem . . . 149
5.3.1 Evaluation of the convolution integral . . . 149
5.3.2 Computation and fitting of the dispersive curve . . . 151
5.3.3 Discontinuous Galerkin discretization . . . 152
5.3.4 Implicit–explicit time–stepping scheme . . . 153
5.4 Numerical results . . . 154
5.4.1 Effective viscoelastic modulus computation . . . 154
5.4.2 Fitting the dispersion curve . . . 156
5.4.3 Wave propagation computations . . . 160
5.4.4 Orthotropic and isotropic behavior . . . 162

Bibliographie 165

Introduction et présentation des travaux

Nous présentons dans ce document les résultats obtenus au cours de cette thèse sous la direction de Céline Grandmont et Yvon Maday. Notre travail s'inscrit dans la thématique générale de la modélisation mathématique et numérique de systèmes biologiques et en particulier du système pulmonaire humain, dont le but est de permettre une meilleure compréhension de problèmes rencontrés en pratique médicale.

Nous avons cherché à modéliser d'un point de vue mécanique le parenchyme pulmonaire, que nous définirons ici comme l'ensemble des tissus mous du poumon, comprenant les alvéoles et les bronchioles, et qui forme la majeure partie des tissus pulmonaires. Plus précisément, notre travail a pris deux directions, correspondant à des échelles de temps différentes :

- Établir et étudier mathématiquement comme numériquement un modèle permettant de simuler le processus de ventilation du parenchyme par l'arbre bronchique, ce qui fait l'objet de la première partie du manuscrit ;
- Établir et étudier un modèle permettant de comprendre et simuler la propagation d'ondes sonores à travers le poumon, ce qui fait l'objet de la seconde partie.

Voyage au centre du poumon

« Lisons ! », m'écriai-je, après avoir refait dans mes poumons
une ample provision d'air.
Axel Lindenbrock.

Le poumon humain est un organe extraordinaire, essentiellement la réponse de la nature aux questions : comment replier en un volume de 5L une surface de 130 m^2, épaisse de quelques microns, et tapissée de capillaires sanguins ; et comment assurer que chaque élément de cette surface est relié précisément, rapidement et efficacement, d'un côté au réseau sanguin et au coeur, de l'autre à l'air extérieur. On y remarque notamment les caractéristiques d'une géométrie fractale [Man82]. Avant de décrire notre approche de modélisation, nous proposons au lecteur une exploration du poumon en quelques pages et images. Nous nous limiterons principalement aux aspects qui nous intéresseront par la suite : la structure et les propriétés mécaniques, liées à la ventilation ou à la propagation du son. Pour l'essentiel, cette présentation est issue du livre de J. T. Bates [Bat09] et du livre de E.R. Weibel [Wei84].

Architecture de l'appareil respiratoire. L'appareil respiratoire se situe à l'intérieur de la cage thoracique dans lequel il est enfermé comme dans une boîte (voir la Figure 1). Le médiastin, partie centrale qui contient notamment le péricardium avec le coeur, sépare cet espace en deux cavités pleurales dans lesquelles sont placés respectivement le poumon droit et le poumon gauche. La surface du poumon est constituée d'une membrane hermétique, la plèvre viscérale, elle–même en contact avec la plèvre pariétale qui tapisse toute la cavité pleurale. Ces deux membranes se rejoignent là où les bronches et les vaisseaux sanguins pénètrent dans les poumons (Figure 1). Entre

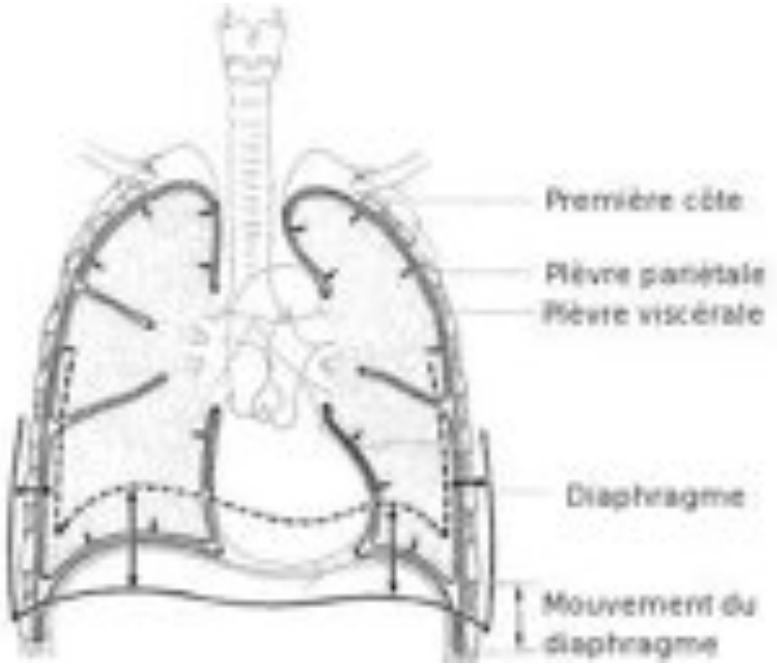

Figure 1 – Section frontale de la cage thoracique et des poumons [Wei84]

les deux plèvres, l'espace pleural, hermétique, contient une petite quantité d'un liquide lubrifiant. Le poumon est constamment maintenu en état d'extension par une pression négative au niveau de l'espace pleural.

Lorsque la cage thoracique se dilate ou se contracte, le poumon suit ce mouvement. L'ensemble agit comme une pompe pour faire pénétrer l'air à intérieur des poumons, sous l'action de différents muscles. Le principal d'entre eux est le diaphragme (voir la Figure 1), un muscle en forme de dôme qui constitue la limite inférieure de la cavité thoracique, accroché au bas des côtes. En se contractant, le diaphragme s'aplanit et étire verticalement la cavité thoracique. Le volume de la cage thoracique augmente et l'air extérieur entre par les bronches dans les poumons qui se dilatent. Ensuite, quand le diaphragme se relâche, l'élasticité des poumons les font retourner à leur position d'équilibre et l'air est expiré.

L'arbre bronchique. L'arbre bronchique conduit l'air lors de ce trajet aller–retour. Les voies aériennes des poumons prennent leur origine dans un tube unique d'un diamètre de l'ordre de 2 cm, la trachée, pénètrent chaque poumon par une bronche principale, puis continuent de se diviser de manière quasiment dichotomique tout en réduisant progressivement leur diamètre (Figure 2). Au bout de 23 générations en moyenne, on arrive ainsi aux conduits alvéolaires d'un diamètre de l'ordre du demi–millimètre.

On peut distinguer parmi ces voies aériennes deux régions aux fonctions différentes.

- Les bronches et bronchioles, jusqu'à la 17e génération de l'arbre en moyenne, sont des structures dont le seul rôle est d'assurer la conduction de l'air vers les dernières générations. Plutôt dissymétriques au début, en particulier en raison de la présence du coeur du côté gauche, les bifurcations dichotomiques deviennent assez rapidement quasiment homothétiques d'une génération sur l'autre avec un facteur de réduction constant à environ 0.85 [Wei63].
- Les acini constituent la partie terminale, dite distale, de l'arbre bronchique, chacun d'entre eux constitué par un sous–arbre du poumon d'environ 6 générations et irrigué par une bronchiole

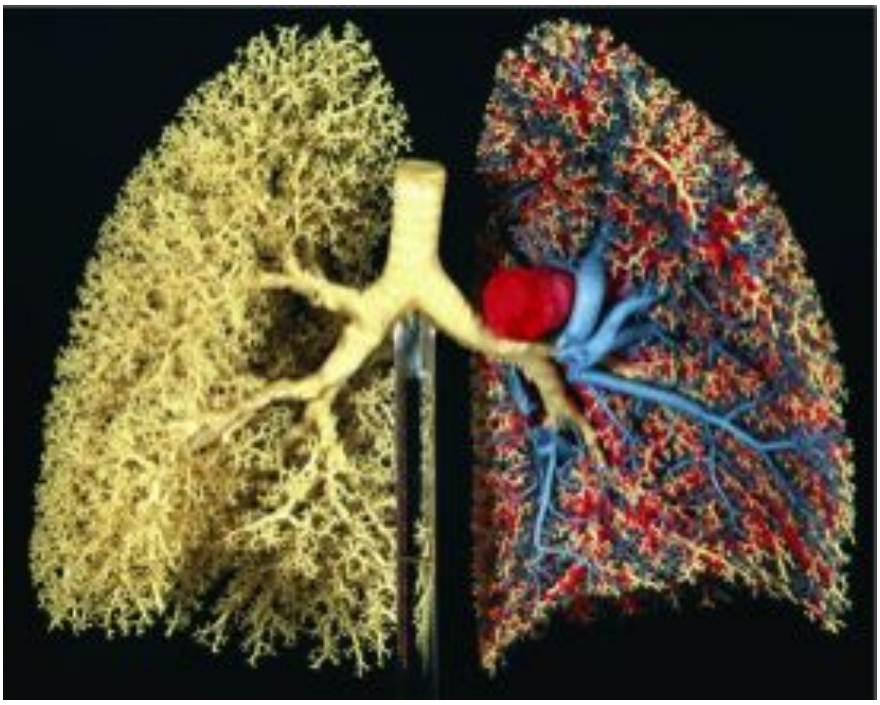

Figure 2 – Moulage de l'arbre bronchique d'un poumon humain, effectué par Weibel [Wei63]

respiratoire d'ordre un. Celles ci se divisent ensuite pour donner naissance aux les conduits alvéolaires. Leur surface se recouvre d'un nombre croissant d'alvéoles au fur des branchements, comme on peut le voir sur la Figure 3, jusqu'à atteindre les sacs alvéolaires qui sont comme des grappes d'alvéoles et forment la dernière génération du poumon. Le diamètre des canaux est plutôt constant dans cette région.

On notera quelques chiffres : l'ensemble de la zone de conduction ne contient que 170 mL d'air (appelé espace–mort), alors que les acini, qui forment 90% du volume du poumon, peuvent en contenir jusqu'à 6L à inflation maximale. L'air constitue environ 80% du volume du poumon en lors de la respiration non forcée. Il y a environ 150000 acini dans le poumon, d'un diamètre de quelques millimètres chacun, contenant environ 10000 alvéoles.

Les alvéoles. Les alvéoles sont de petites cavités remplies d'air, regroupées au sein d'un acinus. Lorsque le poumon est suffisamment gonflé, ce sont des structures polyhédrales auxquelles il manque un côté, comparables dans leur agencement à un nid d'abeille ou aux bulles d'air dans une mousse. La paroi de toutes ces alvéoles est à son tour finement maillée de capillaires sanguins (Figure 4).

En plus du sang, qui forme environ 50% du volume de la paroi alvéolaire, on retrouve dans celle–ci quatre composants :

- la substance fondamentale (espèce de gel hydraté visqueux) ;
- des cellules composant les parois des capillaires et du tissu ;
- du surfactant, contenu dans un un film aqueux qui recouvre la paroi ;
- des fibres d'élastine et de collagène.

L'ensemble de cette structure, notamment les capillaires, est maintenu par le réseau de fibres qui sont le support mécanique du poumon.

Propriétés mécaniques du tissu pulmonaire. Les expériences montrent que le tissu pulmonaire se comporte macroscopiquement comme un matériau viscoélastique non–linéaire, isotropique

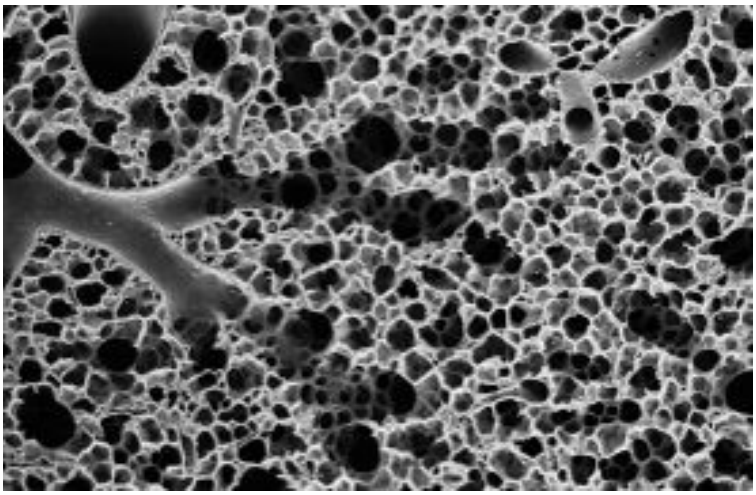

Figure 3 – Coupe au microscope électronique d'un poumon (voir [Wei09]), montrant la bifurcation d'une petite bronchiole terminale en deux conduits alvéolaires irriguant des sacs alvéolaires

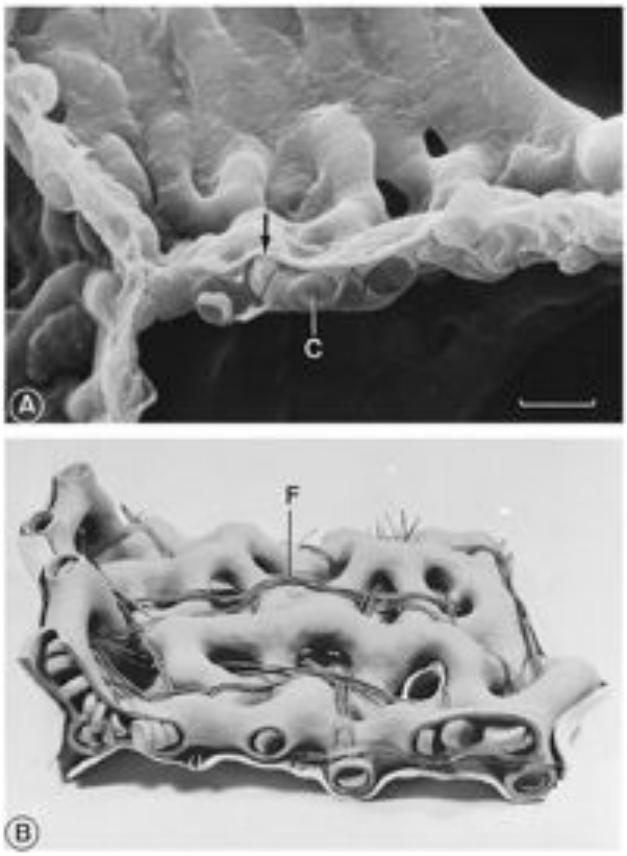

Figure 4 – Paroi alvéolaire (voir [Wei84]) (a) au microscope électronique et (b) en modèle, on note les réseaux de capillaires (C) et de fibres élastiques (F). Le marqueur d'échelle mesure 10 μm.

et compressible. C'est un matériau constamment sous tension du fait des forces d'étirement exercées sur le poumon au niveau de la plèvre et des forces de gravité. Il s'agit donc d'un matériau précontraint. Ses propriétés dépendent de l'intégrité du réseau de fibres élastiques notamment pour maintenir les bronchioles et les alvéoles ouvertes.

Retrouver ces propriétés mécaniques à partir des constituants individuels est un problème toujours d'actualité [SB11]. Peu de données quantitatives existent pour décrire le comportement des matériaux au niveau microscopique de la paroi alvéolaire. Voici quelques caractéristiques connues de chacun d'entre eux.

- Les fibres de collagène forment un matériau élastique, très résistant et pratiquement inextensible (moins de 2% de leur longueur). Lorsque le poumon est peu distendu, ces fibres sont repliées et détendues.
- Les fibres d'élastine sont un matériau élastique très extensible. Elles peuvent s'étendre relativement facilement d'un facteur deux par rapport à leur longueur au repos. On peut les modéliser par une loi hyperélastique.
- la substance fondamentale est un gel visqueux dans lequel s'insèrent et coulissent les fibres élastiques.
- Le sang est un fluide, que l'on peut modéliser comme un fluide non–Newtonien.
- Le surfactant réduit la tension de surface due au film aqueux, et participe aux propriétés élastiques de la paroi en augmentant la tension de surface lorsque la surface alvéolaire augmente, et en la réduisant quand la surface se réduit.
- L'air, qui en constitue 80%, est un gaz compressible, faiblement visqueux par rapport à la structure.

Fréquence sonore (Hz)	10^1 – 10^2 – 10^3	10^4	10^5 – 10^6 – 10^7
Expériences	Transmission du son	Pas de son	Ultrason efficace / Ultrason inefficace
Vitesse du son	30–50 m/s	Filtre coupe–bande	$>$ 1000 m/s
Applications	Auscultation percussion		Contrôle du poumon Imagerie
			⟷ Comportement dynamique

Table 1 – Propagation des ondes sonores dans le poumon : étude par [RHD+10]

Propagation du son. La structure poreuse du poumon lui confère des propriétés de transmission du son bien particulières parmi les organes du corps humain. On observe une forte dépendance en fréquence, résumée dans le tableau 1. En particulier, il est connu que les sons entre 1 kHz et 10 kHz ne se propagent pas du tout à travers le tissu pulmonaire et que les ultrasons au dessus de 1 Mhz (au niveau des fréquences des ultrasons utilisés pour l'imagerie médicale) sont reflétés et dispersés par les inclusions d'air dans le tissu pulmonaire [PKW97]. C'est pour cette raison qu'il n'est pas possible de réaliser une échographie du poumon.

Au contraire, les ultrasons de basse fréquence, entre 10 kHz et 1Mhz, ont été relativement peu étudiés [MP02]. *Ex vitro*, les poumons semblent quasiment imperméables aux ondes ultrasonores dans ces fréquences [Dun86]. Des résultats récents [RHD+10] montrent que les ultrasons de basse fréquence (10–750 kHz) peuvent se transmettre à travers le thorax d'un patient, et à travers le poumon, avec un comportement de filtre passe–haut et à la vitesse de 1500 m/s, comme dans les tissus mous incompressibles. Autour de 15 kHz, ce comportement est dynamique et dépend de l'état d'inflation du poumon ainsi que des pathologies dont souffre le poumon du patient. Le niveau

d'absorption du signal ultrasonore montre ainsi une variabilité de plusieurs dizaines de dB. Le mécanisme de cette propagation du son dans le poumon *in vivo* reste encore inexpliqué [MBW+12].

La respiration. La respiration est essentiellement un procédé mécanique dont le but est la ventilation des alvéoles en air frais, et donc en oxygène. Lors de l'inspiration, le diaphragme se contracte et exerce une traction vers le bas sur le poumon au niveau de la plèvre, qui est transmise au niveau des acini par le réseau de fibres élastiques. Ceci crée une différence de pression entre l'air extérieur et l'air présent dans le poumon. Un flux d'air frais s'établit alors de l'extérieur vers les alvéoles à travers l'arbre bronchique.

D'abord très rapide au niveau de la trachée, de l'ordre d'un mètre par seconde au repos, le flux d'air ralentit au fur et à mesure que l'on avance dans l'arbre bronchique. En effet, la surface d'une section augmente géométriquement d'une génération sur l'autre : on a vu que le facteur de réduction de la taille des voies aériennes entre deux générations successives était de 0.85, et comme il y a aussi deux fois plus de voies aériennes d'une génération sur l'autre on obtient approximativement une diminution de la vitesse du flux d'un facteur $2 \times 0.85^2 = 1.5$ à chaque génération. A l'entrée de l'acinus, la vitesse de l'air est de l'ordre de quelques fractions de centimètres par secondes.

Lors de l'expiration, le diaphragme se relâche. Les tissus pulmonaires élastiques tendus tendent à retourner à leur position d'équilibre en raison de leur élasticité naturelle (lors de la respiration normale) ou bien avec l'aide de muscles (lors d'une expiration forcée). La différence de pression avec l'atmosphère extérieure devient positive et l'air ressort du poumon par l'arbre bronchique.

L'expiration dure en moyenne trois secondes, et l'inspiration deux secondes.

Quelques mots sur la modélisation du poumon

> There are many different cells, membranes, vesicles, and other structures along the pathway that O_2 has presumably to follow. Are they important ? The morphologist will say yes, and he is right ; the physiologist will say no, and he is right too.
>
> *The Pathway for Oxygen*, E.R. Weibel

Les performances du système respiratoire sont les conséquences de la structure et des propriétés fonctionnelles du poumon que nous venons de décrire en partie. Chacun des détails de ce système d'une complexité énorme influence à sa manière son comportement. Heureusement, la plupart de ces fonctions n'ont qu'un effet indirect sur le processus de ventilation et le comportement mécanique global du poumon. Il est possible, pour comprendre les relations dynamiques entre les mesures de pression, de flux, de volume à la bouche obtenues par le médecin de faire appel à des modèles relativement simples.

Modèle linéaire à un compartiment. Le modèle le moins complexe pour modéliser le processus de la respiration est le modèle dit à un compartiment esquissé en Figure 5. Lorsque le tissu pulmonaire est distendu (le volume du compartiment V augmente), il produit naturellement une force élastique (ici une pression P_{el}) qui tend à le faire revenir à son volume original lorsque les forces extérieures cessent d'agir. De manière simplifiée, on peut assimiler ce comportement à celui d'un ressort Hookéen que l'on étire à partir de sa position de repos. La tension de ce ressort est proportionnelle à la variation de sa longueur par rapport à sa position détendue. En supposant que le tissu pulmonaire réagit de la même façon, la relation entre V et P_{el} se caractérise à l'aide d'un simple nombre, l'élastance E :

$$P_{el} = EV \tag{0.1}$$

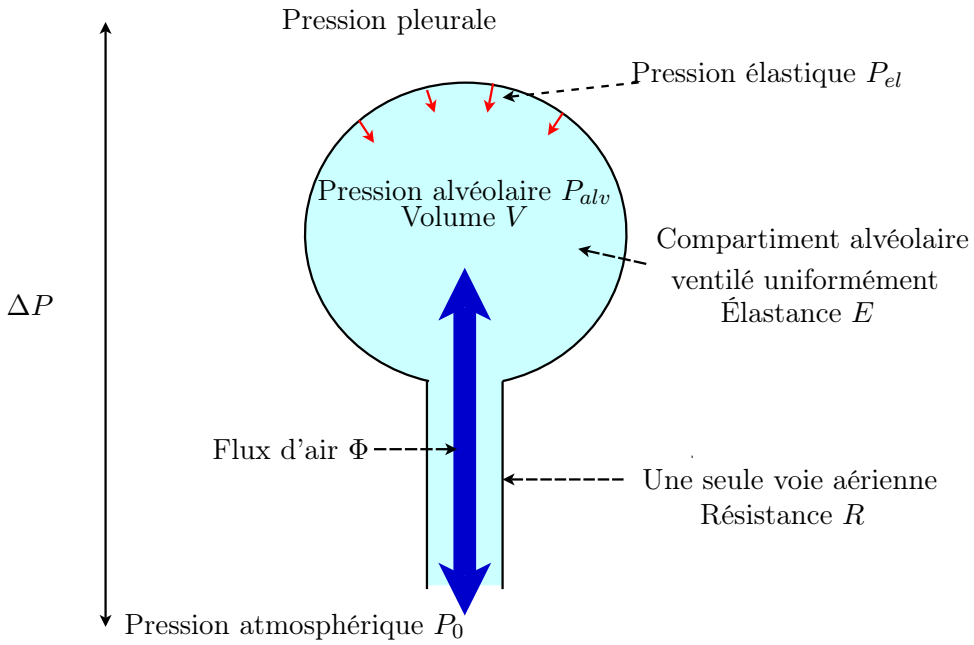

Figure 5 – Le modèle le plus simple du poumon : un ballon élastique en bout d'un tube rigide. Le ballon représente les tissus élastiques du poumon, le tube représente l'arbre bronchique qui relie le nez et la bouche à la région alvéolaire du poumon.

où l'on suppose que V mesure la variation de volume du compartiment quand le tissu est complètement au repos. Le coefficient E mesure ainsi à quel point il est difficile d'étirer le tissu élastique.

Par ailleurs, pour entraîner le passage d'un flux d'air (ou d'un fluide quelconque) à travers un conduit rigide, il est nécessaire d'appliquer entre ses deux extrémités une différence de pression. Si la vitesse du fluide n'est pas trop importante, et si la forme du conduit est assez simple, on peut considérer que le flux d'air Φ qui entre dans le compartiment à travers le conduit et la chute de pression entre ses extrémités sont proportionnels. La résistance au flux du conduit est le coefficient qui relie la chute de pression et le flux d'air entre les deux extrémités du conduit :

$$P_0 - P_{alv} = R\Phi = R\Phi = R\frac{\mathrm{d}}{\mathrm{d}t}V, \tag{0.2}$$

où P_0 est la pression à l'entrée du conduit (pression à la bouche), et P_{alv} est la pression à l'intérieur du compartiment alvéolaire. La résistance R mesure ainsi à quel point il est difficile de faire passer l'air à travers le conduit. Dans le cas idéalisé où le conduit est un long tube cylindrique rigide dans lequel circule un fluide visqueux newtonien incompressible, comme sur la Figure 6, il est possible de résoudre exactement les équations de Stokes. On peut dans ce cas obtenir une expression exacte de la résistance en fonction des dimensions du conduit et de la viscosité de l'air. La loi (0.2) est connue sous le nom de Loi de Poiseuille :

$$P_0 - P_{alv} = \frac{8\nu L}{\pi D^4}\Phi, \tag{0.3}$$

où ν est la viscosité de l'air.

En combinant les équations (0.1) et (0.2), on obtient ainsi la loi mécanique du modèle linéaire à un compartiment du poumon qui relie la différence de pression totale ΔP entre la pression à l'entrée du conduit et la pression pleurale à l'extérieur du compartiment alvéolaire :

$$\begin{aligned}\Delta P &= P_{el} + P_0 - P_{alv} \\ &= EV + R\frac{\mathrm{d}}{\mathrm{d}t}V.\end{aligned} \tag{0.4}$$

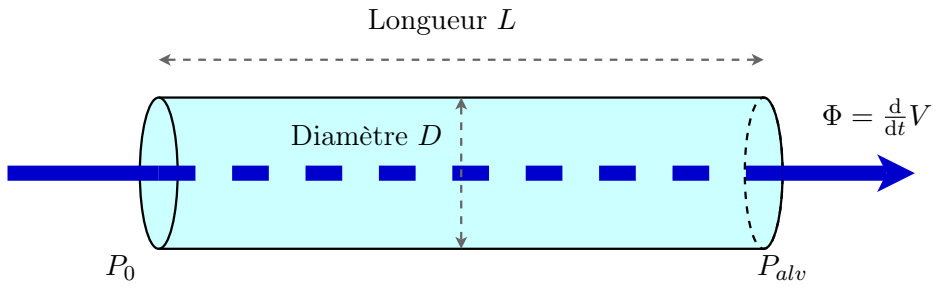

Figure 6 – Loi de Poiseuille et flux d'air à travers un conduit cylindrique.

Cette équation différentielle du premier ordre relie les variables ΔP, V et $\frac{\mathrm{d}}{\mathrm{d}t}V$ qui sont facilement mesurables par les médecins : ce sont respectivement la *pression transpulmonaire*, le *volume à la bouche* et le *flux à la bouche*. L'équation (0.4) a ainsi une grande importance historique dans la description du poumon [Bat09], et elle est couramment utilisée pour décrire simplement la ventilation. Il s'agit du modèle le plus simple capable de représenter la mécanique du poumon. Notons que chacun des deux paramètres du modèle, l'*élasticité* du tissu pulmonaire et la *résistance* des voies aériennes ont une vraie signification physique, de sorte qu'on peut aisément relier des pathologies à des modifications de ces paramètres, dans les limites du modèle (l'asthme se traduit par une augmentation de la résistance des voies aériennes, par exemple).

Le cadre de la modélisation suivi dans cette thèse. Le modèle à un compartiment que nous venons de proposer est toutefois une représentation très simplifiée du mécanisme de la respiration. Il ne prend en compte qu'un petit nombre de variables scalaires qui sont reliées de manière linéaire et uniquement deux paramètres. De nombreux modèles plus complexes ont été proposés pour rendre compte de différents aspects du comportement du poumon humain (voir e.g. [Bat09]). Une première façon de créer de tels modèles consiste par exemple à utiliser des courbes pression–volume non–linéaires obtenues par des expériences à la place de l'équation (0.1). On peut obtenir ainsi des modèles $0D$ mieux capables de reproduire les courbes expérimentales de pression et volume à la bouche. De même, pour modéliser le déplacement tri–dimensionel du parenchyme, on peut utiliser des lois de comportement mécanique dont les paramètres ont été ajustés par des expériences sur des morceaux de tissu pulmonaire. On parle d'approche phénoménologique.

Pour construire notre modèle, nous nous intéressons dans cette thèse à une autre approche, qui vise à retrouver le comportement macroscopique à partir du comportement mécanique modélisé au niveau de la structure microscopique du parenchyme pulmonaire. Il s'agit là d'un objectif classique de la modélisation multi–échelle : dériver rigoureusement des modèles effectifs à l'échelle macroscopique à partir de modèles décrivant des échelles inférieures. On parle ainsi de modèle *microscopique* pour faire référence à un modèle présentant un grand nombre de degrés de liberté, et de modèle *macroscopique* pour faire référence à un modèle à nombre de degrés de liberté réduit. Le modèle microscopique est ainsi posé sur le domaine macroscopique mais présente une description fine du problème, à partir de laquelle nous cherchons à obtenir une description plus grossière.

Dans le cas de notre étude du parenchyme pulmonaire humain, les équations de notre modèle microscopique modélisent la déformation de l'ensemble des parois alvéolaires, qui constituent le tissu du parenchyme. Ces équations sont posées sur un domaine à la géométrie perforée et complexe. Notre but est d'obtenir une description macroscopique de la déformation du parenchyme avec un problème posé sur un *domaine macroscopique* à la géométrie simple, qui est le volume rempli par l'air et le parenchyme ensemble. Nous utilisons pour cela la théorie mathématique de l'homogénénisation double-échelle. Nous obtenons un modèle de complexité réduite, mais qui prend en compte certains effets dus à la microstructure et à l'organisation hiérarchique du matériau. Avant de décrire notre

démarche, nous présentons différents modèles mathématiques et numériques du poumon qui entrent dans ce cadre et permettent d'étudier plus précisément les mécanismes en jeu lors de la ventilation du poumon ou de la propagation du son.

Etat de l'art

Modèles de l'arbre bronchique. En vue d'étudier précisément l'écoulement de l'air dans les voies aériennes pulmonaires, des modèles permettant des simulations numériques en géométrie réelle du flux d'air dans la partie supérieure de l'arbre bronchique ont été récemment étudiés, voir par exemple [LMB+02, CS04, FMP+05]. Ces modèles permettent de prendre en compte les effets inertiels de l'écoulement de l'air tri–dimensionnel dans les premières générations de l'arbre bronchique, d'étudier les effets de la géométrie et de l'asymétrie des bifurcations [MFAS03, Mau05], voire le dépôt d'aérosol sur les parois [BBJM05, Mou09]. Etant posés dans un arbre bronchique dont on a tronqué les voies aériennes au–delà de la génération 6 ou 7, ces modèles sont pour la plupart découplés du parenchyme en adoptant des conditions aux limites posées *a priori*, par exemple en imposant une pression nulle en sortie et un profil d'écoulement prédéterminé en entrée. Plus récemment, des modèles complets de ventilation ont été proposés en couplant trois sous–systèmes [Sou07, BGM10] : un modèle tri–dimensionnel des premières générations de l'arbre bronchique est couplé à des tubes résistifs modélisant la partie distale de l'arbre, eux–mêmes couplés à un modèle 0D du parenchyme. Ces modèles permettent de prendre en compte le fait que l'écoulement dépend de la partie distale de l'arbre, et notamment est entraîné par le mouvement du diaphragme et du parenchyme.

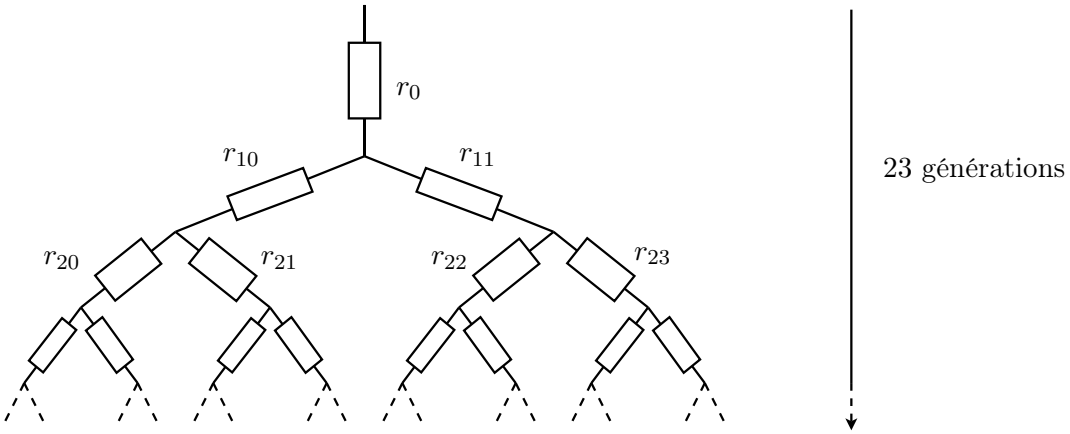

Figure 7 – Représentation idéalisée de l'arbre bronchique par un arbre résistif

Toutefois, le caractère fractal de l'arbre bronchique limite ces efforts de modélisation en géométrie réelle aux premières générations de l'arbre, pour des raisons de complexité numérique autant que pour les difficultés liées aux limites de l'imagerie médicale. Afin de décrire la partie distale de l'arbre bronchique qui ne peut pas être prise en compte dans une approche tri-dimensionnelle, d'autres modèles proposent d'utiliser une représentation par un *arbre dyadique résistif*. Ces modèles font l'hypothèse que la loi de Poiseuille (0.3) est vérifiée dans chaque voie aérienne par un conduit cylindrique comme sur la Figure 6. Les données biologiques de dimension des bronches étant connues [Wei63], on peut en calculer les résistances, qui résument les propriétés dynamiques de l'écoulement de l'air à travers chaque bronche. Ces dernières sont reliées ensuite en réseau comme présenté sur la Figure 7. L'écoulement de l'air à travers l'arbre se calcule en utilisant la loi de Poiseuille sur chaque branche pour relier les pressions à chaque noeud (bifurcation) de l'arbre et le flux sur chaque arête. Ce modèle permet de se faire une idée de l'impact des différents paramètres de la structure fractale sur la distribution d'air aux alvéoles, comme par exemple l'importance du facteur de réduction du

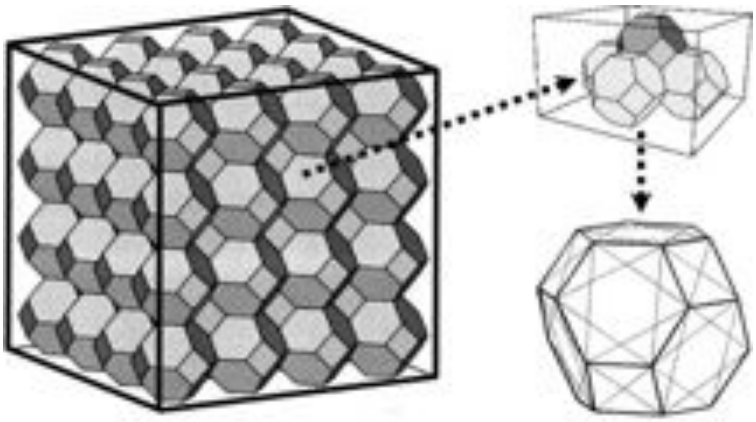

Figure 8 – Assemblage d'octaèdres tronqués modélisant un bloc cubique de parenchyme pulmonaire, tiré de [DS06]

diamètre et de la longueur des bronches à chaque branchement dichotomique [MFWS04], ou encore les effets de l'asymétrie de l'arbre [FSF11]. Une étude détaillée des propriétés mathématiques de ces arbres, et notamment du passage à la limite vers un nombre de générations infini pour brancher les sorties de l'arbre dans un espace continu a été réalisée dans [Van09, VSM09].

On notera que cette représentation est basée sur des hypothèses fortes : les effets inertiels sont négligés, les bronches sont représentées comme des conduits rigides et cylindriques, et l'effet des bifurcations sur l'écoulement n'est pas pris en compte. Dans le cas du poumon humain, on note en particulier que les effets inertiels sont importants au niveau de la trachée où la vitesse de l'air atteint plusieurs mètres par seconde [Wei84]. Des simulations numériques ont montré qu'ils ne pouvaient pas être négligés pour calculer le flux d'air dans les premières générations de l'arbre [MFAS03]. Toutefois, ils s'atténuent rapidement au fur et à mesure que l'on avance dans l'arbre, jusqu'à devenir négligeables à partir de la cinquième génération en régime de repos. Ainsi, bien qu'il ne soit pas réaliste de représenter l'ensemble de l'arbre bronchique par un arbre dyadique résistif, on pourra considérer que l'arbre dyadique résistif modélise bien la partie distale de l'arbre, à partir de la génération 5 en respiration normale par exemple [Van09].

Modèles du tissu alvéolaire. La littérature est moins abondante en ce qui concerne la façon de déduire les propriétés mécaniques du tissu pulmonaire. Son comportement ne ressemble à aucun de celui de ses composants individuels, mais résulte plutôt de leur interaction et leur agencement : dans [SB11], le recrutement progressif des fibres de collagène dans le réseau de fibres élastiques est modélisé à l'aide de réseaux de ressorts. Ce modèle montre un effet de percolation, responsable du comportement non–linéaire.

D'autres auteurs proposent de se baser sur le calcul numérique des propriétés d'un modèle mécanique d'alvéole pour extrapoler les propriétés macroscopiques du parenchyme pulmonaire. Un octaèdre tronqué (Figure 8) est le plus souvent utilisé pour représenter les alvéoles. Dans [DMS80], l'alvéole est représentée comme un réseau de fibres élastiques. Dans [KSMH86], la tension de surface est ajoutée au modèle. Dans [DS06], un bloc de 91 alvéoles assemblées en cube est étudié numériquement pour en déduire une loi de comportement mécanique. Dans [Sni08], la ventilation au niveau de l'acinus est étudiée.

En ce qui concerne la propagation du son, les modèles théoriques sont en général simples et basés sur le modèle de Rice [Ric83] où le parenchyme est représenté par une mixture homogène de gaz et de tissu. Un modèle uni–dimensionnel est aussi présenté dans [GWN02].

Plus récemment, des modèles mathématiques du parenchyme basés sur la théorie de l'homogé-

néisation ont été développés, en se basant sur des développements asymptotiques [OL01, SJTL08]. Dans le cas statique, une dérivation rigoureuse du comportement macroscopique du parenchyme est proposée dans l'article [BGMO08] en utilisant la théorie de la convergence double–échelle, en partant d'une modélisation microscopique du parenchyme comme un matériau poreux satisfaisant les équations de l'élasticité linéarisée et contenant des cavités déconnectées, réparties périodiquement, remplies d'air satisfaisant par la loi des gaz parfaits.

Couplage arbre bronchique et parenchyme. Peu de modèles existent qui proposent à la fois une représentation détaillée de l'arbre bronchique et du parenchyme et cherchent à coupler ces deux éléments dans un modèle mécanique. Récemment, des modèles multiéchelles purement numériques cherchant à coupler tous les niveaux (alvéoles, parenchyme tri–dimensionnel et arbre bronchique) ont été développés [WWCR10, WCRW11]. L'article [GMM06] est un premier pas dans la direction d'une dérivation rigoureuse d'une loi mécanique pour le parenchyme pulmonaire en étudiant un système de masses et de ressorts 1D branché avec un arbre dyadique résistif (Figure 7).

Problèmes considérés et notre approche de modélisation

Modélisation du parenchyme en prenant en compte la ventilation. Nous avons dans un premier temps cherché à obtenir un modèle de complexité réduite qui permette de modéliser au niveau macroscopique le déplacement tri-dimensionnel du parenchyme pulmonaire tout en prenant en compte la ventilation de celui–ci par l'arbre bronchique. Nous reprenons ici la démarche adoptée dans [GMM06], en l'étendant à un cadre tri–dimensionnel, pour définir un modèle microscopique du parenchyme pulmonaire de manière à pouvoir rigoureusement en dériver un modèle effectif. Notons que ce modèle microscopique est aussi présenté dans [Van09], mais le passage au modèle macroscopique n'y est pas réalisé.

La première difficulté de cette étape de modélisation est le fait que le couplage du mouvement tri–dimensionnel du parenchyme (qui nous intéresse) avec le flux d'air lié à l'arbre qui ventile ce même parenchyme se réalise au niveau des alvéoles. Celles ci sont ainsi couplées entre elles de manière mécanique par le déplacement d'air à travers l'arbre. Les deux grandes classes de modèles prenant en compte les effets tri–dimensionels existant dans la littérature ne permettent ainsi pas d'étudier ce couplage :

- Lorsque l'on tronque l'arbre bronchique après quelques générations pour effectuer des simulations numériques détaillées, on coupe aussi ses liens mécaniques avec le déplacement du parenchyme ;
- Lorsque l'on obtient une représentation macroscopique du parenchyme comme un milieu élastique ou viscoélastique homogène, les alvéoles qui forment son lien avec l'arbre bronchique ont disparu du modèle qui devient donc indépendant de l'arbre bronchique.

Pour modéliser les connexions entre l'arbre bronchique et les alvéoles au sein du parenchyme, il est ainsi nécessaire de modéliser la partie distale de l'arbre bronchique. Nous considérons un **arbre dyadique résistif** que nous avons présenté plus tôt (Figure 7) pour représenter l'arbre bronchique dans notre modèle, y compris la partie distale. Nous faisons ainsi l'hypothèse que le flux d'air à travers l'arbre obéit à la loi de Poiseuille (0.3) dans chaque voie aérienne. L'arbre bronchique n'a pas de réalité géométrique au sein du modèle, mais est représenté de manière abstraite.

Cet arbre dyadique est ensuite connecté à un modèle tri–dimensionnel du parenchyme pulmonaire. Nous faisons l'hypothèse que le déplacement de l'air entre les alvéoles se fait uniquement au travers de l'arbre bronchique. Celui–ci ayant une représentation abstraite, nous représentons chaque alvéole comme une cavité isolée dans un matériau élastique. Ce matériau élastique représente le parenchyme pulmonaire composant le mur des alvéoles. Nous avons fait le choix de modéliser le comportement de ce matériau par les équations de l'élasticité linéarisée. Nous supposons de plus que

matériau est homogène, isotrope et non précontraint. Ces dernières hypothèses simplificatrices ne modifient pas l'étude théorique dans le contexte de l'élasticité linéarisée (voir par exemple [BG11]). Le couplage entre une alvéole et une branche terminale de l'arbre résistif dyadique est réalisé comme dans le modèle uni–dimensionnel [GMM06] en faisant correspondre :

- Variation de volume de l'alvéole et flux d'air entrant dans la branche de l'arbre,
- Pression de l'air dans l'alvéole, supposée uniforme, et pression au niveau de la sortie de la branche de l'arbre.

Enfin, nous faisons l'hypothèse que les alvéoles sont réparties périodiquement dans le parenchyme avec une période ε qui est donc la taille caractéristique de notre microstructure. Cette hypothèse simplificatrice nous permet d'utiliser la théorie de l'homogénéisation double–échelle. Au vu de la régularité de la distribution et de la taille des alvéoles dans le poumon (Figure 3), cela semble une hypothèse raisonnable, utilisée dans la plupart des modèles microscopiques du tissu alvéolaire (par exemple Figure 8). Notons d'ailleurs que les conduits alvéolaires, c'est–à–dire les voies aériennes les plus nombreuses et les plus directement au contact des sacs alvéolaires, n'ont pas de paroi bien définie et ne participent pas autrement à la mécanique que les parois alvéolaires. Nous proposons en Figure 9 une représentation en deux dimensions de notre modèle de parenchyme pulmonaire après cette étape de modélisation.

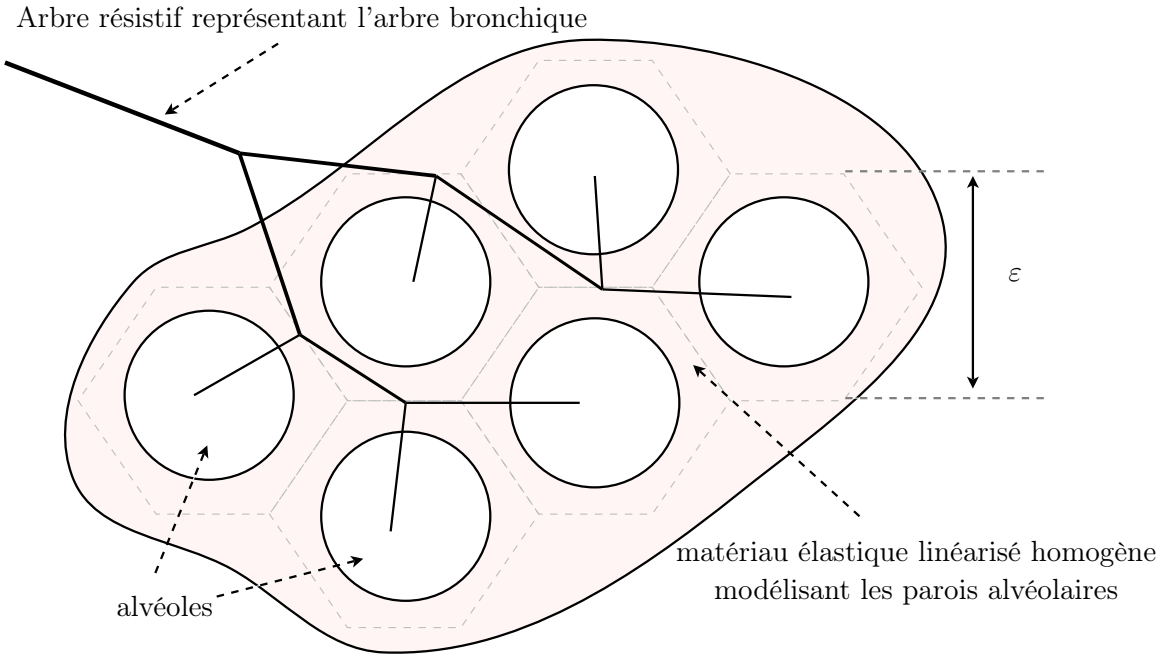

Figure 9 – Modèle du parenchyme pulmonaire

En complétant ce modèle par des conditions aux bords sur le domaine macroscopique et en fixant la pression à l'entrée de l'arbre bronchique, on obtient le déplacement du parenchyme comme solution d'un système d'équations bien posé [Van09]. Ceci constitue notre modèle microscopique du parenchyme pulmonaire.

Passage à la limite et difficultés particulières liées à l'arbre. L'étape suivante de cette modélisation multi–échelle consiste, comme nous l'avons annoncé, à obtenir rigoureusement un modèle macroscopique à partir de cette représentation microscopique. Pour réaliser ce passage, nous employons la théorie mathématique de l'homogénéisation double–échelle. L'idée est de faire tendre vers zéro le paramètre ε, qui est la taille caractéristique de l'échelle microscopique, et d'étudier le

comportement asymptotique des solutions du problème microscopique paramétré par ε. En l'absence de l'arbre, le problème se ramène à l'homogénéisation périodique des équations de l'élasticité linéaire posées sur un domaine perforé, qui est un problème classique, voir e.g. [BLP78]. Nous retrouvons aussi dans notre étude certaines difficultés résolues dans l'article [BGMO08] liées aux conditions aux bords particulières au niveau des alvéoles.

Les difficultés nouvelles que nous avons étudiées lors de notre étude asymptotique par la méthode de la convergence double–échelle sont reliées à la présence de l'arbre dyadique résistif. Celui–ci couple de manière non–locale les conditions aux bords posées sur le matériau élastique au niveau des alvéoles. Au vu du modèle présenté sur la Figure 9, il est nécessaire, avant de passer à la limite double–échelle, de décrire son comportement c'est–à–dire son action dans le modèle lorsque ε tend vers zéro. Pour simplifier l'analyse et identifier les conditions nécessaires à la convergence, nous avons choisi le formalisme suivant. En reliant de façon linéaire les flux et les pressions aux niveau des alvéoles, l'action de l'arbre peut être représentée par un opérateur Dirichlet–to–Neumann. Comme ces quantités peuvent être assimilées à des fonctions constantes par morceaux sur chaque alvéole du domaine macroscopique, nommé Ω, l'action de l'arbre prend ainsi naturellement la forme d'un opérateur appartenant à $\mathcal{L}\left(L^2(\Omega)\right)$ que l'on nomme $\mathcal{R}_\varepsilon$, voir la Figure 10. Cette description étend naturellement au cas multi–dimensionel l'analyse développée dans [GMM06] pour plonger les bouts d'un arbre résistif dans le segment $[0, 1]$.

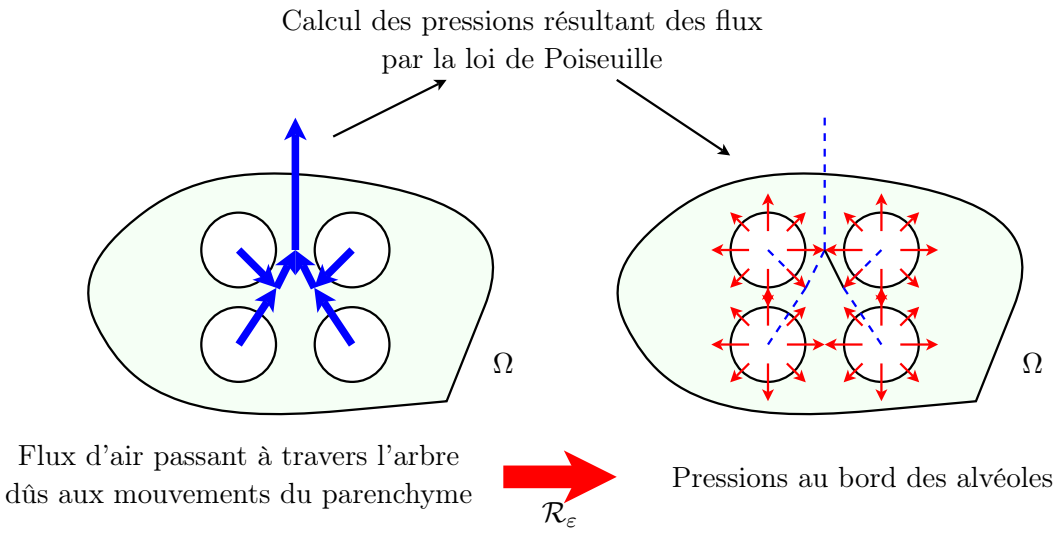

Figure 10 – Représentation schématique de l'action de l'opérateur Dirichlet–to–Neumann $\mathcal{R}_\varepsilon$.

Nous proposons de caractériser la convergence de l'action de l'arbre par convergence de la suite des opérateurs $\mathcal{R}_\varepsilon$ dans $\mathcal{L}\left(L^2(\Omega)\right)$ vers un certain opérateur $\mathcal{R}$ que l'on identifie et que l'on peut associer à un arbre infini dont les bouts irriguent chaque point du domain Ω. On retrouve ainsi à la limite l'opérateur Dirichlet–to–Neumann associé à un arbre infini étudié dans [VSM09]. L'analyse théorique de l'homogénéisation double–échelle peut alors se diviser en deux questions, et donc deux difficultés, que nous traiterons de manière distincte :

- La convergence de la suite $\mathcal{R}_\varepsilon$ vers un opérateur $\mathcal{R}$ dans l'espace $\mathcal{L}\left(L^2(\Omega)\right)$ est–elle bien une condition suffisante pour obtenir rigoureusement un problème macroscopique à partir du modèle microscopique proposé ? Pour répondre à cette question dans le Chapitre 1, nous avons fait appel aux outils de la convergence double–échelle et de l'analyse des équations aux dérivées partielles.
- Comment construire des suites d'arbres résistifs dyadiques, connectés aux alvéoles du domaine Ω pour chaque $\varepsilon > 0$, tels que les opérateurs $\mathcal{R}_\varepsilon$ convergent ? La réponse à cette question n'est

pas unique, et nous présentons dans le Chapitre 2 deux constructions possibles, partant de représentations de l'irrigation du poumon par l'arbre bronchique différentes. Dans les deux cas, il faut résoudre d'abord une difficulté d'ordre géométrique : comment organiser les connexions entre les alvéoles et l'arbre dyadique pour chaque $\varepsilon > 0$, et ensuite s'intéresser aux conditions nécessaires sur les résistances de ces arbres pour assurer la convergence de l'opérateur $\mathcal{R}_\varepsilon$.

Pour répondre à cette deuxième question, il est en particulier nécessaire d'identifier comment l'arbre connecte géométriquement les différentes parties du domaine. Nous nous sommes ici appuyés sur l'analyse présentée dans [VSM09] pour décrire comment connecter un arbre infini et un domaine multi–dimensionnel. L'idée est d'introduire une décomposition dyadique du domaine, qui correspond à la répartition du domaine en portions irriguées chacune par une bronche. En suivant les bifurcations des voies aériennes, on organise hiérarchiquement cette décomposition, voir la Figure 11. Ces décompositions sont basées sur l'observation naturelle que chaque bronche irrigue un sous–ensemble déterminé du poumon, ce qui permet, en descendant l'arbre bronchique, de former la hiérarchie des unités fonctionnelles du poumon : poumon droit/gauche, lobes pulmonaires, acini, etc...

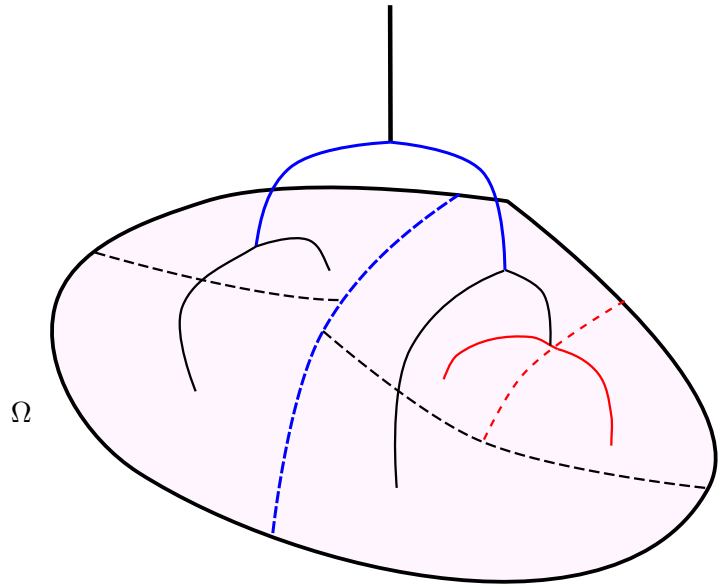

Figure 11 – Irrigation d'un domaine par un arbre dyadique, et une décomposition de domaine associée.

Propagation du son. Dans la deuxième partie, nous modifions notre modèle microscopique de parenchyme pour étudier les propriétés de propagation du son, c'est–à–dire le comportement mécanique à haute fréquence du matériau. Toujours dans une optique de modélisation multi–échelle, nous cherchons ensuite à obtenir rigoureusement un modèle macroscopique qui rende compte de certaines des propriétés curieuses du matériau présentées sur la Table 1. L'arbre bronchique ne participant pas à la propagation du son à travers le parenchyme pour des fréquences supérieures à une ou deux centaines de Hertz [Kra83, BLD87], nous nous sommes intéressés à un simple modèle de mousse fermée en retirant l'arbre résistif du modèle précédent et en modélisant l'air présent dans les alvéoles comme un gaz compressible.

Nous étudions ensuite successivement deux variations de ce modèle :

- d'abord, nous étudions le couplage d'un matériau élastique dans la structure avec l'air modélisé par un gaz parfait satisfaisant l'équation des ondes acoustiques. Afin de mieux comprendre le phénomène de propagation d'ondes, nous nous plaçons à fréquence fixée c'est–à–dire en régime harmonique. Cette étude est présentée dans le Chapitre 4 ;
- ensuite, nous cherchons à comprendre et calculer l'influence possible de l'hétérogénéité de la paroi alvéolaire, en particulier l'influence possible entre des composants visqueux et élastique. Nous remplaçons dans ce cas le matériau élastique qui forme la structure dans les deux modèles précédents par un matériau viscoélastique hétérogène, et nous modélisons l'air contenu dans les alvéoles comme un gaz parfait compressible. Cette étude est présentée dans le Chapitre 5.

Avant de décrire nos résultats concernant ces différents problèmes, nous présentons la théorie de l'homogénéisation double–échelle, et en particulier les applications de l'homogénéisation à la modélisation des déformations ou des vibrations des milieux poreux périodiques.

Outil mathématique : l'homogénéisation

Le principal outil mathématique qui nous permet d'étudier le passage à la limite lorsque la taille de la micro–structure ε tend vers zéro dans nos trois modèles est la théorie de l'homogénéisation, et plus précisément puisque nous travaillons dans un cadre périodique la **convergence à deux échelles** [Ngu89, All92]. L'idée de cette méthode est de découpler à la limite la dépendance de quantités du modèle telles que le déplacement en la variable macroscopique, $\mathbf{x}$, et en la position microscopique $\mathbf{y} = \mathbf{x}/\varepsilon$. La variable $\mathbf{x}$ donne la position du point considéré à l'intérieur du domaine macroscopique, et la variable $\mathbf{y}$ donne sa position à l'intérieur d'une cellule périodique $\mathcal{Y}$ représentative de la microstructure du matériau.

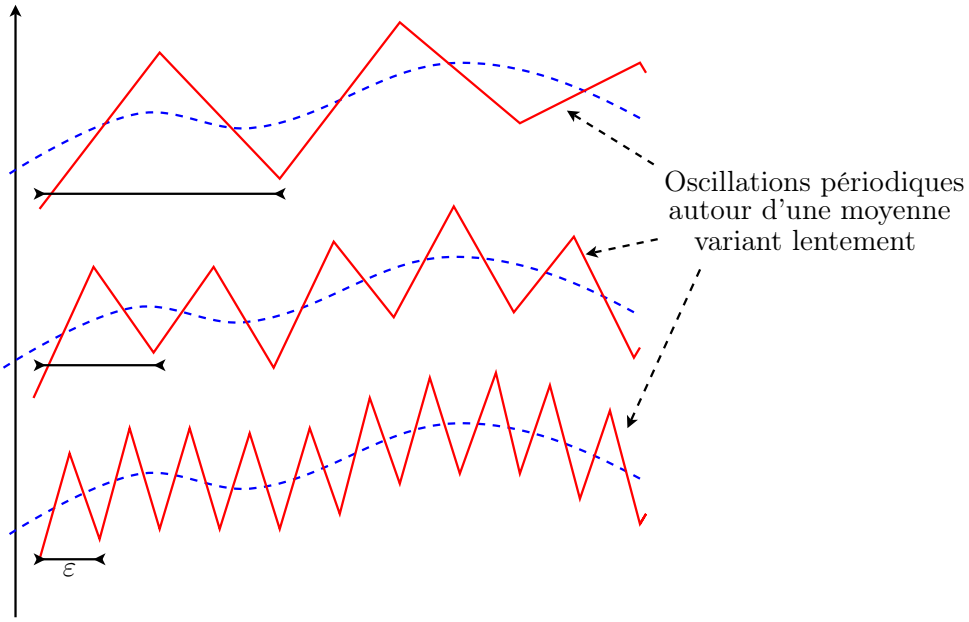

Figure 12 – Suite de fonctions oscillantes sur un segment : dans ce cas $\mathcal{Y} = [0, 1]$

Par exemple, si une suite de fonctions $(u_\varepsilon)_{\varepsilon>0}$ admet un développement asymptotique sous la forme

$$u_\varepsilon(\mathbf{x}) = u(\mathbf{x}, \mathbf{x}/\varepsilon) + \varepsilon u^1(\mathbf{x}, \mathbf{x}/\varepsilon) + \dots,$$

alors sa limite double échelle est la fonction $u(\mathbf{x}, \mathbf{y})$ définie sur $\Omega \times \mathcal{Y}$. Ainsi, la limite double–échelle d'une suite de fonctions oscillant avec la période ε garde la trace de ces oscillations. Notons que la

limite faible dans $L^2(\Omega)$ donne la moyenne de ces oscillations sur une période, soit $\mathbf{x} \mapsto \int_{\mathcal{Y}} u(\mathbf{x}, \mathbf{y}) \mathrm{d}\mathbf{y}$ (voir Figure 12).

L'étude par homogénéisation des milieux poreux, dont le poumon fait partie, est un sujet très étudié car il propose une description très efficace notamment des ondes sonores dans ce milieu. Nous proposons ici une revue des cas déjà traités, sans prétendre à une bibliographie exhaustive, en nous intéressant plus particulièrement à l'homogénéisation des équations de la propagation du son ou bien des vibrations dans un milieu poreux périodique couplant une structure élastique connectée et une partie fluide. Des résultats généraux sur l'homogénéisation périodique sont présentés dans [BLP78, All92, LNW02].

De l'histoire ancienne. Lord Rayleigh, en 1883 [Str83], proposait déjà de décrire la propagation et l'absorption du son dans un milieu périodique, constitué d'un échantillon perforé périodiquement de tubes perpendiculaires à la surface, et en modélisant la structure comme rigide. En conduisant des calculs sur le flux d'air dans un seul tube de la structure il en déduit des propriétés pour l'ensemble du matériau, idée qui constitue l'essence de l'homogénéisation périodique.

L'étape suivante fut franchie par Biot en 1956 [Bio56a, Bio56b, Bio62] avec l'introduction d'un élément représentatif du volume, c'est–à–dire d'une **cellule périodique** dont la géométrie est représentative de la microstructure du matériau. La structure satisfait les équations de l'élasticité linéarisée et le fluide par les équations de Navier–Stokes linéarisées. En étudiant le système fluide–structure couplé sur la cellule représentative, Biot en déduit un modèle pour la propagation des ondes acoustiques dans le milieu poreux au niveau macroscopique qui sert encore de référence aux physiciens aujourd'hui.

Homogénéisation par développements asymptotiques. L'étude mathématique rigoureuse de ces matériaux poreux commence ensuite avec l'utilisation des développements asymptotiques formels. Les premiers résultats sont proposés par Ene, Lévy et Sanchez–Palencia en étudiant un fluide visqueux incompressible en régime stationnaire [ESP75, L77] ou un fluide acoustique [LSP77] dans une structure rigide. L'homogénéisation du couplage d'un fluide visqueux avec une structure élastique est étudiée ensuite par Lévy [L79], Sanchez–Hubert [SH79] ou encore Sanchez–Palencia [SP80] (chapitre 8). Enfin Auriault [Aur80] ainsi que Burridge et Keller [BK82] retrouvent formellement les équations de Biot. Une revue des résultats nombreux obtenus par les développements asymptotiques formels est proposée dans [SP86]. La méthode de l'énergie de Tartar est utilisée pour prouver certains de ces résultats, voir par exemple [Tar80].

Homogénéisation double–échelle. La convergence double–échelle [Ngu89, All92] a ensuite permis d'étudier de manière rigoureuse toutes sortes de problèmes liés aux milieux poreux. Cette méthode est particulièrement adaptée à l'homogénéisation de problèmes périodiques car elle permet de combiner en une étape la recherche du problème homogénéisé et la preuve de la convergence. La méthode de l'énergie de Tartar [Tar80], que l'on peut utiliser dans des cas plus généraux que le cas périodique, demande en effet l'étude préalable du problème en utilisant les développements asymptotiques formels. L'étude des équations de Stokes stationnaires couplées avec une structure rigide est proposée par Allaire [All89]. Une preuve rigoureuse dans le cas d'une structure élastique couplée avec un fluide faiblement compressible et visqueux est donnée par Nguetseng [Ngu90], qui souligne la différence dans les matériaux homogénéisés obtenus suivant la connexité du domaine fluide. Dans [ESJP95], Saint–Jean Paulin et Ene présentent l'étude d'une structure élastique périodique mince immergée dans un fluide visqueux et étudient la convergence en fonction de deux paramètres : la taille de la cellule de référence ε et aussi l'épaisseur du solide. Dans [Das95], le cas d'un fluide visqueux incompressible couplé avec une structure élastique est étudié par pénalisation en utilisant la méthode de Laplace pour obtenir la limite du problème instationnaire en temps. On

peut citer aussi l'extension de l'étude aux équations d'Euler, donc pour un fluide instationnaire, incompressible et non visqueux, soit dans le cas linéarisé couplé à une structure élastique [FM03], soit dans le cas non–linéaire dans une structure rigide [LM05]. Une étude comportant une structure viscoélastique est présentée par exemple dans [SS11].

Les applications à des problèmes de modélisation issus de la physique ont ensuite été étudiées. Dans [GM00, CFGM01], l'étude motivée par la propagation du son dans les fonds marins montre l'existence de quatre comportements possibles suivant le contraste entre la viscosité ν du fluide et les coefficients élastiques du solide, choisis d'ordre $O(1)$:

- pas de contraste, $\nu = O(1)$: le comportement macroscopique est monophasique et *viscoélastique* et on peut voir apparaître des effets de mémoire en temps long,
- faible contraste, $\nu = O(\varepsilon)$: le comportement macroscopique est monophasique et *élastique*,
- contraste élevé, $\nu = O(\varepsilon^2)$: le comportement macroscopique est *diphasique*, c'est–à–dire que le fluide et la structure sont en mouvement relatif et exercent des forces l'un sur l'autre, à condition que l'espace poreux du fluide soit connexe,
- Contraste très élevé, $\nu = O(\varepsilon^3)$: le matériau macroscopique présente deux phases découplées fluide et structure, avec notamment l'acoustique d'un fluide dans une matrice rigide comme dans [Ĺ77], toujours à condition que le domaine du fluide soit connexe.

On peut citer également les travaux de Meirmanov dans [Mei08a, Mei08b, Mei08c] qui s'attachent à retrouver les équations de Biot en couplant les variables physiques de température, pression, et déplacement dans un problème fluide–structure écrit en temps.

Plus récemment, cette méthode a également été appliquée à la modélisation de la propagation du son dans de la laine de verre [Aug10, AAGM12] en considérant les équations couplées d'une structure élastique et d'un fluide incompressible et visqueux dans le domaine fréquentiel, un cas qui pose quelques problèmes spécifiques que nous rencontrerons aussi dans l'analyse de la propagation du son proposée dans le Chapitre 4, ou encore à la modélisation de la peau [BG11] en utilisant la méthode de l'éclatement périodique.

Enfin, l'article [BGMO08] utilise la convergence double–échelle pour obtenir un modèle homogénéisé du parenchyme dans le cas statique. Dans ce travail, la structure est modélisée par les équations de l'élasticité linéarisée et contient des cavités isolées, réparties de façon périodique, contenant l'air modélisé comme un gaz compressible satisfaisant l'équation des gaz parfaits. On verra les liens que ce modèle peut avoir avec les modèles que nous avons développé.

Présentation des résultats de cette thèse

Partie 1 : Modélisation de la ventilation

La première partie de cette thèse est consacrée à l'étude du modèle de parenchyme que nous avons représenté dans ses grandes lignes sur la Figure 3. L'étude repose sur les propriétés asymptotiques de l'opérateur de résistance de l'arbre que nous avons introduit (Figure 10).

Nous divisons l'analyse théorique en deux parties. Dans le premier chapitre, nous montrons que la condition de convergence des opérateurs $\mathcal{R}_\varepsilon$ est une condition suffisante pour réaliser l'homogénéisation du modèle. Dans le deuxième chapitre, nous regardons de plus près la construction des opérateurs $\mathcal{R}_\varepsilon$ et analysé sous quelles conditions on pouvait obtenir cette convergence. Finalement, nous proposons dans le troisième chapitre un algorithme numérique permettant d'utiliser le modèle homogénéisé pour simuler numériquement la ventilation du parenchyme dans quelques cas test.

Chapitre 1 Nous commençons par une description précise de notre modèle de ventilation du parenchyme. Nous reprenons le formalisme géométrique de l'article [BGMO08] tout en connectant

les alvéoles à un arbre dyadique résistif et en décrivant la construction et les propriétés de l'opérateur $\mathcal{R}_\varepsilon$. Nous procédons ensuite à l'analyse mathématique du modèle et à son homogénéisation par la méthode de la convergence double–échelle [All92] dans les deux cas d'une structure compressible et incompressible. Dans ce chapitre, le comportement de l'arbre lorsque ε tend vers zéro est résumé par la condition abstraite de convergence des opérateurs $\mathcal{R}_\varepsilon$ dans $\mathcal{L}\left(L^2(\Omega)\right)$.

Dans un premier temps, nous traitons le cas compressible pour lequel l'existence et l'unicité de solutions ont été montrées dans [Van09] pour ε fixé, c'est–à–dire un nombre fini d'alvéoles. Nous reprenons brièvement l'analyse réalisée dans [Van09] pour montrer que l'on peut, en sus de l'existence et de l'unicité des solutions, obtenir des estimations *a priori* indépendantes de ε grâce à notre formalisme. En utilisant les propriétés fondamentales de la convergence double échelle que nous rappelons brièvement, ces estimations *a priori* nous permettent d'obtenir les limites double échelle des inconnues qui décrivent le déplacement du matériau mais aussi le flux et la pression à travers les alvéoles. Nous obtenons ensuite le système homogénéisé double échelle en utilisant la condition abstraite de convergence de l'arbre. En appliquant les techniques classiques, nous éliminons ensuite les variables microscopiques du problème à l'aide de correcteurs, et nous obtenons enfin le problème homogénéisé. Celui ci fait apparaître comme variable macroscopiques à la fois le déplacement moyenné du matériau et aussi une variable de pression qui rappelle l'action de l'air dans les alvéoles. Les nouveaux coefficients décrivant le matériau, par exemple les coefficients élastiques, sont obtenus en résolvant des *problèmes de cellule* sur la cellule périodique adimensionnalisée. Nous montrons que ce système homogénéisé est bien posé. L'analyse de la loi mécanique obtenue ainsi montre que le matériau homogénéisé présente un comportement *viscoélastique* avec des effets de mémoire en temps long ainsi que des effets de dissipation non–locale en espace induits par l'arbre résistif.

Dans un deuxième temps, nous étudions l'homogénéisation du modèle dans le cas d'une structure incompressible. Par rapport au cas précédent, les éléments nouveaux sont liés à l'apparition d'une variable de pression dans la structure liée à la contrainte d'incompressibilité : pour montrer une estimation *a priori* indépendante de ε, nous utilisons la démarche introduite par Conca [Con85] pour étendre la pression à tout le domaine, puis nous poursuivons la même analyse que dans le cas compressible pour obtenir le problème homogénéisé. Nous comparons le modèle obtenu avec le cas compressible : on s'aperçoit que les effets de mémoire en temps long disparaissent. Le matériau homogénéisé dans le cas incompressible présente ainsi des effets de dissipation non–locale en espace, mais instantanés en temps.

Chapitre 2 Nous nous intéressons ensuite à la question, d'ordre plus géométrique, de la convergence de la suite des opérateurs $\mathcal{R}_\varepsilon$. Pour étudier cette question, nous rappelons dans un premier temps le formalisme des décompositions de domaine dyadiques et multi–échelles (voir Figure 11) introduites dans [VSM09]. Nous proposons ensuite deux constructions géométriques qui permettent de connecter une suite d'arbres résistifs aux alvéoles réparties périodiquement sur le domaine Ω pour chaque $\varepsilon > 0$, d'étudier les conditions à imposer à l'arbre résistif pour obtenir la convergence et enfin d'étudier le taux de convergence des opérateurs.

Tout d'abord, nous proposons une construction idéalisée dont nous donnons un exemple dans un carré ou un cube, inspirée par la construction de modèles d'arbres fractals par Mandelbrot [Man82] qui remplissent l'espace, comme l'exemple proposé en Figure 13. Dans ce cas, on se restreint à la suite de paramètres $\varepsilon_n = 2^{-n}$ en associant naturellement un arbre dyadique résistif (à dn générations en dimension d) à l'arbre fractal qui est connecté aux cellules carrées de côté 2^{-n} comme sur la Figure 13 (b). Nous étendons l'analyse présentée dans [GMM06] au cas multi–dimensionnel pour montrer la convergence de l'opérateur $\mathcal{R}_\varepsilon \equiv \mathcal{R}_n$ associé à l'arbre vers un opérateur $\mathcal{R}$ associé à l'arbre infini. De plus, on peut préciser le taux de convergence dans le cas d'un arbre régulier et géométrique c'est–à–dire dont les résistances (voir la Figure 7) sont égales à chaque génération et

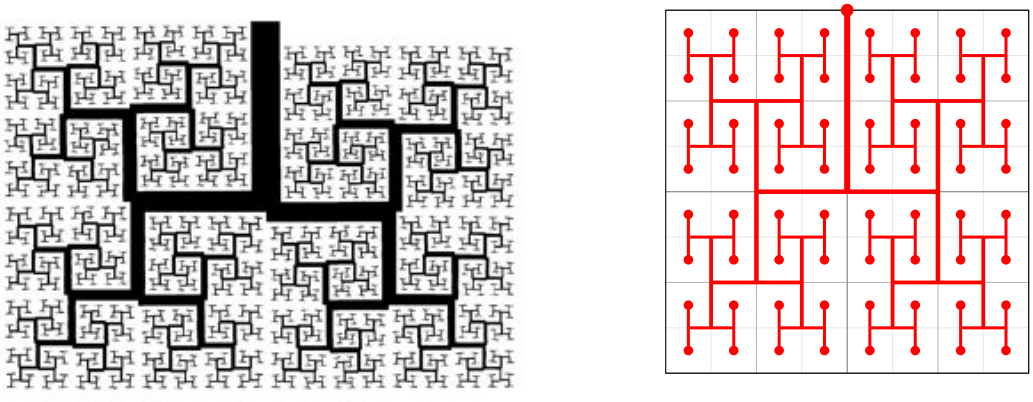

(a) modèle proposé par Mandelbrot [Man82] (b) Construction itérative d'un arbre dyadique

Figure 13 – Construction idéalisée d'arbre bronchique

données par une loi géométrique de paramètre $\alpha \in]0, 2[$:

$$r_{n,k} = r_0 \alpha^n.$$

On obtient ainsi un taux de convergence également géométrique :

$$\|\mathcal{R} - \mathcal{R}_n\|_{\mathcal{L}(L^2(\Omega))} \sim \left(\frac{\alpha}{2}\right)^{dn+1} = (\varepsilon_n)^q \quad \text{avec } q = d\left(1 - \frac{\ln(\alpha)}{\ln(2)}\right).$$

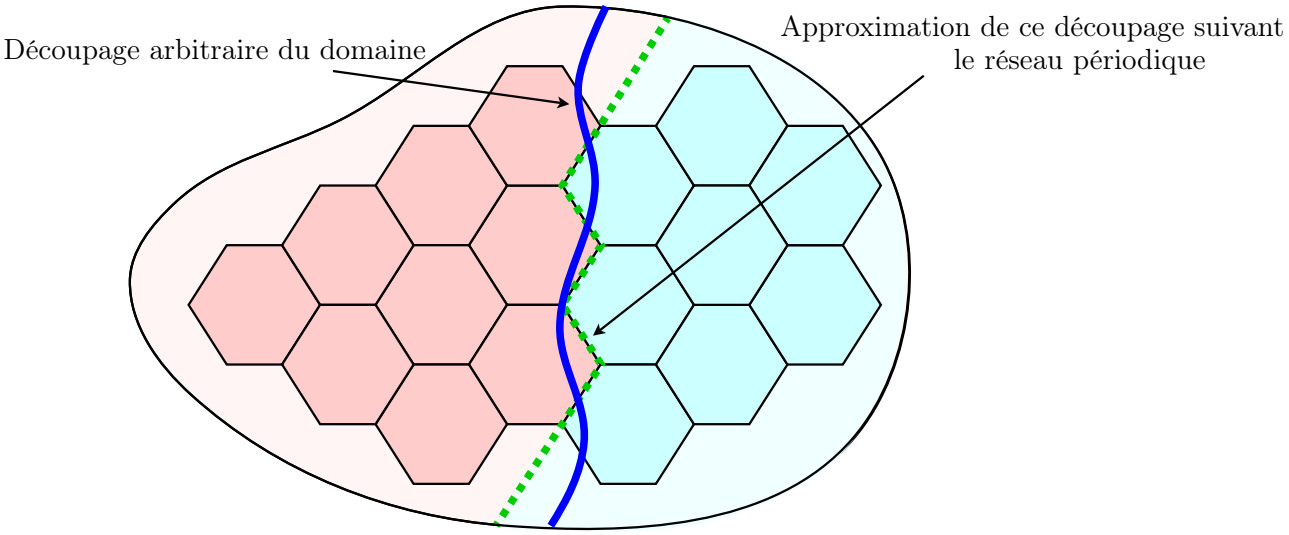

Figure 14 – Approximation d'un découpage du parenchyme en suivant le pavage périodique

Ensuite, nous nous sommes intéressés au problème de faire correspondre un domaine divisé de manière arbitraire avec notre réseau d'alvéoles périodiquement réparties. Partant cette fois d'une décomposition multi–échelle donnée *a priori* et vérifiant une nouvelle condition de régularité uniforme, que nous appelons condition d'approximabilité, nous montrons comment répartir les alvéoles parmi les sous–domaines de la décomposition pour chaque $\varepsilon > 0$ de manière à respecter autant que possible le découpage du parenchyme prescrit *a priori* (voir la Figure 14).

Cette méthode permet en particulier de justifier l'utilisation de cellules périodiques telles que les hexagones en 2D ou les octaèdres tronqués en 3D, qui ne peuvent pas être pavés par des copies réduites d'eux mêmes contrairement aux carrés, ou encore de s'intéresser à des décompositions de domaine asymétriques. Grâce aux propriétés d'approximation de notre algorithme, dont la preuve est donnée en annexe du chapitre, nous sommes en mesure d'analyser la convergence des opérateurs $\mathcal{R}_\varepsilon$ construits par notre algorithme vers l'opérateur $\mathcal{R}$ associé à la décomposition initiale. Nous obtenons aussi une estimation de la vitesse de convergence des opérateurs, sous une condition intuitive qui traduit le fait que les plus grosses bronches doivent irriguer les plus gros sous domaines dans le cas d'un découpage asymétrique du domaine. En se plaçant dans le cas d'un découpage symétrique pour comparer avec la première construction, nous obtenons pour un arbre géométrique le taux de convergence suivant :

$$\|\mathcal{R} - \mathcal{R}_\varepsilon\|_{\mathcal{L}(L^2(\Omega))} \sim \varepsilon^q \quad \text{avec } q = \min\left(\frac{1}{2}, \frac{d}{2}\left(1 - \frac{\ln(\alpha)}{\ln(2)}\right)\right).$$

Chapitre 3 Pour terminer l'étude de notre modèle de ventilation, nous nous sommes intéressés à la simulation numérique de notre matériau homogénéisé à l'aide d'une méthode des éléments finis. La difficulté est ici l'opérateur non–local $\mathcal{R}$ qui se transforme en matrice pleine s'il est discrétisé sur la base des éléments finis, rendant la poursuite des calculs rédhibitoire. Nous proposons une méthode de discrétisation qui permet d'utiliser deux algorithmes basés sur la structure d'arbre. Ces algorithmes permettent de calculer très rapidement les produits matrice–vecteur associés à l'opérateur approximant $\mathcal{R}$ dans la base des éléments finis. Nous utilisons de cette façon la méthode du gradient conjugué pour résoudre les systèmes linéaires rapidement même si la matrice du système discrétisé, jamais construite, est une matrice pleine (mais définie positive). Nous avons utilisé le logiciel FreeFem++ [Hec12] pour obtenir des premiers résultats numériques sur un cas bi–dimensionnel en simulant la ventilation et en étudiant l'effet des modifications de certains paramètres. Enfin, nous proposons une étude numérique de la dissipation d'énergie en fonction du paramètre α des résistances de l'arbre.

Partie 2 : Modélisation de la propagation du son à travers le parenchyme

Les deux derniers chapitres de cette thèse sont consacrés à l'élaboration et à l'exploitation d'un modèle de propagation du son à travers le poumon. Cette étude a été réalisée en collaboration avec Jan Hesthaven à Brown University. Aucune analyse rigoureuse n'ayant été proposée dans la littérature pour modéliser le parenchyme pulmonaire dans le régime acoustique, nous avons commencé par essayer de retrouver par nos méthodes d'homogénéisation double–échelle le modèle de Rice [Ric83] qui correspond assez bien à l'expérience, du moins dans le régime des basses fréquences, en prédisant une vitesse du son très basse, de l'ordre de $30m/s$. Dans un deuxième temps, nous avons essayé de voir si nous pouvions reproduire avec un modèle homogénéisé de parenchyme la dépendance curieuse en fréquence observée dans le poumon humain (Table 1), et si nous pouvions utiliser ce modèle homogénéisé pour conduire des expériences numériques de propagation d'onde. Dans les deux cas, nous n'avons pas considéré l'effet de l'arbre bronchique sur la propagation des ondes sonores.

Chapitre 4 Pour débuter cette étude, nous avons commencé par regarder un modèle relativement simple couplant une structure hétérogène satisfaisant les équations de l'élasticité linéaire, et perforée périodiquement par des cavités fermées et remplies d'un gaz satisfaisant les équations de l'acoustique, c'est–à–dire un fluide compressible et non visqueux. Pour mieux comprendre la propagation des ondes acoustiques, nous nous sommes placés à fréquence fixée et nous avons donc posé les équations dans le domaine fréquentiel, le but étant de mieux comprendre les caractéristiques de

notre parenchyme homogénéisé à chaque fréquence donnée. Ce modèle, qui n'avait pas été étudié auparavant, pose un problème mathématique particulier car la formulation en fréquence rend la forme sesquilinéaire associée à la formulation variationnelle du problème non coercive dans l'espace où nous cherchons nos solutions. Ceci nous empêche de prouver l'existence et l'unicité pour toutes les valeurs de la fréquence ω, mais aussi de prouver des estimations *a priori* qui permettent de passer à la limite double–échelle [All92]. Toutefois, il est possible de montrer que le problème satisfait une alternative de Fredholm. Pour contourner cette difficulté, nous utilisons un raisonnement par l'absurde utilisé précédemment par exemple dans [BF04,AGMR08,AAGM12] qui permet de justifier le passage à la limite grâce au procédé d'homogénéisation, en montrant que les fréquences de résonance du problème homogénéisé sont justement les seules fréquences où le passage à la limite n'est pas possible. Nous retrouvons au final un matériau satisfaisant les équations de élasticité linéarisée, dont les coefficients élastiques homogénéisés sont égaux à ceux obtenus pour le problème statique étudié dans [BGMO08].

Chapitre 5 L'étude du chapitre précédent montre que les propriétés du matériau obtenu par homogénéisation d'un simple matériau élastique, même hétérogène, ne permettent pas d'obtenir une dépendance en fréquence des propriétés du matériau. Dans cette seconde étude, nous modélisons les parois des alvéoles de notre modèle par un matériau *viscoélastique* et hétérogène. En effet, il est bien connu que l'addition d'une mince couche visqueuse entre deux couches élastiques a un effet important sur les qualités d'absorption d'un matériau [Rao03] et la géométrie particulière d'une alvéole, avec sa paroi mince composée de fibres élastiques et de matériaux visqueux (sang, substance fondamentale), peut présenter cet effet. L'air présent dans les alvéoles est modélisé par la loi des gaz parfaits comme dans [BGMO08], sans considérer la propagation des ondes acoustiques dans chaque alvéole, ce qui ne change pas le résultat dans la mesure où ces alvéoles sont fermées dans notre modèle. Par simplicité, nous étudions l'homogénéisation de ce modèle dans le domaine temporel suivant la méthode usuelle de convergence double–échelle. Le matériau homogénéisé que nous avons obtenu de cette façon présente des effets de mémoire nouveaux par rapport à ses composants, comme dans le cas de l'homogénéisation d'un matériau poreux couplant une structure élastique et un fluide visqueux [SP80].

Nous nous consacrons ensuite à la formulation d'une stratégie permettant de simuler numériquement le matériau obtenu et d'en étudier les propriétés. La loi limite présente des effets de mémoire en temps long, ce qui rend les simulations numériques extrêmement coûteuses si l'on essaie de discrétiser directement les termes intégrés en temps. Nous proposons d'éviter le calcul de cet intégrale en approchant le module de relaxation du matériau homogénéisé par une série de Prony, ce qui correspond à l'utilisation d'un modèle de Maxwell généralisé. Chaque terme de la série de Prony se traduit dans la méthode par la résolution d'une équation différentielle ordinaire additionnelle à chaque point du domaine discrétisé. Une stratégie utilisant la méthode des élements finis Galerkin discontinus est ensuite élaborée pour résoudre efficacement le problème de propagation de l'onde dans le milieu homogénéisé ainsi approché.

Finalement, nous présentons les résultats numériques de l'étude. Les calculs du module viscoélastique homogénéisé sont menés pour un grand nombre de valeurs de la fréquence, sur une géométrie test en 2D en utilisant FreeFem++. Ensuite nous discutons les résultats de l'optimisation par la méthode des moindres carrés des coefficients d'une série de Prony pour approcher au mieux la courbe suivie par les coefficients homogénéisés dans la gamme de fréquence considérée. Enfin, nous présentons des simulations numériques de propagations d'ondes dans le matériau homogénéisé, réalisées en utilisant le solveur Hedge [Klo10]. L'ensemble de ces résultats montre bien une grande dépendance du comportement du matériau en fonction de la fréquence, et montre aussi quelques artefacts dus à l'utilisation d'une cellule périodique carrée que nous commentons.

Part I

Mechanical Behavior of the Lungs during the Respiration Process

Introduction and Motivation

We propose in this first part to develop a macroscopic model for the ventilation of the human lung. Breathing involves the transport of air through the respiratory tract from its external entries, the nose and the mouth. During inspiration, the airflow moves down the pharynx and the trachea, where it is divided between left and right bronchi and enters the lungs. It is then distributed by the bronchial tree to the acini or alveolar sacs, embedded in a viscoelastic tissue, made in particular of blood capillaries and a network of elastic fibers. The alveoli are tiny bubble-like units where the gaseous exchanges occur. Thus, it is the function of the bronchial tree to efficiently supply them with fresh air via a tree-shaped structure, which we can call *fractal*. The coupled movement of air and tissue is achieved by displacement of the diaphragm and of the connective tissue framework of the lungs, which is usually called the parenchyma, [Wei84].

Modeling the mechanical behavior of the lungs, including both the air flow in the airway network and the 3D displacement of the parenchyma is difficult because of the complexity of the bronchial tree geometry and the porous, foam–like structure of the parenchyma. Moreover, for the time being it is far from possible to compute 3D Navier–Stokes airflow simulations on such a complex fractal geometry as that of the full airway tree, let alone a full fluid–structure interaction problem modeling the whole ventilation process on a realistic geometry of the lung.

It is thus necessary to develop models of reduced complexity, both to further the understanding of the lungs' mechanics and to be able to compute numerical simulations of the ventilation process. A possible choice is to describe the evolution of the air flux by a simple ODE model, as presented e.g. in [MSSM08]. Such models are certainly helpful for understanding the respiration mechanisms, but cannot yield precise information on the coupled 3D displacement of the parenchyma and airflow. Fully resolved computations are possible for the upper airways and the proximal part of the bronchial tree [LMB$^+$02, CS04, FMP$^+$05], but usually choose a set of *ad hoc* boundary conditions on the part of the tree which has been cut off. In [BGM10], a coupled ventilation model was developed to include the parenchyma, represented by a simple spring model and connected to the ends of the upper part of the bronchial tree by a resistance. To couple such models of the bronchial tree with a three–dimensional representation of the parenchyma, the mechanics of the set of acini have to be represented by a reduced model. The purpose of the present work is to obtain rigorously such a model of reduced complexity for the alveolar region by using the tools of two–scale periodic homogenization, involving fluid–structure interaction in the porous domain and flow of air through the bronchial tree.

Modeling aspects

Our approach is based on a series of important simplifying assumptions of the description of the lung mechanics. To obtain a macroscopic description of the parenchyma, we are going to let the size of the microstructure, denoted by ε, go to zero and study the convergence of the displacement of the structure in our mathematical model. Our aim is to obtain a model for the displacement of the parenchyma that takes into account the effect of the ventilation by the bronchial tree. As the number of alveoli grows to infinity, so does the number of generations of the bronchial tree that is

feeding them with air. The core of our approach is then to use simply Poiseuille's law, which relates linearly the pressure drop and the flow rate for a viscous fluid flowing through a cylindrical pipe. As the bronchial tree can be modeled as a branching network of such pipes, we represent the airways in our model as a dyadic resistive tree [MFWS04]. The airflow through the three is then completely characterized by the knowledge of the individual resistances of the branches, which depends only on the dimensions of the bronchi and can be computed from available anatomical data [Wei63]. Strictly speaking, the Poiseuille law is not valid for the first generations of the bronchial tree where one needs to take into account inertial effects. However, as the airflow progresses down the airways it slows down geometrically because the cross–section of the whole bronchial tree at a given generation increases exponentially [MFAS03]. Hence, the assumption that the airflow follows the Poiseuille law is reasonable if we consider a small piece of lung parenchyma connected to a subtree of the full tree of airways, stemming from a small bronchus at generation 6 or 7 of the bronchial tree. We will nevertheless assume here, for simplicity, that this description is valid for the whole airway tree.

The mathematical description of the bronchial tree as an abstract dyadic resistive tree was studied in depth in [VSM09], and especially the behavior as the number of generations of the tree grows to infinity. Moreover, this description has been used in [GMM06] to obtain a one–dimensional model of the parenchyma by connecting a dyadic resistive tree with a system of springs and masses. To extend this one–dimensional model to a multi–dimensional setting, we propose to model the alveoli as closed cavities in an elastic matrix, filled with air, as in the static parenchyma model proposed in [BGMO08]. Following [Van09], each alveolus is then connected to one end of our abstract dyadic resistive tree representing the bronchial tree, as in Figure 15. The air can flow in and out of the alveolus through this terminal branch of the tree. We further assume that the alveoli

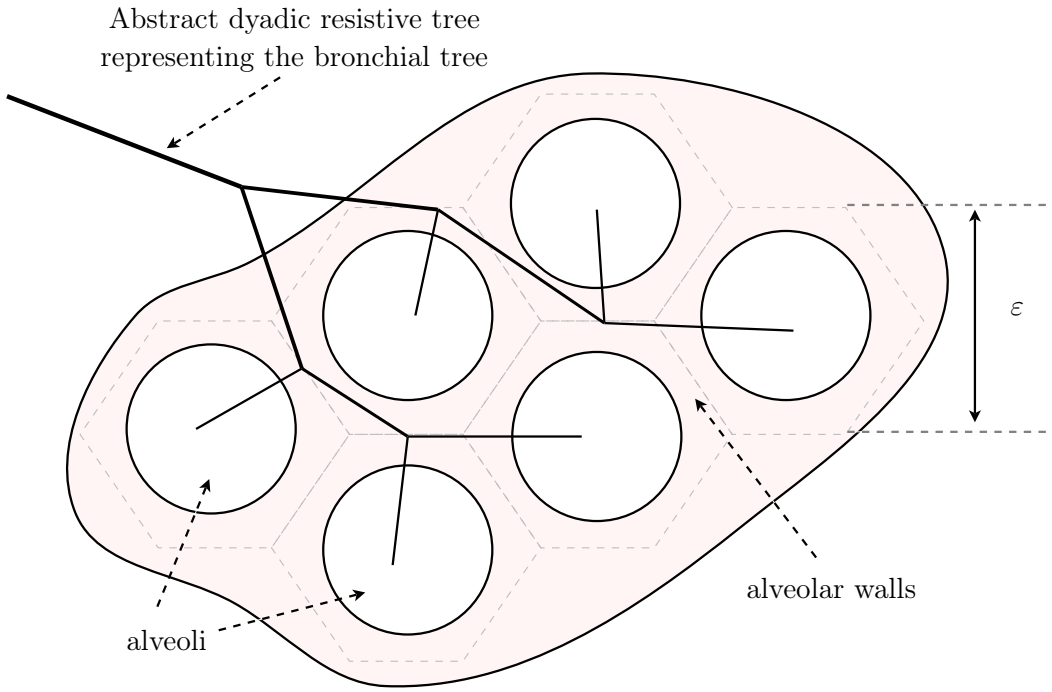

Figure 15 – Parenchyma model

are periodically arranged with a small period $\varepsilon > 0$, as is suggested by the spatial arrangement of the acinus. Since in our model each alveolus is isolated, we do not consider the airways or the alveolar ducts in our geometry. Finally, we assume that the air has a uniform pressure and behaves like an incompressible perfect gas inside each pore, so that volume changes are proportional to the air flow going into or out of the tree by the corresponding outlet. We assume also the parenchyma

behaves like a linearized elastic material (i.e. the deformations are small). We propose to study the two cases of a compressible and an incompressible wall material. In both cases, we obtain boundary value problems (1.15) and (1.16) respectively in the compressible and incompressible case. Note that the well–posedness of this problem in the compressible case was studied in [Van09].

Description of the results

Once the geometric setting and the model are in place, we study the asymptotic behavior of the displacement fields as the microscale parameter ε goes to zero and the number of generations of the tree goes to infinity. Unlike in the one–dimensional setting proposed in [GMM06], there are many ways of connecting a tree to the periodically distributed alveoli in a three–dimensional domain. To deal with this difficulty, we use a representation of the action of the tree as a Dirichlet–to–Neumann operator relating the fluxes and the pressures in the alveoli, which can be seen as constant–by–cell functions in the domain Ω representing the parenchyma. This resistance operator is then a linear operator in $\mathcal{L}(L^2(\Omega))$. We propose to use the strong convergence of the sequence of these resistance operators in the space $\mathcal{L}(L^2(\Omega))$, as ε goes to zero, as an abstract condition to model the convergent behavior of the sequence of trees ventilating our parenchyma domain. This allows us to divide the theoretical analysis in two parts: first, we show that this condition is sufficient to pass to the two–scale limit and obtain a homogenized model of the lung, and then we investigate how to build a connection between the sequence of trees and the alveoli and the condition on the resistances of the tree that allow this condition to hold.

To begin the first part of this analysis, which is presented in Chapter 1, we study the well–posedness for both problems and we show *a priori* bounds independent of ε. Then, using the two–scale homogenization method [Ngu89, All92] we analyze the asymptotic behavior of the displacement field solution of (1.15) and (1.16) as the micro–scale parameter ε goes to zero. We focus in particular on the convergence of the non–standard terms describing the interaction of the tree and the structure, and we show that they converge under the abstract condition that the sequence of resistance operator describing the tree converges as ε goes to zero. The main results of the Chapter are the convergence Theorems 1.2.19 and 1.3.10, which describe the macroscopic homogenized problems in the case of a compressible and an incompressible parenchyma structure, respectively.

We can analyze physically the mechanical behavior of the homogenized material we obtain in each case. When we suppose that the wall material is compressible, the homogenized parenchyma behaves like a compressible viscoelastic material with non–local damping both in space and time, thus showing some long–term memory effects. On the other hand, when the wall material is supposed to be incompressible, the homogenized material is compressible and viscoelastic with non–local damping in the space variable only. The non–local behavior is due to the effect of the abstract resistive tree which connects the different points of the domain.

In the second part of the theoretical analysis, presented in Chapter 2, we investigate the abstract convergence condition on the sequence of resistance operators $\mathcal{R}_\varepsilon$. We study in particular how to connect the dyadic resistive tree to the 3D parenchyma domain. Note that the bronchial tree is an example of space–filling structure of great complexity, for which there is no canonical construction process. We base our analysis on the dyadic decomposition framework introduced in [VSM09], by associating each airway of the tree to the portion of parenchyma it irrigates. This process allows us to identify a hierarchical structure of subdivisions of the domain, which completely describes how it is irrigated by a dyadic resistive tree. We then propose two geometrical constructions:

- the first is based on an idealized representation of the parenchyma, using recursive tilings of the square and space–filling fractal trees to build recursively a sequence of nested dyadic decompositions of the square;
- the other is an algorithmic construction, based on the prior knowledge of a multi–scale dyadic

decomposition of the domain satisfying some regularity assumptions. We show how to approximate this arbitrary decomposition while following the constraint of distributing the alveoli on a given ε–periodic grid, so as to obtain convergence as ε goes to zero.

Under appropriate conditions on the resistances of the tree, we then obtain convergence results in both cases, respectively Proposition 2.2.7 and Theorem 2.3.5.

Finally, in Chapter 3 we conclude this work by a numerical study of our homogenized ventilation model. We present a finite elements numerical method designed to tackle the homogenized problems obtained in Chapter 1. The main difficulty is the need to deal with the non–local operator associated with the tree as it writes as a full matrix in the finite elements basis. Our method is based on fast algorithms which exploit the tree structure to compute quickly the matrix–vector products associated with the viscous non–local operator. We present then some numerical simulations. The results show that we can make our parenchyma model breathe and that we can study the effects of the modification of some parameters, like the distal resistances or the stiffness of the material. We also propose a numerical investigation of the total energy dissipation by our model as a function of the resistances of the tree.

Related works Other works related to multiscale modeling of the lungs' parenchyma include [OL01] and [SJTL08], where the alveoli structure is considered as a porous media and a formal homogenization approach is applied to a system coupling the linearized Navier–Stokes equations for air and linear viscoelasticity for the solid tissue. Other approaches have been proposed, such as discrete spring–mass systems [GWN02] or equations empirically derived at the continuous level [Lan83]. We also refer to [KTS99, TPH00] for computational algorithms designed to generate a three–dimensional airway tree geometry inside the lung cavity, or to generate the acinus geometry [KTT00]. For the homogenization of fluid–structure interaction systems, one may refer in particular to [SP80, Ngu90, GM00], where the homogenization of the Stokes equations coupled to an elastic frame is performed.

Structure

This part is organized as follows. Chapter 1 is devoted to obtaining a homogenized mechanical law for the ventilation of the parenchyma. In the first section, we describe precisely the geometry and then write the equations of the coupled fluid–structure interaction models that we shall study. In section 1.2, we derive the homogenized limit of the compressible model (1.15) by the method of two–scale convergence. In section 1.3, we work out the same analysis for the incompressible model (1.16). In Chapter 2, we study two geometrical constructions modeling the way the bronchial tree irrigates the parenchyma and the associated convergence properties relevant to our model. Finally, in Chapter 3, we present a numerical method adapted to the homogenized model, and we present a few examples of numerical simulations with parameters inspired by realistic lung's anatomical data.

Chapter 1

A Multiscale Viscoelastic Model with Nonlocal Damping

In this first Chapter, we present a homogenized multi–scale model for the ventilation process of the lungs' parenchyma. We begin by describing our microscopic model for the parenchyma. We model the alveoli as closed air–filled cavities of size ε in a periodically perforated medium governed by the linearized elasticity equation. The alveoli are then connected to the exterior air by a dyadic resistive tree modeling the bronchial tree. We obtain two boundary value problems (1.15) and (1.16) corresponding to the two cases of a compressible and an incompressible structure.

In Sections 1.2 and 1.3, we first study the well–posedness of each problem and then use the two–scale homogenization method to study the asymptotic behavior of the displacement field solution as ε goes to zero. The operator representing the action of the resistive dyadic tree is assumed to converge in this Chapter as this condition will be investigated later on in Chapter 2. The main results of the Chapter are the two–scale convergence theorems 1.2.13 and 1.3.7, respectively for the compressible and incompressible structure model.

Using these results we identify and then study the macroscopic homogenized problems, see (1.81) and (1.117) . In the compressible case, the homogenized law describes a viscoelastic material with a viscous damping term which is non–local both in space and time, so the homogenized material exhibits some long–term memory effects. This viscous damping term represents the effect of the bronchial tree. In the incompressible case, the viscous damping term is non–local only in the space variable and the viscoelastic homogenized material shows only short–term memory effects.

Contents

1.1 Presentation of the model 30
1.1.1 Geometric setting 30
1.1.2 Description of the parenchyma model 32
1.1.3 Poiseuille flow through a finite resistive dyadic tree 33
1.1.4 Coupling the elastic structure and the resistive dyadic tree 35
1.1.5 A multiscale kernel describing the action of the resistive dyadic tree 36
1.1.6 Two–scale convergence 37
1.2 Study in the compressible case: homogenization limit 38
1.2.1 Variational formulation and *a priori* estimates 39
1.2.2 Two–scale convergence result 43
1.2.3 Cell problems, correctors and the homogenized problem 52
1.3 Study in the incompressible case 57
1.3.1 Mixed variational formulation 57
1.3.2 Pressure extension and *a priori* estimates 58
1.3.3 Two–scale convergence 59

Notations We use the Einstein convention for summing and the common Kronecker symbol $\delta_{ij} = 1$ if $i = j$ and 0 if $i \neq j$. The symbol Id denotes the identity matrix, and given two tensors of order 2 A and B, we denote the contraction of tensors as

$$A : B = a_{ij} b_{ji}.$$

We will denote with bold characters vectors, vector–valued fields and functional spaces of vector–valued fields. Given any vector field $\mathbf{v}$, we denote $e(\mathbf{v})$ its symmetrized gradient

$$e(\mathbf{v}) = \frac{1}{2} \left(\nabla \mathbf{v} + (\nabla \mathbf{v})^T \right).$$

1.1 Presentation of the model

1.1.1 Geometric setting

The parenchyma model we propose to study is a porous media, obtained by a periodic arrangement of closed pores (modeling the alveoli), connected in an abstract way by a dyadic resistive tree modeling the pulmonary airways. Let us give a formal description of this material.

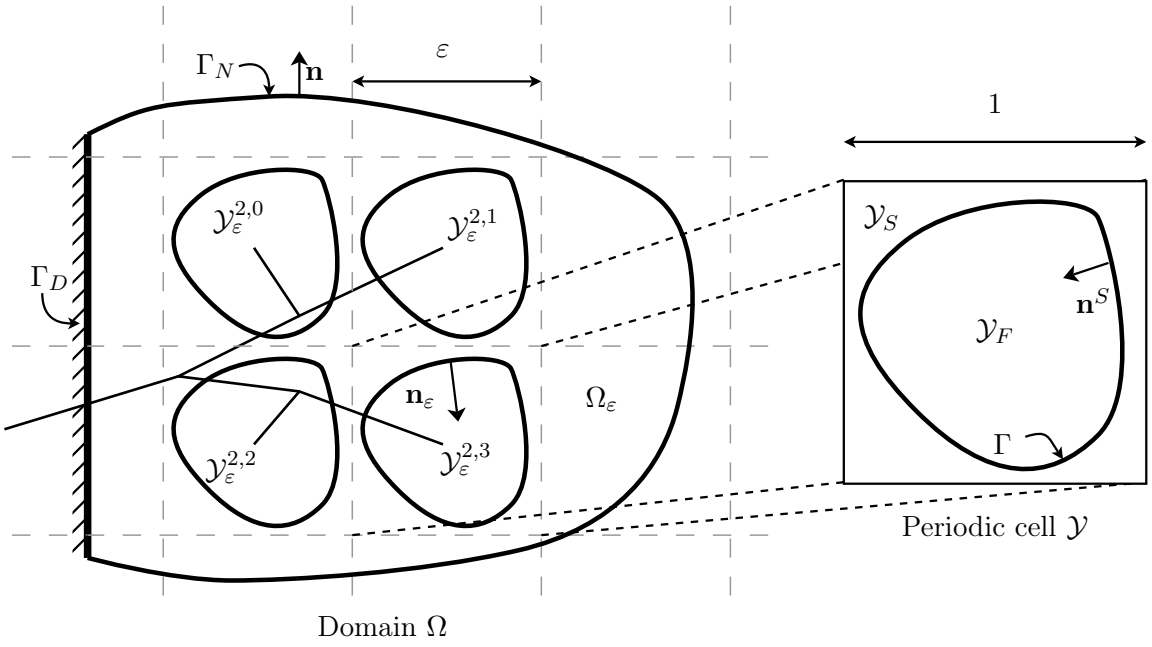

Figure 1.1 – Parenchyma model

Let d be the dimension, $d = 2,\ 3$. First, we describe the geometrical setting of the alveoli by defining an open periodic cell $\mathcal{Y}$, normalized so that $|\mathcal{Y}| = 1$. This unit cell is associated with a periodic array $\mathbf{Z}$ of $\mathbb{R}^d$, which is the discrete set of translation vectors such that $\mathcal{Y} + \mathbf{Z}$ is a tiling of the whole space.

Remark 1.1.1. *The standard and most simple such unit cell is a square or a cube, associated with $\mathbf{Z} = \mathbb{Z}^d$, which we use as an example in Figure 1.1. However other structures are more representative of the geometry of the alveoli, in particular the truncated octahedron is often used in the biology litterature [TPH00]. In 2D, the macroscopic isotropy of the material after homogenization can be captured using hexagonal cells, whereas using square cells result in a highly anisotropic behavior.*

We further divide $\mathcal{Y}$ into two open sets: $\mathcal{Y}_F$ that represents an air cavity and $\mathcal{Y}_S$ that represents the elastic walls of the alveolus. Let $\theta = |\mathcal{Y}_S|$ be the volume fraction of the elastic material. More precisely, we suppose that $\mathcal{Y}_F$ is smooth, simply connected and that:

$$\overline{\mathcal{Y}_F} \cup \overline{\mathcal{Y}_S} = \overline{\mathcal{Y}}, \qquad \mathcal{Y}_F \cap \mathcal{Y}_S = \emptyset, \qquad \overline{\mathcal{Y}_F} \subset \mathring{\mathcal{Y}}.$$

We also define $\Gamma = \partial\mathcal{Y}_F$ as the interior fluid–structure interface in the unit cell with unit normal $\mathbf{n}^S$ pointing into the fluid part.

Next, we model the space occupied by the lungs' parenchyma (or portion of the parenchyma) as Ω, a nonempty bounded open domain in $\mathbb{R}^d$ with Lipschitz boundary $\partial\Omega$ and unit outward normal $\mathbf{n}$. An example is given in Figure 1.1. The boundary is decomposed as $\overline{\partial\Omega} = \overline{\Gamma_D} \cup \overline{\Gamma_N}$ where $\Gamma_N \cap \Gamma_D = \emptyset$ and $|\Gamma_D| > 0$. We will suppose that the parenchyma is fixed at the portion of the boundary Γ_D.

Given a small parameter $\varepsilon > 0$ and a multi–index $\mathbf{k} \in \mathbf{Z}$, we define

$$\mathcal{Y}_\varepsilon^{\mathbf{k}} = \varepsilon(\mathcal{Y} + \mathbf{k}), \quad \mathcal{Y}_{F,\varepsilon}^{\mathbf{k}} = \varepsilon(\mathcal{Y}_F + \mathbf{k}), \quad \mathcal{Y}_{S,\varepsilon}^{\mathbf{k}} = \varepsilon(\mathcal{Y}_S + \mathbf{k}), \quad \Gamma_\varepsilon^{\mathbf{k}} = \varepsilon(\Gamma + \mathbf{k}),$$

that is a translation and a homothetic transformation of the reference cells $\mathcal{Y}$, $\mathcal{Y}_F$, $\mathcal{Y}_S$ and of the fluid–structure interface Γ. Furthermore, by introducing the set of multi–indexes $\mathbf{Z}_\varepsilon^\Omega$ as:

$$\mathbf{Z}_\varepsilon^\Omega = \left\{ \mathbf{k} \in \mathbf{Z} \mid Y^{\varepsilon,\mathbf{k}} \subset \Omega \right\}, \tag{1.1}$$

we define the periodically perforated structure domain and the interior interface as

$$\Omega_\varepsilon = \Omega \setminus \bigcup_{\mathbf{k}\in\mathbf{Z}_\varepsilon^\Omega} \overline{\mathcal{Y}_{F,\varepsilon}^{\mathbf{k}}}, \qquad \Gamma_\varepsilon = \bigcup_{\mathbf{k}\in\mathbf{Z}_\varepsilon^\Omega} \Gamma_\varepsilon^{\mathbf{k}}. \tag{1.2}$$

We define a unit normal vector $\mathbf{n}_\varepsilon$ defined on the fluid–structure interface Γ_ε and pointing to the exterior of the structure domain Ω_ε. Let χ_F and χ_S be the characteristic functions of $\mathcal{Y}_F$ and $\mathcal{Y}_S$ respectively, $\chi_{F,\varepsilon}$, $\chi_{S,\varepsilon}$ the characteristic functions of $\Omega \setminus \Omega_\varepsilon = \bigcup_{\mathbf{k}\in\mathbf{Z}_\varepsilon^\Omega} \overline{\mathcal{Y}_{F,\varepsilon}^{\mathbf{k}}}$ and Ω_ε, respectively, and $\chi_\varepsilon^{\mathbf{k}}$ the characteristic function of $\mathcal{Y}_\varepsilon^{\mathbf{k}}$.

Finally, we connect the alveoli $\mathcal{Y}_{F,\varepsilon}^{\mathbf{k}}$ filled with air to an abstract finite dyadic tree $\mathcal{T}_\varepsilon$ representing the geometrical connexions of the bifurcating airway tree (see Figure 1.2). The tree $\mathcal{T}_\varepsilon$ is a subtree of the larger, infinite dyadic tree $\mathcal{T}$ characterized by the set of nodes

$$V = X_0 \cup \{X_{n,\,k} : \; n \in \mathbb{N},\; 0 \le k \le 2^n - 1\}.$$

The tree $\mathcal{T}_\varepsilon$ is supposed to be full, meaning that if $X_{n,k} \in V$ is a node of $\mathcal{T}_\varepsilon$, then either both children of $X_{n,k}$ belong to $\mathcal{T}_\varepsilon$ ($X_{n,k}$ is then called an *internal node* of $\mathcal{T}_\varepsilon$), or neither does and $X_{n,k}$ is a *terminal node* (or a leaf) of $\mathcal{T}_\varepsilon$. We define the set of indexes $\mathcal{I}_\varepsilon$ and $\mathcal{E}_\varepsilon \subset \mathbb{N}^2$, indexing respectively the internal and terminal nodes of $\mathcal{T}_\varepsilon$:

$$\begin{aligned} \mathcal{I}_\varepsilon &= \left\{(n,k) \in \mathbb{N}^2, X_{n,k} \text{ is an internal node of the tree } \mathcal{T}_\varepsilon\right\}, \\ \mathcal{E}_\varepsilon &= \left\{(n,k) \in \mathbb{N}^2, X_{n,k} \text{ is a leaf of the tree } \mathcal{T}_\varepsilon\right\}, \end{aligned} \tag{1.3}$$

and we suppose that $\mathcal{E}_\varepsilon$ and $\mathbf{Z}_\varepsilon^\Omega$ have the same number of elements. Let ω_ε be a one–to–one mapping

$$\omega_\varepsilon : \begin{cases} \mathbf{Z}_\varepsilon^\Omega & \to \mathcal{E}_\varepsilon, \\ \mathbf{k} & \mapsto (n,k). \end{cases} \tag{1.4}$$

The mapping ω_ε describes the connexion between the tree and the alveoli. This lets us enumerate the cells of the periodically perforated domain Ω_ε following either the tree indexing by $\mathcal{E}_\varepsilon$, or the

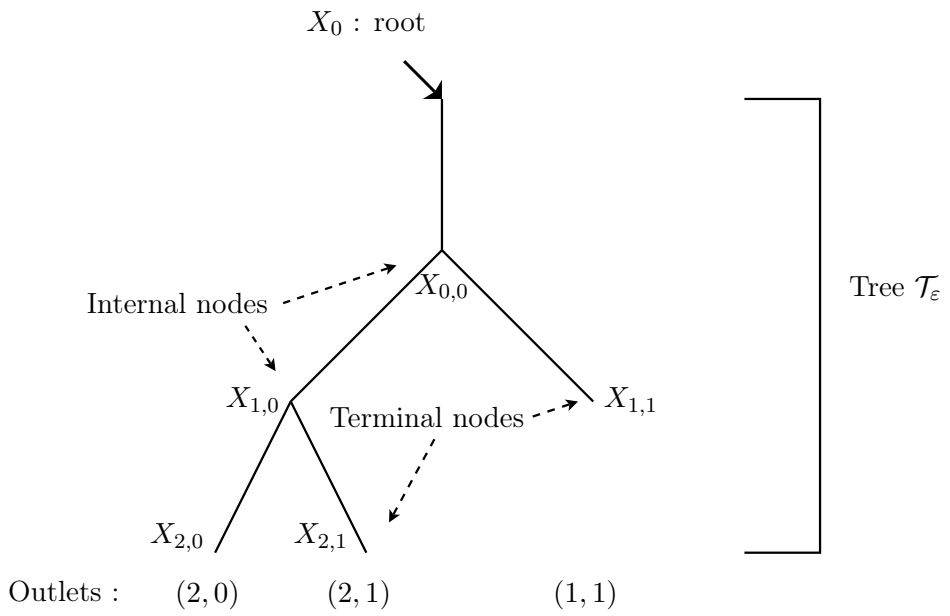

Figure 1.2 – Finite dyadic tree

spatial indexing by $\mathbf{Z}_\varepsilon^\Omega$, and as long as there is no possible confusion we will use either set of indexes indifferently, for example:

$$\mathcal{Y}_\varepsilon^{n,k} = \mathcal{Y}_\varepsilon^{\mathbf{k}} \quad \text{where } (n,k) = \omega_\varepsilon(\mathbf{k}) \in \mathcal{E}_\varepsilon \text{ for } \mathbf{k} \in \mathbf{Z}_\varepsilon^\Omega. \tag{1.5}$$

Remark 1.1.2. *We do not detail here how the geometric arrangement of the alveoli is related to their connexions to the tree. Rather, to keep a setup as simple and generic as possible in Section 1.2 and Section 1.3, we will rely on an abstract condition to describe the asymptotic behavior of the tree as ε goes to zero. In Chapter 2, we will show actual geometrical constructions of the arrangement, based on realistic hypothesis, which ensure convergence as ε goes to zero.*

The key goal for obtaining a two–scale continuum is to derive a macroscopic description of the material from the description of the microstructure, here the alveolar set. The assumption of a small parameter, $\varepsilon > 0$, implies that the fields depends on two spatial variables which belong to well–separated scales: the ordinary position vector $\mathbf{x} \in \Omega$, and the position vector in a stretched coordinate system $\mathbf{y} = \varepsilon^{-1}\mathbf{x}$. The variable $\mathbf{x}$ will be called *slow* and the variable $\mathbf{y}$ *fast*. By performing the asymptotic analysis when ε goes to zero, we expect the two sets of variables to become independent.

1.1.2 Description of the parenchyma model

We now turn to the description of the mechanical behavior of the parenchyma. Here ε is fixed, and we suppose that Ω_ε is a reference configuration for the elastic media when the air inside the alveoli is at the atmospheric pressure. We shall analyze two cases: first, we will consider a linear homogeneous elastic material and then we will add to this model an incompressibility constraint.

We denote by $\mathbf{u}_\varepsilon$ the displacement field of the elastic media. In the structure part Ω_ε, see (1.2), we are interested in small displacements around the reference configuration and we suppose that

the material obeys the laws of linearized elasticity, see [Cia88]:

$$\begin{cases} \rho\partial_{tt}\mathbf{u}_\varepsilon - \mathbf{div}\sigma = \mathbf{f}, & \text{in } \Omega_\varepsilon, \\ \sigma\mathbf{n}_\varepsilon = -p_\varepsilon^{\mathbf{k}}\mathbf{n}_\varepsilon, & \text{on } \Gamma_\varepsilon^{\mathbf{k}},\ \forall\, \mathbf{k} \in \mathbf{Z}_\varepsilon^\Omega, \\ \sigma\mathbf{n} = -p_N\mathbf{n}, & \text{on } \Gamma_N, \\ \mathbf{u}_\varepsilon = \mathbf{0}, & \text{on } \Gamma_D, \end{cases} \tag{1.6}$$

Here, in the compressible case, σ stands for the stress tensor associated with the displacement $\mathbf{u}_\varepsilon$, i.e.

$$\sigma(\mathbf{u}_\varepsilon) = \lambda \mathrm{div}(\mathbf{u}_\varepsilon)\mathrm{Id} + 2\mu e(\mathbf{u}_\varepsilon) \text{ (Hooke's law)}, \tag{1.7}$$

where the parameters $\lambda > 0$ and $\mu > 0$ are the Lamé constants, constitutive of the elastic media. Additionally, $\rho > 0$ is the density of the elastic media and $\mathbf{f}$ is a volumic force acting on the structure (the gravity field, for example). In the incompressible case that we will study separately, the stress tensor writes

$$\sigma(\mathbf{u}_\varepsilon, \eta_\varepsilon) = -\eta_\varepsilon \mathrm{Id} + 2\mu e(\mathbf{u}_\varepsilon), \tag{1.8}$$

where η_ε is the Lagrange multiplier, homogeneous to a pressure, associated with the additional incompressibility constraint div $\mathbf{u}_\varepsilon = 0$.

In both cases, initial conditions on the displacement and velocity complete the system. On the external boundary Γ_D, we impose no–slip boundary conditions on the displacement. On the external boundary Γ_N and the internal alveolar boundaries $\Gamma_\varepsilon^{\mathbf{k}}$, we consider a pressure force exerted on the boundary. The external pressure p_N is given, modeling the action of the diaphragm, whereas the pressures $p_\varepsilon^{\mathbf{k}}$, which denote the uniform air pressure inside each alveolus $\mathcal{Y}_{F,\varepsilon}^{\mathbf{k}}$, are unknowns and depend on the airflow through the dyadic tree, which we describe next.

Remark 1.1.3. *For simplicity, we present our analysis with constant λ and μ, but all our results hold more generally for spatially varying Lamé parameters $\lambda(\mathbf{x})$ and $\mu(\mathbf{x})$ for example in $C(\overline{\Omega})$, modeling macroscopic inhomogeneities in the tissue.*

1.1.3 Poiseuille flow through a finite resistive dyadic tree

We consider here the circulation of air through a tree of connected pipes. First, let us consider the flow of an incompressible, viscous, non–inertial fluid through a single pipe. According to Poiseuille's law, which we assume is valid in all branches, the flow rate Φ through the pipe is proportional to the pressure drop between its two end points, which is expressed by the equation

$$P_{in} - P_{out} = r\Phi,$$

where r is the resistance of the pipe, a positive coefficient which varies with the fluid viscosity and with L/D^4, where L is the length of the pipe and D is its width. According to this description, we can fully characterize the airflow through the full dyadic tree $\mathcal{T}_\varepsilon$ by introducing a fixed sequence of resistances

$$r_{n,k} > 0 \qquad \text{for } n \in \mathbb{N} \text{ and } 0 \le k \le 2^n - 1, \tag{1.9}$$

which are associated with each edge of the trees $\mathcal{T}_\varepsilon$ and $\mathcal{T}$ as in Figure 1.3. We suppose that these resistances do not depend on the parameter ε. We call such trees *resistive dyadic trees*, and will still denote by $\mathcal{T}_\varepsilon$ and $\mathcal{T}$ the set of vertices and the associated resistances when no confusion is possible.

Given a set of pressures at the outlets, it is now possible to compute the corresponding set of fluxes thanks to Poiseuille's law, and vice versa. Let the pressure at the root node be denoted by p_e. Let

$$\mathbf{p}_\varepsilon = (p_\varepsilon^{n,k})_{n,k\in\mathcal{E}_\varepsilon} \quad \text{and} \quad \boldsymbol{\phi}_\varepsilon = (\phi_\varepsilon^{n,k})_{n,k\in\mathcal{E}_\varepsilon}$$

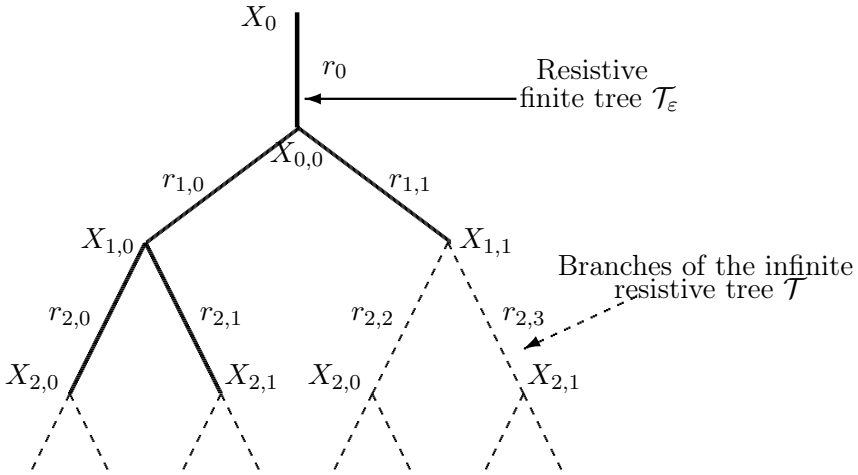

Figure 1.3 – Resistive finite and infinite trees

be the pressure and flux vectors at the outlets of the tree, with the convention that the fluxes are considered positive when air is entering the tree through the corresponding outlet. Since Poiseuille's law is linear, there exists also a linear relation between $\mathbf{p}_\varepsilon$ and $\boldsymbol{\phi}_\varepsilon$, i.e. a matrix A^ε indexed by $\mathcal{E}_\varepsilon$ and such that

$$\mathbf{p}_\varepsilon - p_e\mathbf{1} = A^\varepsilon \boldsymbol{\phi}_\varepsilon, \tag{1.10}$$

where $\mathbf{1}$ is the vector $(1,\dots,1)$. The appearance of this unit vector follows from the observation that at rest, when there are no air fluxes in the tree, the air pressure is equal at all the outlets including the root node. Then the left–hand side of the equation (1.10) must be zero.

For convenience, we introduce the following notation:

Definition 1.1.4. *Given $a = (m,i)$ and $b = (n,j)$ two elements of $\mathbb{N}^2$ with $0 \le i \le 2^m - 1$, $0 \le j \le 2^n - 1$, we define $\nu(a,b)$ as the index of the lowest common ancestor of the nodes $X_a = X_{m,i}$ and $X_b = X_{n,j}$ in the tree $\mathcal{T}$.*

It can be easily checked that $\nu(a,b)$ is explicitly defined by the following formula:

$$\nu(a,b) = (p,k) \text{ with } \begin{cases} p = \max\left\{ q \le min(m,n), \quad \dfrac{i}{2^{m-q}} = \dfrac{j}{2^{n-q}} \right\}, \\ k = \dfrac{i}{2^{n-p}} = \dfrac{j}{2^{n-p}}, \end{cases}$$

where the fractions denote the integer quotient of the division. The following Proposition gives us some important information about the matrix A^ε. We do not give the details of the proof here, but we refer to [GMM06] for a proof which extends readily to our setting and to [VSM09] for a detailed study of the properties of resistive dyadic trees and the associated flux–pressure operator.

Proposition 1.1.5. *The matrix A^ε introduced in (1.10) is symmetric definite positive, and its entries are given by*

$$A^\varepsilon_{a,b} = R_{\nu(a,b)} \text{ for } a,\ b \in \mathcal{E}_\varepsilon, \tag{1.11}$$

where $R_{n,k} = r_0 + r_{1,k/2^{n-1}} + \cdots + r_{n,k}$ is the cumulated resistance on the path from the root node to the node $X_{n,k}$.

With a slight abuse of notation, we will also call A^ε the same matrix reindexed by $\mathbf{Z}_\varepsilon^\Omega$ as an alternate numbering of the alveoli, with the convention that

$$A^\varepsilon_{\mathbf{k},\mathbf{l}} = A^\varepsilon_{a,b} \text{ for } a = \omega_\varepsilon(\mathbf{k}) \text{ and } b = \omega_\varepsilon(\mathbf{l}), \tag{1.12}$$

where ω_ε is the one–to–one mapping defined in (1.4).

1.1.4 Coupling the elastic structure and the resistive dyadic tree

We are now in a position to write the fully coupled fluid–structure interaction model by giving a value to the pressures $p_\varepsilon^\mathbf{k}$ which appear in the system (1.6). We model the air in the alveoli as incompressible, so when the volume of the holes changes the air escapes through the tree. The pressures generated by this flow are related to the change in volume of the alveoli by (1.10).

The deformed volume $V_\varepsilon^\mathbf{k}$ of a cavity $\mathcal{Y}_{F,\varepsilon}^\mathbf{k}$ can be evaluated as a function of $\mathbf{u}_\varepsilon$ by (see [Cia88]):

$$V_\varepsilon^\mathbf{k}(t) = \int_{\mathcal{Y}_{F,\varepsilon}^\mathbf{k}} \det\, \nabla\left(\mathbf{x} + \mathbf{u}_\varepsilon(\mathbf{x},t)\right) \mathrm{d}\mathbf{x} = \int_{\mathcal{Y}_{F,\varepsilon}^\mathbf{k}} \det\, \left(\mathrm{Id} + \nabla \mathbf{u}_\varepsilon(\mathbf{x},t)\right) \mathrm{d}\mathbf{x},$$

where $\mathbf{u}_\varepsilon$ has been extended inside the hole by any H^1 extension operator. Taking the time derivative, we get by Jacobi's formula the identity

$$\frac{\mathrm{d}}{\mathrm{d}t} V_\varepsilon^\mathbf{k}(t) = \int_{\mathcal{Y}_{F,\varepsilon}^\mathbf{k}} \mathrm{Tr}\, \left(\mathrm{Cof}\, \left(\mathrm{Id} + \nabla \mathbf{u}_\varepsilon(\mathbf{x},t)\right)^T \frac{\partial}{\partial t} \nabla \mathbf{u}_\varepsilon(\mathbf{x},t) \right) \mathrm{d}\mathbf{x}.$$

Now we linearize this relation around the rest state where $\mathbf{u}_\varepsilon = \mathbf{0}$ and $\partial_t \mathbf{u}_\varepsilon = \mathbf{0}$. Assuming that $\nabla \mathbf{u}_\varepsilon$ is small we can keep only the leading order in the Taylor expansion of the matrix of cofactors:

$$\mathrm{Cof}\, \left(\mathrm{Id} + \nabla \mathbf{u}_\varepsilon(\mathbf{x},t)\right) \approx \mathrm{Id}.$$

We remind the convention that the flux is positive when air enters the tree through the outlet, so we obtain the flux of air $\phi_\varepsilon^\mathbf{k}$ associated with the alveolus $\mathcal{Y}_{F,\varepsilon}^\mathbf{k}$ by the formula:

$$\phi_\varepsilon^\mathbf{k} = -\int_{\mathcal{Y}_{F,\varepsilon}^\mathbf{k}} \frac{\partial}{\partial t} \mathrm{div} \mathbf{u}_\varepsilon = \int_{\Gamma_\varepsilon^\mathbf{k}} \partial_t \mathbf{u}_\varepsilon \cdot \mathbf{n}_\varepsilon, \tag{1.13}$$

where we remind that the normal vector $\mathbf{n}_\varepsilon$ points out into $\mathcal{Y}_{F,\varepsilon}^\mathbf{k}$. Moreover, using equation (1.10) and the matrix A^ε introduced in (1.12), we can write the pressure $p_\varepsilon^\mathbf{k}$ inside each hole $\mathcal{Y}_{F,\varepsilon}^\mathbf{k}$ for $\mathbf{k} \in \mathbf{Z}_\varepsilon^\Omega$ as a function of the normal displacement field $\mathbf{u}_\varepsilon$ on the whole interior interface Γ_ε:

$$p_\varepsilon^\mathbf{k} - p_e = \sum_{\mathbf{l} \in \mathbf{Z}_\varepsilon^\Omega} A^\varepsilon_{\mathbf{k},\mathbf{l}} \left(\int_{\Gamma_\varepsilon^\mathbf{l}} \partial_t \mathbf{u}_\varepsilon \cdot \mathbf{n}_\varepsilon \right). \tag{1.14}$$

We now state two models we will analyze in the next two sections. In the first case we shall study, corresponding to a compressible structure, the displacement field $\mathbf{u}_\varepsilon$ satisfies the system:

$$\begin{cases} \rho \partial_{tt} \mathbf{u}_\varepsilon - \mathbf{div} \sigma(\mathbf{u}_\varepsilon) = \mathbf{f}, & \text{in } \Omega_\varepsilon, & \text{(1.15a)} \\ \sigma(\mathbf{u}_\varepsilon)\mathbf{n}_\varepsilon = -\left(p_e + \displaystyle\sum_{\mathbf{l} \in \mathbf{Z}_\varepsilon^\Omega} A^\varepsilon_{\mathbf{k},\mathbf{l}} \left(\int_{\Gamma_\varepsilon^\mathbf{l}} \partial_t \mathbf{u}_\varepsilon \cdot \mathbf{n}_\varepsilon \right) \right) \mathbf{n}_\varepsilon, & \text{on } \Gamma_\varepsilon^\mathbf{k},\ \forall \mathbf{k} \in \mathbf{Z}_\varepsilon^\Omega, & \text{(1.15b)} \\ \sigma(\mathbf{u}_\varepsilon)\mathbf{n} = -p_N \mathbf{n}, & \text{on } \Gamma_N, & \text{(1.15c)} \\ \mathbf{u}_\varepsilon = \mathbf{0}, & \text{on } \Gamma_D, & \text{(1.15d)} \\ \mathbf{u}_\varepsilon(0) = \mathbf{u}_0, \quad \partial_t \mathbf{u}_\varepsilon(0) = \mathbf{u}_1, & \text{in } \Omega_\varepsilon. & \text{(1.15e)} \end{cases}$$

We remind that the stress tensor $\sigma(\mathbf{u}_\varepsilon)$ introduced in (1.7) reads

$$\sigma(\mathbf{u}_\varepsilon) = \lambda \mathrm{div}(\mathbf{u}_\varepsilon)\mathrm{Id} + 2\mu e(\mathbf{u}_\varepsilon),$$

and $\mathbf{u}_0$, $\mathbf{u}_1$ are initial conditions describing the state of the elastic media at $t = 0$, chosen independently of the microscale parameter ε and thus defined on the whole domain Ω.

In the second case we shall study, corresponding to a linear incompressible structure, the unknowns of the model are the displacement field $\mathbf{u}_\varepsilon$ and the scalar–valued variable η_ε, homogeneous to a pressure and satisfying:

$$\begin{cases} \rho\partial_{tt}\mathbf{u}_\varepsilon - \mathbf{div}\sigma(\mathbf{u}_\varepsilon, \eta_\varepsilon) = \mathbf{f}, & \text{in } \Omega_\varepsilon, \quad (1.16a) \\ \mathrm{div}\mathbf{u}_\varepsilon = 0, & \text{in } \Omega_\varepsilon, \quad (1.16b) \\ \sigma(\mathbf{u}_\varepsilon, \eta_\varepsilon)\mathbf{n}_\varepsilon = -\left(p_e + \displaystyle\sum_{\mathbf{l}\in\mathbf{Z}_\varepsilon^\Omega} A^\varepsilon_{\mathbf{k},\mathbf{l}} \left(\int_{\Gamma^{\mathbf{l}}_\varepsilon} \partial_t\mathbf{u}_\varepsilon \cdot \mathbf{n}_\varepsilon\right)\right)\mathbf{n}_\varepsilon, & \text{on } \Gamma^{\mathbf{k}}_\varepsilon,\ \forall \mathbf{k}\in\mathbf{Z}^\Omega_\varepsilon, \quad (1.16c) \\ \sigma(\mathbf{u}_\varepsilon, \eta_\varepsilon)\mathbf{n} = -p_N\mathbf{n}, & \text{on } \Gamma_N, \quad (1.16d) \\ \mathbf{u}_\varepsilon = \mathbf{0}, & \text{on } \Gamma_D, \quad (1.16e) \\ \mathbf{u}_\varepsilon(0) = \mathbf{u}_0, \quad \partial_t\mathbf{u}_\varepsilon(0) = \mathbf{u}_1, & \text{in } \Omega_\varepsilon, \quad (1.16f) \end{cases}$$

where the stress tensor $\sigma(\eta_\varepsilon, \mathbf{u}_\varepsilon)$ introduced in (1.8) now reads:

$$\sigma(\mathbf{u}_\varepsilon, \eta_\varepsilon) = -\eta_\varepsilon\mathrm{Id} + 2\mu e(\mathbf{u}_\varepsilon).$$

Remark 1.1.6. *This kind of averaged boundary conditions, non–local at the alveolar level, appears in other fluid–structure models, such as in the static foam model studied in [BGMO08] or when studying vibrations of rigid tubes immersed in a fluid [AC96]. Here we deal with a special case where the boundary conditions are also globally coupled by the matrix A^ε, so in addition to being non–local at the microscopic level there is a non–local coupling at the macroscopic level between the alveoli.*

We conclude this presentation by introducing an integral operator which replaces the discrete matrix A^ε by a continuous description of the interaction between airflow through the tree and elastic structure. The properties of this operator are essential to our asymptotic analysis as ε goes to zero.

1.1.5 A multiscale kernel describing the action of the resistive dyadic tree

The relation (1.10) describes the action of the tree at the discrete level. We are going to give a sense at the continuous level to this discrete description, which is more convenient when passing to the limit $\varepsilon \to 0$. Recall that thanks to (1.5), we have a one–to–one mapping between the leafs of $\mathcal{T}_\varepsilon$ and the alveoli $\mathcal{Y}^{\mathbf{k}}_{F,\varepsilon}$ which allows us to identify the outlets of the resistive dyadic tree and the alveoli. This motivates the introduction of the following projection operator, recalling that $|\mathcal{Y}| = 1$:

Definition 1.1.7. *Let Π_ε be the L^2–projector on the set of functions taking constant values on each cell $\mathcal{Y}^{\mathbf{k}}_\varepsilon$ for $\mathbf{k}\in\mathbf{Z}^\Omega_\varepsilon$:*

$$\Pi_\varepsilon(q) = \sum_{\mathbf{k}\in\mathbf{Z}^\Omega_\varepsilon} \varepsilon^{-d}\left(\int_{\mathcal{Y}^{\mathbf{k}}_\varepsilon} q\right)\chi^{\mathbf{k}}_\varepsilon. \quad (1.17)$$

Given a continuous flux function $\phi_\varepsilon \in L^2(\Omega)$, we define a vector of discrete fluxes as

$$\boldsymbol{\phi}_\varepsilon = \left(q^{\mathbf{k}}_\varepsilon\right)_{\mathbf{k}\in\mathbf{Z}^\Omega_\varepsilon}, \quad \text{with } \phi^{\mathbf{k}}_\varepsilon = \int_{\mathcal{Y}^{\mathbf{k}}_\varepsilon} \phi_\varepsilon. \quad (1.18)$$

The corresponding pressure vector is defined as

$$\mathbf{p}_\varepsilon = \left(p_\varepsilon^{\mathbf{k}}\right)_{\mathbf{k}\in\mathbf{Z}_\varepsilon^\Omega} = A^\varepsilon \boldsymbol{\phi}_\varepsilon, \tag{1.19}$$

where A^ε is the matrix indexed by $\mathbf{Z}_\varepsilon^\Omega$ defined in (1.12). Finally we introduce the pressure function $p_\varepsilon \in L^2(\Omega)$ as the function which takes constant value $p_\varepsilon^{\mathbf{k}}$ in each cell $\mathcal{Y}_\varepsilon^{\mathbf{k}}$ for $\mathbf{k} \in \mathbf{Z}_\varepsilon^\Omega$, and 0 elsewhere. We denote by $\mathcal{R}_\varepsilon$ the following operator

$$\begin{cases} L^2(\Omega) & \to L^2(\Omega), \\ \phi_\varepsilon & \mapsto p_\varepsilon. \end{cases}$$

Proposition 1.1.8. *The resistance operator $\mathcal{R}_\varepsilon$ can be expressed as a kernel integral operator:*

$$p_\varepsilon = \mathcal{R}_\varepsilon \phi_\varepsilon \qquad \Longleftrightarrow \qquad p_\varepsilon(\mathbf{x}_1) = \int_\Omega K_\varepsilon(\mathbf{x}_1, \mathbf{x}_2)\phi_\varepsilon(\mathbf{x}_2)\mathrm{d}\mathbf{x}_2 \quad \forall \mathbf{x}_1 \in \Omega, \tag{1.20}$$

where $K_\varepsilon \in L^1(\Omega \times \Omega)$ is a piecewise constant function defined as:

$$K_\varepsilon(\mathbf{x}_1, \mathbf{x}_2) = \begin{cases} A^\varepsilon_{\mathbf{k},\mathbf{l}} & \text{if } \mathbf{x}_1 \in \mathcal{Y}_\varepsilon^{\mathbf{k}},\ \mathbf{x}_2 \in \mathcal{Y}_\varepsilon^{\mathbf{l}} \text{ for some } \mathbf{k} \in \mathbf{Z}_\varepsilon^\Omega,\ \mathbf{l} \in \mathbf{Z}_\varepsilon^\Omega, \\ 0 & \text{elsewhere.} \end{cases} \tag{1.21}$$

Since the matrix A^ε is symmetric and positive, these properties are transposed to the operator $\mathcal{R}_\varepsilon$: for all ϕ, ψ in $L^2(\Omega)$ we have

$$\int_\Omega (\mathcal{R}_\varepsilon \phi)\,\psi = \int_\Omega (\mathcal{R}_\varepsilon \psi)\,\phi \quad \text{and} \quad \int_\Omega (\mathcal{R}_\varepsilon \phi)\,\phi \geq 0. \tag{1.22}$$

As a consequence, the following Cauchy–Schwartz inequality holds: for all ϕ, ψ in $L^2(\Omega)$,

$$\left|\int_\Omega (\mathcal{R}_\varepsilon \phi)\,\psi\right|^2 \leq \left(\int_\Omega (\mathcal{R}_\varepsilon \phi)\,\phi\right)\left(\int_\Omega (\mathcal{R}_\varepsilon \psi)\,\psi\right). \tag{1.23}$$

Remark 1.1.9. *The operator $\mathcal{R}_\varepsilon$ sums up the interaction of the tree with the structure, acting as a Dirichlet to Neumann operator by relating the rate of compression of the structure to the pressure forces on the boundary of the holes in a non–local way.*

The convergence properties of $\mathcal{R}_\varepsilon$ as ε goes to zero have been studied extensively in the 1D case in [GMM06] and in a more generic setting in [VSM09].

1.1.6 Two–scale convergence

To prove the main convergence results of this Chapter, we use the method of two–scale convergence which was introduced by G. Nguetseng [Ngu89] and then generalized and applied to several important cases by G. Allaire [All92], including the case of perforated domains. For the sake of completeness, we recall here the results we will use throughout the Chapter 1. The basic idea is to formalize an asymptotic expansion such as

$$u_\varepsilon(\mathbf{x}) = u(\mathbf{x}, \mathbf{x}/\varepsilon) + \varepsilon u^1(\mathbf{x}, \mathbf{x}/\varepsilon) + \varepsilon^2 u^2(\mathbf{x}, \mathbf{x}/\varepsilon) + \dots$$

where the functions $u(\mathbf{x}, \mathbf{y})$, $u^k(\mathbf{x}, \mathbf{y})$ are assumed to be $\mathcal{Y}$–periodic in the fast variable $\mathbf{y}$. In this expansion, we can consider u as the macroscopic variable, while u^1, u^2 are the microscopic displacements. We denote by the subscript "$\#$" the property of $\mathcal{Y}$-periodicity for functions defined on $\mathcal{Y}$. We recall the following definition:

Definition 1.1.10. *Let (u_ε) be a sequence of functions in $L^2(\Omega)$. This sequence is said to two–scale converge to a limit $u \in L^2(\Omega \times \mathcal{Y})$ if for any function $\psi(t, \mathbf{x}, \mathbf{y}) \in L^2(\Omega; C_\#(\mathcal{Y}))$ we have*

$$\lim_{\varepsilon \to 0} \int_\Omega u_\varepsilon(\mathbf{x}) \psi\left(\mathbf{x}, \frac{\mathbf{x}}{\varepsilon}\right) \mathrm{d}\mathbf{x} = \int_\Omega \int_{\mathcal{Y}} u(\mathbf{x}, \mathbf{y}) \psi(\mathbf{x}, \mathbf{y}) \mathrm{d}\mathbf{y} \mathrm{d}\mathbf{x}.$$

The definition extends readily to vector– or tensor–valued functions.

Remark 1.1.11. *If we replace the space of test functions $L^2(\Omega; C_\#(\mathcal{Y}))$ by $\mathcal{D}(\Omega; C^\infty_\#(\mathcal{Y}))$ in the definition of two–scale convergence, it is necessary to add the assumption that the sequence $(\mathbf{u}_\varepsilon)$ is uniformly bounded in $L^2(\Omega)$ [LNW02].*

Remark 1.1.12. *The question of determining which test functions are admissible is a delicate one, and has been addressed in [All92]. In particular, some amount of continuity in one variable or the other is necessary to ensure the measurability of $\mathbf{x} \mapsto \psi(\mathbf{x}, \mathbf{x}/\varepsilon)$. For example, any test function $\psi \in L^2_\#(Y, C(\overline{\Omega}))$ is an admissible test function for the two–scale convergence. Moreover, two–scale convergence implies weak convergence in the sense that if u_ε two–scale converges to a function u in $L^2(\Omega \times Y)$, u_ε converges weakly in $L^2(\Omega)$ to $\mathbf{x} \mapsto \int_Y u(\mathbf{x}, \mathbf{y}) \mathrm{d}\mathbf{y}$.*

Here, we wish to use two–scale convergence to tackle a time-dependent problem. Hence, we extend this definition as in [Mil95].

Definition 1.1.13. *Let (u_ε) be a sequence of functions in $L^2((0,T) \times \Omega)$. This sequence is said to two–scale converge to a limit $u \in L^2((0,T) \times \Omega \times \mathcal{Y})$ if we have:*

$$\begin{aligned} &\forall \psi(t, \mathbf{x}, \mathbf{y}) \in L^2((0,T) \times \Omega; C_\#(\mathcal{Y})), \\ &\lim_{\varepsilon \to 0} \int_0^T \int_\Omega u_\varepsilon(t, \mathbf{x}) \psi\left(t, \mathbf{x}, \frac{\mathbf{x}}{\varepsilon}\right) \mathrm{d}\mathbf{x} = \int_0^T \int_\Omega \int_Y u(t, \mathbf{x}, \mathbf{y}) \psi(t, \mathbf{x}, \mathbf{y}) \mathrm{d}\mathbf{y} \mathrm{d}\mathbf{x}, \end{aligned} \tag{1.24}$$

and we denote this convergence by a double arrow:

$$u_\varepsilon \twoheadrightarrow u.$$

From the analogous results in [All92], we extend to time–dependent functions the following compactness result as in [GM00]:

Lemma 1.1.14. a) *Each bounded sequence in $L^2((0,T) \times \Omega)$ contains a subsequence which two–scale converges to a limit $u \in L^2((0,T) \times \Omega \times Y)$.*

b) *Let (u_ε) be a bounded sequence in $L^2(0,T; H^1(\Omega))$. Then, there exists $u \in L^2(0,T; H^1(\Omega))$ and $u^1 \in L^2((0,T) \times \Omega; H^1_\#(Y)/\mathbb{R}^d)$ such that up to a subsequence,*

$$u_\varepsilon \twoheadrightarrow u \text{ and } \nabla u_\varepsilon \twoheadrightarrow \nabla_{\mathbf{x}} u(t, \mathbf{x}) + \nabla_{\mathbf{y}} u^1(t, \mathbf{x}, \mathbf{y}).$$

If in addition $\partial_t u_\varepsilon$ is bounded in $L^2((0,T) \times \Omega)$, then $\partial_t u \in L^2((0,T) \times \Omega)$ and

$$\partial_t u_\varepsilon \twoheadrightarrow \partial_t u.$$

1.2 Study in the compressible case: homogenization limit

The analysis will proceed in several steps: first, we prove that (1.15) is well–posed and we derive *a priori* estimates independent of the parameter ε. Afterwards, we study the limit as ε goes to zero, and we obtain the two–scale problem and rigorously justify the asymptotic limit in a single step thanks to the two–scale convergence method. Finally, we study the limit problem and describe its specificities, and we show that it is well–posed.

1.2.1 Variational formulation and *a priori* estimates

In this part, we write the variational formulation associated with problem (1.15) and derive an existence and uniqueness result for it. Afterwards, we introduce an extension operator for functions defined on the parameter–dependent domain Ω_ε to functions defined on the fixed domain Ω that allows us to obtain *a priori* estimates independent of ε on the weak solutions of (1.15).

1.2.1.1 Variational formulation

Let $\mathbf{V}_\varepsilon = \{\mathbf{v} \in \mathbf{H}^1(\Omega_\varepsilon) \mid \mathbf{v}|_{\Gamma_D} = \mathbf{0}\}$ and $\mathbf{V} = \{\mathbf{v} \in \mathbf{H}^1(\Omega) \mid \mathbf{v}|_{\Gamma_D} = \mathbf{0}\}$ where $\mathbf{v}|_{\Gamma_D}$ denotes the trace of $\mathbf{v}$ on Γ_D, and $\mathbf{X}_\varepsilon = \mathbf{L}^2(\Omega_\varepsilon)$, $\mathbf{X} = \mathbf{L}^2(\Omega)$. Let us denote by $\|\cdot\|_{0,\Omega_\varepsilon}$ and $\|\cdot\|_{0,\Omega}$ the respective L^2–norms and by $|\cdot|_{1,\Omega_\varepsilon} = \|\nabla(\,\cdot\,)\|_{0,\Omega_\varepsilon}$ and $|\cdot|_{1,\Omega} = \|\nabla(\,\cdot\,)\|_{0,\Omega}$ the respective H^1 Sobolev semi–norms.

Let $T > 0$ be an arbitrary time. We make the following assumptions:

$$\mathbf{f} \in \mathbf{L}^2((0,T)\times\Omega), \quad p_N,\ p_e \in H^1(0,T), \quad \mathbf{u}_0 \in \mathbf{V} \text{ and } \mathbf{u}_1 \in \mathbf{L}^2(\Omega). \tag{1.25}$$

We obtain a variational formulation associated to (1.15) by using test functions in $\mathbf{V}_\varepsilon$: find $\mathbf{u}_\varepsilon \in L^\infty(0,T;\mathbf{V}_\varepsilon)$ with $\partial_t \mathbf{u}_\varepsilon \in L^\infty(0,T;\mathbf{X}_\varepsilon)$ such that:

$$\begin{cases} \text{For all } \mathbf{v}_\varepsilon \in \mathbf{V}_\varepsilon, \quad \text{and in } \mathcal{D}'(0,T), \\ \dfrac{\mathrm{d}}{\mathrm{d}t}(\rho\partial_t \mathbf{u}_\varepsilon, \mathbf{v}_\varepsilon)_{0,\Omega_\varepsilon} + \dfrac{\mathrm{d}}{\mathrm{d}t} r_\varepsilon(\mathbf{u}_\varepsilon, \mathbf{v}_\varepsilon) + a_\varepsilon(\mathbf{u}_\varepsilon, \mathbf{v}_\varepsilon) = \ell_\varepsilon(\mathbf{v}_\varepsilon), \\ \mathbf{u}_\varepsilon(0) = \mathbf{u}_0,\ \partial_t \mathbf{u}_\varepsilon(0) = \mathbf{u}_1, \end{cases} \tag{1.26}$$

where $(\cdot,\cdot)_{0,\Omega_\varepsilon}$ is the L^2–scalar product in $\mathbf{X}_\varepsilon$, $a_\varepsilon(\cdot,\cdot) : \mathbf{V}_\varepsilon \times \mathbf{V}_\varepsilon \to \mathbb{R}$ and $r_\varepsilon(\cdot,\cdot) : \mathbf{V}_\varepsilon \times \mathbf{V}_\varepsilon \to \mathbb{R}$ are the bilinear forms defined by:

$$a_\varepsilon(\mathbf{u}_\varepsilon, \mathbf{v}_\varepsilon) = \int_{\Omega_\varepsilon} \lambda \mathrm{div}(\mathbf{u}_\varepsilon)\mathrm{div}(\mathbf{v}_\varepsilon) + 2\mu e(\mathbf{u}_\varepsilon) : e(\mathbf{v}_\varepsilon), \tag{1.27}$$

$$r_\varepsilon(\mathbf{u}_\varepsilon, \mathbf{v}_\varepsilon) = \sum_{\mathbf{k},\mathbf{l}\in\mathbf{Z}_\varepsilon^\Omega} A^\varepsilon_{\mathbf{k},\mathbf{l}} \left(\int_{\Gamma^\mathbf{k}_\varepsilon} \mathbf{u}_\varepsilon \cdot \mathbf{n}_\varepsilon\right)\left(\int_{\Gamma^\mathbf{l}_\varepsilon} \mathbf{v}_\varepsilon \cdot \mathbf{n}_\varepsilon\right), \tag{1.28}$$

and $\ell_\varepsilon(\cdot)$: $\mathbf{V}_\varepsilon \to \mathbb{R}$ is the linear form

$$\ell_\varepsilon(\mathbf{v}_\varepsilon) = \int_{\Omega_\varepsilon} \mathbf{f}\cdot\mathbf{v}_\varepsilon + \int_{\Gamma_N} p_N \mathbf{v}_\varepsilon \cdot \mathbf{n} - \int_{\Gamma_\varepsilon} p_e \mathbf{v}_\varepsilon \cdot \mathbf{n}_\varepsilon. \tag{1.29}$$

For a given $\varepsilon > 0$, this problem has been studied in [Van09], Section 6.2. The variational formulation (1.26) holds at least in $H^{-1}(0,T)$, and the initial conditions have a meaning in a weak sense under the assumptions of Proposition 1.2.1 below. We have the following existence and uniqueness result:

Proposition 1.2.1. *Under hypothesis* (1.25)*, the variational problem* (1.26) *has a unique solution* $\mathbf{u}_\varepsilon$ *with:*

$$\mathbf{u}_\varepsilon \in L^\infty(0,T;\mathbf{V}_\varepsilon), \quad \textit{and} \quad \partial_t \mathbf{u}_\varepsilon \in L^\infty(0,T;\mathbf{X}_\varepsilon).$$

The proof of existence and uniqueness is given in details in [Van09] and follows the classical Faedo–Galerkin method, see [LM68, Lio69] for reference. The key of the proof is the coercivity of the symmetric bilinear form a_ε, which results from the fact that λ, $\mu > 0$ and that the Poincaré' and Korn's inequalities hold in $\mathbf{V}_\varepsilon$ since $|\Gamma_D| > 0$ (see [DL72]).

1.2.1.2 Extension operator and *a priori* estimates

Because $\mathbf{u}_\varepsilon$ is defined on the porous domain Ω_ε and belongs to the ε–dependent space $\mathbf{V}_\varepsilon$, the estimates derived in [Van09] or that we could compute directly from (1.26) depend *a priori* on ε. To apply Lemma 1.1.14, we need to prove *a priori* bounds that are uniform in ε. Moreover, as is standard when dealing with porous multiscale domains, we need an extension operator from functions defined on Ω_ε to functions defined on Ω since convergence cannot be described in ε–dependent domains. In the remainder of this section, C will denote a constant independent of ε unless otherwise explicitely specified. The previous considerations motivate the introduction of an extension operator $\widehat{\cdot}$ defined for time–dependent functions in $\mathbf{V}_\varepsilon$, whose existence and properties follow from the following Lemma which follows with slight modifications from the proof of Lemma 2.1 in [CD89]:

Lemma 1.2.2. *There exists a linear continuous extension operator denoted by $\widehat{\cdot}$ belonging to the space $\mathcal{L}\left(L^\infty(0,T;\mathbf{H}^k(\Omega_\varepsilon));L^\infty(0,T;\mathbf{H}^k(\Omega))\right)$ for $k=1,2$ such that, for some constant $C>0$ independent of ε and for any $\mathbf{v}_\varepsilon \in L^\infty(0,T;\mathbf{H}^k(\Omega_\varepsilon)) \cap W^{1,\infty}(0,T;\mathbf{L}^2(\Omega_\varepsilon))$,*

1. $\widehat{\mathbf{v}_\varepsilon} = \mathbf{v}_\varepsilon$ *in* $\Omega_\varepsilon \times (0,T)$,
2. $\widehat{\partial_t \mathbf{v}_\varepsilon} = \partial_t(\widehat{\mathbf{v}_\varepsilon})$ *in* $\Omega_\varepsilon \times (0,T)$,
3. $\|\widehat{\mathbf{v}_\varepsilon}\|_{\mathbf{L}^2(\Omega)} \leq C\|\mathbf{v}_\varepsilon\|_{\mathbf{L}^2(\Omega_\varepsilon)}$, *a.e.* $t \in (0,T)$,
4. $\|\widehat{\partial_t \mathbf{v}_\varepsilon}\|_{\mathbf{L}^2(\Omega)} \leq C\|\partial_t \mathbf{v}_\varepsilon\|_{\mathbf{L}^2(\Omega_\varepsilon)}$, , *a.e.* $t \in (0,T)$,
5. $\|\nabla(\widehat{\mathbf{v}_\varepsilon})\|_{L^2(\Omega)} \leq C\|\nabla \mathbf{v}_\varepsilon\|_{L^2(\Omega_\varepsilon)}$, , *a.e.* $t \in (0,T)$,
6. *Moreover, if* $\mathbf{v}_\varepsilon \in \mathbf{V}_\varepsilon$, *a.e.* $t \in (0,T)$,

$$\|e(\widehat{\mathbf{v}_\varepsilon})\|_{L^2(\Omega)} \leq C\|e(\mathbf{v}_\varepsilon)\|_{L^2(\Omega_\varepsilon)}. \tag{1.30}$$

We are now in a position to obtain uniform *a priori* estimates for the sequence $(\widehat{\mathbf{u}_\varepsilon})_{\varepsilon>0}$, defined on the fixed space $\mathbf{V}$:

Proposition 1.2.3. *Under hypothesis (1.25), the sequence of solutions $\mathbf{u}_\varepsilon$ of problem (1.15) is such that*

$$|\widehat{\mathbf{u}_\varepsilon}|^2_{1,\Omega} + \|\widehat{\partial_t \mathbf{u}_\varepsilon}\|^2_{0,\Omega} + \mathcal{V}_\varepsilon(t) \leq C, \qquad \text{a.e. } t \in [0,T], \tag{1.31}$$

for some $C>0$ independent of ε, where

$$\mathcal{V}_\varepsilon(t) = \int_0^t \sum_{\mathbf{k},\mathbf{l}\in\mathbf{Z}^\Omega_\varepsilon} A^\varepsilon_{\mathbf{k},\mathbf{l}} \left(\frac{\mathrm{d}}{\mathrm{d}t}\int_{\Gamma^\mathbf{k}_\varepsilon} \mathbf{u}_\varepsilon \cdot \mathbf{n}_\varepsilon\right)\left(\frac{\mathrm{d}}{\mathrm{d}t}\int_{\Gamma^\mathbf{l}_\varepsilon} \mathbf{u}_\varepsilon \cdot \mathbf{n}_\varepsilon\right) \geq 0. \tag{1.32}$$

Remark 1.2.4. *The quantity $\mathcal{V}_\varepsilon$ measures the dissipation of energy by the viscous forces in the bronchial tree. It is positive, since the matrix A^ε is positive. We can also write $\mathcal{V}_\varepsilon$ using the integral operator $\mathcal{R}_\varepsilon$ defined in Proposition 1.1.8:*

$$\mathcal{V}_\varepsilon(t) = \int_0^t \int_\Omega \frac{\partial}{\partial t}\mathcal{R}_\varepsilon\left(\chi_{F,\varepsilon}\mathrm{div}\ \widehat{\mathbf{u}_\varepsilon}\right)\frac{\partial}{\partial t}\Pi_\varepsilon\left(\chi_{F,\varepsilon}\mathrm{div}\ \widehat{\mathbf{u}_\varepsilon}\right). \tag{1.33}$$

Thanks to these bounds, we can derive some additional regularity results, which are dependent on ε, for the functions $\mathbf{u}_\varepsilon$:

Corollary 1.2.5. *For a given $\varepsilon>0$, the solution $\mathbf{u}_\varepsilon$ of problem (1.15) satisfies:*

$$t \mapsto \int_{\Gamma^\mathbf{k}_\varepsilon} \mathbf{u}_\varepsilon \cdot \mathbf{n}_\varepsilon \in H^1(0,T) \text{ for all } \mathbf{k} \in \mathbf{Z}^\Omega_\varepsilon, \tag{1.34a}$$

$$\partial_{tt}\mathbf{u}_\varepsilon \in L^2(0,T;\mathbf{V}'_\varepsilon). \tag{1.34b}$$

Remark 1.2.6. *The results of Corollary 1.2.5 give a meaning to the strong formulation (1.15). Indeed, it is not clear a priori that the air fluxes computed on each hole* $\int_{\Gamma_\varepsilon^{\mathbf{k}}} \partial_t \mathbf{u}_\varepsilon \cdot \mathbf{n}_\varepsilon$ *are well defined, since* $\partial_t \mathbf{u}_\varepsilon$ *belongs to* $L^\infty(0,T;\mathbf{X}_\varepsilon)$ *so we lack the regularity to define a trace of* $\partial_t \mathbf{u}_\varepsilon$ *on* $\Gamma_\varepsilon^{\mathbf{k}}$*. Now, thanks to (1.34a), we know that the fluxes are defined at least in* $L^2(0,T)$*.*

Also, it is well–known that the result (1.34b) means that $\mathbf{u}_\varepsilon$ *and* $\partial_t \mathbf{u}_\varepsilon$ *are continuous in the time variable, taking values respectively in* $\mathbf{X}_\varepsilon$ *and* $\mathbf{V}'_\varepsilon$*, see e.g. Lemma 1.2 in [Lio69]. Hence the solution* $\mathbf{u}_\varepsilon$ *satisfies the initial conditions* $\mathbf{u}_\varepsilon(0) = \mathbf{u}_0$ *and* $\partial_t \mathbf{u}_\varepsilon(0) = \mathbf{u}_1$ *in a strong sense.*

Proof of Proposition 1.2.3. Let us describe the main ideas of the proof of (1.31) by taking formally $\mathbf{v}_\varepsilon = \partial_t \mathbf{u}_\varepsilon$ as a test function in (1.15). We get the following identity:

$$\begin{cases} \dfrac{1}{2}\dfrac{\mathrm{d}}{\mathrm{d}t}\left(\rho\|\partial_t \mathbf{u}_\varepsilon\|^2_{0,\Omega_\varepsilon} + a(\mathbf{u}_\varepsilon,\mathbf{u}_\varepsilon)\right) + \displaystyle\sum_{\mathbf{k},\mathbf{l}\in\mathbf{Z}_\varepsilon^\Omega} A^\varepsilon_{\mathbf{k},\mathbf{l}} \int_{\Gamma_\varepsilon^{\mathbf{k}}} \partial_t \mathbf{u}_\varepsilon \cdot \mathbf{n}_\varepsilon \int_{\Gamma_\varepsilon^{\mathbf{l}}} \partial_t \mathbf{u}_\varepsilon \cdot \mathbf{n}_\varepsilon \\ \qquad = \displaystyle\int_{\Omega_\varepsilon} \mathbf{f}\cdot\partial_t \mathbf{u}_\varepsilon + \int_{\Gamma_N} p_N \partial_t \mathbf{u}_\varepsilon \cdot \mathbf{n} - \sum_{\mathbf{k}\in\mathbf{Z}_\varepsilon^\Omega} \int_{\Gamma_\varepsilon^{\mathbf{k}}} p_e \partial_t \mathbf{u}_\varepsilon \cdot \mathbf{n}_\varepsilon. \end{cases} \tag{1.35}$$

This equality leads us to introduce the energy term, defined for any $t \in [0,T]$ by:

$$\mathcal{W}_\varepsilon(t) = \frac{1}{2}\rho\|\partial_t \mathbf{u}_\varepsilon\|^2_{0,\Omega_\varepsilon} + \frac{1}{2} a_\varepsilon(\mathbf{u}_\varepsilon,\mathbf{u}_\varepsilon). \tag{1.36}$$

Note that, since the Lamé parameters λ, μ are strictly positive, we have

$$a_\varepsilon(\mathbf{u}_\varepsilon,\mathbf{u}_\varepsilon) = \int_{\Omega_\varepsilon} \lambda\,|\mathrm{div}\ \mathbf{u}_\varepsilon|^2 + 2\mu\,|e(\mathbf{u}_\varepsilon)|^2 \geq 2\mu\|e(\mathbf{u}_\varepsilon)\|^2_{0,\Omega_\varepsilon}.$$

Hence, thanks to the properties of the extension operator $\widehat{\cdot}$, see Lemma 1.2.2, and since Korn's inequality holds in the space $\mathbf{V}$, we know that there exists constants $\gamma_1,\ \gamma_2 > 0$ independent of ε such that

$$\gamma_1\left(\|\widehat{\partial_t \mathbf{u}_\varepsilon}\|^2_{0,\Omega} + |\widehat{\mathbf{u}_\varepsilon}|^2_{1,\Omega}\right) \leq \mathcal{W}_\varepsilon(t) \leq \gamma_2\left(\|\widehat{\partial_t \mathbf{u}_\varepsilon}\|^2_{0,\Omega} + |\widehat{\mathbf{u}_\varepsilon}|^2_{1,\Omega}\right). \tag{1.37}$$

Let $t \in [0,T]$, integrating (1.35) from 0 to t we obtain:

$$\mathcal{W}_\varepsilon(t) - \mathcal{W}_\varepsilon(0) + \mathcal{V}_\varepsilon(t) = \int_0^t \left(\int_{\Omega_\varepsilon} \mathbf{f}\cdot\partial_t \mathbf{u}_\varepsilon + p_N \int_{\Gamma_N} \partial_t \mathbf{u}_\varepsilon \cdot \mathbf{n} - p_e \sum_{\mathbf{k}\in\mathbf{Z}_\varepsilon^\Omega} \int_{\Gamma_\varepsilon^{\mathbf{k}}} \partial_t \mathbf{u}_\varepsilon \cdot \mathbf{n}_\varepsilon \right). \tag{1.38}$$

Let us evaluate each term in the right–hand side of (1.38). Firstly, we obtain using the Cauchy-Schwartz and Young inequalities:

$$\int_0^t \int_{\Omega_\varepsilon} \mathbf{f}\cdot\partial_t \mathbf{u}_\varepsilon \leq \int_0^t \frac{1}{2}\|\widehat{\partial_t \mathbf{u}_\varepsilon}\|^2_{0,\Omega} + \int_0^t \frac{1}{2}\|\mathbf{f}\|^2_{0,\Omega}. \tag{1.39}$$

Secondly, integrating by parts we write:

$$\int_0^t \int_{\Gamma_N} p_N \partial_t \mathbf{u}_\varepsilon \cdot \mathbf{n}_\varepsilon = \left[\int_{\Gamma_N} p_N(s)\mathbf{u}_\varepsilon(s)\cdot\mathbf{n}\right]_{s=0}^t - \int_0^t \int_{\Gamma_N} \partial_t p_N \mathbf{u}_\varepsilon \cdot \mathbf{n}.$$

Using the trace inequality on Γ_N in the space $\mathbf{V}$, we obtain:

$$\left|\int_0^t \int_{\Gamma_N} p_N \partial_t \mathbf{u}_\varepsilon \cdot \mathbf{n}_\varepsilon\right| \leq C\left(|p_N(t)|\ |\widehat{\mathbf{u}_\varepsilon}(t)|_{1,\Omega} + |p_N(0)|\ |\widehat{\mathbf{u}_\varepsilon}(0)|_{1,\Omega} + \int_0^t |\partial_t p_N|\ |\widehat{\mathbf{u}_\varepsilon}|_{1,\Omega}\right).$$

Using Hölder's and Young's inequality, we write for any $\beta > 0$:

$$\left|\int_0^t \int_{\Gamma_N} p_N \partial_t \mathbf{u}_\varepsilon \cdot \mathbf{n}_\varepsilon\right| \leq \frac{\beta}{2}|\widehat{\mathbf{u}_\varepsilon(t)}|^2_{1,\Omega} + \frac{C^2\beta^{-1}}{2}|p_N(t)|^2 + C\left(|p_N(0)|\ |\widehat{\mathbf{u}_\varepsilon}(0)|_{1,\Omega} + \frac{1}{2}\|\partial_t p_N\|^2_{L^2(0,t)} + \frac{1}{2}\int_0^t |\widehat{\mathbf{u}_\varepsilon}|^2_{1,\Omega}\right).$$

Finally, thanks to the initial conditions, we get for any $\beta > 0$,

$$\left|\int_0^t \int_{\Gamma_N} p_N \partial_t \mathbf{u}_\varepsilon \cdot \mathbf{n}_\varepsilon\right| \leq \frac{\beta}{2}|\widehat{\mathbf{u}_\varepsilon(t)}|^2_{1,\Omega} + \frac{C}{2}\int_0^t |\widehat{\mathbf{u}_\varepsilon}|^2_{1,\Omega} + C\left(|p_N(0)|\ |\mathbf{u}_0|_{1,\Omega} + \frac{1}{2}\|\partial_t p_N\|^2_{L^2(0,t)} + \frac{C\beta^{-1}}{2}|p_N(t)|^2\right). \tag{1.40}$$

To obtain for the third term an estimate independent of ε we use the formula:

$$\sum_{\mathbf{k}\in\mathbf{Z}^\Omega_\varepsilon} \int_{\Gamma^{\mathbf{k}}_\varepsilon} \mathbf{u}_\varepsilon \cdot \mathbf{n}_\varepsilon = \int_{\Omega\setminus\Omega_\varepsilon} \operatorname{div} \widehat{\mathbf{u}_\varepsilon}.$$

This leads us to the estimate, valid for all $\beta > 0$:

$$\left|\int_0^t p_e \sum_{\mathbf{k}\in\mathbf{Z}^\Omega_\varepsilon} \int_{\Gamma^{\mathbf{k}}_\varepsilon} \partial_t \mathbf{u}_\varepsilon \cdot \mathbf{n}_\varepsilon\right| \leq \frac{\beta}{2}|\widehat{\mathbf{u}_\varepsilon(t)}|^2_{1,\Omega} + \frac{C}{2}\int_0^t |\widehat{\mathbf{u}_\varepsilon}|^2_{1,\Omega} + C\left(|p_e(0)|\ |\mathbf{u}_0|_{1,\Omega} + \frac{1}{2}\|\partial_t p_e\|^2_{L^2(0,t)} + \frac{C\beta^{-1}}{2}|p_e(t)|^2\right). \tag{1.41}$$

Finally, combining (1.38) and all three estimates (1.39), (1.40) and (1.41) and we obtain the following estimate:

$$\mathcal{W}_\varepsilon(t) + \mathcal{V}_\varepsilon(t) \leq \beta|\widehat{\mathbf{u}_\varepsilon}(t)|^2_{1,\Omega} + \int_0^t \left(\frac{1}{2}\|\partial_t\widehat{\mathbf{u}_\varepsilon}\|^2_{0,\Omega} + C|\widehat{\mathbf{u}_\varepsilon}|^2_{1,\Omega}\right) + K,$$

where K is a constant depending on the initial conditions and the parameters of the problem, but independent of ε thanks the hypothesis (1.25):

$$\begin{aligned} K = \frac{1}{2}\|\mathbf{f}\|^2_{\mathbf{L}^2((0,T)\times\Omega)} &+ C\left(\|p_e\|_{L^\infty(0,T)}\ |\mathbf{u}_0|_{1,\Omega} + \frac{1}{2}|p_e|^2_{H^1(0,T)} + \frac{C\beta^{-1}}{2}\|p_e\|^2_{L^\infty(0,T)}\right) \\ &+ C\left(\|p_e\|_{L^\infty(0,T)}\ |\mathbf{u}_0|_{1,\Omega} + \frac{1}{2}|p_e|^2_{H^1(0,T)} + \frac{C\beta^{-1}}{2}\|p_e\|^2_{L^\infty(0,T)}\right) \\ &+ \gamma_2\left(\|\mathbf{u}_0\|^2_{1,\Omega} + \|\mathbf{u}_1\|^2_{0,\Omega}\right). \end{aligned}$$

Using the bound (1.37), we choose now $\beta = \gamma_1/2$. Gathering all the constants into C, we obtain the following estimate, which holds for all $t \in [0,T]$:

$$\|\widehat{\partial_t\mathbf{u}_\varepsilon}(t)\|^2_{0,\Omega} + |\widehat{\mathbf{u}_\varepsilon}(t)|^2_{1,\Omega} + \mathcal{V}_\varepsilon(t) \leq C\left(1 + \int_0^t \left(\|\widehat{\partial_t\mathbf{u}_\varepsilon}\|^2_{0,\Omega} + |\widehat{\mathbf{u}_\varepsilon}|^2_{1,\Omega}\right)\right).$$

We can then apply Gronwall's Lemma to the real–valued function $t \mapsto \|\widehat{\partial_t\mathbf{u}_\varepsilon}(t)\|^2_{0,\Omega} + |\widehat{\mathbf{u}_\varepsilon}(t)|^2_{1,\Omega} + \mathcal{V}_\varepsilon(t)$. We obtain that for all $t \in [0,T)$,

$$\|\widehat{\partial_t\mathbf{u}_\varepsilon}(t)\|^2_{0,\Omega} + |\widehat{\mathbf{u}_\varepsilon}(t)|^2_{1,\Omega} + \mathcal{V}_\varepsilon(t) \leq C. \tag{1.42}$$

This ends our formal proof of the *a priori* bounds (1.31). Note that the rigorous proof follows the standard Faedo–Galerkin method, for which an example can be found in the proof of Theorem 8.1, p. 287 in [LM68]. For the problem at hand, the details of the method can be found in [VSM09] except for the inclusion of the dissipation term $\mathcal{V}_\varepsilon$ in the *a priori* bounds and the study of the dependence of the constants in the parameter ε. Given a well–chosen sequence of finite–dimensional spaces $\mathbf{V}_\varepsilon^m \subset \mathbf{V}_\varepsilon$ for $m \geq 0$, one constructs a sequence $\mathbf{u}_\varepsilon^m \in L^\infty(0,T;\mathbf{V}_\varepsilon^m)$ solution of the variational formulation (1.26) with test functions in $\mathbf{V}_\varepsilon^m$. Because the system satisfied by the $\mathbf{u}_\varepsilon^m$ is an ODE system, it is possible to use the previous arguments to rigorously prove bounds similar to (1.42) for $\mathbf{u}_\varepsilon^m$, with a constant C independent of both m and ε. Then by passing to the limit in m, one obtains rigorously both existence of $\mathbf{u}_\varepsilon$ and the bounds (1.42). □

Proof of Corollary 1.2.5. We begin by proving (1.34a). We know that the matrix A^ε is symmetric definite positive (Proposition 1.1.5), so for some constant $\alpha_\varepsilon > 0$,

$$\alpha_\varepsilon \sum_{\mathbf{k}\in\mathbf{Z}_\varepsilon^\Omega} \int_0^t \left| \frac{\mathrm{d}}{\mathrm{d}t} \int_{\Gamma_\varepsilon^{\mathbf{k}}} \mathbf{u}_\varepsilon \cdot \mathbf{n}_\varepsilon \right|^2 \leq \int_0^t \sum_{\mathbf{k},\mathbf{l}\in\mathbf{Z}_\varepsilon^\Omega} A_{\mathbf{k},\mathbf{l}}^\varepsilon \left(\frac{\mathrm{d}}{\mathrm{d}t} \int_{\Gamma_\varepsilon^{\mathbf{k}}} \mathbf{u}_\varepsilon \cdot \mathbf{n}_\varepsilon \right) \left(\frac{\mathrm{d}}{\mathrm{d}t} \int_{\Gamma_\varepsilon^{\mathbf{l}}} \mathbf{u}_\varepsilon \cdot \mathbf{n}_\varepsilon \right) \leq \mathcal{V}_\varepsilon(t) \leq C.$$

Hence, the real–valued functions $t \mapsto \int_{\Gamma_\varepsilon^{\mathbf{k}}} \mathbf{u}_\varepsilon \cdot \mathbf{n}_\varepsilon$ belong to $H^1(0,T)$ for any $\mathbf{k} \in \mathbf{Z}_\varepsilon^\Omega$.

We go on to show (1.34b). Thanks to (1.34a) and the Cauchy–Schwartz inequality, we write for any $\mathbf{v}_\varepsilon \in L^2(0,T;\mathbf{V}_\varepsilon)$:

$$\left| \sum_{\mathbf{k},\mathbf{l}\in\mathbf{Z}_\varepsilon^\Omega} A_{\mathbf{k},\mathbf{l}}^\varepsilon \int_0^T \left(\frac{\mathrm{d}}{\mathrm{d}t} \int_{\Gamma_\varepsilon^{\mathbf{k}}} \mathbf{u}_\varepsilon \cdot \mathbf{n}_\varepsilon \right) \left(\int_{\Gamma_\varepsilon^{\mathbf{l}}} \mathbf{v}_\varepsilon \cdot \mathbf{n}_\varepsilon \right) \right| \leq C(\varepsilon) \|\mathbf{v}_\varepsilon\|_{L^2(0,T;\mathbf{V}_\varepsilon)},$$

where $C(\varepsilon) > 0$ is a constant that depends possibly on ε. Now from the variational formulation (1.26) and using a density argument, we get in the sense of distributions:

$$\int_0^T \int_{\Omega_\varepsilon} \partial_{tt}\mathbf{u}_\varepsilon \cdot \mathbf{v}_\varepsilon = \int_0^T \left(\ell_\varepsilon(\mathbf{v}_\varepsilon) - a_\varepsilon(\mathbf{u}_\varepsilon, \mathbf{v}_\varepsilon) - \sum_{\mathbf{k},\mathbf{l}\in\mathbf{Z}_\varepsilon^\Omega} A_{\mathbf{k},\mathbf{l}}^\varepsilon \left(\frac{\mathrm{d}}{\mathrm{d}t} \int_{\Gamma_\varepsilon^{\mathbf{k}}} \mathbf{u}_\varepsilon \cdot \mathbf{n}_\varepsilon \right) \left(\int_{\Gamma_\varepsilon^{\mathbf{l}}} \mathbf{v}_\varepsilon \cdot \mathbf{n}_\varepsilon \right) \right),$$

for all $\mathbf{v}_\varepsilon \in L^2(0,T,\mathbf{V}_\varepsilon)$. Since the right–hand side is a continuous linear form of $\mathbf{v}_\varepsilon$, this proves that $\partial_{tt}\mathbf{u}_\varepsilon$ belongs to $L^2(0,T;\mathbf{V}_\varepsilon')$, hence (1.34b). Note that this does not yield an ε–independent estimate. □

1.2.2 Two–scale convergence result

In this Section, we apply the two–scale convergence method with the framework described in Section 1.1.6 to obtain and rigorously justify the homogenized problem as the microscale parameter ε goes to zero. We focus in particular on the behavior of the functions describing the flow of the air component across the domain, for which the two–scale convergence has not been studied in other papers. Until now, we have not taken into account the geometric behavior of the connexion between the tree and the domain as ε goes to zero and thus the number of generations of the tree goes to infinity. In the remainder of Chapter 1, we will work with the following abstract condition:

$$\begin{aligned} &\text{There exists } \mathcal{R} \in \mathcal{L}\left(L^2(\Omega);L^2(\Omega)\right) \text{ such that} \\ &\mathcal{R}_\varepsilon \to \mathcal{R} \text{ strongly in } \mathcal{L}\left(L^2(\Omega);L^2(\Omega)\right), \end{aligned} \tag{1.43}$$

where $\mathcal{L}\left(L^2(\Omega);L^2(\Omega)\right)$ is equiped with the strong topology associated with the operator norm. As the operators $\mathcal{R}_\varepsilon$ are definite positive and have finite rank, it follows that their strong limit $\mathcal{R}$ is a compact positive operator.

Note that this is a strong statement on the geometry and the resistances of the tree. In Chapter 2, we will describe and investigate some realistic cases where we show that condition (1.43) is verified.

1.2.2.1 Convergence of the sequence of solutions

In this paragraph, we study the convergence properties of the sequence $(\mathbf{u}_\varepsilon)_{\varepsilon>0}$ of solutions of the problem (1.15). In addition to the structure displacement, we will use two new piecewise constant quantities related to the movement of the air as follows:

$$q_\varepsilon = -\Pi_\varepsilon(\chi_{F,\varepsilon}\mathrm{div}\ \widehat{\mathbf{u}_\varepsilon}) \tag{1.44}$$

$$\pi_\varepsilon = \mathcal{R}_\varepsilon q_\varepsilon. \tag{1.45}$$

The field q_ε describes the local change in volume of the individual air cavities: we have

$$\int_{\mathcal{Y}_\varepsilon^{\mathbf{k}}} q_\varepsilon = \varepsilon^d q_\varepsilon(\mathbf{x}) = \int_{\Gamma_\varepsilon^{\mathbf{k}}} \mathbf{u}_\varepsilon \cdot \mathbf{n}_\varepsilon \quad \text{for all } \mathbf{k} \in \mathbf{Z}_\varepsilon^\Omega \text{ and } \mathbf{x} \in \mathcal{Y}_\varepsilon^{\mathbf{k}}.$$

This expression can be compared to (1.13). As a consequence, $d^{-1}\pi_\varepsilon$ is a primitive with respect to the time variable of the difference between the fluid pressure field and the pressure at the root node, see (1.14). Moreover, the quantity $\mathcal{V}_\varepsilon(t)$ writes simply:

$$\mathcal{V}_\varepsilon(t) = \int_0^t \int_\Omega (\mathcal{R}_\varepsilon \partial_t q_\varepsilon)\, \partial_t q_\varepsilon = \int_0^t \int_\Omega \partial_t \pi_\varepsilon \partial_t q_\varepsilon. \tag{1.46}$$

We deduce from the previous analysis the following result:

Lemma 1.2.7. *The functions q_ε and π_ε belong to $H^1(0,T;L^2(\Omega))$. Moreover, there exists $C>0$ independent of ε such that:*

$$\|q_\varepsilon\|_{L^2(0,T;L^2(\Omega))} + \|\mathcal{R}_\varepsilon \partial_t q_\varepsilon\|_{L^2(0,T;L^2(\Omega))} \leq C. \tag{1.47}$$

Proof. We obtain the regularity of q_ε and π_ε as well as the uniform bound on q_ε in $L^2(0,T;L^2(\Omega))$ as an immediate consequence of (1.34a) and the *a priori* bounds (1.31). To bound uniformly $\mathcal{R}_\varepsilon \partial_t q_\varepsilon$, we use the reflexivity of the L^2 spaces. Let $\psi \in L^2((0,T)\times\Omega)$, the Cauchy–Schwartz inequality (1.23) yields:

$$\begin{aligned}\left|\int_0^T \int_\Omega (\mathcal{R}_\varepsilon \partial_t q_\varepsilon)\, \psi\right|^2 &\leq \left(\int_0^T \int_\Omega (\mathcal{R}_\varepsilon \partial_t q_\varepsilon)\, \partial_t q_\varepsilon\right)\left(\int_0^T \int_\Omega (\mathcal{R}_\varepsilon \psi)\, \psi\right) \\ &\leq \mathcal{V}_\varepsilon(T)\|\mathcal{R}_\varepsilon\|_{\mathcal{L}(L^2(\Omega))}\|\psi\|^2_{L^2((0,T)\times\Omega)}.\end{aligned}$$

But we know that $\mathcal{V}_\varepsilon(T)$ is uniformly bounded thanks to the *a priori* bounds (1.31), and the sequence $(\mathcal{R}_\varepsilon)_{\varepsilon>0}$ converges strongly, hence it is also uniformly bounded in the operator norm, with respect to ε.

Therefore, $\psi \mapsto \int_0^T \int_\Omega (\mathcal{R}_\varepsilon \partial_t q_\varepsilon)\, \psi$ is uniformly bounded as a linear form on $L^2(\Omega)$ so $\mathcal{R}_\varepsilon \partial_t q_\varepsilon$ is uniformly bounded in $L^2((0,T)\times\Omega)$, with respect to ε. □

Then, we have the following result:

Proposition 1.2.8. *Suppose (1.25) and (1.43) hold. Then, there exists $\mathbf{u} \in L^2(0,T;\mathbf{V})$ such that $\partial_t \mathbf{u} \in L^2(0,T;\mathbf{X})$ and $\mathbf{u}^1 \in L^2((0,T)\times\Omega;\mathbf{H}^1_\#(\mathcal{Y})/\mathbb{R}^d)$ and up to a subsequence, still denoted by ε,*

$$\begin{cases} \widehat{\mathbf{u}_\varepsilon} \twoheadrightarrow \mathbf{u} \\ \nabla\widehat{\mathbf{u}_\varepsilon} \twoheadrightarrow \nabla_{\mathbf{x}}\mathbf{u} + \nabla_{\mathbf{y}}\mathbf{u}^1 \\ \widehat{\partial_t \mathbf{u}_\varepsilon} \twoheadrightarrow \partial_t \mathbf{u} \end{cases} \qquad \text{two-scale in } L^2((0,T)\times\Omega\times\mathcal{Y}). \tag{1.48}$$

Moreover, the function q_ε two–scale converges in $L^2((0,T)\times\Omega\times\mathcal{Y})$ to a function $q\in L^2((0,T)\times\Omega)$:

$$q_\varepsilon \twoheadrightarrow q = -\left((1-\theta)\mathrm{div}_{\mathbf{x}}\mathbf{u} - \int_\Gamma \mathbf{u}^1\cdot\mathbf{n}^S\right), \qquad \text{two–scale in } L^2((0,T)\times\Omega\times\mathcal{Y}), \tag{1.49}$$

and the function π_ε converges to $\pi\in H^1(0,T;L^2(\Omega))$ as follows:

$$\pi_\varepsilon = \mathcal{R}_\varepsilon q_\varepsilon \to \pi = \mathcal{R}q \qquad \text{strongly in } L^2((0,T)\times\Omega), \tag{1.50}$$

$$\partial_t\pi_\varepsilon = \mathcal{R}_\varepsilon\partial_t q_\varepsilon \twoheadrightarrow \partial_t\pi = \partial_t(\mathcal{R}q) \qquad \text{two–scale in } L^2((0,T)\times\Omega\times\mathcal{Y}). \tag{1.51}$$

Remark 1.2.9. *The a priori bounds (1.31) do not enable us to control the L^2–norm of $\partial_t q_\varepsilon$, which is why we only obtain convergence of $\partial_t\mathcal{R}_\varepsilon q_\varepsilon$. However, in the case where $\mathcal{R}$ is also definite positive, we can control $\partial_t q_\varepsilon$ by using the norm $u\mapsto\int_0^T(\mathcal{R}u,u)^{1/2}$ on $L^2((0,T)\times\Omega)$, which means that $\partial_t q_\varepsilon$ converges to a function which belongs to the complete closure of $L^2((0,T)\times\Omega)$ with respect to the norm $\int_0^T(\mathcal{R}u,u)^{1/2}_{L^2(\Omega)}$.*

This space depends on the properties of the compact operator $\mathcal{R}$, and it can sometimes be identified: if the tree is geometric (see Section 2.2), then the complete closure of $L^2(\Omega)$ with respect to the norm $u\mapsto(\mathcal{R}u,u)^{1/2}_{L^2(\Omega)}$ can be identified as a Sobolev negative space $H^s(\Omega)$ with $s<0$ for adequate values of the parameters, see e.g. [GMM06, VSM09].

Proof. Thanks to the *a priori* bounds (1.31), we can apply Lemma 1.1.14. We deduce that there exists $\mathbf{u}\in L^2(0,T;\mathbf{V})$ with $\partial_t\mathbf{u}\in L^2(0,T;\mathbf{X})$ and $\mathbf{u}^1\in L^2((0,T)\times\Omega;\mathbf{H}^1_\#(\mathcal{Y})/\mathbb{R}^d)$ such that up to a subsequence, the following two–scale convergence hold in $\Omega\times\mathcal{Y}$:

$$\widehat{\mathbf{u}_\varepsilon}\twoheadrightarrow\mathbf{u}(t,x), \qquad \nabla\widehat{\mathbf{u}_\varepsilon}\twoheadrightarrow\nabla_{\mathbf{x}}\mathbf{u}(t,x)+\nabla_{\mathbf{y}}\mathbf{u}^1(t,x,y), \qquad \partial_t\widehat{\mathbf{u}_\varepsilon}\twoheadrightarrow\partial_t\mathbf{u}(t,x). \tag{1.52}$$

Moreover, the sequence $(q_\varepsilon)_{\varepsilon>0}$ is uniformly bounded with respect to ε in $L^\infty(0,T;L^2(\Omega))$ thanks to the *a priori* bounds (1.31). To investigate the convergence of q_ε and π_ε as ε goes to zero, we use the following technical Lemma (see e.g. [BGMO08]):

Lemma 1.2.10. *Let Π_ε be the projection operator defined in Definition 1.1.7. Then, for all $\phi\in\mathcal{D}(\Omega,C^\infty_\#(\mathcal{Y}))$,*

$$\Pi_\varepsilon\left(\phi(\cdot,\frac{\cdot}{\varepsilon})\right)\to\int_{\mathcal{Y}}\phi(\cdot,\mathbf{y})\mathrm{d}\mathbf{y}, \qquad L^2(\Omega)\text{–strongly},$$

$$\Pi_\varepsilon\left(\chi_{F,\varepsilon}\phi(\cdot,\frac{\cdot}{\varepsilon})\right)\to\int_{\mathcal{Y}_F}\phi(\cdot,\mathbf{y})\mathrm{d}\mathbf{y} \qquad L^2(\Omega)\text{–strongly}.$$

Thanks to this Lemma, we are going to determine the two–scale limit of q_ε. For any test function $\phi\in\mathcal{D}((0,T)\times\Omega,C^\infty_\#(Y))$, we write:

$$\begin{aligned}\int_0^T\int_\Omega q_\varepsilon(\mathbf{x},t)\phi\left(\mathbf{x},\frac{\mathbf{x}}{\varepsilon},t\right) &= -\int_0^T\int_\Omega\Pi_\varepsilon\left(\chi_{F,\varepsilon}\mathrm{div}\,\widehat{\mathbf{u}_\varepsilon}\right)(\mathbf{x},t)\phi\left(\mathbf{x},\frac{\mathbf{x}}{\varepsilon},t\right)\\ &= -\int_0^T\int_\Omega\left(\chi_{F,\varepsilon}\mathrm{div}\,\widehat{\mathbf{u}_\varepsilon}\right)(\mathbf{x},t)\Pi_\varepsilon\left(\phi(\cdot,\frac{\cdot}{\varepsilon},t)\right)(\mathbf{x}).\end{aligned} \tag{1.53}$$

Now due to the two–scale convergence of $\mathbf{u}_\varepsilon$ (1.52), we have the weak convergence result:

$$\chi_{F,\varepsilon}\mathrm{div}\,\widehat{\mathbf{u}_\varepsilon}\rightharpoonup\int_{\mathcal{Y}_F}\left(\mathrm{div}_{\mathbf{x}}\mathbf{u}+\mathrm{div}_{\mathbf{y}}\mathbf{u}^1\right), \qquad \text{weakly in } L^2((0,T)\times\Omega).$$

Combining this weak convergence with the strong convergence result from Lemma 1.2.10, we can pass to the limit in (1.53) and we get:

$$\lim_{\varepsilon\to 0}\int_0^T\int_\Omega q_\varepsilon(\mathbf{x},t)\phi\left(\mathbf{x},\frac{\mathbf{x}}{\varepsilon},t\right)=-\int_0^T\int_\Omega\left(\int_{\mathcal{Y}_F}\mathrm{div}_{\mathbf{x}}\mathbf{u}+\mathrm{div}_{\mathbf{y}}\mathbf{u}^1\right)\int_{\mathcal{Y}}\phi.$$

Consequently, q_ε two–scale converges (up to a subsequence) to a function $q\in L^2(\Omega)$ and we can identify the two–scale limit:

$$q_\varepsilon \twoheadrightarrow q=-\left((1-\theta)\mathrm{div}_{\mathbf{x}}\mathbf{u}-\int_\Gamma \mathbf{u}^1\cdot\mathbf{n}^S\right). \tag{1.54}$$

We remind that $\theta=|\mathcal{Y}_S|$ is the proportion of structure in the material. Now we are going to show that $\pi_\varepsilon=\mathcal{R}_\varepsilon q_\varepsilon$ converges strongly in L^2 towards $\mathcal{R}q$ up to a subsequence. Let us write

$$\mathcal{R}_\varepsilon q_\varepsilon-\mathcal{R}q=\left(\mathcal{R}_\varepsilon-\mathcal{R}\right)q_\varepsilon+\mathcal{R}\left(q_\varepsilon-q\right).$$

We derive from (1.54) the weak convergence of $(q_\varepsilon)_{\varepsilon>0}$ towards q; combined with the compactness of $\mathcal{R}$, we deduce that, up to a subsequence, $\mathcal{R}(q_\varepsilon-q)$ converges strongly to zero in $L^2((0,T)\times\Omega)$.

Moreover, the uniform bounds on q_ε (1.47) combined with the strong convergence of the sequence $(\mathcal{R}_\varepsilon)_{\varepsilon>0}$ imply that $\left(\mathcal{R}_\varepsilon-\mathcal{R}\right)q_\varepsilon$ converges strongly to zero in $L^2((0,T)\times\Omega)$. Thus, we obtain the desired result:

$$\mathcal{R}_\varepsilon q_\varepsilon\to\mathcal{R}q\quad\text{strongly in } L^2((0,T)\times\Omega).$$

As a consequence,

$$\mathcal{R}_\varepsilon\partial_t q_\varepsilon\to\partial_t\left(\mathcal{R}q\right)\qquad\text{in } \mathcal{D}'(0,T;L^2(\Omega)). \tag{1.55}$$

We know that the pressure field $(\mathcal{R}_\varepsilon\partial_t q_\varepsilon)$ forms a uniformly bounded sequence in $L^2((0,T)\times\Omega)$, see (1.47), so it converges weakly up to a subsequence in that space. Combined with (1.55), we can identify this limit with $\partial_t\left(\mathcal{R}q\right)$ so we have obtained:

$$\mathcal{R}q\in H^1(0,T;L^2(\Omega))\text{ and }\mathcal{R}_\varepsilon\partial_t q_\varepsilon\rightharpoonup\partial_t\left(\mathcal{R}q\right)\qquad\text{weakly in } L^2((0,T)\times\Omega).$$

Since $\mathcal{R}_\varepsilon\partial_t q_\varepsilon$ is piecewise constant on the cells $\mathcal{Y}_\varepsilon^{\mathbf{k}}$, we also obtain a stronger result of two–scale convergence: for any test functions $\phi\in\mathcal{D}(\Omega,C^\infty_\#(\mathcal{Y}))$, we have the identity

$$\int_\Omega\left(\mathcal{R}_\varepsilon\partial_t q_\varepsilon\right)(\mathbf{x})\ \phi(\mathbf{x},\mathbf{x}/\varepsilon)\mathrm{d}\mathbf{x}=\int_\Omega\left(\mathcal{R}_\varepsilon\partial_t q_\varepsilon\right)(\mathbf{x})\ \Pi_\varepsilon\left(\phi(\cdot,\cdot/\varepsilon)\right)(\mathbf{x})\mathrm{d}\mathbf{x}.$$

Because $\mathbf{x}\mapsto\Pi_\varepsilon\left(\phi(\cdot,\cdot/\varepsilon)\right.$ converges strongly to $\mathbf{x}\mapsto\int_{\mathcal{Y}}\phi(\mathbf{x},\mathbf{y})$ by Lemma 1.2.10, the weak convergence of $\mathcal{R}_\varepsilon\partial_t q_\varepsilon$ ensures that

$$\lim_{\varepsilon\to 0}\int_\Omega\left(\mathcal{R}_\varepsilon\partial_t q_\varepsilon\right)\phi\mathrm{d}\mathbf{x}=\int_\Omega\int_{\mathcal{Y}}\partial_t\left(\mathcal{R}q\right)(\mathbf{x})\phi(\mathbf{x},\mathbf{y})\mathrm{d}\mathbf{y}\mathrm{d}\mathbf{x}\qquad\forall\phi\in\mathcal{D}(\Omega,C^\infty_\#(\mathcal{Y})).$$

Hence, $\mathcal{R}_\varepsilon\partial_t q_\varepsilon$ two–scale converges towards $\partial_t\left(\mathcal{R}q\right)$. This concludes the proof of the Proposition. □

1.2.2.2 The two–scale limit problem: main result

Define the Hilbert space

$$\mathbf{H}=L^2(\Omega;\mathbf{H}^1_\#(\mathcal{Y}_S)/\mathbb{R}^d)).$$

We are now in a position to prove how the two–scale convergence process sketched in Proposition 1.2.8 gives us an effective macroscopic description of the parenchyma model. First, let us study the

problem obtained by taking the two–scale limit term by term in the variational formulation (1.26). Let us introduce the two bilinear forms $a_\#$, $r_\#$ and the linear form $\ell_\#$ on $\mathbf{V}\times\mathbf{H}$ defined as:

$$a_\#((\mathbf{u},\mathbf{u}^1),(\mathbf{v},\mathbf{v}^1)) = \int_\Omega\int_{\mathcal{Y}_S} \lambda(\mathrm{div}_{\mathbf{x}}\mathbf{u}+\mathrm{div}_{\mathbf{y}}\mathbf{u}^1)(\mathrm{div}_{\mathbf{x}}\mathbf{v}+\mathrm{div}_{\mathbf{y}}\mathbf{v}^1) \tag{1.56}$$
$$+2\mu\left(e_{\mathbf{x}}(\mathbf{u})+e_{\mathbf{y}}(\mathbf{u}^1)\right):\left(e_{\mathbf{x}}(\mathbf{v})+e_{\mathbf{y}}(\mathbf{v}^1)\right),$$

$$r_\#((\mathbf{u},\mathbf{u}^1),(\mathbf{v},\mathbf{v}^1)) = \int_\Omega \mathcal{R}\left((1-\theta)\mathrm{div}_{\mathbf{x}}\mathbf{u}-\int_\Gamma \mathbf{u}^1\cdot\mathbf{n}^S\right)\left((1-\theta)\mathrm{div}_{\mathbf{x}}\mathbf{v}-\int_\Gamma \mathbf{v}^1\cdot\mathbf{n}^S\right), \tag{1.57}$$

$$\ell_\#(\mathbf{v},\mathbf{v}^1) = \int_\Omega \theta\mathbf{f}\cdot\mathbf{v}+\int_{\Gamma_N} p_N\mathbf{v}\cdot\mathbf{n}-\int_\Omega p_e\left((1-\theta)\mathrm{div}_{\mathbf{x}}\mathbf{v}-\int_\Gamma \mathbf{v}^1\cdot\mathbf{n}^S\right). \tag{1.58}$$

We remind that $\theta=|\mathcal{Y}_S|$ is the volume fraction of the elastic material.

Proposition 1.2.11. *The following two–scale variational problem has a unique solution* $(\mathbf{u}_\infty,\mathbf{u}^1_\infty)$ *in* $L^\infty(0,T;\mathbf{V})\cap W^{1,\infty}(0,T;\mathbf{X})\times L^\infty(0,T;\mathbf{H})$, *such that* $\mathcal{R}\left(\int_\Gamma \mathbf{u}^1_\infty\cdot\mathbf{n}_S\right)\in H^1((0,T),L^2(\Omega))$*:*

$$\begin{cases} \text{For all } \mathbf{v}\in\mathbf{V},\ \mathbf{v}^1\in\mathbf{H}, \text{ and in } \mathcal{D}'(0,T), \\ \dfrac{\mathrm{d}}{\mathrm{d}t}(\theta\rho\partial_t\mathbf{u}_\infty,\mathbf{v})_{0,\Omega}+\dfrac{\mathrm{d}}{\mathrm{d}t}r_\#((\mathbf{u}_\infty,\mathbf{u}^1_\infty),(\mathbf{v},\mathbf{v}^1))+a_\#((\mathbf{u}_\infty,\mathbf{u}^1_\infty),(\mathbf{v},\mathbf{v}^1))=\ell_\#(\mathbf{v},\mathbf{v}^1), & \text{(1.59a)} \\ \mathbf{u}_\infty(0)=\mathbf{u}_0,\ \mathbf{u}^1_\infty(0)=\mathbf{0},\ \partial_t\mathbf{u}_\infty(0)=\mathbf{u}_1 \text{ in } \Omega, & \text{(1.59b)} \end{cases}$$

Moreover,

$$\partial_{tt}\mathbf{u}_\infty\in L^2(0,T;\mathbf{V}').$$

Remark 1.2.12. *Since* $\mathbf{u}^1_\infty$ *is not continuous in time, the initial condition on* $\mathbf{u}^1_\infty(0)$ *has only a weak meaning associated with the computation of the following quantity introduced in Proposition 1.2.8:*

$$\pi_\infty=\mathcal{R}\left((1-\theta)\mathrm{div}_{\mathbf{x}}\mathbf{u}_\infty-\int_\Gamma \mathbf{u}^1_\infty\cdot\mathbf{n}^S\right).$$

We know that π_∞ *belongs to* $H^1(0,T;L^2(\Omega))$*, hence its trace at* $t=0$ *has a meaning. This quantity can be interpreted as the initial state of pressure inside the alveoli. Here it is initially identically zero because of our assumption that* $\mathbf{u}_0$ *is independent of* ε*, ruling out any initial deformations at the alveolar level in the limit.*

Proof. As a first step, we sketch the proof of existence and uniqueness of solutions for the two–scale problem (1.59). This follows the classical Galerkin method and is very similar to the proof of the same result for the original problem (1.26).

The main argument is that $a_\#(\cdot,\cdot)$ is a symmetric, continuous, coercive bilinear form on $\mathbf{V}\times\mathbf{H}$. This results from a special Korn inequality which holds on $\mathbf{V}\times\mathbf{H}$, see for example [BGMO08]. Then, since $\mathcal{R}$ is symmetric and positive, we can follow the classical Faedo-Galerkin method used to prove existence and uniqueness in Proposition 1.2.3:

a) First, we construct a sequence of finite dimensional spaces based on the eigenvectors $(\mathbf{w}_m,\mathbf{w}^1_m)$ of $a_\#$:
$$H_m\subset\mathbf{V}\times\mathbf{H},$$

b) Then, we solve a finite dimensional version of (1.59) using general ordinary differential equation theory to construct a sequence of approximate solutions $(\mathbf{u}_m,\mathbf{u}^1_m)$ with $(\mathbf{u}_m,\mathbf{u}^1_m)\in H_m$,

c) We derive an energy estimate for some $C>0$ independent of m:
$$\|\partial_t\mathbf{u}_m\|^2_{0,\Omega}+\|(\mathbf{u}_m,\mathbf{u}^1_m)\|^2_{\mathbf{V}\times\mathbf{H}}\le C,\qquad \text{a.e. } t\in(0,T).$$

d) Passing to the weak-* limit, we find solutions $(\mathbf{u}_\infty, \mathbf{u}^1_\infty)$ of (1.59) with the regularity stated in the Theorem.

Next, let us prove in detail the uniqueness of the solution. This is an important point, from which depends the identification of the two–scale limits. Let $(\mathbf{u}_1, \mathbf{u}^1_1)$ and $(\mathbf{u}_2, \mathbf{u}^1_2)$ be two solutions of (1.59) and let $(\mathbf{w}, \mathbf{w}^1) = (\mathbf{u}_1 - \mathbf{u}_2, \mathbf{u}^1_1 - \mathbf{u}^2_2)$. Let $s \in [0, T)$. We introduce the following test functions, following a classical idea (see [LM68]):

$$\mathbf{v} = \begin{cases} -\int_t^s \mathbf{w} & 0 \le t \le s \\ 0 & t > s \end{cases}, \qquad \mathbf{v}^1 = \begin{cases} -\int_t^s \mathbf{w}^1 & 0 \le t \le s \\ 0 & t > s \end{cases}.$$

Then we have, using (1.59a) with zero right–hand side,

$$\int_0^T \langle \theta\rho\partial_{tt}\mathbf{w}, \mathbf{v}\rangle + a_\# \left((\mathbf{w}, \mathbf{w}^1), (\mathbf{v}, \mathbf{v}^1)\right) + \int_0^T \int_\Omega \frac{\partial}{\partial t}\mathcal{R}\left((1-\theta)\mathrm{div}_{\mathbf{x}}\mathbf{w} - \int_\Gamma \mathbf{w}^1 \cdot \mathbf{n}^S\right)\left((1-\theta)\mathrm{div}_{\mathbf{x}}\mathbf{v} - \int_\Gamma \mathbf{v}^1 \cdot \mathbf{n}^S\right) = 0,$$

where $\langle \cdot, \cdot \rangle$ is the duality pairing between $\mathbf{V}'$ and $\mathbf{V}$. Integrating by parts in time, we obtain:

$$\int_0^T -(\theta\rho\partial_t\mathbf{w}, \partial_t\mathbf{v})_{0,\Omega} + a_\# \left((\mathbf{w}, \mathbf{w}^1), (\mathbf{v}, \mathbf{v}^1)\right) - \int_0^T \int_\Omega \mathcal{R}\left((1-\theta)\mathrm{div}_{\mathbf{x}}\mathbf{w} - \int_\Gamma \mathbf{w}^1 \cdot \mathbf{n}^S\right)\frac{\partial}{\partial t}\left((1-\theta)\mathrm{div}_{\mathbf{x}}\mathbf{v} - \int_\Gamma \mathbf{v}^1 \cdot \mathbf{n}^S\right) = 0,$$

where we have used the fact that

$$\partial_t\mathbf{w}(0) = \mathbf{u}_1 - \mathbf{u}_1 = \mathbf{0}, \quad \mathbf{v}(T) = \mathbf{0}, \quad \mathbf{v}^1(T) = \mathbf{0},$$

and also

$$\mathcal{R}\left((1-\theta)\mathrm{div}_{\mathbf{x}}\mathbf{w} - \int_\Gamma \mathbf{w}^1 \cdot \mathbf{n}^S\right)\Big|_{t=0} = \mathcal{R}\left((1-\theta)\mathrm{div}_{\mathbf{x}}(\mathbf{u}_0 - \mathbf{u}_0)\right) = 0. \tag{1.60}$$

Since $\mathcal{R}$ is a positive operator and $\partial_t\mathbf{v} = \mathbf{w}$, $\partial_t\mathbf{v}^1 = \mathbf{w}^1$, this yields:

$$\int_0^s \frac{1}{2}\frac{\mathrm{d}}{\mathrm{d}t}\left(-\theta\rho\|\mathbf{w}\|^2_{0,\Omega} + a_\#\left((\mathbf{v}, \mathbf{v}^1), (\mathbf{v}, \mathbf{v}^1)\right)\right) \ge 0.$$

Hence, because $\mathbf{w}(0) = \mathbf{u}_0 - \mathbf{u}_0 = \mathbf{0}$:

$$-\theta\rho\|\mathbf{w}(s)\|^2_{0,\Omega} - a_\#\left((\mathbf{v}(0), \mathbf{v}^1(0)), (\mathbf{v}(0), \mathbf{v}^1(0))\right) \ge 0.$$

Since $a_\#$ is positive, we obtain $\mathbf{w}(s) = \mathbf{0}$ for all $s \in (0, T)$. We conclude that the solution of (1.59) is unique. □

The following Theorem is the main result of this section.

Theorem 1.2.13. *(Asymptotic two–scale formulation)*
Suppose conditions (1.25) and (1.43) hold. Let $(\mathbf{u}_\varepsilon)_{\varepsilon>0}$ be the sequence of solutions of the family of problems (1.15) when ε varies.

Then the three sequences $(\widehat{\mathbf{u}_\varepsilon}\chi_{S,\varepsilon})_{\varepsilon>0}$, $(\widehat{\partial_t\mathbf{u}_\varepsilon}\chi_{S,\varepsilon})_{\varepsilon>0}$ and $(\nabla(\widehat{\mathbf{u}_\varepsilon})\chi_{S,\varepsilon})_{\varepsilon>0}$ two–scale converge respectively to $\mathbf{u}\chi_S$, $\partial_t\mathbf{u}\chi_S$ and $\left(\nabla_{\mathbf{x}}\mathbf{u} + \nabla_{\mathbf{y}}\mathbf{u}^1\right)\chi_S$ in $L^2((0,T)\times\Omega\times\mathcal{Y})$, where $(\mathbf{u}, \mathbf{u}^1|_{\Omega\times\mathcal{Y}_S})$ can be identified with $(\mathbf{u}_\infty, \mathbf{u}^1_\infty)$, the unique solution of the two–scale variational problem (1.59).

Remark 1.2.14. *We can make a few observations on the behavior of the homogenized material from the two–scale formulation* (1.59). *There is no added mass effect from the fluid onto the structure, as can be seen in the inertial term which is the same as in the original formulation* (1.26). *In addition, the instantaneous elastic reponse of the material differs from the static case presented in [BGMO08], because the compressibility of the air in the alveoli is not taken into account here: if the air does not have time to escape through the tree, each air cavity acts as if it is incompressible.*

Proof. We proceed in two steps. First,we show that the two–scale limit of the sequence of solutions $(\mathbf{u}_\varepsilon)$ of the family of problems (1.15) satisfies the variational formulation (1.59) by taking the limit term by term in the variational formulation (1.26) with well–chosen test functions, thanks to the properties of two–scale convergence. Finally, we identify the two–scale limits with the solutions of the two–scale variational formulation thanks to the uniqueness property.

Two–scale limit. Next, we need to prove that the solutions $(\mathbf{u}_\infty, \mathbf{u}^1_\infty)$ of (1.59) are indeed equal to $(\mathbf{u}, \mathbf{u}^1)$ the two–scale limits of the solutions of (1.26). The idea is to reduce the problem to an elliptic setting, which can be achieved through Laplace transformation or by multiplying the equation by a test function ϕ in $\mathcal{D}((0,T))$. Here we use the latter technique. For any $\mathbf{w}$ in $L^2(0,T;\mathbf{X})$ (respectively $L^2(0,T;\mathbf{L}^2(\Omega\times\mathcal{Y}))$) and $\phi\in\mathcal{D}((0,T))$ we define $\mathbf{w}(\phi)$ in $\mathbf{X}$ (respectively $\mathbf{L}^2(\Omega\times\mathcal{Y})$) by:

$$\mathbf{w}(\phi)(\mathbf{x}) = \int_0^T \mathbf{w}(\mathbf{x},t)\phi(t)\mathrm{d}t \quad \left(\text{respectively} \quad \mathbf{w}(\phi)(\mathbf{x},\mathbf{y}) = \int_0^T \mathbf{w}(\mathbf{x},\mathbf{y},t)\phi(t)\mathrm{d}t.\right) \tag{1.61}$$

We will denote the time derivatives of ϕ by ϕ', ϕ'' to simplify notations. By virtue of Proposition 1.2.8, up to a subsequence we have:

$$\widehat{\mathbf{u}_\varepsilon}(\phi) \twoheadrightarrow \mathbf{u}(\phi) \qquad \text{two–scale in } L^2(\Omega\times\mathcal{Y}), \tag{1.62a}$$

$$\nabla\widehat{\mathbf{u}_\varepsilon}(\phi) \twoheadrightarrow \nabla_{\mathbf{x}}\mathbf{u}(\phi) + \nabla_{\mathbf{y}}\mathbf{u}^1(\phi) \qquad \text{two–scale in } L^2(\Omega\times\mathcal{Y}). \tag{1.62b}$$

Let now $\mathbf{v}$ in $\mathbf{V}\cap C^\infty(\overline{\Omega})$, $\mathbf{v}^1$ in $\mathcal{D}(\Omega; C^\infty_\#(\mathcal{Y}))$; we choose the test function $\mathbf{v}_\varepsilon\in\mathbf{V}_\varepsilon$ in the variational formulation (1.26) as follows:

$$\mathbf{v}_\varepsilon(\mathbf{x}) = \mathbf{v}(\mathbf{x}) + \varepsilon\mathbf{v}^1\left(\mathbf{x}, \frac{\mathbf{x}}{\varepsilon}\right).$$

These test functions are admissible for the two–scale convergence definition (see [All92]). We integrate in time against ϕ and we use the extension operator $\widehat{\cdot}$ to write all integrals over Ω_ε in variational formulation (1.26) as integrals over Ω, this yields, since ϕ has compact support in $(0,T)$:

$$\begin{aligned}\int_\Omega \rho\widehat{\mathbf{u}_\varepsilon}(\phi'')\cdot\mathbf{v}_\varepsilon\chi_{S,\varepsilon}\mathrm{d}\mathbf{x} + \lambda\int_\Omega \mathrm{div}\left(\widehat{\mathbf{u}_\varepsilon}(\phi)\right)\mathrm{div}\left(\mathbf{v}_\varepsilon\right)\chi_{S,\varepsilon}\mathrm{d}\mathbf{x} + 2\mu\int_\Omega e(\widehat{\mathbf{u}_\varepsilon}(\phi)) : e(\mathbf{v}_\varepsilon)\chi_{S,\varepsilon}\mathrm{d}\mathbf{x} \\ - r_\varepsilon(\widehat{\mathbf{u}_\varepsilon}(\phi'),\mathbf{v}_\varepsilon) = \ell^\phi_\varepsilon(\mathbf{v}_\varepsilon),\end{aligned} \tag{1.63}$$

where we have introduced the linear form

$$\begin{aligned}\ell^\phi_\varepsilon(\mathbf{v}_\varepsilon) &= \int_\Omega \mathbf{f}(\phi)\cdot\mathbf{v}_\varepsilon\chi_{S,\varepsilon}\mathrm{d}\mathbf{x} + \left(\int_0^T p_N(t)\phi(t)\right)\int_{\Gamma_N}\mathbf{v}_\varepsilon\cdot\mathbf{n} - \left(\int_0^T p_e(t)\phi(t)\right)\int_{\Gamma_\varepsilon}\mathbf{v}_\varepsilon\cdot\mathbf{n}_\varepsilon \\ &= \int_0^T \ell_\varepsilon(\mathbf{v}_\varepsilon)\phi(t)\mathrm{d}t \qquad \text{for all } \mathbf{v}_\varepsilon\in\mathbf{V}_\varepsilon.\end{aligned}$$

Using the definition of two–scale convergence (1.24), we pass to the limit easily in the first three terms in the left–hand side of (1.63) as ε goes to zero. Note that to compute the limits the indicator

function of the structure domain is associated with the test function, thanks to the Remark 1.1.12. As a result the integrals obtained after the limit are supported on $\Omega \times \mathcal{Y}_S$. We have indeed:

$$\int_\Omega \rho \widehat{\mathbf{u}_\varepsilon}(\phi'') \cdot \mathbf{v}_\varepsilon \chi_{S,\varepsilon} \to \int_\Omega \theta\rho \mathbf{u}(\phi'') \cdot \mathbf{v}, \tag{1.64}$$

$$\lambda \int_\Omega \operatorname{div} \widehat{\mathbf{u}_\varepsilon}(\phi) \operatorname{div}(\mathbf{v}_\varepsilon) \chi_{S,\varepsilon} \to \lambda \int_\Omega \int_{\mathcal{Y}_S} \left(\operatorname{div}_{\mathbf{x}} \mathbf{u}(\phi) + \operatorname{div}_{\mathbf{y}} \mathbf{u}^1(\phi)\right) \left(\operatorname{div}_{\mathbf{x}} \mathbf{v} + \operatorname{div}_{\mathbf{y}} \mathbf{v}^1\right), \tag{1.65}$$

$$2\mu \int_\Omega e(\widehat{\mathbf{u}_\varepsilon}(\phi)) : e(\mathbf{v}_\varepsilon) \chi_{S,\varepsilon} \to 2\mu \int_\Omega \int_{\mathcal{Y}_S} \left(e_{\mathbf{x}}(\mathbf{u}(\phi)) + e_{\mathbf{y}}(\mathbf{u}^1(\phi))\right) : \left(e_{\mathbf{x}}(\mathbf{v}) + e_{\mathbf{y}}(\mathbf{v}^1)\right). \tag{1.66}$$

To pass to the limit in the fourth term, we rewrite $r_\varepsilon(\widehat{\mathbf{u}_\varepsilon}(\phi'), \mathbf{v}_\varepsilon)$ using the flux function q_ε introduced in Proposition 1.2.8. We have:

$$-\mathcal{R}_\varepsilon\left(\chi_{F,\varepsilon} \operatorname{div} \widehat{\mathbf{u}_\varepsilon}\right) = -\mathcal{R}_\varepsilon\left(\chi_{F,\varepsilon} \Pi_\varepsilon\left(\operatorname{div} \widehat{\mathbf{u}_\varepsilon}\right)\right) = \mathcal{R}_\varepsilon q_\varepsilon,$$

and so

$$r_\varepsilon(\widehat{\mathbf{u}_\varepsilon}(\phi'), \mathbf{v}_\varepsilon) = \int_0^T \int_\Omega \left(\mathcal{R}_\varepsilon q_\varepsilon\right) \Pi_\varepsilon\left(\chi_{F,\varepsilon} \operatorname{div} \mathbf{v}_\varepsilon\right) \mathrm{d}\mathbf{x}\phi' \mathrm{d}t.$$

Now using the convergences presented in Proposition 1.2.8 and Lemma 1.2.10 , we obtain immediately:

$$\begin{aligned} r_\varepsilon\left(\widehat{\mathbf{u}_\varepsilon}(\phi'), \mathbf{v}_\varepsilon\right) &\to \int_0^T \int_\Omega \mathcal{R}(q) \left(|\mathcal{Y}_F| \operatorname{div}_{\mathbf{x}} \mathbf{v} - \int_\Gamma \mathbf{v}^1 \cdot \mathbf{n}^S\right) \mathrm{d}\mathbf{x}\phi' \mathrm{d}t \\ &= \int_0^T \int_\Omega \mathcal{R}\left(|\mathcal{Y}_F| \operatorname{div}_{\mathbf{x}} \mathbf{u} - \int_\Gamma \mathbf{u}^1 \cdot \mathbf{n}^S\right) \left(|\mathcal{Y}_F| \operatorname{div}_{\mathbf{x}} \mathbf{v} - \int_\Gamma \mathbf{v}^1 \cdot \mathbf{n}^S\right) \mathrm{d}\mathbf{x}\phi' \mathrm{d}t \\ &= r_\# \left(\left(\mathbf{u}(\phi'), \mathbf{u}^1(\phi')\right), \left(\mathbf{v}, \mathbf{v}^1\right)\right). \end{aligned} \tag{1.67}$$

Finally, we pass to the limit in the right–hand side of (1.63). Let us compute the limit of $\ell_\varepsilon^\phi(\mathbf{v}_\varepsilon)$. We rewrite the boundary integrals using the divergence theorem:

$$\begin{aligned} \ell_\varepsilon^\phi(\mathbf{v}_\varepsilon) = &\int_\Omega \mathbf{f}(\phi) \cdot \mathbf{v}_\varepsilon \chi_{S,\varepsilon} \mathrm{d}\mathbf{x} \\ &+ \left(\int_0^T p_N(t)\phi(t)\right) \int_\Omega \operatorname{div}(\mathbf{v}_\varepsilon) \mathrm{d}\mathbf{x} - \left(\int_0^T p_e(t)\phi(t)\right) \int_\Omega \operatorname{div}(\mathbf{v}_\varepsilon) \chi_{F,\varepsilon} \mathrm{d}\mathbf{x}. \end{aligned}$$

Hence, we obtain the limit as ε goes to zero as:

$$\begin{aligned} \ell_\varepsilon^\phi(\mathbf{v}_\varepsilon) \to &\int_\Omega \theta \mathbf{f}(\phi) \cdot \mathbf{v} \mathrm{d}\mathbf{x} \\ &+ \left(\int_0^T p_N(t)\phi(t)\right) \int_{\Omega \times \mathcal{Y}} \operatorname{div}_{\mathbf{x}}(\mathbf{v}) + \operatorname{div}_{\mathbf{y}}(\mathbf{v}^1) \mathrm{d}\mathbf{y}\mathrm{d}\mathbf{x} \\ &- \left(\int_0^T p_e(t)\phi(t)\right) \int_{\Omega \times \mathcal{Y}_F} \operatorname{div}_{\mathbf{x}}(\mathbf{v}) + \operatorname{div}_{\mathbf{y}}(\mathbf{v}^1) \mathrm{d}\mathbf{y}\mathrm{d}\mathbf{x}. \end{aligned}$$

Using the periodicity of $\mathbf{v}^1$ on $\mathcal{Y}$ and the divergence theorem, we get:

$$\begin{aligned} \ell_\varepsilon^\phi(\mathbf{v}_\varepsilon) \to &\int_\Omega \theta \mathbf{f}(\phi) \cdot \mathbf{v} \mathrm{d}\mathbf{x} \\ &+ \left(\int_0^T p_N(t)\phi(t)\right) \int_{\Gamma_N} \mathbf{v} \cdot \mathbf{n} \\ &- \left(\int_0^T p_e(t)\phi(t)\right) \int_\Omega \left((1-\theta) \operatorname{div}_{\mathbf{x}} \mathbf{v} - \int_\Gamma \mathbf{v}^1 \cdot \mathbf{n}^S\right) \mathrm{d}\mathbf{x} \\ &= \int_0^T \ell_\#(\mathbf{v}, \mathbf{v}^1)\phi(t) \mathrm{d}t. \end{aligned} \tag{1.68}$$

Combining the results (1.64)–(1.68), we have proved that $(\mathbf{u}, \mathbf{u}^1)$ are solutions of the problem:

$$(\theta\rho\mathbf{u}(\phi''), \mathbf{v})_{0,\Omega} - r_{\#}\left(\left(\mathbf{u}(\phi'), \mathbf{u}^1(\phi')\right), (\mathbf{v}, \mathbf{v}^1)\right) + a_{\#}((\mathbf{u}(\phi), \mathbf{u}^1(\phi)), (\mathbf{v}, \mathbf{v}^1)) = \int_0^T \ell_{\#}(\mathbf{v}, \mathbf{v}^1)\phi(t)\mathrm{d}t.$$

Identification of the limit. Since ϕ is arbitrary, it follows by a density argument that the two–scale limits $(\mathbf{u}, \mathbf{u}^1)$ also solve the variational formulation (1.59a). Let us now investigate the initial conditions. The following result is known (see Corollary 4, p85 in [Sim87]):

Lemma 1.2.15. *Let X, Y be two Banach spaces with X compactly imbedded in Y. Then $W^{1,r}(0,T;X) \cap L^\infty(0,T;Y)$ is compactly imbedded in $C([0,T];X)$ for $r > 1$.*

In particular, $W^{1,\infty}(0,T;\mathbf{X}) \cap L^\infty(0,T;\mathbf{V})$ is compactly imbedded in $C([0,T];\mathbf{X})$ and also $W^{1,\infty}(0,T;\mathbf{V}') \cap L^\infty(0,T;\mathbf{X})$ is compactly imbedded in $C([0,T];\mathbf{V}')$.

Therefore, since $(\widehat{\mathbf{u}_\varepsilon})_{\varepsilon>0}$ is a bounded sequence in $W^{1,\infty}(0,T;\mathbf{X}) \cap L^\infty(0,T;\mathbf{V})$, up to a subsequence we have strong convergence of $\widehat{\mathbf{u}_\varepsilon}$ to $\mathbf{u}$ in $C(0,T;\mathbf{X})$. As a consequence, $\widehat{\mathbf{u}_\varepsilon}(0)$ converges strongly to $\mathbf{u}(0)$ in $\mathbf{X}$. However, we know that:

$$\widehat{\mathbf{u}_\varepsilon}(0)\chi_{S,\varepsilon} = \mathbf{u}_0\chi_{S,\varepsilon},$$

so by taking the two–scale limit in both sides of this identity, we obtain

$$\mathbf{u}(0)\chi_S = \mathbf{u}_0\chi_S \text{ in } \Omega \times \mathcal{Y}.$$

Hence, the initial condition passes to the limit and we obtain

$$\mathbf{u}(0) = \mathbf{u}_0 \text{ a.e. in } \Omega.$$

A similar argument yields

$$\partial_t\mathbf{u}(0) = \mathbf{u}_1 \text{ a.e. in } \Omega.$$

Finally, let us check that (see Remark 1.2.12):

$$\mathcal{R}\left((1-\theta)\mathrm{div}_{\mathbf{x}}\mathbf{u} - \int_\Gamma \mathbf{u}^1 \cdot \mathbf{n}^S\right)\Big|_{t=0} = \mathcal{R}\left((1-\theta)\mathrm{div}_{\mathbf{x}}\mathbf{u}_0\right). \tag{1.69}$$

Now, it is a consequence of Proposition 1.2.8 and Lemma 1.2.15 that:

$$\pi_\varepsilon(0) = -\mathcal{R}_\varepsilon\left(\chi_{F,\varepsilon}\mathrm{div}\ \mathbf{u}_0\right) \quad \text{converges strongly to} \quad \pi(0) = -\mathcal{R}\left((1-\theta)\mathrm{div}_{\mathbf{x}}\mathbf{u} - \int_\Gamma \mathbf{u}^1 \cdot \mathbf{n}^S\right)\Big|_{t=0}.$$

Moreover, we compute the following convergences:

$$\chi_{F,\varepsilon}\mathrm{div}\ \mathbf{u}_0 \rightharpoonup (1-\theta)\mathrm{div}_{\mathbf{x}}\mathbf{u}_0 \text{ weakly in } L^2(\Omega),$$
$$\pi_\varepsilon(0) = -\mathcal{R}_\varepsilon\left(\chi_{F,\varepsilon}\mathrm{div}\ \mathbf{u}_0\right) \to -\mathcal{R}\left((1-\theta)\mathrm{div}_{\mathbf{x}}\mathbf{u}_0\right) \text{ strongly in } L^2(\Omega).$$

Hence,

$$\mathcal{R}\left((1-\theta)\mathrm{div}_{\mathbf{x}}\mathbf{u} - \int_\Gamma \mathbf{u}^1 \cdot \mathbf{n}^S\right)\Big|_{t=0} = \mathcal{R}\left((1-\theta)\mathrm{div}_{\mathbf{x}}\mathbf{u}_0\right),$$

which is precisely (1.60).

Thus $(\mathbf{u}, \mathbf{u}^1)$ is a solution of the variational formulation (1.59a) which satisfies the initial conditions (1.59b). Since problem (1.59) admits a unique solution in $\left(W^{1,\infty}(0,T;\mathbf{X}) \cap L^\infty(0,T;\mathbf{V})\right) \times L^\infty(0,T;\mathbf{H})$, it follows that $\mathbf{u}$ and $\mathbf{u}^1$ coincide with $\mathbf{u}_\infty$ and $\mathbf{u}^1_\infty$ respectively on Ω and $\Omega \times \mathcal{Y}_S$.

Now, we find that up to a subsequence,

$$\widehat{\mathbf{u}_\varepsilon}\chi_{S,\varepsilon} \twoheadrightarrow \mathbf{u}\chi_S \qquad \text{two–scale in } L^2((0,T)\times\Omega\times\mathcal{Y}),$$
$$\nabla(\widehat{\mathbf{u}_\varepsilon})\chi_{S,\varepsilon} \twoheadrightarrow \left(\nabla_{\mathbf{x}}\mathbf{u}+\nabla_{\mathbf{y}}\mathbf{u}^1\right)\chi_S \qquad \text{two–scale in } L^2((0,T)\times\Omega\times\mathcal{Y}).$$

Since this limit is uniquely defined, the whole sequence converges to $\mathbf{u}$ and the proof of Theorem 1.2.13 is complete. □

1.2.3 Cell problems, correctors and the homogenized problem

In this part, we are going to eliminate the microscopic additional unknown $\mathbf{u}^1$ from the two–scale variational problem (1.59). This is a standard step to exhibit the macroscopic properties (memory effects, effective elastic tensor...) of the homogenized material associated with the homogenized problem. For simplicity, we will consider from now on that $\mathbf{u}^1$ is defined on $\Omega\times\mathcal{Y}_S$ only by making the identification with $\mathbf{u}^1_\infty$.

The two–scale formulation derived in Theorem 1.2.13, despite having twice the variables, has a simple structure inherited from the original problem that is lost when we eliminate $\mathbf{u}^1$. In particular, we have to introduce an additional pressure variable to decouple the cell problems. Let us begin by reformulating (1.59) as a mixed problem:

Proposition 1.2.16. *Suppose condition (1.43) holds. Let $(\mathbf{u},\mathbf{u}^1)$ be the unique solution of the two–scale variational problem (1.59) and π defined as:*

$$\pi = \mathcal{R}q = -\mathcal{R}\left((1-\theta)\mathrm{div}_{\mathbf{x}}\mathbf{u} - \int_\Gamma \mathbf{u}^1\cdot\mathbf{n}^S\right) \qquad \text{in } \Omega. \tag{1.70}$$

Then $(\mathbf{u},\mathbf{u}_1,\pi)$ is the unique solution in $L^\infty(0,T;\mathbf{V})\cap W^{1,\infty}(0,T;\mathbf{X})\times L^\infty(0,T;\mathbf{H})\times H^1(0,T;L^2(\Omega))$ of the following variational mixed problem:

$$\begin{cases} \text{For all } \mathbf{v}\in\mathbf{V},\ \mathbf{v}^1\in\mathbf{H} \text{ and } \phi\in L^2(\Omega),\ \text{a.e. in } (0,T), & \\ \langle\theta\rho\partial_{tt}\mathbf{u},\mathbf{v}\rangle + a_\#((\mathbf{u},\mathbf{u}^1),(\mathbf{v},\mathbf{v}^1)) - b_\#(\partial_t\pi,(\mathbf{v},\mathbf{v}^1)) = \ell_\#(\mathbf{v},\mathbf{v}^1), & (1.71a)\\ (\pi,\phi)_{0,\Omega} + b_\#\left(\mathcal{R}\phi,(\mathbf{u},\mathbf{u}^1)\right) = 0, & (1.71b)\\ \mathbf{u}(0)=\mathbf{u}_0,\quad \partial_t\mathbf{u}(0)=\mathbf{u}_1,\quad \pi(0)=-(1-\theta)\mathcal{R}(\mathrm{div}_{\mathbf{x}}\mathbf{u}_0) \quad \text{in } \Omega, & (1.71c)\end{cases}$$

where $\langle\cdot,\cdot\rangle$ is the duality pairing between $\mathbf{V}'$ and $\mathbf{V}$, $a_\#$ and $\ell_\#$ are defined respectively in (1.56) and (1.58) and $b_\#$ is the mixed bilinear form on $\mathbf{X}\times(\mathbf{V}\times\mathbf{H})$ defined by:

$$b_\#\left(\phi,(\mathbf{v},\mathbf{v}^1)\right) = \int_\Omega \phi\left((1-\theta)\mathrm{div}_{\mathbf{x}}\mathbf{v} - \int_\Gamma \mathbf{v}^1\cdot\mathbf{n}^S\right).$$

Proof. The relation (1.71b) is equivalent to (1.70) because $\mathcal{R}$ is a symmetric operator. Replacing π by its expression we find equations (1.59) and (1.71a) to be equivalent. □

Fluid cell problem To eliminate the microscopic variable $\mathbf{u}^1$, we are going to parameterize its values by the macroscopic variables $\mathbf{u}$ and π. To this end, we write the so-called cell problem, taking the test function $\mathbf{v}$ to be 0 in equation (1.71a). Keeping only $\mathbf{u}^1$ in the left–hand side, we have:

$$\begin{cases} \text{For all } \mathbf{v}^1\in\mathbf{H}, \quad \text{a.e. } t\in(0,T), & \\ \displaystyle\int_\Omega\int_{\mathcal{Y}_S}\left(\lambda\mathrm{div}_{\mathbf{y}}(\mathbf{u}^1)\mathrm{div}_{\mathbf{y}}(\mathbf{v}^1)+2\mu e_{\mathbf{y}}(\mathbf{u}^1):e_{\mathbf{y}}(\mathbf{v}^1)\right) & \\ \qquad = -\displaystyle\int_\Omega\int_{\mathcal{Y}_S}\left(\lambda\mathrm{div}_{\mathbf{x}}(\mathbf{u})\mathrm{div}_{\mathbf{y}}(\mathbf{v}^1)+2\mu e_{\mathbf{x}}(\mathbf{u}):e_{\mathbf{y}}(\mathbf{v}^1)\right) + \int_\Omega(\partial_t\pi-p_e)\int_\Gamma\mathbf{v}^1\cdot\mathbf{n}^S. & \end{cases}$$

Since neither $\mathbf{u}$ nor π depend on $\mathbf{y}$, this problem can be transformed into a family of problems in the $\mathbf{x}$ variable by a density argument using test functions of the form $\mathbf{w}^1(\mathbf{x},\mathbf{y}) = \phi(\mathbf{x})\mathbf{v}^1(\mathbf{y})$, using $e_{\mathbf{x}}(\mathbf{u})$ and $\pi' - p^{ext}$ as parameters:

$$\left\{\begin{array}{l} \text{For all } \mathbf{v}^1 \in \mathbf{H}^1_{\#}(\mathcal{Y}_S)/\mathbb{R}^d, \quad \text{a.e. } (t,\mathbf{x}) \in (0,T)\times\Omega, \\ \displaystyle\int_{\mathcal{Y}_S} \left(\lambda \mathrm{div}_{\mathbf{y}}(\mathbf{u}^1)\mathrm{div}_{\mathbf{y}}(\mathbf{v}^1) + 2\mu e_{\mathbf{y}}(\mathbf{u}^1) : e_{\mathbf{y}}(\mathbf{v}^1)\right) \\ \qquad = \left(\pi' - p_e\right)\left(\displaystyle\int_\Gamma \mathbf{v}^1\cdot\mathbf{n}^S\right) - \left(\lambda \mathrm{div}_{\mathbf{x}}(\mathbf{u})\mathrm{Id} + 2\mu e_{\mathbf{x}}(\mathbf{u})\right) : \left(\displaystyle\int_{\mathcal{Y}_S} e_{\mathbf{y}}(\mathbf{v}^1)\right). \end{array}\right. \tag{1.72}$$

This is a linear elliptic problem, and we are going to take advantage of the superposition principle by introducing the so–called correctors. We define the auxiliary functions $\mathbf{p}^{kl} \in \mathbf{H}^1(Y_S)$ by:

$$\mathbf{p}^{kl}(\mathbf{y}) = \frac{1}{2}\left(y_k\mathbf{e}^l + y_l\mathbf{e}^k\right) \qquad \text{for } 1\le k,l\le d, \tag{1.73}$$

where the vectors $\mathbf{e}^k$ for $1\le k\le d$ are the unit vectors of $\mathbb{R}^d$ whose components are $\mathbf{e}^k_l = \delta_{kl}$ for $1\le k,\ l\le d$. Now, we compute

$$e_{\mathbf{y}}(\mathbf{p}^{kl}) = \frac{1}{2}\left(\mathbf{e}^k\otimes\mathbf{e}^l + \mathbf{e}^l\otimes\mathbf{e}^k\right).$$

Therefore, the family $e_{\mathbf{y}}(\mathbf{p}^{kl})$ forms a basis of the set of symmetric tensors of order 2, and in particular

$$e_{\mathbf{x}}(\mathbf{u}) = e_{\mathbf{x}}(\mathbf{u})_{kl}e_{\mathbf{y}}(\mathbf{p}^{kl}).$$

We remind that we use the Einstein convention for summing. In view of (1.72), we can decompose the solution $\mathbf{u}^1$ using the superposition principle:

$$\mathbf{u}^1 = e_{\mathbf{x}}(\mathbf{u})_{kl}\boldsymbol{\chi}^{kl} + \left(\partial_t\pi - p_e\right)\boldsymbol{\chi}^0, \tag{1.74}$$

where the functions $\boldsymbol{\chi}^{kl}$ are correctors, solution of the variational cell problems: find $\boldsymbol{\chi}^{kl}$ in $\mathbf{H}^1_{\#}(\mathcal{Y}_S)/\mathbb{R}^d$ such that

$$\left\{\begin{array}{l} \text{For all } \mathbf{v}^1 \in \mathbf{H}^1_{\#}(\mathcal{Y}_S)/\mathbb{R}^d, \\ \displaystyle\int_{\mathcal{Y}_S}\left(\lambda\mathrm{div}_{\mathbf{y}}(\boldsymbol{\chi}^{kl})\mathrm{Id} + 2\mu e_{\mathbf{y}}(\boldsymbol{\chi}^{kl})\right) : e_{\mathbf{y}}(\mathbf{v}^1) \\ \qquad = -\displaystyle\int_{\mathcal{Y}_S}\left(\lambda\mathrm{div}_{\mathbf{y}}(\mathbf{p}^{kl})\mathrm{Id} + 2\mu e_{\mathbf{y}}(\mathbf{p}^{kl})\right) : e_{\mathbf{y}}(\mathbf{v}^1), \end{array}\right. \tag{1.75}$$

and the corrector $\boldsymbol{\chi}^0$ is associated with the variational cell problem: find $\boldsymbol{\chi}^0$ in $\mathbf{H}^1_{\#}(\mathcal{Y}_S)/\mathbb{R}^d$ such that

$$\left\{\begin{array}{l} \text{For all } \mathbf{v}^1 \in \mathbf{H}^1_{\#}(\mathcal{Y}_S)/\mathbb{R}^d, \\ \displaystyle\int_{\mathcal{Y}_S}\left(\lambda\mathrm{div}_{\mathbf{y}}\boldsymbol{\chi}^0\mathrm{Id} + 2\mu e_{\mathbf{y}}(\boldsymbol{\chi}^0)\right) : e_{\mathbf{y}}(\mathbf{v}^1) = \displaystyle\int_\Gamma \mathbf{v}^1\cdot\mathbf{n}^S. \end{array}\right. \tag{1.76}$$

These problems are elliptic thanks to Korn's inequality on $\mathcal{Y}_S$, so it is standard to show that they have a unique solution.

Macroscopic homogenized problem We now use the decomposition (1.74) to write the homogenized problem uniquely in terms of $\mathbf{u}$ and π. Using test functions $\mathbf{v} \in \mathbf{V}$ and $\phi \in L^2(\Omega)$ with $\mathbf{v}^1 = \mathbf{0}$ in (1.59), we find that $\mathbf{u}_\varepsilon$ and π satisfy the following variational system:

$$\begin{aligned}\frac{\mathrm{d}}{\mathrm{d}t}\langle\theta\rho\partial_t\mathbf{u},\mathbf{v}\rangle+\int_\Omega e_{\mathbf{x}}(\mathbf{u})_{kl}\left(\int_{\mathcal{Y}_S}\lambda\left(\mathrm{div}_{\mathbf{y}}\mathbf{p}^{kl}+\mathrm{div}_{\mathbf{y}}\boldsymbol{\chi}^{kl}\right)\mathrm{Id}+2\mu\left(e_{\mathbf{y}}(\mathbf{p}^{kl})+e_{\mathbf{y}}(\boldsymbol{\chi}^{kl})\right)\right):e_{\mathbf{x}}(\mathbf{v})\\ -\frac{\mathrm{d}}{\mathrm{d}t}\int_\Omega\pi\left((1-\theta)\mathrm{Id}+\int_{\mathcal{Y}_S}\left(\lambda\mathrm{div}_{\mathbf{y}}\boldsymbol{\chi}^0\mathrm{Id}+2\mu e_{\mathbf{y}}(\boldsymbol{\chi}^0)\right)\right):e_{\mathbf{x}}(\mathbf{v})\\ =\int_\Omega\theta\mathbf{f}\cdot\mathbf{v}+\int_{\Gamma_N}p_N\mathbf{v}\cdot\mathbf{n}\\ -\int_\Omega p_e\left((1-\theta)\mathrm{Id}+\int_{\mathcal{Y}_S}\left(\lambda\mathrm{div}_{\mathbf{y}}\boldsymbol{\chi}^0\mathrm{Id}+2\mu e_{\mathbf{y}}(\boldsymbol{\chi}^0)\right)\right):e_{\mathbf{x}}(\mathbf{v}),\end{aligned}$$

and

$$\pi=-\mathcal{R}\left(\sum_{k,l=1}^d e_{\mathbf{x}}(\mathbf{u})_{kl}\left((1-\theta)\delta_{kl}-\int_\Gamma\boldsymbol{\chi}^{kl}\cdot\mathbf{n}^S\right)+(\partial_t\pi-p_e)\int_\Gamma\boldsymbol{\chi}^0\cdot\mathbf{n}^S\right).$$

These expressions motivate the introduction of the homogenized coefficients: the fourth-order elasticity tensor

$$\mathcal{A}^{hom}_{ijkl}=\int_{\mathcal{Y}_S}\left(\lambda\mathrm{div}_{\mathbf{y}}(\mathbf{p}^{kl}+\boldsymbol{\chi}^{kl})\mathrm{Id}+2\mu e_{\mathbf{y}}(\mathbf{p}^{kl}+\boldsymbol{\chi}^{kl})\right)_{ij}, \tag{1.77}$$

the cell relaxation constant

$$\tau_{hom}=\int_\Gamma\boldsymbol{\chi}^0\cdot\mathbf{n}^S, \tag{1.78}$$

and the fluid flux matrix

$$B^{hom}_{ij}=(1-\theta)\delta_{ij}-\int_\Gamma\boldsymbol{\chi}^{ij}\cdot\mathbf{n}^S. \tag{1.79}$$

The following properties of the homogenized coefficients are classical:

Proposition 1.2.17. *The fourth-order tensor $\mathcal{A}^{hom}$ defined in (1.77) has the following properties:*

a) *Symmetry:*

$$\mathcal{A}^{hom}_{ijkl}=\mathcal{A}^{hom}_{klij}=\mathcal{A}^{hom}_{ijlk}.$$

b) *Ellipticity: there exists $\beta>0$ such that for any $d\times d$ symmetric matrix ξ,*

$$(\mathcal{A}^{hom}\xi):\xi\geq\beta\xi:\xi.$$

c) *Positive definitness:*

$$\mathcal{A}^{hom}\xi:\xi=0 \text{ iff } \xi=0.$$

Moreover, the cell relaxation constant defined by (1.78) satisfies

$$\tau_{hom}>0,$$

and the matrix B^{hom} defined by (1.79) is symmetric, and its entries satisfy:

$$B^{hom}_{ij}=(1-\theta)\delta_{ij}-\int_\Gamma\boldsymbol{\chi}^{ij}\cdot\mathbf{n}^S=(1-\theta)\delta_{ij}+\int_{\mathcal{Y}_S}\left(\lambda\mathrm{div}_{\mathbf{y}}\boldsymbol{\chi}^0\mathrm{Id}+2\mu e_{\mathbf{y}}(\boldsymbol{\chi}^0)\right)_{ij}.$$

Remark 1.2.18. *The coefficients $\mathcal{A}^{hom}$ and $\mathcal{B}^{hom}$ appear also in the homogenization of porous elastic solids filled with slightly viscous fluids, see [SP80]. In our case, we do not require a particular scaling of the fluid viscosity but the abstract tree convergence (1.43) to preserve a relative motion through the homogenization process, described here by the new macroscopic pressure $\partial_t \pi$.*

Physically $\mathcal{A}^{hom}$ is the effective elastic tensor and $\mathcal{B}^{hom}$ describes the symmetric interaction between stresses in the structure and pressure in the fluid.

Proof. The properties of $\mathcal{A}^{\text{hom}}$ and $\mathcal{B}^{hom}$ are classical and we do not reproduce the proof here, see e.g. Lemma 5.1 in [SP80] or [Ngu90].

To show that τ_{hom} is positive, we compute, using $\boldsymbol{\chi}^0$ as a test function in the cell problem (1.76),

$$\begin{aligned}
\tau_{hom} &= \int_\Gamma \boldsymbol{\chi}^0 \cdot \mathbf{n}^S \\
&= \int_{\mathcal{Y}_S} \left(\lambda \mathrm{div}_{\mathbf{y}} \boldsymbol{\chi}^0 \mathrm{Id} + 2\mu e_{\mathbf{y}}(\boldsymbol{\chi}^\pi)\right) : e_{\mathbf{y}}(\boldsymbol{\chi}^0) \\
&= \int_{\mathcal{Y}_S} \lambda \left(\mathrm{div}_{\mathbf{y}}(\boldsymbol{\chi}^0)\right)^2 + 2\mu e_{\mathbf{y}}(\boldsymbol{\chi}^0) : e_{\mathbf{y}}(\boldsymbol{\chi}^0) \\
&\geq 2\mu \| e_{\mathbf{y}}(\boldsymbol{\chi}^0) \|^2_{0,\mathcal{Y}_S}.
\end{aligned}$$

Since $\boldsymbol{\chi}^0$ is different from $\mathbf{0}$ and Korn's inequality holds on $\mathbf{H}^1_\#(\mathcal{Y}_S)$, we have $\tau_{hom} > 0$. □

Using these homogenized parameters, we are able to write and describe the macroscopic limit problem verified by $(\mathbf{u}, \pi)$ when the tree operator converges:

Theorem 1.2.19. *Suppose (1.25) and (1.43) holds. Then,*

$$\widehat{\mathbf{u}_\varepsilon} \rightharpoonup \mathbf{u} \qquad \text{weak}-* \text{ in } L^\infty(0,T;\mathbf{V}), \tag{1.80a}$$

$$\widehat{\mathbf{u}_\varepsilon \chi_{S,\varepsilon}} \rightharpoonup \theta \mathbf{u} \qquad \text{weak}-* \text{ in } L^\infty(0,T;\mathbf{X}), \tag{1.80b}$$

$$\widehat{\partial_t \mathbf{u}_\varepsilon \chi_{S,\varepsilon}} \rightharpoonup \theta \partial_t \mathbf{u} \qquad \text{weak}-* \text{ in } L^\infty(0,T;\mathbf{X}), \tag{1.80c}$$

$$\pi_\varepsilon \rightharpoonup \pi \qquad \text{weak}-* \text{ in } L^\infty(0,T;L^2(\Omega)) \cap H^1(0,T;L^2(\Omega)), \tag{1.80d}$$

where $(\mathbf{u}, \pi)$ are the unique weak solutions of the coupled homogenized problem:

$$\begin{cases} \theta \rho \partial_{tt} \mathbf{u} - \mathbf{div}\left(\mathcal{A}^{hom} e(\mathbf{u}) - \partial_t \pi \mathcal{B}^{hom}\right) = \theta \mathbf{f}, & \text{in } (0,T)\times\Omega, \quad (1.81a) \\ \pi + \tau_{hom} \partial_t \left(\mathcal{R}\pi\right) = \mathcal{R}\left(\tau_{hom} p_e - \mathcal{B}^{hom} : e(\mathbf{u})\right), & \text{in } (0,T)\times\Omega, \quad (1.81b) \end{cases}$$

with the boundary conditions:

$$\mathcal{A}^{hom} e(\mathbf{u})\mathbf{n} - \partial_t \pi \mathcal{B}^{hom}\mathbf{n} = -\left(p_N \mathrm{Id} - p_e \mathcal{B}^{hom}\right)\mathbf{n}, \qquad \text{on } (0,T)\times\Gamma_N, \tag{1.81c}$$

$$\mathbf{u} = \mathbf{0}, \qquad \text{on } (0,T)\times\Gamma_D, \tag{1.81d}$$

and the initial conditions:

$$\mathbf{u}(0) = \mathbf{u}_0, \qquad \partial_t \mathbf{u}(0) = \mathbf{u}_1, \qquad \pi(0) = -(1-\theta)\mathcal{R}(\mathrm{div}_{\mathbf{x}} \mathbf{u}_0), \qquad \text{in } \Omega. \tag{1.81e}$$

Remark 1.2.20. *We recognize in equation (1.81a) the usual linearized elasticity equation perturbed by a viscous pressure term. Observe that the elastic tensor $\mathcal{A}^{hom}$ is the same as for the elliptic (static) case without a tree, see [All92, BGMO08]. The input of the tree appears through the evolution of the pressure field $\partial_t \pi$. Equation (1.81b) describes a nonlocal relaxation effect on the fluid pressure and also induces dissipation of energy in the material. Hence the homogenized material behaves like a viscoelastic material with fading memory depending on the history of displacement, see e.g. [Han05, FM92] but an unusual one since the dissipation is non–local.*

Remark 1.2.21. *The relaxation effect described by the first–order differential equation (1.81b) is best described by decomposing the functions onto the basis of eigenvectors of the selfadjoint compact operator $\mathcal{R}$, in the case where $\mathcal{R}$ is positive definite (see Section 2.2.2). Write $(\psi_m)_{m\geq 1}$ the sequence of eigenvectors of $\mathcal{R}$, associated with the sequence (λ_m) of eigenvalues such that $\lambda_m \to 0$ and*

$$\lambda_1 \geq \cdots \geq \lambda_m \geq \cdots > 0.$$

Then, (ψ_m) is a basis of $L^2(\Omega)$, and decomposing π as

$$\pi = \sum_{m=1}^{\infty} \pi_m \psi_m,$$

we can rewrite (1.81b) as a system of independent ordinary differential equations:

$$\tau_{hom}\lambda_m \frac{\mathrm{d}\pi_m}{\mathrm{d}t} + \pi_m = \lambda_m \int_\Omega \Big(\tau_{hom} p_e - \mathcal{B}^{hom} : e(\mathbf{u})\Big)\,\psi_m, \qquad \forall m \geq 0.$$

Each relaxation mode ψ_m is associated with a characteristic relaxation time $\lambda_m\tau_{hom}$, which can be computed from the properties of the infinite resistive tree via the kernel operator $\mathcal{R}$. Hence, there is not a unique characteristic timescale associated with the memory effect but an infinity of increasingly small relaxation times associated with the multiple scales of the dyadic tree. A more detailed study can be performed in the case of a geometric regular tree, see Section 2.2.2, and also the papers [GMM06, VSM09]

Proof. Let us begin by justifying the convergences (1.80). Thanks to the *a priori* bounds on the solutions $\mathbf{u}_\varepsilon$, we know that the sequences $(\widehat{\mathbf{u}_\varepsilon})_{\varepsilon>0}$, $(\widehat{\mathbf{u}_\varepsilon\chi_{S,\varepsilon}})_{\varepsilon>0}$, $(\widehat{\partial_t\mathbf{u}_\varepsilon\chi_{S,\varepsilon}})_{\varepsilon>0}$ and $(\pi_\varepsilon)_{\varepsilon>0}$ converge weak-$*$ respectively in $L^\infty(0,T;\mathbf{V})$, $L^\infty(0,T;\mathbf{X})$, $L^\infty(0,T;\mathbf{X})$ and $H^1(0,T;L^2(\Omega))$ up to a subsequence. Since the limit is uniquely defined as $\mathbf{u}$, $\mathbf{u}\chi_S$, $\partial_t\mathbf{u}\chi_S$ and π respectively thanks to Theorem 1.2.13, the whole sequences converge.

Now, we know by construction that $(\mathbf{u},\pi)$ satisfy the homogenized problem (1.81). Hence, we do not have to prove existence of a solution of the homogenized problem. Let us check that this solution is unique. Let $(\mathbf{u}_1,\pi_1)$ and $(\mathbf{u}_2,\pi_2)$ in $L^\infty(0,T;\mathbf{V})\cap W^{1,\infty}(0,T;\mathbf{X})\times H^1(0,T;L^2(\Omega))$ be two weak solutions of problem (1.81) with the same initial conditions. Then the difference $(\mathbf{w},\psi) = (\mathbf{u}_1-\mathbf{u}_2,\pi_1-\pi_2)$ satisfies, for all $\mathbf{v}\in\mathcal{D}([0,T);\mathbf{V})$ and $\phi\in\mathcal{D}([0,T);L^2(\Omega))$:

$$\int_0^T\int_\Omega -\theta\rho\partial_t\mathbf{w}\cdot\partial_t\mathbf{v} + \Big(\mathcal{A}^{hom}e(\mathbf{w}) - \partial_t\psi\mathcal{B}^{hom}\Big) : e(\mathbf{v}) = \mathbf{0}, \tag{1.82a}$$

$$\int_0^T\int_\Omega \psi\phi + \mathcal{R}(\tau_{hom}\partial_t\psi + \mathcal{B}_{hom} : e(\mathbf{w}))\phi = 0. \tag{1.82b}$$

By a density argument, this variational formulation is also valid for $\mathbf{v}\in H^1(0,T;\mathbf{V})$ with $\mathbf{v}(T)=0$ and $\phi\in L^2((0,T)\times\Omega)$. Let $s\in(0,T)$. We introduce the following test functions in the variational formulation (1.82):

$$\mathbf{v}(t) = \begin{cases} \int_t^s \mathbf{w} & \text{if } t\leq s,\\ \mathbf{0} & \text{else,}\end{cases} \qquad \text{in } H^1(0,T;\mathbf{V}),$$

$$\phi = \tau_{hom}\partial_t\psi + \mathcal{B}_{hom} : e(\mathbf{w}) \qquad \text{in } L^2((0,T)\times\Omega).$$

Since $\psi(0)=0$, $\mathbf{w}(0)=\mathbf{0}$ and $\partial_t\mathbf{v}(t)=\mathbf{w}(t)$ for $0\leq t\leq s$, this yields:

$$\int_0^s\int_\Omega \theta\rho\partial_t\mathbf{w}\cdot\mathbf{w} - \mathcal{A}^{hom}e(\partial_t\mathbf{v}) : e(\mathbf{v}) - \psi\mathcal{B}^{hom} : e(\mathbf{w}) = \mathbf{0},$$

$$\int_0^s\int_\Omega \tau_{hom}\pi\partial_t\psi + \psi\mathcal{B}_{hom} : e(\mathbf{w}) + \mathcal{R}(\phi)\phi = 0.$$

Adding the two equations, we obtain:

$$\frac{1}{2}\int_0^s \frac{\mathrm{d}}{\mathrm{d}t}\left(\theta\rho\|\mathbf{w}\|_{0,\Omega}^2+\tau_{hom}\|\psi\|_{0,\Omega}^2-\int_\Omega \mathcal{A}^{hom}e(\mathbf{v}):e(\mathbf{v})\right)+\int_0^T\int_\Omega \mathcal{R}(\phi)\phi=0.$$

Using the fact that $\psi(0)=\mathbf{0}$, $\mathbf{w}(0)=0$, $\mathbf{v}(T)=\mathbf{0}$ and the positivity of the operator $\mathcal{R}$, we obtain:

$$\theta\rho\|\mathbf{w}(s)\|_{0,\Omega}^2+\tau_{hom}\|\psi(s)\|_{0,\Omega}^2+\int_\Omega \mathcal{A}^{hom}e(\mathbf{v}(0)):e(\mathbf{v}(0))\leq 0.$$

Since s is arbitrary, $\mathbf{w}$ and ψ are identically equal to zero. This proves that the solution of the homogenized problem is unique and ends the proof of the Theorem. □

1.3 Study in the incompressible case

We now turn to the study of case where the elastic media is assumed to be incompressible. To the displacement, we add a new unknown, the pressure η_ε, which is the Lagrange multiplier associated with the incompressibility constraint (not to be confused with the fluid pressure, which we denote π_ε). The model now reads as the system of equations (1.16) and we remind that the stress tensor is now defined by:

$$\sigma(\mathbf{u}_\varepsilon,\eta_\varepsilon)=-\eta_\varepsilon\mathrm{Id}+2\mu e(\mathbf{u}_\varepsilon).$$

In this section, we proceed as in the previous section and use the same notations: first, we write the mixed variational formulation and prove that problem (1.16) is well–posed and the solutions satisfy *a priori* bounds independently of ε; then, we use the two–scale convergence method in order to pass to the limit as ε goes to zero; and finally we exhibit the homogenized model.

1.3.1 Mixed variational formulation

Let $M_\varepsilon=L^2(\Omega_\varepsilon)$, $M=\{\phi\in L^2(\Omega_\varepsilon)\mid \int_\Omega\phi=0\}$, $\mathbf{V}_\varepsilon^{inc}=\{\mathbf{v}_\varepsilon\in\mathbf{V}_\varepsilon\mid \mathrm{div}(\mathbf{v}_\varepsilon)=0 \text{ a.e. } \mathbf{x}\in\Omega_\varepsilon\}$ and $\mathbf{V}^{inc}=\{\mathbf{v}\in\mathbf{V}\mid \mathrm{div}(\mathbf{v})=0 \text{ a.e. } \mathbf{x}\in\Omega\}$.

We make the following assumptions, in similar fashion to the compressible case:

$$\mathbf{f}\in L^2((0,T);\mathbf{X}),\quad p_N,\ p_e\in H^1(0,T),\quad \mathbf{u}_0\in\mathbf{V}^{inc}\text{ and }\mathbf{u}_1\in L^2(\Omega),\tag{1.83}$$

and

$$\begin{gathered}\text{There exists } \mathcal{R}\in\mathcal{L}\left(L^2(\Omega);L^2(\Omega)\right) \text{ such that}\\ \mathcal{R}_\varepsilon\to\mathcal{R}\text{ strongly in }\mathcal{L}\left(L^2(\Omega);L^2(\Omega)\right).\end{gathered}\tag{1.84}$$

The mixed variational formulation associated to (1.15) is as follows. Find $\mathbf{u}_\varepsilon\in L^\infty(0,T;\mathbf{V}_\varepsilon)$ and $\eta_\varepsilon\in H^{-1}(0,T;M_\varepsilon)$ such that:

$$\begin{cases}\text{For all } \mathbf{v}_\varepsilon\in\mathbf{V}_\varepsilon,\quad \phi_\varepsilon\in M_\varepsilon,\quad \text{and in } \mathcal{D}'(0,T),\\ \dfrac{\mathrm{d}}{\mathrm{d}t}(\rho\partial_t\mathbf{u}_\varepsilon,\mathbf{v}_\varepsilon)_{0,\Omega_\varepsilon}+\dfrac{\mathrm{d}}{\mathrm{d}t}r_\varepsilon(\mathbf{u}_\varepsilon,\mathbf{v}_\varepsilon)+a_\varepsilon^{inc}(\mathbf{u}_\varepsilon,\mathbf{v}_\varepsilon)+b_\varepsilon^{inc}(\eta_\varepsilon,\mathbf{v}_\varepsilon)=\ell_\varepsilon(\mathbf{v}_\varepsilon), & \text{(1.85a)}\\ b_\varepsilon^{inc}(\phi_\varepsilon,\mathbf{u}_\varepsilon)=0, & \text{(1.85b)}\\ \mathbf{u}_\varepsilon(0)=\mathbf{u}_0\quad\text{and}\quad \partial_t\mathbf{u}_\varepsilon(0)=\mathbf{u}_1, & \text{(1.85c)}\end{cases}$$

where $a_\varepsilon^{inc}(\cdot,\cdot):\mathbf{V}_\varepsilon\times\mathbf{V}_\varepsilon\to\mathbb{R}$ and $b_\varepsilon^{inc}(\cdot,\cdot):M_\varepsilon\times\mathbf{V}_\varepsilon\to\mathbb{R}$ are the bilinear forms defined by:

$$\begin{aligned}a_\varepsilon^{inc}(\mathbf{u}_\varepsilon,\mathbf{v}_\varepsilon)&=\int_{\Omega_\varepsilon}2\mu e(\mathbf{u}_\varepsilon):e(\mathbf{v}_\varepsilon),\\ b_\varepsilon^{inc}(\phi,\mathbf{v}_\varepsilon)&=-\int_{\Omega_\varepsilon}\phi\mathrm{div}(\mathbf{v}_\varepsilon),\end{aligned}$$

and the forms $r_\varepsilon(\cdot,\cdot)$, $\ell_\epsilon(\cdot)$ are as in the section 1.2, defined in (1.28) and (1.29) respectively.

1.3.2 Pressure extension and *a priori* estimates

The variational formulation (1.85) of the system (1.16) is similar to the variational formulation (1.26) studied in Section 1.2 but for the introduction of the pressure term. We introduce an extension operator for the pressure defined on Ω_ε as follows. Given $\eta_\varepsilon \in M_\varepsilon$, we extend it by (see [Con85, BGMO08]):

$$\widetilde{\eta_\varepsilon}(\mathbf{x}) = \begin{cases} \eta_\varepsilon(\mathbf{x}) & \text{if } \mathbf{x} \in \Omega_\varepsilon, \\ -\dfrac{1}{|\Omega \setminus \Omega_\varepsilon|} \displaystyle\int_{\Omega_\varepsilon} \eta_\varepsilon(\mathbf{x}) \mathrm{d}\mathbf{x} & \text{if } \mathbf{x} \in \Omega \setminus \Omega_\varepsilon. \end{cases} \tag{1.86}$$

This extension is such that $\widetilde{\eta_\varepsilon} \in M$, and:

$$\|\widetilde{\eta_\varepsilon}\|_M \leq C \|\eta_\varepsilon\|_{M_\varepsilon},$$

with C independent of ε. We have the following existence and uniqueness result:

Proposition 1.3.1. *Under hypothesis (1.83) and (1.84), the problem (1.16) has a unique weak solution $(\mathbf{u}_\varepsilon, \eta_\varepsilon)$, which satisfies:*

$$\mathbf{u}_\varepsilon \in L^\infty(0,T;\mathbf{V}_\varepsilon) \quad \text{and} \quad \partial_t \mathbf{u}_\varepsilon \in L^\infty(0,T;\mathbf{X}_\varepsilon), \tag{1.87a}$$

$$\eta_\varepsilon \in H^{-1}(0,T;M_\varepsilon). \tag{1.87b}$$

In addition, the sequence of extended solutions $(\widehat{\mathbf{u}_\varepsilon}, \widetilde{\eta_\varepsilon})$ satisfies the a priori bounds:

$$|\widehat{\mathbf{u}_\varepsilon}|^2_{1,\Omega} + \|\widehat{\partial_t \mathbf{u}_\varepsilon}\|^2_{0,\Omega} + \mathcal{V}_\varepsilon(t) \leq C, \ \text{a.e. } t \in [0,T], \tag{1.88a}$$

$$\|\widetilde{\eta_\varepsilon}\|_{H^{-1}(0,T;M)} \leq C, \tag{1.88b}$$

for some $C > 0$ independent of ε, where $\mathcal{V}_\varepsilon(t)$ is defined as in section 1.2 by (1.32).

Proof. As a first step, we study the auxiliary variational formulation obtained by using only divergence–free test functions in (1.85a): find $\mathbf{u}_\varepsilon \in L^\infty(0,T;\mathbf{V}^{inc}_\varepsilon)$ such that

$$\begin{cases} \text{For all } \mathbf{v}_\varepsilon \in \mathbf{V}^{inc}_\varepsilon, \quad \text{and in } \mathcal{D}'(0,T), \\ \dfrac{\mathrm{d}}{\mathrm{d}t}(\rho \partial_t \mathbf{u}_\varepsilon, \mathbf{v}_\varepsilon)_{0,\Omega_\varepsilon} + \dfrac{\mathrm{d}}{\mathrm{d}t} r_\varepsilon(\mathbf{u}_\varepsilon, \mathbf{v}_\varepsilon) + a_\varepsilon(\mathbf{u}_\varepsilon, \mathbf{v}_\varepsilon) = \ell_\varepsilon(\mathbf{v}_\varepsilon), & \text{(1.89a)} \\ \mathbf{u}_\varepsilon(0) = \mathbf{u}_0 \text{ and } \partial_t \mathbf{u}_\varepsilon(0) = \mathbf{u}_1. & \text{(1.89b)} \end{cases}$$

By using the same arguments as in the compressible case (see also [Van09]), we can prove that there exists a unique solution to the auxiliary variational problem (1.89) such that (1.87a) and (1.88a) hold.
Next, we prove the existence of a pressure η_ε in $H^{-1}(0,T;M_\varepsilon)$ such that the full formulation (1.85) is satisfied. Given $\psi_\varepsilon \in H^1_0(0,T;M_\varepsilon)$, its extension by the operator $\widetilde{\cdot}$ is such that $\widetilde{\psi_\varepsilon} \in H^1_0(0,T;M)$, and:

$$|\widetilde{\psi_\varepsilon}|_{H^1(0,T;M)} \leq C_1 |\psi_\varepsilon|_{H^1(0,T;M_\varepsilon)} \tag{1.90}$$

with C_1 independent of ε. We know that there exists $\widetilde{\mathbf{v}} \in H^1_0(0,T;\mathbf{V})$ (see [GR86]) such that

$$\operatorname{div} \widetilde{\mathbf{v}} = \psi_\varepsilon, \ \text{in } (0,T) \times \Omega,$$

and

$$\|\widetilde{\mathbf{v}}\|_{H^1_0(0,T;\mathbf{V})} \leq C_2 |\widetilde{\psi_\varepsilon}|_{H^1(0,T;M)} \tag{1.91}$$

where C_2 also does not depend on ε. Let $\mathbf{v}_\varepsilon$ be the restriction of $\widetilde{\mathbf{v}}$ to Ω_ε, we have:

$$\text{div } \mathbf{v}_\varepsilon = \psi_\varepsilon, \text{ in } (0,T)\times\Omega_\varepsilon,$$

and thanks to (1.90) and (1.91),

$$\|\mathbf{v}_\varepsilon\|_{H_0^1(0,T;\mathbf{V}_\varepsilon)} \leq C_1C_2|\psi_\varepsilon|_{H^1(0,T;M_\varepsilon)}. \tag{1.92}$$

Now we denote by $\langle\cdot,\cdot\rangle_{(0,T)}$ the duality pairing between $H^{-1}(0,T;M_\varepsilon)$ and $H_0^1(0,T;M_\varepsilon)$ and we rewrite equation (1.85a) as:

$$\begin{aligned}\langle\eta_\varepsilon,\psi_\varepsilon\rangle_{(0,T)} = \int_0^T\int_{\Omega_\varepsilon}\rho\partial_t\mathbf{u}_\varepsilon\cdot\partial_t\mathbf{v}_\varepsilon + 2\mu e(\mathbf{u}_\varepsilon):e(\mathbf{v}_\varepsilon) - \mathcal{R}_\varepsilon(\chi_{F,\varepsilon}\text{div }\widehat{\mathbf{u}_\varepsilon})\chi_{F,\varepsilon}\text{div}(\partial_t\widehat{\mathbf{v}_\varepsilon})\\ - \int_0^T\int_{\Omega_\varepsilon}\mathbf{f}\cdot\mathbf{v}_\varepsilon - \int_0^T p_e\int_{\Omega\setminus\Omega_\varepsilon}\text{div }\widehat{\mathbf{v}_\varepsilon}.\end{aligned} \tag{1.93}$$

Thanks to (1.92), the right–hand side is a continuous linear form of ψ_ε. This yields the existence and uniqueness of η_ε in $H^{-1}(0,T;M_\varepsilon)$. In addition, we have

$$|\langle\eta_\varepsilon,\psi_\varepsilon\rangle_{(0,T)}| \leq C|\psi_\varepsilon|_{H^1(0,T;M_\varepsilon)}$$

where C does not depend on ε, thanks to (1.93), (1.83), (1.88a) and the properties of the extension operator given in Lemma 1.2.2. This proves (1.87b) and (1.88b) and ends the proof of the Proposition. □

1.3.3 Two–scale convergence

As in the compressible case, we apply the two–scale convergence method to find the homogenized problem. To deal with the pressure term we define the two–scale convergence in $H^{-1}(0,T)$ as follows:

Definition 1.3.2. *Let $(\phi_\varepsilon)_{\varepsilon>0}$ be a sequence in $H^{-1}(0,T;M)$. We say that ϕ_ε two–scale converges to ϕ in $H^{-1}(0,T;L^2_0(\Omega\times\mathcal{Y}))$ when:*

$$\begin{aligned}&\forall\psi(t,\mathbf{x},\mathbf{y})\in\mathcal{H}_0^1((0,T);L^2(\Omega;C_\#(\mathcal{Y}))),\\ &\lim_{\varepsilon\to0}\int_0^T\int_\Omega\phi_\varepsilon(t,\mathbf{x})\psi\left(t,\mathbf{x},\frac{\mathbf{x}}{\varepsilon}\right)\mathrm{d}\mathbf{x} = \int_0^T\int_\Omega\int_Y\phi(t,\mathbf{x},\mathbf{y})\psi(t,\mathbf{x},\mathbf{y})\mathrm{d}\mathbf{y}\mathrm{d}\mathbf{x}.\end{aligned} \tag{1.94}$$

Since the time variable is only a parameter in the two–scale convergence defined by (1.94) and $H^{-1}(0,T)$ is separable, the weak two–scale convergence defined by (1.94) has the same compactness property as in the square–integrable in time case (Lemma 1.1.14).

1.3.3.1 Convergence of the sequence of solutions

As in the compressible case, we define q_ε and π_ε as:

$$q_\varepsilon = -\Pi_\varepsilon(\chi_{F,\varepsilon}\text{div }\widehat{\mathbf{u}_\varepsilon}) \in H^1(0,T;L^2(\Omega)) \tag{1.95}$$

$$\pi_\varepsilon = \mathcal{R}_\varepsilon q_\varepsilon \in H^1(0,T;L^2(\Omega)). \tag{1.96}$$

Then, we have the following convergences:

Proposition 1.3.3. *Suppose (1.83) and (1.84) hold. Then, there exists* $\mathbf{u} \in L^2(0,T;\mathbf{V})$, $\mathbf{u}^1 \in L^2((0,T)\times\Omega;\mathbf{H}^1_\#(\mathcal{Y})/\mathbb{R}^d)$ *and* $\eta \in H^{-1}(0,T;M)$ *such that* $\partial_t\mathbf{u} \in L^2(0,T;\mathbf{X})$ *and up to a subsequence, still denoted by* ε*,*

$$\begin{cases} \widehat{\mathbf{u}_\varepsilon} \twoheadrightarrow \mathbf{u} & \\ \nabla\widehat{\mathbf{u}_\varepsilon} \twoheadrightarrow \nabla_x\mathbf{u} + \nabla_y\mathbf{u}^1 & \text{two–scale in } L^2((0,T)\times\Omega\times\mathcal{Y}), \\ \widehat{\partial_t\mathbf{u}_\varepsilon} \twoheadrightarrow \partial_t\mathbf{u} & \\ \widetilde{\eta_\varepsilon} \twoheadrightarrow \eta & \text{two–scale in } H^{-1}(0,T;L^2(\Omega\times\mathcal{Y})). \end{cases} \tag{1.97}$$

We also have

$$\mathrm{div}_{\mathbf{x}}\mathbf{u} + \mathrm{div}_{\mathbf{y}}\mathbf{u}^1 = 0 \text{ on } (0,T)\times\Omega\times\mathcal{Y}_S. \tag{1.98}$$

The function q_ε *two–scale converges in* $L^2((0,T)\times\Omega\times\mathcal{Y})$ *to a function* $q \in L^2(0,T;L^2(\Omega))$*:*

$$q_\varepsilon \twoheadrightarrow q = -\mathrm{div}_{\mathbf{x}}\mathbf{u}, \qquad \text{two–scale in } L^2((0,T)\times\Omega\times\mathcal{Y}). \tag{1.99}$$

and the function π_ε *converges to* $\pi \in H^1(0,T;L^2(\Omega))$ *as follows:*

$$\pi_\varepsilon = \mathcal{R}_\varepsilon q_\varepsilon \to \pi = \mathcal{R}q \qquad \text{strongly in } L^2((0,T)\times\Omega), \tag{1.100}$$

$$\partial_t\pi_\varepsilon = \mathcal{R}_\varepsilon\partial_t q_\varepsilon \twoheadrightarrow \partial_t\pi = \frac{\partial}{\partial t}(\mathcal{R}q) \qquad \text{two–scale in } L^2((0,T)\times\Omega\times\mathcal{Y}). \tag{1.101}$$

Proof. Thanks to the *a priori* bounds (1.88), we obtain all the convergences (up to a subsequence) of the sequences $(\mathbf{u}_\varepsilon)_{\varepsilon>0}$, $(\nabla\mathbf{u}_\varepsilon)_{\varepsilon>0}$, $(\partial_t\mathbf{u}_\varepsilon)_{\varepsilon>0}$ as in the compressible case. Moreover, the extended pressure sequence $(\widetilde{\eta_\varepsilon})_{\varepsilon>0}$ is bounded in $H^{-1}(0,T;L^2(\Omega\times\mathcal{Y}))$, uniformly in ε. Consequently, there exists a subsequence which two–scale converges in the sense given by (1.94). Hence, we have obtained the convergences (1.97).

As a consequence, we can take the two–scale limit of the divergence of $\mathbf{u}_\varepsilon$, which yields:

$$\chi_{S,\varepsilon}(\mathrm{div}_{\mathbf{x}}\widehat{\mathbf{u}_\varepsilon}) = 0 \twoheadrightarrow \chi_S(\mathrm{div}_{\mathbf{x}}\mathbf{u} + \mathrm{div}_{\mathbf{y}}\mathbf{u}^1) \qquad \text{two–scale in } L^2((0,T)\times\Omega\times\mathcal{Y}).$$

This proves (1.98).

Finally, notice that $\mathrm{div}\,\widehat{\mathbf{u}_\varepsilon} = 0$ on $\mathcal{Y}_S$. Hence the definition of q_ε given in the compressible case by (1.18) can be simplified since

$$q_\varepsilon = -\Pi_\varepsilon(\chi_{F,\varepsilon}\mathrm{div}\,\widehat{\mathbf{u}_\varepsilon}) = -\Pi_\varepsilon(\mathrm{div}\,\widehat{\mathbf{u}_\varepsilon}).$$

As a consequence, we obtain by Lemma 1.2.10 that q_ε two–scale converges to:

$$q = -\int_{\mathcal{Y}} \mathrm{div}_{\mathbf{x}}\mathbf{u} + \mathrm{div}_{\mathbf{y}}\mathbf{u}^1 = -\mathrm{div}_{\mathbf{x}}\mathbf{u},$$

since $\mathbf{u}^1$ is Y–periodic. Then, the convergences (1.99) to (1.101) follow as in the compressible case. □

1.3.3.2 The two–scale limit problem

Next, we deduce from Proposition 1.3.3 the asymptotic two–scale formulation. First, we introduce the bilinear form $a^{inc}_\#$ on $\mathbf{V}\times\mathbf{H}$ and the mixed bilinear form $b^{inc}_\#$ on $L^2(\Omega\times\mathcal{Y}_S)\times(\mathbf{V}\times\mathbf{H})$ as:

$$a^{inc}_\#((\mathbf{u},\mathbf{u}^1),(\mathbf{v},\mathbf{v}^1)) = \int_\Omega\int_{\mathcal{Y}_S} 2\mu\left(e_{\mathbf{x}}(\mathbf{u}) + e_{\mathbf{y}}(\mathbf{u}^1)\right) : \left(e_{\mathbf{x}}(\mathbf{v}) + e_{\mathbf{y}}(\mathbf{v}^1)\right), \tag{1.102}$$

$$b^{inc}_\#(\eta,(\mathbf{v},\mathbf{v}^1)) = -\int_\Omega\int_{\mathcal{Y}_S} \eta\left(\mathrm{div}_{\mathbf{x}}\mathbf{v} + \mathrm{div}_{\mathbf{y}}\mathbf{v}^1\right). \tag{1.103}$$

We remind that $r_\#$ and $\ell_\#$ are defined by (1.57) and (1.58).

Proposition 1.3.4. *The following two–scale mixed variational problem has a unique solution* $(\mathbf{u}_\infty, \mathbf{u}^1_\infty, \eta_\infty)$ *in* $L^\infty(0,T;\mathbf{V}) \cap W^{1,\infty}(0,T;\mathbf{X}) \times L^\infty(0,T;\mathbf{H}) \times L^2((0,T)\times\Omega\times\mathcal{Y}_S)$*:*

$$\begin{cases} \text{For all } \mathbf{v}\in\mathbf{V},\ \mathbf{v}^1\in\mathbf{H},\ \phi\in L^2(\Omega\times\mathcal{Y}_S), \quad \text{and in } \mathcal{D}'(0,T), \\ \dfrac{\mathrm{d}}{\mathrm{d}t}(\theta\rho\partial_t\mathbf{u}_\infty,\mathbf{v})_{0,\Omega} + \dfrac{\mathrm{d}}{\mathrm{d}t} r_\#\left((\mathbf{u}_\infty,\mathbf{u}^1_\infty),(\mathbf{v},\mathbf{v}^1)\right) + a^{inc}_\#((\mathbf{u}_\infty,\mathbf{u}^1_\infty),(\mathbf{v},\mathbf{v}^1)) \\ \qquad\qquad + b^{inc}_\#\left(\eta_\infty,(\mathbf{v},\mathbf{v}^1)\right) = \ell_\#(\mathbf{v},\mathbf{v}^1), \qquad (1.104a) \\ b^{inc}_\#(\phi,(\mathbf{u}_\infty,\mathbf{u}^1_\infty)) = 0, \qquad (1.104b) \\ \mathbf{u}_\infty(0)=\mathbf{u}_0,\ \mathbf{u}^1_\infty(0)=\mathbf{0},\ \partial_t\mathbf{u}_\infty(0)=\mathbf{u}_1 \text{ in } \Omega. \qquad (1.104c) \end{cases}$$

Moreover,

$$\partial_{tt}\mathbf{u}_\infty \in L^2(0,T;\mathbf{V}').$$

Remark 1.3.5. *Note that the two–scale incompressibility condition* (1.104b) *implies that*

$$\mathrm{div}_{\mathbf{x}}\mathbf{u}_\infty + \mathrm{div}_{\mathbf{y}}\mathbf{u}^1_\infty = 0 \text{ in } \Omega\times\mathcal{Y}_S.$$

This calls for two comments. First, as in the static case (see [BGMO08]), we recover in the limit a compressible material thanks to the inclusion of gas bubbles, as should be expected. Second, the non–local viscous term can be written without the microscopic variable $\mathbf{u}^1$ *thanks to the resulting relations:*

$$\int_\Gamma \mathbf{u}^1_\infty\cdot\mathbf{n}^S = \int_{\mathcal{Y}_S}\mathrm{div}_{\mathbf{y}}\mathbf{u}^1_\infty = -\int_{\mathcal{Y}_S}\mathrm{div}_{\mathbf{x}}\mathbf{u}_\infty = -\theta\mathrm{div}_{\mathbf{x}}\mathbf{u}_\infty.$$

Indeed, we have the following expression:

$$r_\#((\mathbf{u}_\infty,\mathbf{u}^1_\infty),(\mathbf{v},\mathbf{v}^1)) = \int_\Omega(\mathcal{R}\mathrm{div}_{\mathbf{x}}\mathbf{u}_\infty)\left((1-\theta)\mathrm{div}_{\mathbf{x}}\mathbf{v} - \int_\Gamma \mathbf{v}^1\cdot\mathbf{n}^S\right).$$

This is different from the compressible case, where the equivalent term couples the values of $\mathbf{u}^1_\infty$ *globally across* Ω*. As a result, the cell problems are decoupled in the incompressible case and we will not need an additional fluid pressure variable to describe the macroscopic law of the homogenized material. Consequently, the homogenized material does not exhibit a fading memory in time as in the compressible case, but only an instantaneous non–local viscoelastic behavior.*

Remark 1.3.6. *As in the compressible case, the initial condition* $\mathbf{u}^1_\infty(0)=\mathbf{0}$ *has to be understood in a weak sense. It is only needed to compute an initial condition for the fluid pressure term, that is*

$$\left((1-\theta)\mathrm{div}_{\mathbf{x}}\mathbf{u}_\infty - \int_\Gamma \mathbf{u}^1_\infty\cdot\mathbf{n}^S\right)\Big|_{t=0} = (1-\theta)\mathrm{div}_{\mathbf{x}}\mathbf{u}_0.$$

This is in apparent contradiction with the previous remark, where we show that we can write the left–hand side as $\mathrm{div}_{\mathbf{x}}\mathbf{u}_0$ *thanks to the incompressibility constraint. Hence we are left with the equality*

$$(1-\theta)\mathrm{div}_{\mathbf{x}}\mathbf{u}_0 = \mathrm{div}_{\mathbf{x}}\mathbf{u}_0.$$

However, $\mathbf{u}_0$ *satisfies itself the incompressibility constraint* $\mathrm{div}\mathbf{u}_0 = 0$ *thanks to the assumption* (1.83)*, so there is no contradiction: we have in fact*

$$\left((1-\theta)\mathrm{div}_{\mathbf{x}}\mathbf{u}_\infty - \int_\Gamma \mathbf{u}^1_\infty\cdot\mathbf{n}^S\right)\Big|_{t=0} = 0.$$

Proof. The proof of Proposition 1.3.4 can be decomposed in two parts. First, we consider an auxiliary variational formulation without the pressure. We can then follow exactly the same proof as in the compressible case in a closed subspace of $\mathbf{V}\times\mathbf{H}$. Then, we consider the full mixed variational formulation (1.104a)–(1.104b) and we show that there exists a unique pressure η such that (1.104a) holds.

Existence and uniqueness of $(\mathbf{u}_\infty, \mathbf{u}_\infty^1)$ First, let us consider the following Hilbert space:

$$\mathbf{W} = \{(\mathbf{v}, \mathbf{v}^1) \in \mathbf{V} \times \mathbf{H} \mid \mathrm{div}_{\mathbf{x}}\mathbf{v} + \mathrm{div}_{\mathbf{y}}\mathbf{v}^1 = 0 \text{ on } \Omega \times \mathcal{Y}_S\}. \tag{1.105}$$

Using the same Faedo–Galerkin strategy as in the proof of Proposition 1.2.11 in the compressible case, we can prove that there exists a unique solution $(\mathbf{u}_\infty, \mathbf{u}_\infty^1) \in L^\infty(0,T;\mathbf{W})$ to the following auxiliary two–scale variational problem:

$$\begin{cases} \text{For all } (\mathbf{v}, \mathbf{v}^1) \in \mathbf{W}, \quad \text{and in } \mathcal{D}'(0,T), \\ \dfrac{\mathrm{d}}{\mathrm{d}t}(\theta\rho\partial_t \mathbf{u}_\infty, \mathbf{v})_{0,\Omega} + \dfrac{\mathrm{d}}{\mathrm{d}t} r_\# \left((\mathbf{u}_\infty, \mathbf{u}_\infty^1), (\mathbf{v}, \mathbf{v}^1)\right) + a_\#^{inc}((\mathbf{u}_\infty, \mathbf{u}_\infty^1), (\mathbf{v}, \mathbf{v}^1)) = \ell_\#(\mathbf{v}, \mathbf{v}^1), & \text{(1.106a)} \\ \mathbf{u}_\infty(0) = \mathbf{u}_0, \ \mathbf{u}_\infty^1(0) = \mathbf{0}, \ \partial_t \mathbf{u}_\infty(0) = \mathbf{u}_1 \text{ in } \Omega. & \text{(1.106b)} \end{cases}$$

Moreover, $\mathbf{u}_\infty$ and $\mathbf{u}_\infty^1$ satisfy *a priori* bounds:

$$\|\partial_t \mathbf{u}_\infty\|_{0,\Omega} + \|(\mathbf{u}_\infty, \mathbf{u}_\infty^1)\|_{\mathbf{V}\times\mathbf{H}} \leq C, \quad \text{a.e. } t \in (0,T), \tag{1.107}$$

and

$$\|\mathcal{R}(\mathrm{div}_{\mathbf{x}}\mathbf{u}_\infty)\|_{H^1(0,T;L^2(\Omega))} \leq C, \tag{1.108}$$

where $C > 0$ is some constant.

Regularity result for $\partial_{tt}\mathbf{u}_\infty$. We have seen that $\mathbf{u}_\infty$ belongs in $W^{1,\infty}(0,T;\mathbf{X}) \cap L^\infty(0,T;\mathbf{V})$. Let us show that $\partial_{tt}\mathbf{u}_\infty$ is in $L^2(0,T;\mathbf{V}')$. Let $\mathbf{v}$ be in $\mathbf{V}$. To use $\mathbf{v}$ as a test function in (1.106), we want to find $\mathbf{v}^1$ in $\mathbf{H}$ such that $(\mathbf{v}, \mathbf{v}^1)$ belongs in $\mathbf{W}$. Such a $\mathbf{v}^1$ has to satisfy $\mathrm{div}_{\mathbf{y}}\mathbf{v}^1 = \phi$ where:

$$\phi = -\mathrm{div}_{\mathbf{x}}\mathbf{v} \text{ in } \Omega \times \mathcal{Y}_S.$$

Let us extend ϕ on $\Omega \times \mathcal{Y}$ by defining $\widetilde{\phi}$ as follows:

$$\widetilde{\phi} = \begin{cases} \phi & \text{in } \Omega \times \mathcal{Y}_S, \\ -\frac{1}{|\mathcal{Y}_F|}\int_{\mathcal{Y}_S} \phi & \text{in } \Omega \times \mathcal{Y}_F. \end{cases}$$

Then, we have clearly $\widetilde{\phi} \in L^2(\Omega \times \mathcal{Y})$ and $\int_{\mathcal{Y}} \widetilde{\phi}(\mathbf{x}) = 0$ for every $\mathbf{x}$ in Ω. To find $\mathbf{v}^1$, we study the following problem: for $g \in L^2_0(\mathcal{Y})$, find $z \in H^1_\#(\mathcal{Y})$ such that:

$$\Delta z = g \text{ in } \mathcal{Y}.$$

This periodic problem is well–posed since $\int_{\mathcal{Y}} g = 0$, and by elliptic regularity, we have $z \in H^2(\mathcal{Y})$ and $|\nabla z|_{1,\mathcal{Y}} \leq C\|g\|_{0,\Omega}$ for some constant $C > 0$ depending only on $\mathcal{Y}$. Now the application $g \mapsto \nabla z|_{\mathcal{Y}_S}$ is linear, continuous and a right inverse to the divergence operator in $\mathbf{H}^1_\#(\mathcal{Y}_S)$. Hence, we can find $\mathbf{v}^1$ in $\mathbf{H}$ such that $\mathrm{div}_{\mathbf{y}}\mathbf{v}^1 = \phi = -\mathrm{div}_{\mathbf{x}}\mathbf{v}$ in $\Omega \times \mathcal{Y}_S$ and $\|\mathbf{v}^1\|_{\mathbf{H}} \leq C|\mathbf{v}|_{\mathbf{V}}$.
Therefore, $(\mathbf{v}, \mathbf{v}^1)$ belongs in $\mathbf{W}$ and:

$$\|(\mathbf{v}, \mathbf{v}^1)\|_{\mathbf{W}} \leq C|\mathbf{v}|_{1,\Omega}. \tag{1.109}$$

Using $(\mathbf{v}, \mathbf{v}^1)$ as a test function in (1.106), we see that $\partial_{tt}\mathbf{u}$ satisfies, in the sense of distributions:

$$(\theta\rho\partial_{tt}\mathbf{u}_\infty, \mathbf{v})_{0,\Omega} = \ell_\#(\mathbf{v}, \mathbf{v}^1) - a_\#((\mathbf{u}_\infty, \mathbf{u}_\infty^1), (\mathbf{v}, \mathbf{v}^1)) - \int_\Omega \partial_t \left(\mathcal{R}\mathrm{div}_{\mathbf{x}}\mathbf{u}_\infty\right) \mathrm{div}_{\mathbf{x}}\mathbf{v}.$$

Thanks to estimate (1.109), we obtain that $\partial_{tt}\mathbf{u}_\infty$ belongs to $\mathbf{V}'$ a.e. in $(0,T)$ and:

$$\|\partial_{tt}\mathbf{u}_\infty\|_{\mathbf{V}'} \leq C\left(1 + \|(\mathbf{u}_\infty, \mathbf{u}_\infty^1)\|_{\mathbf{V}\times\mathbf{H}} + \|\partial_t \mathcal{R}\mathrm{div}_{\mathbf{x}}\mathbf{u}_\infty\|_{L^2(\Omega)}\right).$$

The *a priori* bounds (1.107) and (1.108) show that the right–hand side is square integrable in time, so $\partial_{tt}\mathbf{u}_\infty$ belongs to $L^2(0,T;\mathbf{V}')$.

Existence of the pressure. Next, we show that there exists a unique pressure η_∞ satisfying (1.104a). First, let $\phi \in H_0^1(0,T;L^2(\Omega \times \mathcal{Y}_S))$. By Lemma 3.6 in [BGMO08], we know that there exists a linear continuous application from $L^2(\Omega \times \mathcal{Y}_S)$ to $(\mathbf{V} \times \mathbf{H})$ which is a right inverse to the divergence operator $(\mathbf{v}, \mathbf{v}^1) \mapsto \mathrm{div}_{\mathbf{x}}\mathbf{v} + \mathrm{div}_{\mathbf{y}}\mathbf{v}^1$. By extension, there exists $(\mathbf{v}, \mathbf{v}^1)$ in $H_0^1(0,T;\mathbf{V}\times\mathbf{H})$ such that:

$$\begin{aligned} \mathrm{div}_{\mathbf{x}}\mathbf{v} + \mathrm{div}_{\mathbf{y}}\mathbf{v}^1 &= \phi \text{ in } (0,T)\times\Omega\times\mathcal{Y}_S, \\ \|(\mathbf{v},\mathbf{v}^1)\|_{H^1(0,T;\mathbf{V}\times\mathbf{H})} &\leq C\|\phi\|_{H^1(0,T;L^2(\Omega\times\mathcal{Y}_S))}. \end{aligned} \tag{1.110}$$

Now, let $\langle\cdot,\cdot\rangle_{(0,T)}$ be the duality pairing between the spaces $H^{-1}((0,T);L^2(\Omega\times\mathcal{Y}_S))$ and $H_0^1((0,T);L^2(\Omega\times\mathcal{Y}_S))$. We rewrite equation (1.104a) as:

$$\begin{aligned} \langle\eta_\infty,\phi\rangle_{(0,T)} = &-\int_0^T (\theta\rho\partial_t\mathbf{u}_\infty, \partial_t\mathbf{v})_{0,\Omega} + \int_0^T a_\#((\mathbf{u}_\infty,\mathbf{u}_\infty^1),(\mathbf{v},\mathbf{v}^1)) \\ &- \int_0^T r_\#\left((\mathbf{u}_\infty,\mathbf{u}_\infty^1),(\partial_t\mathbf{v},\partial_t\mathbf{v}^1)\right) - \int_0^T \ell_\#(\mathbf{v},\mathbf{v}^1). \end{aligned} \tag{1.111}$$

Since ϕ is arbitrary, equation (1.111) defines uniquely η_∞ as an element of $H^{-1}((0,T);L^2(\Omega\times\mathcal{Y}_S))$. In fact, since $\partial_{tt}\mathbf{u}_\infty$ belongs in $L^2(0,T;\mathbf{V}')$, we have $\eta_\infty \in L^2((0,T)\times\Omega\times\mathcal{Y}_S)$. To prove this, we transform (1.111) by integrating by parts the terms where the time derivative $\partial_t\mathbf{v}$ appears, using the fact that $\mathbf{v}$ belongs to $H_0^1(0,T;\mathbf{V})$, $\partial_{tt}\mathbf{u}_\infty$ belongs to $\mathbf{L}^2(0,T;\mathbf{V}')$ and $\frac{\partial}{\partial t}(\mathcal{R}\mathrm{div}_{\mathbf{x}}\mathbf{u}_\infty)$ belongs to $L^2((0,T)\times\Omega)$. We obtain the following formula:

$$\begin{aligned} \langle\eta_\infty,\phi\rangle_{(0,T)} = &\int_0^T (\theta\rho\partial_{tt}\mathbf{u}_\infty, \mathbf{v})_{0,\Omega} + \int_0^T a_\#((\mathbf{u}_\infty,\mathbf{u}_\infty^1),(\mathbf{v},\mathbf{v}^1)) \\ &- \int_0^T \int_\Omega \frac{\partial}{\partial t}(\mathcal{R}\mathrm{div}_{\mathbf{x}}\mathbf{u}_\infty)\left((1-\theta)\mathrm{div}_{\mathbf{x}}\mathbf{v} - \int_\Gamma \mathbf{v}^1\cdot\mathbf{n}^S\right) - \int_0^T \ell_\#(\mathbf{v},\mathbf{v}^1). \end{aligned}$$

This ends the proof of the Proposition. □

The main convergence result can then be obtained following the same lines as in the proof of the corresponding Theorem 1.2.13 in the compressible case:

Theorem 1.3.7. *Suppose (1.83) and (1.84) hold.*

Let $(\mathbf{u}_\varepsilon,\eta_\varepsilon)_{\varepsilon>0}$ be the sequence of solutions of the family of problems (1.16) when ε varies. Then the four sequences $(\widehat{\mathbf{u}_\varepsilon}\chi_{S,\varepsilon})_{\varepsilon>0}$, $(\widehat{\partial_t\mathbf{u}_\varepsilon}\chi_{S,\varepsilon})_{\varepsilon>0}$, $(\nabla(\widehat{\mathbf{u}_\varepsilon})\chi_{S,\varepsilon})_{\varepsilon>0}$ and $(\widetilde{\eta_\varepsilon}\chi_{S,\varepsilon})_{\varepsilon>0}$ two–scale converge respectively to $\mathbf{u}\chi_S$, $\partial_t\mathbf{u}\chi_S$, $\left(\nabla_x\mathbf{u}+\nabla_y\mathbf{u}^1\right)\chi_S$ in $L^2((0,T)\times\Omega\times\mathcal{Y})$ and $\eta\chi_S$ in $H^{-1}(0,T;L^2(\Omega\times\mathcal{Y}))$, where $(\mathbf{u},\mathbf{u}^1|_{\Omega\times\mathcal{Y}_S},\eta|_{\Omega\times\mathcal{Y}_S})$ can be identified with $(\mathbf{u}_\infty,\mathbf{u}_\infty^1,\eta_\infty)$, the unique solution of the two–scale variational problem (1.104).

In the following discussion we will make this identification and, for simplicity, denote $\mathbf{u}^1$ and η their respective restriction to $\Omega\times\mathcal{Y}_S$, which is also equal to $\mathbf{u}_\infty^1$ and η_∞.

1.3.3.3 Cell problems and the homogenized law

As in the compressible case, we use appropriate test functions $\mathbf{v}$, $\mathbf{v}^1$ and ϕ to identify two differential problems from the two–scale variational problem (1.104), one in the microscopic variable and one in the macroscopic variable.

Fluid cell problem First, we write the local cell problem by taking the test function $\mathbf{v}$ to be 0 in the two–scale variational formulation (1.104a). Then $\mathbf{u}^1$ and η are the solution of a mixed variational problem on $\mathcal{Y}_S$ parameterized by the macroscopic displacement $\mathbf{u}$:

$$\begin{cases} \text{For all } (\mathbf{v}^1, \phi) \in \mathbf{H} \times L^2(\Omega \times \mathcal{Y}_S), \\ \quad \displaystyle\int_{\mathcal{Y}_S} 2\mu e_{\mathbf{y}}(\mathbf{u}^1) : e_{\mathbf{y}}(\mathbf{v}^1) - \int_{\mathcal{Y}_S} \eta \mathrm{div}_{\mathbf{y}} \mathbf{v}^1 \\ \qquad\qquad = -\displaystyle\int_{\mathcal{Y}_S} 2\mu e_{\mathbf{x}}(\mathbf{u}) : e_{\mathbf{y}}(\mathbf{v}^1) + \left(\frac{\partial}{\partial t}\mathcal{R}(\mathrm{div}_{\mathbf{x}}\mathbf{u}) + p_e\right) \int_{\mathcal{Y}_S} \mathrm{div}_{\mathbf{y}} \mathbf{v}^1, & (1.112a) \\ \displaystyle\int_{\mathcal{Y}_S} \phi \mathrm{div}_{\mathbf{y}} \mathbf{u}^1 = -\int_{\mathcal{Y}_S} \phi \mathrm{div}_{\mathbf{x}} \mathbf{u}. & (1.112b) \end{cases}$$

Now, we introduce the correctors to write $\mathbf{u}^1$ and η uniquely in terms of $\mathbf{u}$. Let us denote by $(\boldsymbol{\chi}^{kl}_{inc}, \eta^{kl})$ the solutions of the auxiliary local problems:

$$\begin{cases} -\mathbf{div}_{\mathbf{y}} \left(-\eta^{kl}\mathrm{Id} + 2\mu e_{\mathbf{y}}(\boldsymbol{\chi}^{kl}_{inc})\right) = \mathbf{0}, & \text{in } \mathcal{Y}_S, & (1.113a) \\ \mathrm{div}_{\mathbf{y}} \boldsymbol{\chi}^{kl}_{inc} = \delta_{kl}, & \text{in } \mathcal{Y}_S, & (1.113b) \\ \left(-\eta^{kl}\mathrm{Id} + 2\mu e_{\mathbf{y}}(\boldsymbol{\chi}^{kl}_{inc})\right) \mathbf{n}^S = -2\mu e_{\mathbf{y}}(\mathbf{p}^{kl})\mathbf{n}^S, & \text{on } \Gamma, & \\ \boldsymbol{\chi}^{kl}_{inc},\ \eta^{kl}\ \mathcal{Y}\text{–periodic}, & & \end{cases}$$

where $1 \leq k, l \leq d$ and $\mathbf{p}^{kl}$ is the polynomial introduced in (1.73). Using the superposition principle in (1.112) we have that:

$$\mathbf{u}^1 = e_{\mathbf{x}}(\mathbf{u})_{kl} \boldsymbol{\chi}^{kl}_{inc}, \tag{1.114a}$$

$$\eta = e_{\mathbf{x}}(\mathbf{u})_{kl} \eta^{kl} - \left(\frac{\partial}{\partial t}\mathcal{R}(\mathrm{div}_{\mathbf{x}}\mathbf{u}) + p_e\right). \tag{1.114b}$$

Remark 1.3.8. *If we compare the incompressible cell problem (1.75) to the compressible case (1.72), it is clear that there is a major simplification in the incompressible case: the problems are no longer coupled across space and time, thanks to the incompressibility condition (1.104b). This is reflected in the decomposition of $\mathbf{u}^1$ and η on the basis of the correctors as in (1.114): we do not need the introduction of the fluid pressure variable π as in the compressible case (1.74).*

Another remarkable new feature is that only the two–scale pressure η is coupled to the tree operator by (1.114b), while the corrector for the deformation $\mathbf{u}^1$ has the same expression as in more classical cases dealing with elastic perforated materials, see [SP80]. Hence the contribution of the air trapped inside the alveoli to the stresses of the homogenized material is an isotropic hydrostatic pressure term, which appears as a non–local reaction to a compression or dilatation of the material.

Homogenized problem Thanks to the decomposition (1.114) we can now identify the macroscopic problem as in the compressible case. Using a test function $\mathbf{v} \in \mathbf{V}$ with $\mathbf{v}^1$ and ϕ equal to zero in (1.104a), we obtain the following variational problem for $\mathbf{u}$:

$$\begin{cases} \qquad\qquad \text{For all } \mathbf{v} \in \mathbf{V}, \quad \text{and in } \mathcal{D}'(0,T), \\ \dfrac{\mathrm{d}}{\mathrm{d}t}(\theta\rho\partial_t\mathbf{u}, \mathbf{v})_{0,\Omega} + \dfrac{\mathrm{d}}{\mathrm{d}t}\displaystyle\int_\Omega (1-\theta)\mathcal{R}\left(\mathrm{div}_{\mathbf{x}}\mathbf{u}\right)\mathrm{div}_{\mathbf{x}}\mathbf{v} \\ \qquad\qquad + \displaystyle\int_\Omega e_{\mathbf{x}}(\mathbf{u})_{kl} \left(\int_{\mathcal{Y}_S} -\eta^{kl}\mathrm{Id} + 2\mu e_{\mathbf{y}}\left(\mathbf{p}^{kl} + \boldsymbol{\chi}^{kl}_{inc}\right)\right) : e_{\mathbf{x}}(\mathbf{v}) \\ \qquad\qquad = \displaystyle\int_\Omega \theta\mathbf{f}\cdot\mathbf{v} + \int_{\Gamma_N} (p_N - p_e)\mathbf{v}\cdot\mathbf{n}, \\ \qquad\qquad \mathbf{u}(0) = \mathbf{u}_0,\ \partial_t\mathbf{u}(0) = \mathbf{u}_1 \text{ in } \Omega. \end{cases}$$

Let us introduce the homogenized elasticity tensor:

$$\left(\mathcal{A}_{inc}^{hom}\right)_{ijkl} = \int_{\mathcal{Y}_S} -\eta^{kl}\delta_{ij} + 2\mu e_{\mathbf{y}}\left(\mathbf{p}^{kl} + \boldsymbol{\chi}_{inc}^{kl}\right)_{ij} \tag{1.115}$$

As in the compressible case, the tensor $\mathcal{A}_{inc}^{hom}$ has the following properties:

Proposition 1.3.9. *The fourth-order tensor $\mathcal{A}_{inc}^{hom}$ defined in (1.115) has the following properties:*

a) *Symmetry:*

$$\left(\mathcal{A}_{inc}^{hom}\right)_{ijkl} = \left(\mathcal{A}_{inc}^{hom}\right)_{klij} = \left(\mathcal{A}_{inc}^{hom}\right)_{ijlk}.$$

b) *Ellipticity: there exists $\beta > 0$ such that for any $d \times d$ symmetric matrix ξ,*

$$(\mathcal{A}_{inc}^{hom}\xi) : \xi \geq \beta\xi : \xi.$$

c) *Positive definitness:*

$$\mathcal{A}_{inc}^{hom}\xi : \xi = 0 \text{ iff } \xi = 0.$$

The proof is classical and follows the same line as in [SP80, BGMO08]. Then, we can describe the limit problem verified by the macroscopic displacement $\mathbf{u}$ as follows:

Theorem 1.3.10. *Suppose (1.83) and (1.84) holds and let $(\mathbf{u}_\varepsilon)_{\varepsilon>0}$ be the sequence of solutions of problem (1.16). Then,*

$$\widehat{\mathbf{u}_\varepsilon} \rightharpoonup \mathbf{u} \qquad \text{weak-}* \text{ in } L^\infty(0,T;\mathbf{V}), \tag{1.116a}$$

$$\widehat{\mathbf{u}_\varepsilon\chi_{S,\varepsilon}} \rightharpoonup \theta\mathbf{u} \qquad \text{weak-}* \text{ in } L^\infty(0,T;\mathbf{X}), \tag{1.116b}$$

$$\widehat{\partial_t\mathbf{u}_\varepsilon\chi_{S,\varepsilon}} \rightharpoonup \theta\partial_t\mathbf{u} \qquad \text{weak-}* \text{ in } L^\infty(0,T;\mathbf{X}), \tag{1.116c}$$

$$\mathcal{R}_\varepsilon\left(\chi_{F,\varepsilon}\text{div }\widehat{\mathbf{u}_\varepsilon}\right) \rightharpoonup (1-\theta)\mathcal{R}\left(\text{div }\mathbf{u}\right) \qquad \text{weak-}* \text{ in } H^1(0,T;L^2(\Omega)), \tag{1.116d}$$

where $\mathbf{u}$ is the unique weak solution of the following homogenized problem:

$$\theta\rho\partial_{tt}\mathbf{u} - \mathbf{div}\left(\mathcal{A}_{inc}^{hom}e(\mathbf{u}) + (1-\theta)\partial_t\mathcal{R}\left(\text{div }\mathbf{u}\right)\text{Id}\right) = \theta\mathbf{f} \qquad \text{in } (0,T)\times\Omega, \tag{1.117a}$$

with the boundary conditions:

$$\left(\mathcal{A}_{inc}^{hom}e(\mathbf{u}) + (1-\theta)\partial_t\mathcal{R}\left(\text{div }\mathbf{u}\right)\text{Id}\right)\mathbf{n} = (p_e - p_N)\,\mathbf{n}, \qquad \text{on } (0,T)\times\Gamma_N, \tag{1.117b}$$

$$\mathbf{u} = \mathbf{0}, \qquad \text{on } (0,T)\times\Gamma_D, \tag{1.117c}$$

and the initial conditions:

$$\mathbf{u}(0) = \mathbf{u}_0, \qquad \partial_t\mathbf{u}(0) = \mathbf{u}_1, \qquad \text{in } \Omega. \tag{1.117d}$$

The proof is exactly the same as in the compressible case.

Remark 1.3.11. *Let us compare the compressible (1.81) and incompressible (1.117) homogenized problems. As in the static case [BGMO08], we can obtain the incompressible coefficients by taking the limit $\lambda \to \infty$ in the compressible cell problems (1.75) and (1.76). In particular, we see that τ_{hom} takes the value 0 in the incompressible case, which is why the memory effect in time disappears. The matrix $\mathcal{B}^{hom}$ also tends to $(1-\theta)$Id.*

Consider now the stress–strain law in the homogenized material:

$$\sigma^{hom}(\mathbf{u}) = \mathcal{A}_{inc}^{hom}e(\mathbf{u}) + (1-\theta)\partial_t\mathcal{R}\left(\text{div }\mathbf{u}\right)\text{Id}. \tag{1.118}$$

Clearly we decompose this expression in two parts: the first term is local and depends only on the properties of the perforated elastic material encoded in the tensor $\mathcal{A}_{inc}^{hom}$. The second term is non–local and describes the pressure forces induced by the dyadic tree through the tree operator $\mathcal{R}$. Remarkably, we do not need to know any other properties of the elastic material than the volume fraction of the gas $1-\theta$ to compute this term, whereas in the compressible case both the characteristic time τ_{hom} and the matrix $\mathcal{B}^{hom}$ have to be computed by solving the cell problems on the periodic elastic cell. This shows that the effects of the dyadic tree and of the elastic perforated structure decouple in the incompressible limit.

Remark 1.3.12. *In the study of a one–dimensional model for the lungs, the authors of [GMM06] also obtain a similar non–local viscoelastic constitutive law. The extension of the tree embedding and of the tree operator $\mathcal{R}$ to a multidimensional framework is described in [VSM09], where (1.118) is proposed, without proof, as the constitutive law for an elastic material irrigated by a dyadic tree.*

Chapter 2

Multi–scale Decompositions and the Tree Operator

We have developed in Chapter 1 an homogenized model describing the mechanical behavior of the lungs' parenchyma under the theoretical assumption that the sequence of operators $\mathcal{R}_\varepsilon$ converges to an operator $\mathcal{R}$ without describing the practical constructions and the properties of the multi–scale operators $\mathcal{R}_\varepsilon$, which encode in our model all the properties of the bronchial tree. We want to investigate in this Chapter the convergence of the tree in the sense of the abstract convergence of operators, more precisely, we want to know when the abstract condition (1.43) or (1.84) is verified:

$$\begin{aligned} &\text{There exists } \mathcal{R} \in \mathcal{L}\left(L^2(\Omega); L^2(\Omega)\right) \text{ such that} \\ &\mathcal{R}_\varepsilon \to \mathcal{R} \text{ strongly in } \mathcal{L}\left(L^2(\Omega); L^2(\Omega)\right). \end{aligned}$$

We propose two different geometrical constructions. The first construction is based on the symmetric model of the lung developed by Weibel [Wei63] and uses the theoretical results proved in [VSM09] in the case of a perfectly regular domain decomposition following the lines of the periodic array. Next, we propose an approach based on the algorithmic constructions of space–filling trees (see [TPH00] for example) that allows for a more flexible choice of decomposition and periodic cells.

Contents

2.1 Multi–scale domain decompositions 67
2.2 Letting a square breathe 70
2.2.1 Geometry 70
2.2.2 Convergence of the resistance operators and geometric resistive trees 73
2.3 An algorithmic approach 76
2.3.1 Geometry: approximation of a multi–scale decomposition 76
2.3.2 Convergence of the resistance operators 80
2.A Annex 89
2.A.1 A geometric Lemma 89
2.A.2 Proof of Proposition 2.3.3 (alias Proposition 2.A.1) 91

2.1 Multi–scale domain decompositions

The approach presented in this Chapter is based on the following idea: each airway of the bronchial tree, represented by a vertex of the infinite dyadic tree $\mathcal{T}$, say $X_{n,k}$, irrigates a portion of the parenchyma, which we denote by $\Omega_{n,k} \subset \Omega$. This irrigation process follows a hierarchical structure. It is then natural to introduce the notion of multi–scale dyadic decomposition of the

domain Ω. Note that this decomposition is different from the paving of the domain with periodic cells introduced in Chapter 1. Following [VSM09], we introduce the following definitions:

Definition 2.1.1. *(Multi–scale decomposition.)*
Let $(\Omega_{n,k})_{n\geq 0,\ k=0,\dots,2^n-1}$ be a sequence of open non–empty connected subsets of Ω. We say that $\mathcal{O} = (\Omega_{n,k})_{n\geq 0,\ k=0,\dots,2^n-1}$ is a multi–scale decomposition of Ω if for every $n \geq 0$,

1. $\bigcup_{k=0}^{2^n-1} \overline{\Omega}_{n,k} = \overline{\Omega}$,
2. $\Omega_{n,j} \cap \Omega_{n,k} = \emptyset$ *as soon as* $j \neq k$,
3. $\overline{\Omega}_{n+1,2k} \cup \overline{\Omega}_{n+1,2k+1} = \overline{\Omega}_{n,k}$, *for all* $k \in \{0, \dots, 2^n - 1\}$.

We will use the standard notation $\mathrm{diam}(A)$ to denote the diameter of a subset A of $\mathbb{R}^d$, defined as

$$\mathrm{diam}(A) = \sup\left(d(\mathbf{x},\mathbf{y}) \text{ for } \mathbf{x},\ \mathbf{y} \in A\right),$$

and denote the symmetric difference between two sets A and B by the symbol Δ:

$$A \Delta B = (A \setminus B) \cup (B \setminus A).$$

Definition 2.1.2. *(Balanced domain decomposition.)*
We say that the multi-scale decomposition $\mathcal{O}$ is balanced if:

$$|\Omega_{n,k}| = 2^{-n}|\Omega|, \quad \forall n \geq 0, \quad \forall k \in \{0, \dots, 2^n - 1\}. \tag{2.1}$$

Definition 2.1.3. *(Regular domain decomposition.)*
We say that the multi–scale decomposition $\mathcal{O}$ is regular if:

1. *There exists a constant $C > 0$ such that for all $n \in \mathbb{N}$, $k \in \{0, \dots, 2^n - 1\}$,*

$$\mathrm{diam}(\Omega_{n,k}) \leq C|\Omega_{n,k}|^{1/d}. \tag{2.2}$$

2. *There exists $C > 0$ such that for all $n \in \mathbb{N}$, $k \in \{0, \dots, 2^n - 1\}$,*

$$|(\tau_{\mathbf{h}}\Omega_{n,k})\,\Delta\Omega_{n,k}| \leq C|\mathbf{h}|\,|\Omega_{n,k}|^{\frac{d-1}{d}} \qquad \forall \mathbf{h} \in \mathbb{R}^d, \tag{2.3}$$

where τ_h is the translation operator: $\tau_h E = \{\mathbf{x} + \mathbf{h}; \mathbf{x} \in E\}$.

Remark 2.1.4. *The definition of a regular domain decomposition ensures that the cells $\Omega_{n,k}$ behave asymptotically like balls as to the relations between diameter, volume and surface measure. In other words, it allows us to control the aspect ratio of the decomposition, which is similar to the hypothesis of a regular triangulation which is familiar in the analysis of Finite Elements methods (see [VSM09]).*

In the first example we will study, the regularity condition is always satisfied because the cells $\Omega_{n,k}$ are composed of a small number of appropriately rescaled periodic cells. This is not the case in the second construction, where we want to impose fewer constraints on the domain decomposition. In this case the regularity condition is crucial as we will need to control how many periodic cells $\mathcal{Y}^{\varepsilon}_{\mathbf{k}}$ intersect the boundaries of any particular cell $\Omega_{n,k}$. We will also need additional information on the regularity of the boundary of the subdomains. We introduce the following definitions.

Definition 2.1.5. *(Cone conditions.)*
We say that a domain D satisfies an interior (resp. exterior) cone condition with parameters (δ, θ) if for every $\mathbf{x} \in \partial D$, there is at least one unit vector $\mathbf{m}$ such that the cone $C(\mathbf{m}) = \{\mathbf{z} \mid \mathbf{z}\cdot\mathbf{m} > |\mathbf{z}| \cos\theta\}$ satisfies

$$(\mathbf{x} + C(\mathbf{m})) \cap B(\mathbf{x}, \delta) \quad \subset D \quad \textit{(resp. } \subset \mathbb{R}^d \setminus D\textit{)}. \tag{2.4}$$

Thus an interior cone condition implies that the "outwards–looking" corners must not be too sharp.

Definition 2.1.6. *(Approximable multi–scale decomposition.)*
We say that a multi–scale decomposition $\mathcal{O}$ is approximable *if it satisfies the following properties:*

- *$\mathcal{O}$ is regular,*
- *There exists constants $r > 0$, $\theta \in (0, \pi/2)$ independent of n and k such that for any $n \geq 0$, $k \in \{0, \dots, 2^n - 1\}$, the subdomain $\Omega_{n,k}$ satisfies an interior and an exterior cone condition with parameters $(\rho_{n,k}, \theta)$, where $\rho_{n,k} = r \operatorname{diam}(\Omega_{n,k})$,*
- *There exists a constant β with $0 < \beta \leq 1/2$ and a constant $C > 0$, such that for all $n \geq 0$ and $k \in \{0, \dots, 2^n - 1\}$,*

$$\beta|\Omega_{n,k}| \leq |\Omega_{n+1,2k}|, \ \beta|\Omega_{n,k}| \leq |\Omega_{n+1,2k+1}|. \tag{2.5}$$

Note that in particular, (2.5) means that the volume of $\Omega_{n,k}$ is bounded geometrically from above and below:

$$\beta^n \leq |\Omega_{n,k}| \leq (1 - \beta)^n.$$

Remark 2.1.7. *Assumption (2.5) generalizes the notion of a balanced multi–scale decomposition. For example, if $\beta = 1/2$, we obtain the balanced regular decompositions studied by Maury, Salort, Meunier in [VSM09]. In general, the case $\beta < 1/2$ allows us to introduce some asymmetry in the multi–scale decomposition. This could be of interest since the real bronchial tree exhibits a systematic asymmetric bifurcation (see e.g. [MAB+05, FSF11]).*

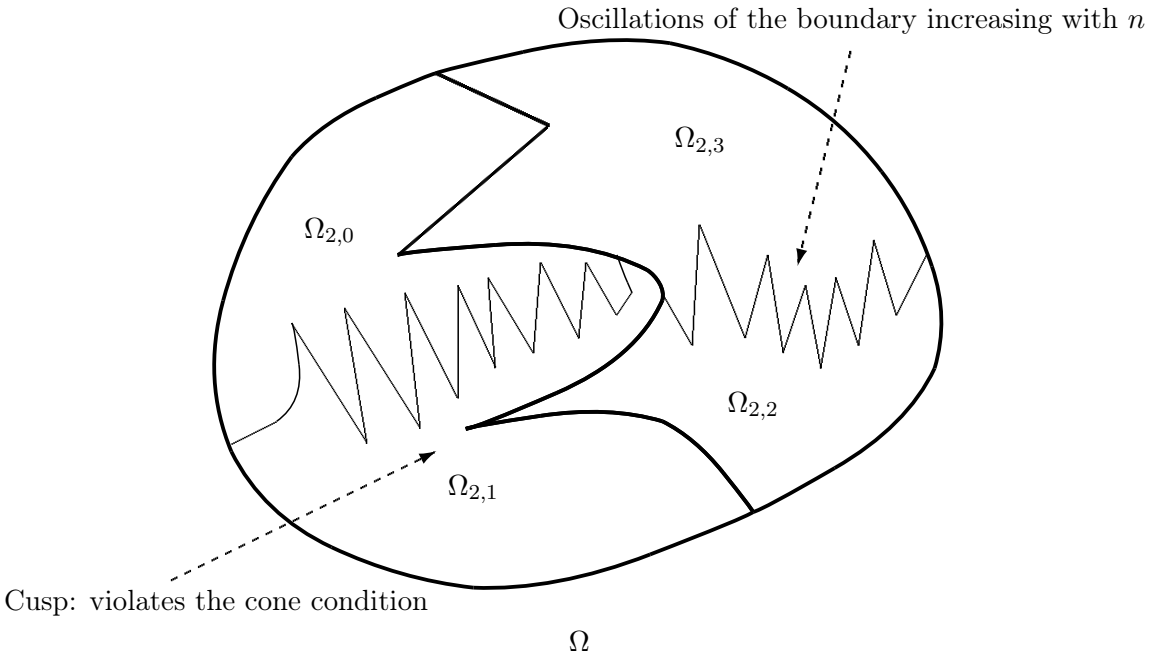

Figure 2.1 – Example of the first two divisions of a non–approximable multi–scale decomposition.

Remark 2.1.8. *Figure 2.1 shows an example of decomposition that is not approximable. In particular, we want to avoid arbitrarily acute peaks and oscillations of the curves (in 2D) or surfaces (in 3D) dividing the subdomains.*

We can now describe completely the interaction of the parenchyma and the bronchial tree in the limit $\varepsilon \to 0$ by a multi–scale decomposition of the domain. However, for a given $\varepsilon > 0$, the dyadic tree $\mathcal{T}_\varepsilon$ and the number of alveoli are finite. Recall that we denote by $\mathcal{I}_\varepsilon$ the set of indexes of internal nodes and $\mathcal{E}_\varepsilon$ the set of terminal nodes of $\mathcal{T}_\varepsilon$. We obtain a sequence, indexed by ε, of *finite* multi–scale decompositions $\mathcal{O}^\varepsilon$ which we define as follows:

Definition 2.1.9. *We say that* $\mathcal{O}^\varepsilon = \left(\Omega^\varepsilon_{n,k}\right)_{(n,k)\in\mathcal{I}_\varepsilon\cup\mathcal{E}_\varepsilon}$ *is a* finite *multi–scale decomposition of* Ω *associated with the finite dyadic tree* $\mathcal{T}_\varepsilon$ *if:*

1. $\Omega^\varepsilon_{0,0} = \Omega$,
2. $\Omega^\varepsilon_{n,j} \cap \Omega^\varepsilon_{n,k} = \emptyset$ *as soon as* (n,j) *and* (n,k) *belong in* $\mathcal{I}_\varepsilon \cup \mathcal{E}_\varepsilon$ *and* $j \neq k$,
3. $\overline{\Omega^\varepsilon}_{n+1,2k} \cup \overline{\Omega^\varepsilon}_{n+1,2k+1} = \overline{\Omega^\varepsilon}_{n,k}$ *if* $(n,k) \in \mathcal{I}_\varepsilon$.

Remark 2.1.10. *Note that if all vertices of a given generation* n *of* $\mathcal{T}$ *belong to* $\mathcal{T}_\varepsilon$*, then we have, as a consequence of items 1. and 3. the same condition as in the infinite multi–scale decomposition definition:*

$$\bigcup_{k=0}^{2^n-1} \overline{\Omega^\varepsilon_{n,k}} = \overline{\Omega}.$$

However, this is not necessarily true for all generations since the tree $\mathcal{T}_\varepsilon$ *may a priori branch asymmetrically.*

Let us investigate now what are the conditions on the structure of a finite decomposition $\mathcal{O}^\varepsilon$ which will allow us to connect the tree to the domain as in Section 1.1.1. For a given $\varepsilon > 0$, the cell located on a terminal node indexed by $(n,k) \in \mathcal{E}_\varepsilon$ must coincide spatially with a periodic cell identified by (1.5):

$$\mathcal{Y}^{n,k}_\varepsilon = \mathcal{Y}^{\mathbf{k}}_\varepsilon \quad \text{where } (n,k) = \omega_\varepsilon(\mathbf{k}) \in \mathcal{E}_\varepsilon \text{ for } \mathbf{k} \in \mathbf{Z}^\Omega_\varepsilon.$$

As a consequence, we can identify the cell $\mathcal{Y}^{n,k}_\varepsilon$ with $\Omega^\varepsilon_{n,k}$ (except maybe along the boundary of Ω: see Section 2.3.) The boundary of the elements of the finite multi–scale decomposition $\mathcal{O}^\varepsilon$ must follow the lines drawn by the periodic array $\mathbf{Z}^\Omega_\varepsilon$, which is characterized by the step $\varepsilon > 0$. This description guides our two constructions.

- In the first case, we start with a space–filling tree in a square domain and a square periodic cell. This allows us to build recursively a multi–scale domain decomposition $\mathcal{O}$ along the lines of the periodic square grids of size 2^{-n}, $n \geq 0$. We follow this structure by taking the micro–scale parameter to be $\varepsilon = 2^{-n}$, for all $n \geq 0$. Then, the subdomains of the finite decompositions $\mathcal{O}^\varepsilon$ coincide exactly with their counterparts in an infinite multi–scale decomposition $\mathcal{O}$. This approach extends to our multi–dimensional setting the results obtained in [GMM06] and allows us to keep a relatively simple setting with few parameters.
- In the second case, we use the convergence of the grid step ε to 0 to approximate a given arbitrary multi–scale decomposition $\mathcal{O}$ by well–chosen finite multi–scale decompositions $\mathcal{O}^\varepsilon$, given a set of suitable regularity conditions. This allows us to deal with domains and periodic arrays of any shape, but adds another layer of approximation (between $\mathcal{O}$ and $\mathcal{O}^\varepsilon$) to the model.

2.2 Letting a square breathe

2.2.1 Geometry

We consider a domain $\Omega = (0,1)^d$, $d = 2$ or 3, and a square lattice $\mathbf{Z} = \mathbb{Z}^d$ associated with the unit periodic cell $\mathcal{Y} = (0,1)^d$. Clearly, for any integer $n \geq 0$, the domain Ω can be tiled by 2^{dn}

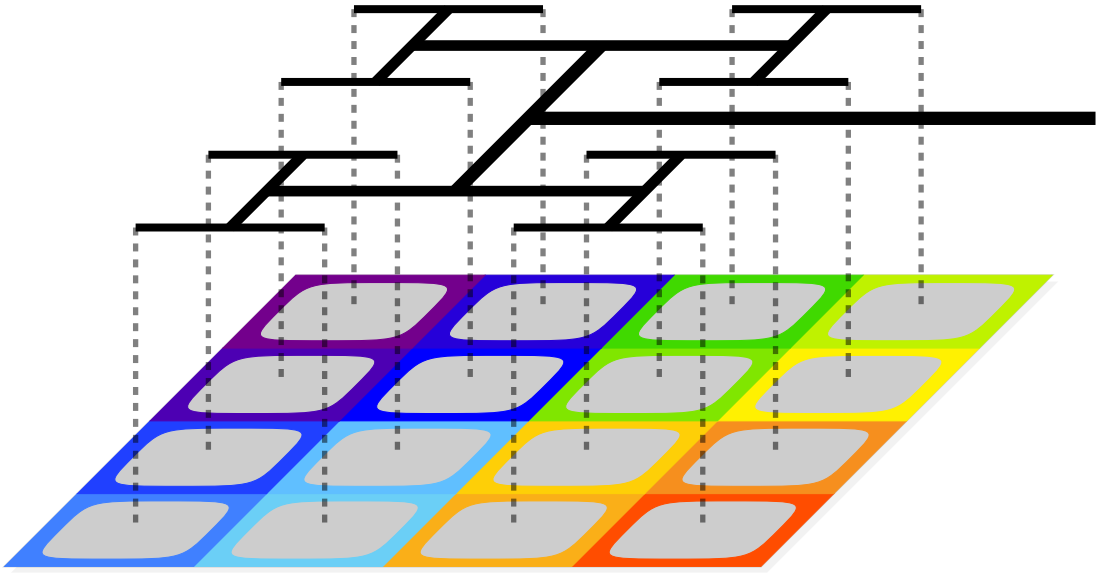

Figure 2.2 – Perforated square domain Ω_n connected by a H–tree, for $n = 2$

translated versions of the unit cell $\mathcal{Y}$ rescaled by a factor 2^{-n}. To organize these cells in a multi–scale decomposition, we suppose that we are given a bifurcating space–filling tree in the square which is a geometrical representation of a dyadic resistive tree $\mathcal{T}$.

Space–filling trees Space-filling bifurcating trees are geometrical objects, which can be constructed by recursion, whose canopy (the branch tips) becomes dense in Ω, see e.g. the H–tree depicted in Figure 2.3 or the numerous examples in [Man82]. To comply with the periodic geometry, we propose the following construction for a square, which can be readily extended to the cube.

One starts with a "trunk", a segment joining a point located on the border of the square Ω, for example $(0, 1/2)$, to the center of Ω at $(1/2, 1/2)$ which is a fertile "bud". This bud then generates two branches, on which only two terminal buds are fertile. These buds again generate each two branches, on which one has now four terminal buds which are located at the centers of the four squares paving Ω. One can then repeat the process for each little square, and so on ad infinitum.

By construction, the buds obtained after an even number $2n$ of bifurcations are located at the center of the square cells $\mathcal{Y}_\varepsilon^{\mathbf{k}}$ for $\varepsilon = 2^{-n}$ (or a number $3n$ of bifurcations for the three–dimensional cubes). Clearly every point in the square is obtained as the limit of a sequence of branch tips, which is why we call such trees "space–filling". Note that the branches of the tree are bounded in length, but become infinite in number.

Remark 2.2.1. *This approach is natural considering the lungs since the bronchial tree is itself a space–filling tree (see e.g. [Wei63]).*

Building the multi–scale decomposition The next step is to use the space–filling tree to build a multi–scale decomposition $\mathcal{O}$ of the square Ω such that for each $n \geq 0$, the subdomains $\Omega_{dn,k}$ coincide with a rescaled periodic cell. To do this, we simply associate each bud of the tree obtained after dn bifurcations and the unique cell $\mathcal{Y}_\varepsilon^{\mathbf{k}}$ with $\varepsilon = 2^{-n}$ located by construction around this bud. Then, using the correspondance between the space–filling tree and the abstract dyadic tree $\mathcal{T}$, we create a one–to–one mapping, noted ω_n, between the cells $\mathcal{Y}_\varepsilon^{\mathbf{k}}$ indexed by $\mathbf{k}$ in $\mathbf{Z}_\varepsilon^\Omega$ for $\varepsilon = 2^{-n}$, and the nodes $X_{dn,k}$, indexed by k in $0 \leq k \leq 2^{dn} - 1$. This allows us to define the subdomains of

generation dn of $\mathcal{O}$ as:

$$\Omega_{dn,k} = \mathcal{Y}_\varepsilon^{\mathbf{k}} \text{ for } k = \omega_n(\mathbf{k}), \text{ for } \mathbf{k} \in \mathbf{Z}_\varepsilon^\Omega, \text{ with } \varepsilon = 2^{-n}. \tag{2.6}$$

Subdomains belonging in an intermediate generation, e.g. m with $dn < m < d(n+1)$ for $n \geq 0$, are then defined by recurrence by the relation

$$\Omega_{m,k} = \text{Interior}\left(\overline{\Omega_{m+1,2k}} \cup \overline{\Omega_{m+1,2k+1}}\right)$$

Clearly, this defines a multi–scale decomposition $\mathcal{O}$ which is automatically both balanced and regular thanks to (2.6).

Remark 2.2.2. *Reciprocally, we can obtain a space–filling tree from a given multi–scale decomposition by joining the barycenters of each cell $\Omega_{n,k}$ to the barycenters of its children $\Omega_{n+1,2k}$ and $\Omega_{n+1,2k+1}$.*

Remark 2.2.3. *To advance one step in the recursive decomposition of the domain by the periodic cells $\mathcal{Y}_\varepsilon^{\mathbf{k}}$, from $\varepsilon = 2^{-n}$ to $\varepsilon = 2^{-(n+1)}$, we need to advance a further d generations in the dyadic decomposition, where d is the dimension, since a square is paved by $4 = 2^2$ squares with half the side length, and a cube by $8 = 2^3$ cubes. Hence it is the generation number n times d of the multi–scale dyadic decomposition which corresponds to cells of size 2^{-n}, and not the n–th generation. The shapes of the subdomains belonging to the intermediate generations are not specified by (2.6): they are rectangles in 2D, formed of two squares, or a connected combination of two or four cubes in 3D.*

Remark 2.2.4. *The main idea behind our construction is that there exists a* recursive *periodic tiling of Ω by the cells $\mathcal{Y}$. For simplicity of exposition, we limit ourselves here to squares and cubes, but such self–replicating cells $\mathcal{Y}$, called rep–tiles (for replicating tiles), have been introduced and studied in the litterature of recreational mathematics, see e.g. [Sol64], as well as fractals, see e.g. [Man82].*

Note that parallelograms are clearly also possible rep–tiles, but hexagons are not. In fact, we could find a rep–tile satisfying more exotic symmetry properties, but such cells are often extremely irregular fractal sets (see [Ban91]). For example, the Gosper flake obeys the hexagonal rotational symmetry and can be covered by 7 versions of itself. However, this does not seem to be a good model for the alveoli, which have relatively smooth walls.

Another point of view: space–filling curves The ordering of the cells described by ω_n is not uniquely associated with the tree: one could flip the order of the two children of any node without changing the tree. Instead, the notion of order suggests a one–dimensional parameterization, i.e. a curve which visits every cell in a linear order. This is why it is also interesting to consider an equivalent construction using a space–filling curve, which should also be constructed recursively and is associated to the same multi–scale decomposition. The duality relation between space–filling curves and space–filling trees has been explored for example in [Man82]. An example of such a tree–curve dual pair is the H–tree associated with the Lebesgue Z-curve, see Figures 2.3 and 2.4.

Remark 2.2.5. *Examples of fractal space–filling continuous curves, called Peano curves, have been first studied by Peano [Pea90] and a number of examples and applications can be found in Chapter 7 of [Man82].*

Remark 2.2.6. *Reciprocally, we can construct a space–filling curve by using the familly of bijections ω_n as follows: let $\widetilde{\omega_n}$ be the function*

$$\widetilde{\omega_n} : \begin{cases} [0,1] \to \Omega, \\ h \mapsto 2^{-n}\left(s\omega_n^{-1}(k) + (1-s)\omega_n^{-1}(k+1) + \frac{1}{2}\mathbf{1}\right) \quad \textit{when } h = \frac{k+s}{2^{dn}-1} \textit{ with } s \in [0,1]\,, \end{cases} \tag{2.7}$$

where $\mathbf{1}$ *is the vector of coordinates* $(1, \ldots, 1)$. *Clearly,* $\widetilde{\omega_n}$ *is a continuous function from* $[0,1]$ *into* Ω *visiting all the cells of the decomposition* $(\Omega_{dn,k})$, *since by construction* $\widetilde{\omega_n}(h)$ *is the center of the cell* $\Omega_{n,k}$, *for each* $h = \frac{k}{2^{dn}-1}$. *Now* $\bigcup_{n\geq 0} 2^{-n}\left(\frac{1}{2}\mathbf{1} + \mathbf{Z}_n^\Omega\right)$ *is dense in* Ω, *hence as* n *goes to infinity the curve* $\widetilde{\omega_n}$ *tends to fill the whole domain* Ω.

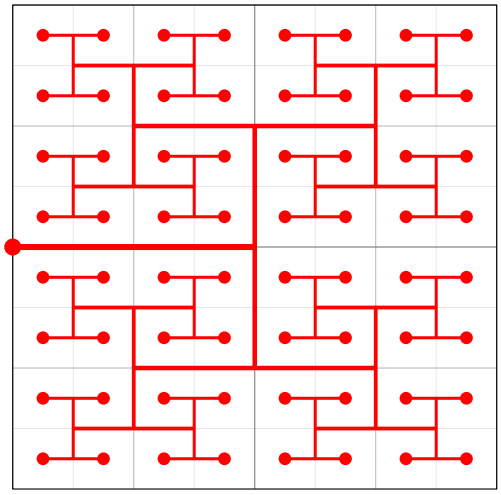

Figure 2.3 – The H–tree (3rd iteration)

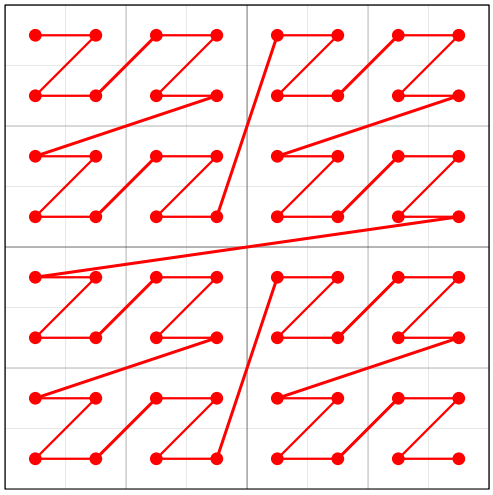

Figure 2.4 – The Lebesgue curve (3rd iteration)

Associated finite multi–scale decomposition In order for the perforated domains Ω_ε and the finite multi–scale decompositions $\mathcal{O}^\varepsilon$ to coincide exactly with the recursive tiling of the domain Ω, we choose in this Section that the micro–scale parameter $\varepsilon > 0$ takes only the values 2^{-n} for n a positive integer. By truncating the multi–scale decomposition $\mathcal{O}$ after dn generations, we then define a finite multi–scale decomposition $\mathcal{O}^\varepsilon$ with $\varepsilon = 2^{-n}$, and the mapping ω_n introduced in (2.6) is naturally equivalent to the one–to–one mapping ω_ε introduced in (1.4) and used in Chapter 1 by setting

$$\omega_\varepsilon : \mathbf{k} \mapsto (dn, \omega_n(\mathbf{k})) \qquad \text{for } \varepsilon = 2^{-n}, \quad n \geq 0.$$

For simplicity, we will now parameterize in this Section the perforated domain by n instead of ε. The characteristic length of the micro–scale, the set of the terminal nodes of the dyadic tree $\mathcal{T}_\varepsilon$ and $\mathbf{Z}_\varepsilon^\Omega$ are related to n by the relations:

$$\varepsilon = 2^{-n}, \qquad \mathcal{E}_\varepsilon \equiv \mathcal{E}_n = \{(dn, k) \mid 0 \leq k \leq 2^{dn} - 1\},$$
$$\mathbf{Z}_\varepsilon^\Omega \equiv \mathbf{Z}_n^\Omega = \left\{ \frac{j}{2^n} \mid 0 \leq j \leq 2^n - 1 \right\}^d.$$

Note that $\mathcal{T}_\varepsilon \equiv \mathcal{T}_n$ is now a dyadic tree with dn full generations, and we can check that $\mathcal{E}_\varepsilon$ and $\mathbf{Z}_\varepsilon^\Omega$ have the same number of elements, which was assumed in Chapter 1.

2.2.2 Convergence of the resistance operators and geometric resistive trees

We now turn our attention to the resistance operator $\mathcal{R}_n$. We introduce a sequence of resistances $(r_{n,k})_{n\geq 0, k=0,\ldots,2^n-1} \subset \mathbb{R}_+^*$ and, as in Chapter 1, we associate these resistances with the edges of the dyadic trees $\mathcal{T}_n$ and $\mathcal{T}$, which will now be referred to as *resistive dyadic trees*. Using the notations of Section 1.1.5, $\mathcal{R}_n$ is defined as a kernel operator in $\mathcal{L}(L^2(\Omega))$ by (1.20), so that for any $q \in L^2(\Omega)$:

$$\mathcal{R}_n q : \mathbf{x}_1 \mapsto \int_\Omega K_n(\mathbf{x}_1, \mathbf{x}_2) q(\mathbf{x}_2) \mathrm{d}\mathbf{x}_2,$$

Note that the kernel K_n is defined by the resistances of the tree $\mathcal{T}$ and the multi–scale decomposition $\mathcal{O}$ (see [GMM06]):

$$K_n(\mathbf{x}_1, \mathbf{x}_2) = \sum_{N=0}^{dn} \sum_{k=0}^{2^N-1} r_{N,k} \chi_N^k(\mathbf{x}_1) \chi_N^k(\mathbf{x}_2), \qquad \text{for } \mathbf{x}_1,\ \mathbf{x}_2 \text{ in } \Omega, \tag{2.8}$$

where χ_N^k is the characteristic function of the cell $\Omega_{N,k}$. We also define the kernel K associated with the infinite resistive tree $\mathcal{T}$ and the dyadic multi–scale decomposition $\mathcal{O}$ as

$$K(\mathbf{x}_1, \mathbf{x}_2) = \begin{cases} \sum_{N=0}^{+\infty} \sum_{k=0}^{2^N-1} r_{N,k} \chi_N^k(\mathbf{x}_1) \chi_N^k(\mathbf{x}_2) & \text{if} \mathbf{x}_1 \neq \mathbf{x}_2, \\ 0 & \text{else.} \end{cases} \tag{2.9}$$

Note that the sum in (2.9) is in fact finite since $\mathbf{x}_1$ and $\mathbf{x}_2$ eventually belong to different cells of the multi–scale decomposition. It is then straightforward to extend to the multi–dimensional setting Theorem 1.7 in [GMM06]:

Proposition 2.2.7. *The kernel K_n converges pointwise to the measurable function K. The convergence is strong in $L^1(\Omega \times \Omega)$ if and only if $\sum_{N\geq 0} \sum_{k=0}^{2^N-1} \frac{r_{N,k}}{2^{2N}} < \infty$. Moreover, under the sufficient condition*

$$\sum_{N\geq 0} \frac{\max_k r_{N,k}}{2^N} < \infty, \tag{2.10}$$

we get the following results:

- *K_n converges to K in $L^\infty(\Omega, L^1(\Omega))$,*
- *$\mathcal{R}_n$ converges to an operator $\mathcal{R}$ in $\mathcal{L}(L^2(\Omega), L^2(\Omega))$ which is also an integral operator with associated kernel K.*

Proof. We refer the reader to [GMM06] for the proof. The key point is that $(K_n(\mathbf{x}_1, \mathbf{x}_2))_{n\geq 0}$ is positive, increasing, and becomes a stationary sequence as soon as $n \geq -\log_2(C\|\mathbf{x}_1 - \mathbf{x}_2\|)$ thanks to the regularity of the domain decomposition (2.2). □

Remark 2.2.8. *Note that strong convergence of K_n in L^1 is not enough to obtain the convergence of the operators $\mathcal{R}_n$. Because the convergence of $\mathcal{R}_n$ depends on an argument in L^∞, it relies strongly upon the fact that the finite multi–scale decomposition associated with K_n is a subset of the limit multi–scale decomposition $\mathcal{O}$.*

We consider now the case where the resistances of the tree are regular and follow a geometric law. In this case, we can write explicitly the eigenvectors and the eigenvalues of the operators $\mathcal{R}_n$ and $\mathcal{R}$.

Definition 2.2.9. *A resistive dyadic tree is called* regular *if all resistances associated with branches located at a common generation of the tree have a common value, i.e. there exists a sequence $(r_n)_{n\geq 0}$ with $r_n > 0$ such that:*

$$r_{n,k} = r_n, \qquad \text{for all } n \geq 0, \quad k \in \{0, \cdots, 2^n - 1\}.$$

A regular resistive dyadic tree is called geometric *if there exists a real constant $\alpha > 0$ such that:*

$$r_n = r_0 \alpha^n \qquad \text{for all } n \geq 0.$$

Remark 2.2.10. *The condition (2.10) implies that the equivalent resistances of the subtrees of $\mathcal{T}$ are uniformly bounded. The asymptotic properties of the resistive dyadic trees and their imbedding in a domain of $\mathbb{R}^d$ have been studied in depth in [VSM09, Van09]. In particular, when the dyadic resistive tree $\mathcal{T}$ is geometric, regular and has a finite equivalent resistance, $\mathcal{R}(L^2(\Omega)) \subset H^s(\Omega)$ for some $s < 1/2$, see also [GMM06].*

Let us assume that $\mathcal{T}$ is geometric with $0 < \alpha < 2$ so that the resistances of the tree satisfy (2.10). Then, $\mathcal{R}$ is well defined as a linear operator from $L^2(\Omega)$ into itself by its kernel K defined by (2.9). Moreover, we know that $\mathcal{R}$ is compact, symmetric and positive. Hence, by Fredholm theory, $L^2(\Omega)$ admits an orthonormal basis of eigenvectors of $\mathcal{R}$, which has a natural interpretation as the Haar basis associated with the dyadic decomposition $\mathcal{O}$:

Proposition 2.2.11. *Let $(\Omega_{n,k})$ be a balanced regular multi–scale decomposition of Ω. Then, the following family of functions $\{\psi_0, (\psi_{n,k})_{N\in\mathbb{N}, 0\le k\le 2^N-1}\} \subset L^2(\Omega)$ is an orthonormal Hilbert basis for $L^2(\Omega)$:*

$$\psi_0(x) := |\Omega|^{-1/2} = 1, \qquad \text{and} \qquad \psi_{n,k}(x) := \begin{cases} 2^{-n/2} & \text{if } x \in \Omega_{n+1,2k}, \\ -2^{-n/2} & \text{if } x \in \Omega_{n+1,2k+1}, \\ 0 & \text{else.} \end{cases}$$

The family $\{\psi_0, (\psi_{n,k})_{n,k}\}$ is the Haar basis associated with the multi–scale decomposition $\mathcal{O}$. If the dyadic resistive tree $\mathcal{T}$ is geometric for some parameter $0 < \alpha < 2$, each base function is an eigenfunction for the operator $\mathcal{R}$, such that

$$\mathcal{R}\psi_0 = \lambda^0\psi_0 \text{ and } \mathcal{R}\psi_{n,k} = \lambda_n\psi_{n,k},$$

with

$$\lambda^0 = \sum_{m=0}^{\infty} \frac{r_m}{2^m} = \frac{r_0}{1-\alpha/2} \text{ and } \lambda_n = \sum_{m=n+1}^{\infty} \frac{r_m}{2^m} = \lambda^0 \left(\frac{\alpha}{2}\right)^{n+1}.$$

In addition, the rate of convergence $\mathcal{R}_n \to \mathcal{R}$ is also geometric:

$$\|\mathcal{R} - \mathcal{R}_n\|_{\mathcal{L}(L^2(\Omega))} = \lambda_{dn} = \lambda^0 \left(\frac{\alpha}{2}\right)^{dn+1}.$$

We refer to [GMM06], Proposition 1.11 for a proof which extends readily to our framework.

Remark 2.2.12. *This decomposition brings to light the physical meaning of the eigenmodes and relaxation times introduced in Remark 1.2.21, by analogy with electrical networks. If we consider only the pressure evolution equation in our homogenized material in the compressible case (1.81b), we obtain:*

$$\tau_{hom}\lambda_m \frac{\mathrm{d}\pi_m}{\mathrm{d}t} + \pi_m = \lambda_m P_m, \qquad \forall m \ge 0,$$

where the coefficients P_m are the coefficients on the Haar basis of a forcing term coupling the fluid pressure to the displacement of the material. This is similar to a RC electrical circuit, and we identify naturally λ_m with the resistance associated to a particular mode and the coefficient τ_{hom} with the capacity of the material to store energy related to compression. Hence, it makes sense that the relaxation coefficient τ_{hom} goes to zero in the incompressible case. Moreover, $\tau_{hom}\lambda_m$ is the characteristic relaxation time constant for the mode π_m.

Remark 2.2.13. *We can also estimate the rate of convergence relative to the characteristic size of the micro–scale $\varepsilon = 2^{-n}$. Then we have*

$$\|\mathcal{R} - \mathcal{R}_n\|_{\mathcal{L}(L^2(\Omega))} = \lambda_{dn} = \frac{\alpha\lambda_0}{2}\varepsilon^q \quad \text{with } q = d\left(1 - \frac{\ln(\alpha)}{\ln(2)}\right).$$

2.3 An algorithmic approach

We present here an approach which offers the possibility of tackling a variety of reasonable geometries beyond the simple square or cube. In general, it is not possible to match exactly the multi–scale domain decomposition describing the perfusion of the parenchyma by the bronchial tree and the periodic grid for any given micro–scale parameter ε. Clearly, this calls for a more flexible approach than the perfectly symmetric construction described in Section 2.2. The idea is to proceed by approximations defined algorithmically for any $\varepsilon > 0$.

Note that this will come at a trade–off: if the multi–scale decomposition is not balanced or the resistive tree isn't regular, the Haar basis does not diagonalize $\mathcal{R}$ any more. Moreover, there is potentially a loss of regularity for the set of pressures [VSM09].

2.3.1 Geometry: approximation of a multi–scale decomposition

Let us go back to an arbitrary geometric setting as presented in Section 2.1, so that the domain and its multi–scale decomposition do not necessarily follow the lines of a recursive periodic tiling. In particular, any periodic cell can be used, for example hexagons in 2D as in Figure 2.5 or the truncated octahedron in 3D which are well–established shapes employed for modeling the alveoli (see e.g. [Fun88]). Without loss of generality, we suppose that $|\Omega| = 1$. We also suppose that we are given a multi–scale decomposition $\mathcal{O}$, not necessarily balanced, which is *approximable* in the sense of Definition 2.1.6.

Remark 2.3.1. *Note that we suppose that we already know the limit decomposition $\mathcal{O}$. While exact anatomical data does not exist for the full tree [PSP+96], there exists a number of algorithms that have been developed to model the growth of the airways inside a constrained volume, see e.g. [KTS99, TPH00] and the references therein. We are in particular interested in a branching model of the airways based on the generation of a fine uniform grid.*

Let $\varepsilon > 0$ be a small parameter. We are going to approximate the multi–scale decomposition $\mathcal{O}$ by a finite multi–scale decomposition $\mathcal{O}^\varepsilon$ which follows the lines of the grid associated with the periodic array $\mathbf{Z}^\Omega_\varepsilon$ (see Figure 2.5). The difficulty is that, by definition, $\mathcal{O}$ is not associated with a particular scale. For a small ε we will be able to approximate very well the first generations of subdomains. However, there is no reason that the small domains $\Omega_{n,k}$ which have a volume close to ε^d fit on the periodic grid, as was the case in Section 2.2. We propose the following algorithm to build the finite tree $\mathcal{T}_\varepsilon$ and $\mathcal{O}^\varepsilon$ recursively:

Algorithm for building an approximative multi–scale decomposition.
We start with a domain Ω, an approximable multi–scale decomposition $\mathcal{O}$ and an array $\mathcal{G}_\varepsilon$ of points located at the barycenter of the alveoli:

$$\mathcal{G}^\varepsilon = \left\{ \varepsilon \left(\mathbf{k} + \mathbf{c}_\mathcal{Y} \right) \ | \ \mathbf{k} \in \mathbf{Z}^\Omega_\varepsilon \right\},$$

where $\mathbf{c}_\mathcal{Y}$ is the barycenter of the periodic cell $\mathcal{Y}$. We suppose that ε is small enough that $\mathcal{G}^\varepsilon$ is not empty. We build a "multi–scale decomposition" of the discrete set $\mathcal{G}^\varepsilon$, and then of Ω, as follows (see Figure 2.6 for a graphical example):

1. Initialize the process by giving a "trunk" to the tree $\mathcal{T}_\varepsilon$ we are building as the root node noted X_0 connected to the node $X_{0,0}$. We associate the whole set of points $\mathcal{G}^\varepsilon \subset \Omega$ to the node $X_{0,0}$.
2. Suppose that $\mathcal{G}^\varepsilon$ contains at least two points. Following the multi–scale decomposition $\mathcal{O}$, we divide Ω in its two subdomains $\Omega_{1,0}$ and $\Omega_{1,1}$. We know that $\overline{\Omega}_{1,0} \cup \overline{\Omega}_{1,1} = \overline{\Omega}$. This enables us to divide $\mathcal{G}^\varepsilon$ in two sets of points defined as:

$$\mathcal{G}^\varepsilon_{1,0} = \mathcal{G}^\varepsilon \cap \overline{\Omega}_{1,0}, \quad \mathcal{G}^\varepsilon_{1,1} = \mathcal{G}^\varepsilon \cap \overline{\Omega}_{1,1} \setminus \overline{\Omega}_{1,0}. \tag{2.11}$$

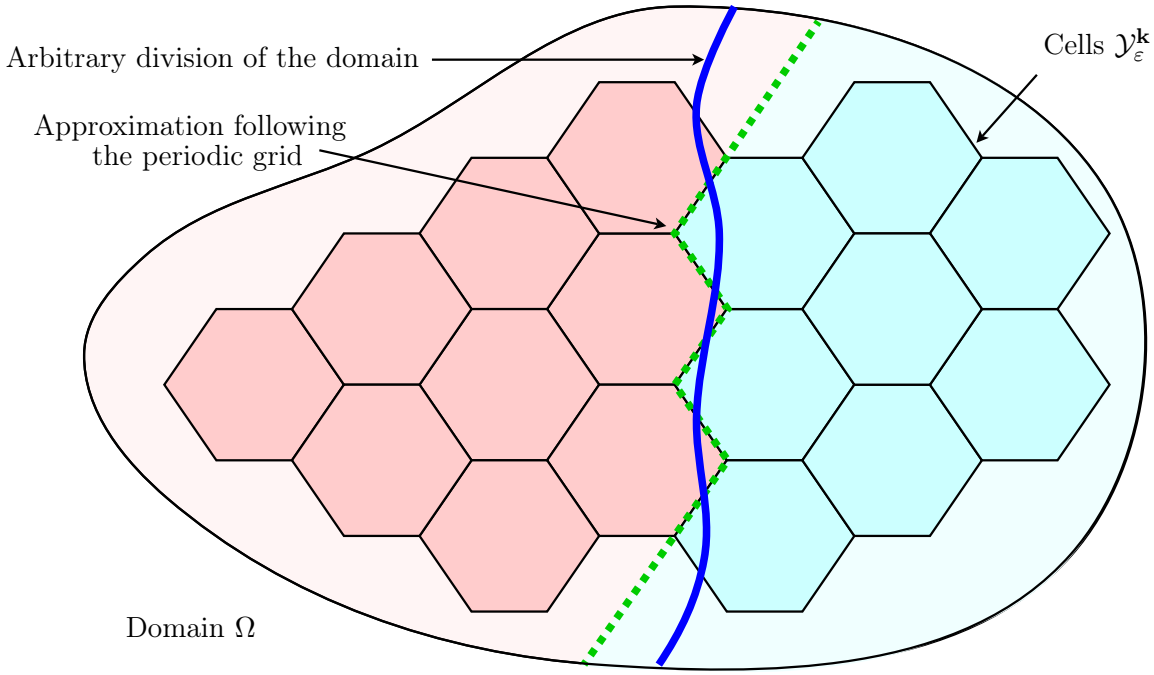

Figure 2.5 – Example: first division of an arbitrary multiscale decomposition approximated on an hexagonal grid

In order for the process to work correctly, we need to amend this rule as follows.

- If the set $\mathcal{G}_{1,0}^\varepsilon$ thus defined is empty, we add to it the closest point, noted $\mathbf{c}_\varepsilon^{1,0}$, in $\mathcal{G}_{1,1}^\varepsilon$. Formally, we modify $\mathcal{G}_{1,0}^\varepsilon$ and $\mathcal{G}_{1,1}^\varepsilon$ as follows:

$$\mathcal{G}_{1,0}^\varepsilon \leftarrow \{\mathbf{c}_\varepsilon^{1,0}\}, \quad \mathcal{G}_{1,1}^\varepsilon \leftarrow \mathcal{G}_{1,1}^\varepsilon \setminus \{\mathbf{c}_\varepsilon^{1,0}\}. \tag{2.12}$$

  Note that $\mathcal{G}_{1,1}^\varepsilon$ still contains at least one point, and $\mathcal{G}_{1,0}^\varepsilon$ is then terminal (it contains exactly one point.)

- If $\mathcal{G}_{1,1}^\varepsilon$ is empty, we proceed in the same way and add to it the closest point to $\Omega_{1,1}$ in $\mathcal{G}_{1,0}^\varepsilon$.

Finally, add the nodes $X_{1,0}$ and $X_{1,1}$ to the tree $\mathcal{T}_\varepsilon$, associated respectively with the nonempty sets of points $\mathcal{G}_{1,0}^\varepsilon$ and $\mathcal{G}_{1,1}^\varepsilon$.

3. Iterate this process by visiting the terminal nodes $X_{n,k}$ of the tree $\mathcal{T}_\varepsilon$ we are building: splitting each subdomain $\Omega_{n,k}$ such that $\mathcal{G}_{n,k}^\varepsilon$ has more than two points into $\Omega_{n+1,2k}$ and $\Omega_{n+1,2k+1}$, we divide $\mathcal{G}_{n,k}^\varepsilon$ into $\mathcal{G}_{n+1,2k}^\varepsilon$ and $\mathcal{G}_{n+1,2k+1}^\varepsilon$ and we add the nodes $X_{n+1,2k}$ and $X_{n+1,2k+1}$ to the tree $\mathcal{T}_\varepsilon$. We continue this process until the sets of points associated with the terminal nodes of $\mathcal{T}_\varepsilon$ are all reduced to a single point.

4. The construction of the tree $\mathcal{T}_\varepsilon$ is now finished and we denote by $\mathcal{E}_\varepsilon$ the set of indexes of the terminal nodes of $\mathcal{T}_\varepsilon$, and, for any $(n,k) \in \mathcal{E}_\varepsilon$, by $\mathbf{c}_\varepsilon^{n,k}$ the unique element in $\mathcal{G}_{n,k}^\varepsilon$ defined as:

$$\mathcal{G}_{n,k}^\varepsilon = \{\mathbf{c}_\varepsilon^{n,k}\} \qquad \forall (n,k) \in \mathcal{E}_\varepsilon. \tag{2.13}$$

Define the periodic cells by:

$$\mathcal{Y}_\varepsilon^{n,k} = \mathbf{c}_\varepsilon^{n,k} + \varepsilon\mathcal{Y} \qquad \text{for all } (n,k) \in \mathcal{E}_\varepsilon.$$

A first idea is then to define simply the subdomains of the decomposition $\Omega^\varepsilon_{n,k}$ as the cells $\mathcal{Y}^{n,k}_\varepsilon$. However, this does not work as the cells do not cover the whole of Ω, there is some uncovered space along the boundary. To extend the decomposition up to the boundary of Ω (see as an example (d) in Figure 2.6), we define the approximate subdomains $\Omega^\varepsilon_{n,k}$ located on the terminal nodes of $\mathcal{T}_\varepsilon$ by:

$$\Omega^\varepsilon_{n,k} = \text{Interior}\left(\left\{\mathbf{x}\in\Omega \mid (n,k)\in \underset{(m,j)\in\mathcal{E}_\varepsilon}{\text{argmin}}\ \text{dist}\left(\mathbf{x},\mathcal{Y}^{m,j}_\varepsilon\right)\right\}\right) \quad \text{for all } (n,k)\in\mathcal{E}_\varepsilon. \tag{2.14}$$

Note that we still have $\mathcal{Y}^{n,k}_\varepsilon \subset \Omega^\varepsilon_{n,k}$, and indeed $\mathcal{Y}^{n,k}_\varepsilon$ is equal to $\Omega^\varepsilon_{n,k}$ everywhere inside the domain where every cell is completely surrounded by other cells.

5. Finally, define recursively the domains $\Omega^\varepsilon_{n,k}$ for any interior node of $\mathcal{T}_\varepsilon$ by the formula:

$$\Omega^\varepsilon_{n,k} = \text{Interior}\left(\overline{\Omega^\varepsilon}_{n+1,2k}\cup\overline{\Omega^\varepsilon}_{n+1,2k+1}\right). \tag{2.15}$$

Note that the one–to–one mapping $(n,k)\mapsto \mathbf{c}^{n,k}_\varepsilon/\varepsilon - \mathbf{c}_\mathcal{Y}$ we have created between $\mathcal{E}_\varepsilon$ and $\mathbf{Z}^\Omega_\varepsilon$ to connect the tree and the set of alveoli is the inverse of the mapping ω_ε introduced in (1.4) and used in Chapter 1.

Remark 2.3.2. *Let us further explain the need for the complicated formula (2.14). The definition of $\mathbf{Z}^\Omega_\varepsilon$ (1.1) eliminates the cells that intersect the boundary, which means that some points in Ω along the boundary do not belong in any cell $\mathcal{Y}^{n,k}_\varepsilon$ for $(n,k)\in\mathcal{E}_\varepsilon$. However, we need the subdomains $\Omega^\varepsilon_{n,k}$ to cover the whole domain. The definition (2.14) describes a Voronoi tesselation process, designed to include these points that are too close to the boundary with the nearest cell $\mathcal{Y}^{n,k}_\varepsilon$ into the subdomain $\Omega^\varepsilon_{n,k}$. As a consequence, it ensures that for a given generation n such that $X_{n,k}$, $\bigcup_{k=0,\dots,2^n-1}\Omega^\varepsilon_{n,k}$ covers Ω, which is necessary for $\mathcal{O}^\varepsilon$ to satisfy the conditions (2.1.9) defining a multi–scale decomposition.*

Analysis First, the algorithm is sure to finish. Indeed, define the quantity:

$$M_\varepsilon(n) = \max_{k=\{0,\dots,2^n-1\},\ X_{n,k}\in\mathcal{T}_\varepsilon} \#\mathcal{G}^\varepsilon_{n,k}.$$

The integer $M_\varepsilon(n)$ bounds from above the amount of points that are left in each subdomain after sorting through the subdomains of generation n. Thanks to the additional rule in the second step of the algorithm, we are sure that $1 < M_\varepsilon(n+1) < M_\varepsilon(n)$ as long as the procedure is not complete. Since $M_\varepsilon(0) = \#\mathcal{G}^\varepsilon$ is finite, the algorithm completes the sorting in a finite amount of steps.

When the procedure is complete, we obtain a full finite dyadic tree $\mathcal{T}_\varepsilon$ such that each node $X_{n,k}$ in $\mathcal{T}_\varepsilon$ is associated with a nonempty set of points $\mathcal{G}^\varepsilon_{n,k}\subset\mathcal{G}^\varepsilon$ and a subdomain $\Omega^\varepsilon_{n,k}$. Moreover, the sequence $\left(\mathcal{G}^\varepsilon_{n,k},\ \Omega^\varepsilon_{n,k}\right)_{(n,k)\in\mathcal{I}_\varepsilon\cup\mathcal{E}_\varepsilon}$ has the following properties.

- If there are more than two points in $\mathcal{G}^\varepsilon_{n,k}$, then $X_{n,k}$ is an interior node of $\mathcal{T}_\varepsilon$. We have then the relations:
$$\mathcal{G}^\varepsilon_{n,k}\subset\overline{\Omega_{n,k}}\cap\Omega^\varepsilon_{n,k}, \quad \text{and} \quad \mathcal{G}^\varepsilon_{n,k} = \mathcal{G}^\varepsilon_{n+1,2k}\cup\mathcal{G}^\varepsilon_{n+1,2k+1}.$$
- If $\mathcal{G}^\varepsilon_{n,k}$ contains only one point, then $X_{n,k}$ is a terminal node of $\mathcal{T}_\varepsilon$ and $\Omega^\varepsilon_{n,k}$ is associated to a single cell $\mathcal{Y}^{n,k}_\varepsilon$ defined by (2.14).
- The sequence $\left(\Omega^\varepsilon_{n,k}\right)_{(n,k)\in\mathcal{I}_\varepsilon\cup\mathcal{E}_\varepsilon}$, associated to the dyadic tree $\mathcal{T}_\varepsilon$, satisfies by construction the conditions of Definition 2.1.9. Hence $\mathcal{O}^\varepsilon = \left(\Omega^\varepsilon_{n,k}\right)_{(n,k)\in\mathcal{I}_\varepsilon\cup\mathcal{E}_\varepsilon}$ is a finite multi–scale decomposition.

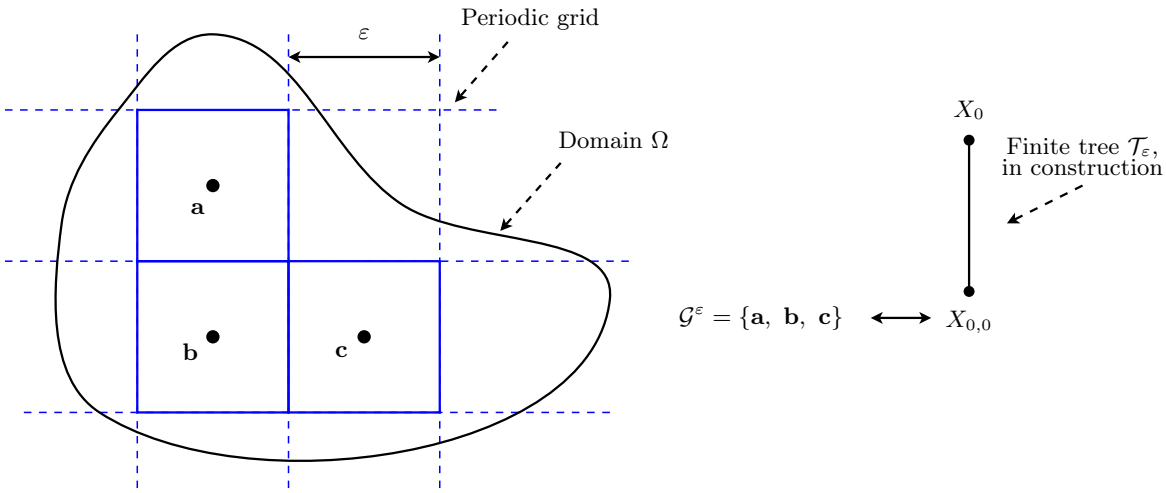

(a) Stage 1: Initialisation: create the array of points $\mathcal{G}^\varepsilon$ and the trunk of the tree $\mathcal{T}_\varepsilon$

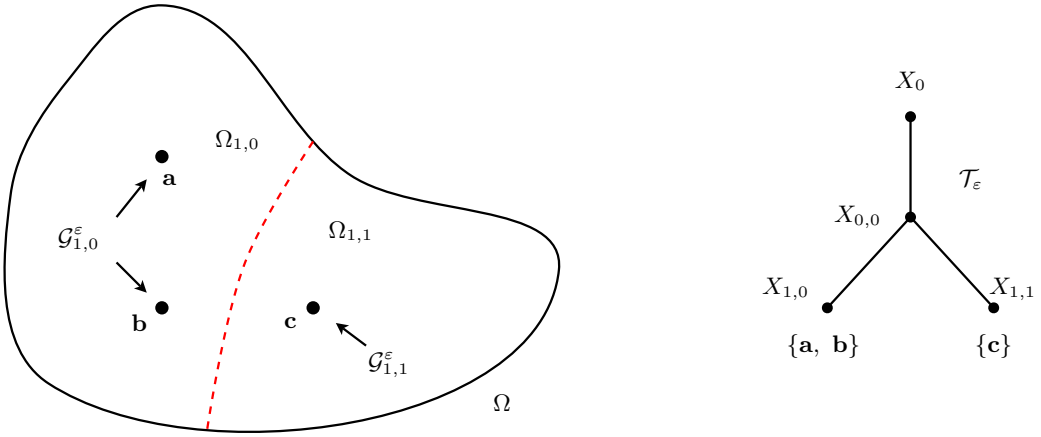

(b) Stage 2: First division: we sort the points of $\mathcal{G}^\varepsilon$ according to their position relative to the interface between $\Omega_{1,0}$ and $\Omega_{1,1}$

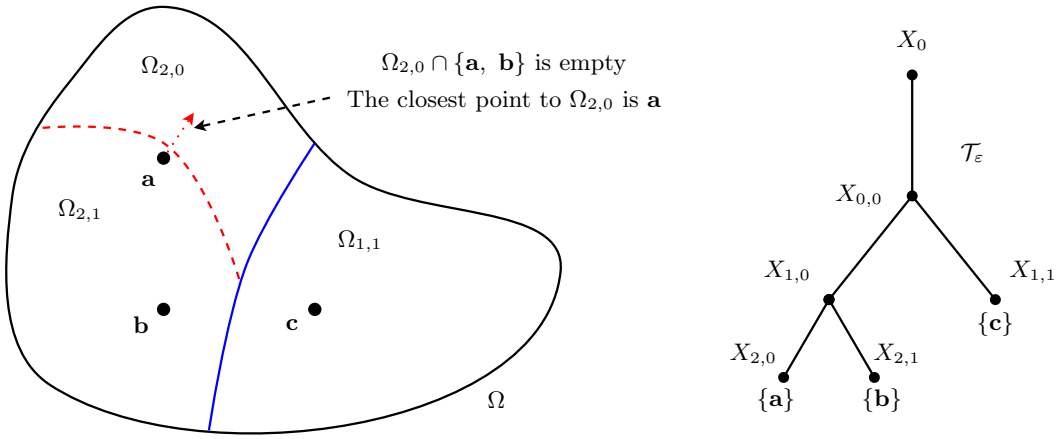

(c) Stage 3: Sort all the points by dichotomy until there is only one per leaf

Figure 2.6 – Algorithmic construction of the approximate multi–scale decomposition

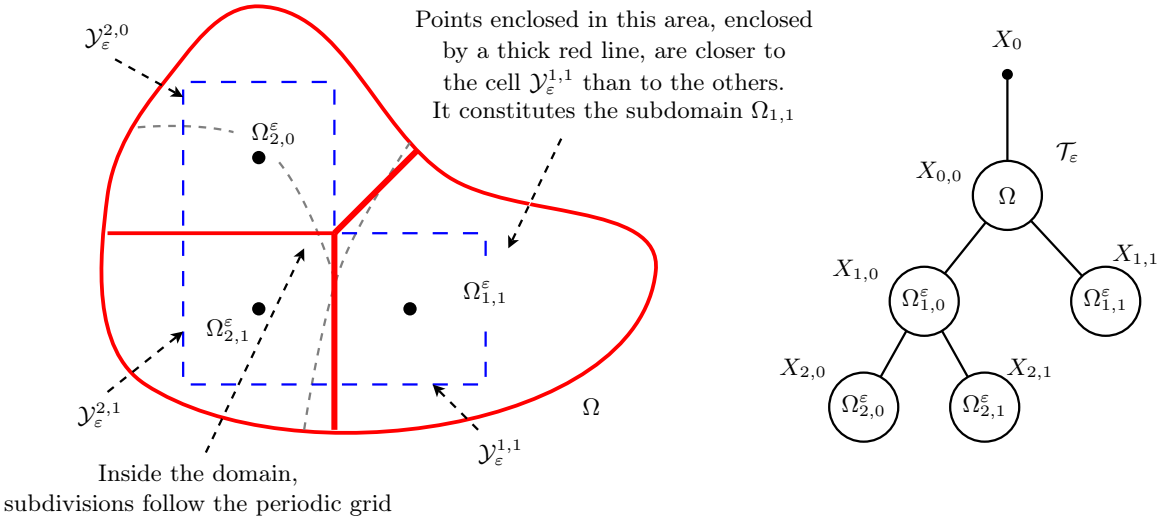

(d) Stage 4 and 5: Construction of the subdomains by Voronoi tesselations

Figure 2.6 – Algorithmic construction of the approximate multi–scale decomposition (cont.)

Moreover, the multi–scale decompositions $\mathcal{O}$ and $\mathcal{O}^\varepsilon$ satisfy the following approximation estimates, which are proved in Annex 2.A for clarity:

Proposition 2.3.3. *Let ε small enough and $\mathcal{O}^\varepsilon$ be the finite multi–scale decomposition of Ω defined by (2.14) and (2.15). Then there exists positive constants C, C_1, $C_2 > 0$ independent of ε such that if $(n,k) \in \mathcal{I}_\varepsilon \cup \mathcal{E}_\varepsilon$ then:*

$$\left|\Omega_{n,k}^\varepsilon \Delta \Omega_{n,k}\right| \leq C\varepsilon \left|\Omega_{n,k}\right|^{\frac{d-1}{d}}, \tag{2.16}$$

and

$$C_1 \left|\Omega_{n,k}\right| \leq \left|\Omega_{n,k}^\varepsilon\right| \leq C_2 \left|\Omega_{n,k}\right|. \tag{2.17}$$

Remark 2.3.4. *The approximation estimate (2.16) shows that we achieve a first–order approximation of the multi–scale decomposition $\mathcal{O}$ with respect to the parameter ε. Since we are using a periodic grid with a fixed step to approximate a Lipschitz domain, this result is reminiscent of the results on regular triangulations: to achieve a second–order approximation, it is well–known that we would need to use curved elements on the boundary of the domain. This effects are especially important here, since we are in a sense approximating boundaries everywhere in Ω. Hence, our result is optimal with respect to the order of convergence.*

2.3.2 Convergence of the resistance operators

We are now in a position to study the convergence of the sequence of resistance operators. As in Section 2.2, we introduce a sequence of resistances $(r_{n,k})_{n\geq 0, k=0,\dots,2^n-1}$ assiociated with the trees $\mathcal{T}_\varepsilon$ and $\mathcal{T}$ which are now resistive dyadic trees. We then define $\mathcal{R}_\varepsilon$ and $\mathcal{R}$ as integral operators associated respectively with the kernels K_ε and K defined pointwise for all $\mathbf{x}_1, \mathbf{x}_2$ in Ω by (see Proposition 1.1.8):

$$K_\varepsilon(\mathbf{x}_1, \mathbf{x}_2) = \sum_{X_{n,k} \in \mathcal{T}_\varepsilon} r_{n,k} \chi_{n,\varepsilon}^k(\mathbf{x}_1) \chi_{n,\varepsilon}^k(\mathbf{x}_2), \tag{2.18}$$

$$K(\mathbf{x}_1, \mathbf{x}_2) = \begin{cases} 0 & \text{if } \mathbf{x}_1 = \mathbf{x}_2, \\ \sum_{n\geq 0} \sum_{k=0}^{2^n-1} r_{n,k} \chi_n^k(\mathbf{x}_1) \chi_n^k(\mathbf{x}_2) & \text{else,} \end{cases} \tag{2.19}$$

where $\chi^k_{n,\varepsilon}$ and χ^k_n are the characteristic functions respectively of $\Omega^\varepsilon_{n,k}$ and $\Omega_{n,k}$. The following Theorem details the convergence of the resistance operators defined by approximation of the multi–scale dyadic domain decomposition $\mathcal{O}_\varepsilon$. This is the main result of this section.

Theorem 2.3.5. *Let $\mathcal{O}$ be an approximable multi–scale decomposition, and $(r_{n,k})$ be a sequence of resistances satisfying the condition:*

$$\sum_{n=0}^{\infty} \max_{0\le k<2^n} \left(|\Omega_{n,k}|\ r_{n,k}\right) < \infty. \tag{2.20}$$

Then, the function K defined by (2.19) belongs to $L^\infty(\Omega, L^1(\Omega))$, and the sequence $(\mathcal{R}_\varepsilon)$ converges in $\mathcal{L}(L^2(\Omega))$ to the integral operator $\mathcal{R}$ associated with the kernel K.

If, in addition, there exists $\alpha \in (0,2)$ and $C_\alpha > 0$ such that for all $n \ge 0$ and $k \in \{0,\dots,2^n-1\}$:

$$|\Omega_{n,k}|\ r_{n,k} \le C_\alpha \left(\frac{\alpha}{2}\right)^n, \tag{2.21}$$

with β as in (2.5) in Definition 2.1.6 then we have the estimate:

$$\|\mathcal{R}_\varepsilon - \mathcal{R}\|_{\mathcal{L}(L^2(\Omega))} \le \begin{cases} C\varepsilon^q & \text{if } \alpha \ne 2\beta^{1/d}, \\ \varepsilon^q |\ln(\varepsilon)| & \text{if } \alpha = 2\beta^{1/d}, \end{cases} \tag{2.22}$$

where $C > 0$ is a constant independent of ε and q is an exponent in $(0, 1/2]$, which can be explicitely written as a function of α and β:

$$q = \begin{cases} \dfrac{d}{2}\left(\dfrac{\ln(2)-\ln(\alpha)}{-\ln(\beta)}\right) & \text{if } \alpha > 2\beta^{1/d}, \\ 1/2 & \text{if } \alpha \le 2\beta^{1/d}. \end{cases}$$

Remark 2.3.6. *The reason for using α in $(0,2)$ in the condition (2.21), instead of $\alpha/2$ which belongs in $(0,1)$, is that this enables us to be consistent with the symmetric case as exposed in Section 2.2 and also with previous papers on the subject, e.g. [GMM06].*

Remark 2.3.7. *The conditions on the resistances (2.20) seem to arise naturally to extend the estimates from the symmetric setup (2.10) to the asymmetric case. Indeed, if the multi–scale decomposition is balanced ($|\Omega_{n,k}| = 2^{-n}$), we recover from (2.20) the condition (2.10).*

Moreover, there is a physiological observation supporting the idea of weighting the resistances of each bronchus by the volume of the subdomain it irrigates: the expression of the resistance of an individual pipe by Poiseuille's law writes

$$r = \frac{8\nu L}{\pi R^4},$$

where ν is the viscosity of the fluid, L is the length of the pipe and R its radius. Hence, the resistances of each airway behaves roughly like the inverse of its volume, since the bronchi exhibit approximately the same length/radius ratio [Wei84]. Now, we expect the asymmetry of the bronchial tree to be correlated to an asymmetry in the induced multi–scale decomposition of the lungs, meaning that bigger bronchi irrigate bigger parts of the lungs. The condition (2.20) translates this into our model, since it means that the resistances on the edges of the tree behave like the inverse of the volume of the corresponding subdomains in the multi–scale decomposition $\mathcal{O}$.

Remark 2.3.8. *The convergence rate deteriorates if the parameter α, which controls the resistances of the tree, grows. If the decomposition is balanced ($\beta = 1/2$), we can relate this behavior to the regularity obtained by Maury, Salort and Vannier for the image of $\mathcal{R}$ (see Theorem 4.11 in [VSM09]). Indeed, their results show that the set of feasible pressures can be identified with a Sobolev fractional space $H^s(\Omega)$ if $s < 1/2$, where $s = \frac{d}{2}\left(1 - \frac{\ln(\alpha)}{\ln(2)}\right)$, and is included in $H^{s'}(\Omega)$ for all $s' < 1/2$ if $s \geq 1/2$. Note that these exponents are precisely the convergence rates we obtain for the resistance operators if $\beta = 1/2$, see (2.22). Hence, the convergence rate we obtain is optimal related to the regularity of the image of $\mathcal{R}$.*

Over the course of the proof of Theorem 2.3.5 we will use the following technical Lemma, which is a well–known result of measure theory (see e.g. [HS78]):

Lemma 2.3.9. *(Schur's Test.)*
Let $G(\mathbf{x}_1, \mathbf{x}_2)$ be a measurable function on $\Omega \times \Omega$ that satisfies the mixed–norm conditions:

$$C_1 = \left\| \int_\Omega |G(\cdot, \mathbf{x}_2)| \mathrm{d}\mathbf{x}_2 \right\|_{L^\infty(\Omega)} < \infty,$$
$$C_2 = \left\| \int_\Omega |G(\mathbf{x}_1, \cdot)| \mathrm{d}\mathbf{x}_1 \right\|_{L^\infty(\Omega)} < \infty.$$

Then we can define an integral operator $\mathcal{G}$ in $\mathcal{L}(L^2(\Omega))$ such that for any $q \in L^2(\Omega)$:

$$\mathcal{G}q : \mathbf{x}_1 \mapsto \int_\Omega G(\mathbf{x}_1, \mathbf{x}_2) q(\mathbf{x}_2) \mathrm{d}\mathbf{x}_2.$$

The operator norm of $\mathcal{G}$ satisfies the estimate:

$$\|\mathcal{G}\|_{\mathcal{L}(L^2(\Omega))} \leq \sqrt{C_1 C_2}. \tag{2.23}$$

Proof of Theorem 2.3.5. We will proceed in three steps. First, we study the kernel function K and we prove that the associated kernel operator $\mathcal{R}$ belongs to $\mathcal{L}(L^2(\Omega))$. Then, we split the difference $\mathcal{R}_\varepsilon - \mathcal{R}$ in three parts and we investigate the convergence of each one separately. Finally, we prove the convergence of $\mathcal{R}_\varepsilon$ and the estimate (2.22). To simplify the notations, we introduce the sequence $(\alpha_n)_{n\geq 0}$ in $\mathbb{R}_+^*$ defined by:

$$\alpha_n = 2^n \max_{0 \leq k < 2^n} \left(|\Omega_{n,k}| r_{n,k} \right). \tag{2.24}$$

Note that if the condition (2.20) is satisfied, $(\alpha_n/2^n)$ is the general term of an absolutely convergent series, and if (2.21) is also satisfied, then this series is dominated by the absolutely convergent series of general term $(\alpha/2)^n$. We will denote by C any constant independent of ε in the computations.

Study of K and existence of $\mathcal{R}$. First, observe that K belongs in $L^1(\Omega \times \Omega)$. Indeed, thanks to the monotone convergence theorem,

$$\iint_\Omega K(\mathbf{x}_1, \mathbf{x}_2) \mathrm{d}\mathbf{x}_1 \mathrm{d}\mathbf{x}_2 \leq \sum_{n=0}^{+\infty} \max\left(|\Omega_{n,k}| r_{n,k} \right) \sum_{k=0}^{2^n - 1} |\Omega_{N,k}| \leq \sum_{n=0}^{+\infty} \frac{\alpha_n}{2^n} < \infty,$$

since by definition of a multi–scale decomposition,

$$\sum_{k=0}^{2^n - 1} |\Omega_{N,k}| = |\Omega| = 1 \quad \forall n \geq 0.$$

Now, we compute the $L^\infty(\Omega, L^1(\Omega))$–norm of K. Let $\mathbf{x}_1$ in Ω. By the monotone convergence theorem, we have naturally from (2.19):

$$\left|\int_\Omega K(\mathbf{x}_1,\mathbf{x}_2)\mathrm{d}\mathbf{x}_2\right| = \left|\sum_{n=0}^{\infty}\sum_{k=0}^{2^n-1} r_{n,k}|\Omega_{n,k}|\chi_n^k(\mathbf{x}_1)\right| \leq \sum_{n=0}^{\infty}\frac{\alpha_n}{2^n} < \infty,$$

since the functions χ_n^k have disjoint support for a given value of n. Hence, the function $K(\mathbf{x}_1,\cdot)$ is bounded in $L^1(\Omega)$ independently of $\mathbf{x}_1$, which ensures that $K \in L^\infty(\Omega, L^1(\Omega))$. Since K is symmetric, we can apply Lemma 2.3.9, and so the kernel K defines an integral operator $\mathcal{R}$ in $\mathcal{L}(L^2(\Omega))$ by:

$$(\mathcal{R}f):\ \mathbf{x}_1 \mapsto \int_\Omega K(\mathbf{x}_1,\mathbf{x}_2)f(\mathbf{x}_2)\mathrm{d}\mathbf{x}_2 \qquad \text{for } f \in L^2(\Omega).$$

Study of the difference $\mathcal{R}_\varepsilon - \mathcal{R}$. Given $\varepsilon > 0$, let us introduce a new parameter $N(\varepsilon) \in \mathbb{N}$ appropriately chosen so that:

$$(n,k) \in \mathcal{I}_\varepsilon \cup \mathcal{E}_\varepsilon, \quad \text{for all } n < N(\varepsilon),\ 0 \leq k \leq 2^n - 1. \tag{2.25}$$

Define the new kernel functions K_ε^1, K_ε^2 and K_ε^3, such that for $(\mathbf{x}_1,\mathbf{x}_2)$ in $\Omega\times\Omega$:

$$K_\varepsilon^1(\mathbf{x}_1,\mathbf{x}_2) = \sum_{n=0}^{N(\varepsilon)-1}\sum_{k=0}^{2^n-1} r_{n,k}\left(\chi_{n,\varepsilon}^k(\mathbf{x}_1)\chi_{n,\varepsilon}^k(\mathbf{x}_2) - \chi_n^k(\mathbf{x}_1)\chi_{n,\varepsilon}^k(\mathbf{x}_2)\right), \tag{2.26}$$

$$K_\varepsilon^2(\mathbf{x}_1,\mathbf{x}_2) = \sum_{n=0}^{N(\varepsilon)-1}\sum_{k=0}^{2^n-1} r_{n,k}\left(\chi_n^k(\mathbf{x}_1)\chi_{n,\varepsilon}^k(\mathbf{x}_2) - \chi_n^k(\mathbf{x}_1)\chi_n^k(\mathbf{x}_2)\right), \tag{2.27}$$

$$K_\varepsilon^3(\mathbf{x}_1,\mathbf{x}_2) = \sum_{n=N(\varepsilon)}^{\infty}\left(\sum_{k \text{ s.t. } (n,k)\in\mathcal{I}_\varepsilon\cup\mathcal{E}_\varepsilon} r_{n,k}\chi_{n,\varepsilon}^k(\mathbf{x}_1)\chi_{n,\varepsilon}^k(\mathbf{x}_2) - \sum_{k=0}^{2^n-1} r_{n,k}\chi_n^k(\mathbf{x}_1)\chi_n^k(\mathbf{x}_2)\right). \tag{2.28}$$

It is easy to check that $K_\varepsilon - K = K_\varepsilon^1 + K_\varepsilon^2 + K_\varepsilon^3$ a.e. in $\Omega\times\Omega$, and that K_ε^1, K_ε^2 belong in $L^\infty(\Omega\times\Omega)$ and K_ε^3 is symmetric and belongs in $L^\infty(\Omega, L^1(\Omega))$. We introduce the integral operators $\mathcal{S}_\varepsilon^1$, $\mathcal{S}_\varepsilon^2$ and $\mathcal{S}_\varepsilon^3$ associated respectively to the kernels K_ε^1, K_ε^2 and K_ε^3, so that:

$$\mathcal{R}_\varepsilon - \mathcal{R} = \mathcal{S}_\varepsilon^1 + \mathcal{S}_\varepsilon^2 + \mathcal{S}_\varepsilon^3.$$

We are going to show that K_ε^1, K_ε^2 and K_ε^3 each converge to zero in $L^\infty(\Omega, L^1(\Omega))$ for at least one of the mixed–norms introduced in Lemma 2.3.9, which is enough to prove that the difference $\mathcal{R}_\varepsilon - \mathcal{R}$ converges to zero in $\mathcal{L}(L^2(\Omega))$.

First, we compute the mixed–norms of K_ε^1 and K_ε^2 on $\Omega\times\Omega$. Let $\mathbf{x}_1$ in Ω. We obtain immediately from (2.26) the following formula:

$$\begin{aligned}\int_\Omega |K_\varepsilon^1(\mathbf{x}_1,\mathbf{x}_2)|\mathrm{d}\mathbf{x}_2 &\leq \sum_{n=0}^{N(\varepsilon)-1}\sum_{k=0}^{2^n-1} r_{n,k}\left|\chi_{n,\varepsilon}^k(\mathbf{x}_1) - \chi_n^k(\mathbf{x}_1)\right||\Omega_{n,k}^\varepsilon| \\ &\leq \sum_{n=0}^{N(\varepsilon)-1}\sum_{k=0}^{2^n-1} r_{n,k}|\Omega_{n,k}^\varepsilon|\left(\chi_{n,\varepsilon}^k(\mathbf{x}_1) + \chi_n^k(\mathbf{x}_1)\right).\end{aligned}$$

We use now the approximation estimates from Proposition 2.3.3. First, for all $n \leq N(\varepsilon)$, $k \in \{0,\dots,2^n-1\}$:

$$|\Omega_{n,k}^\varepsilon| \leq C|\Omega_{n,k}|.$$

For a given $n \leq N(\varepsilon)$, the two families of functions (χ_n^k), $(\chi_{n,\varepsilon}^k)$ indexed by $k \in \{0, \dots, 2^n - 1\}$ have disjoint support. Consequently, we have, thanks to estimate (2.24):

$$\left\| \int_\Omega |K_\varepsilon^1(\mathbf{x}_1, \mathbf{x}_2)| \mathrm{d}\mathbf{x}_2 \right\|_{L^\infty(\Omega)} \leq C \sum_{n=0}^{N(\varepsilon)-1} \frac{\alpha_n}{2^n} \leq C \sum_{n=0}^{\infty} \frac{\alpha_n}{2^n} < \infty.$$

Now, let $\mathbf{x}_2$ in Ω. Because $|\chi_{n,\varepsilon}^k - \chi_n^k|$ is the characteristic function of the symmetric difference $\Omega_{n,k}^\varepsilon \Delta \Omega_{n,k}$, we compute from (2.26) the formula:

$$\int_\Omega |K_\varepsilon^1(\mathbf{x}_1, \mathbf{x}_2)| \mathrm{d}\mathbf{x}_1 \leq \sum_{n=0}^{N(\varepsilon)-1} \sum_{k=0}^{2^n-1} r_{n,k} \left| \Omega_{n,k}^\varepsilon \Delta \Omega_{n,k} \right| \chi_{n,\varepsilon}^k(\mathbf{x}_2).$$

Since, by Proposition 2.3.3,

$$|\Omega_{n,k}^\varepsilon \Delta \Omega_{n,k}| \leq C\varepsilon \, |\Omega_{n,k}|^{\frac{d-1}{d}} \text{ for all } n \leq N(\varepsilon), \ k \in \{0, \dots, 2^n - 1\},$$

we obtain

$$\int_\Omega |K_\varepsilon^1(\mathbf{x}_1, \mathbf{x}_2)| \mathrm{d}\mathbf{x}_1 \leq C\varepsilon \sum_{n=0}^{N(\varepsilon)-1} \sum_{k=0}^{2^n-1} r_{n,k} |\Omega_{n,k}|^{\frac{d-1}{d}} \chi_{n,\varepsilon}^k(\mathbf{x}_2).$$

Now, thanks to (2.5), we know that $\beta^n \leq |\Omega_{n,k}|$ for $k \in \{0, \dots, 2^n - 1\}$. Therefore we have the estimate:

$$r_{n,k} |\Omega_{n,k}|^{\frac{d-1}{d}} \leq \frac{\alpha_n}{2^n \beta^{n/d}}.$$

Hence, since the $\chi_{n,\varepsilon}^k$ have disjoint supports for a given n, we obtain:

$$\left\| \int_\Omega |K_\varepsilon^1(\mathbf{x}_1, \mathbf{x}_2)| \mathrm{d}\mathbf{x}_1 \right\|_{L^\infty(\Omega)} \leq C\varepsilon \sum_{n=0}^{N(\varepsilon)-1} \left(2\beta^{1/d}\right)^{-n} \alpha_n.$$

Following the same steps, we obtain the same bounds for the function K_ε^2 with $\mathbf{x}_1$ and $\mathbf{x}_2$ exchanged:

$$\left\| \int_\Omega |K_\varepsilon^2(\mathbf{x}_1, \mathbf{x}_2)| \mathrm{d}\mathbf{x}_2 \right\|_{L^\infty(\Omega)} \leq C\varepsilon \sum_{n=0}^{N(\varepsilon)-1} \left(2\beta^{1/d}\right)^{-n} \alpha_n,$$

$$\left\| \int_\Omega |K_\varepsilon^2(\mathbf{x}_1, \mathbf{x}_2)| \mathrm{d}\mathbf{x}_1 \right\|_{L^\infty(\Omega)} \leq C \sum_{n=0}^{N(\varepsilon)-1} \frac{\alpha_n}{2^n} \leq C \sum_{n=0}^{\infty} \frac{\alpha_n}{2^n} < \infty.$$

Hence, by Lemma 2.3.9, the integral operators $\mathcal{S}_\varepsilon^1$ and $\mathcal{S}_\varepsilon^1$ are well–defined and their operator norm satisfies:

$$\|\mathcal{S}_\varepsilon^1\|_{\mathcal{L}(L^2(\Omega))} \leq C\sqrt{\varepsilon} \left(\sum_{n=0}^{N(\varepsilon)-1} \left(2\beta^{1/d}\right)^{-n} \alpha_n \right)^{1/2}, \tag{2.29}$$

$$\|\mathcal{S}_\varepsilon^2\|_{\mathcal{L}(L^2(\Omega))} \leq C\sqrt{\varepsilon} \left(\sum_{n=0}^{N(\varepsilon)-1} \left(2\beta^{1/d}\right)^{-n} \alpha_n \right)^{1/2}. \tag{2.30}$$

We now turn to the study of $\mathcal{S}_\varepsilon^3$. Since K_ε^3 is symmetric, it is enough to compute either one of the mixed norms. Given $\mathbf{x}_1$ in Ω, we obtain from (2.28):

$$\int_\Omega |K_\varepsilon^3(\mathbf{x}_1, \mathbf{x}_2)| \mathrm{d}\mathbf{x}_2 \leq \sum_{n=N(\varepsilon)}^{\infty} \left(\sum_{k \text{ s.t. } (n,k) \in \mathcal{I}_\varepsilon \cup \mathcal{E}_\varepsilon} r_{n,k} \chi_{n,\varepsilon}^k(\mathbf{x}_1) |\Omega_{n,k}^\varepsilon| + \sum_{k=0}^{2^n-1} r_{n,k} \chi_n^k(\mathbf{x}_1) |\Omega_{n,k}| \right).$$

For a given n, the families of functions $(\chi_n^k)_{k=0,\dots,2^n-1}$ and $(\chi_{n,\varepsilon}^k)_{k=0,\dots,2^n-1}$ have disjoint support. Hence, taking the maximum over Ω in the right–hand side we compute:

$$\|K_\varepsilon^3(\mathbf{x}_1,\cdot)\|_{L^1(\Omega)} \leq \sum_{n=N(\varepsilon)}^{\infty} \left(\max_{k \text{ s.t. } (n,k)\in\mathcal{I}_\varepsilon\cup\mathcal{E}_\varepsilon} (r_{n,k}|\Omega_{n,k}^\varepsilon|) + \max_{0\leq k<2^n} (r_{n,k}|\Omega_{n,k}|) \right).$$

As a consequence, thanks to Proposition 2.3.3:

$$\|K_\varepsilon^3\|_{L^\infty(\Omega,L^1(\Omega))} \leq C \sum_{n=N(\varepsilon)}^{\infty} \frac{\alpha_n}{2^n}.$$

Finally, we deduce from this estimate and Lemma 2.3.9 a bound on the operator norm of $\mathcal{S}_\varepsilon^2$:

$$\|\mathcal{S}_\varepsilon^3\|_{\mathcal{L}(L^2(\Omega))} \leq C \sum_{n=N(\varepsilon)}^{\infty} \frac{\alpha_n}{2^n}. \tag{2.31}$$

Now, bringing together the two estimates (2.29), (2.30) and (2.31), we compute the operator norm of $\mathcal{R}_\varepsilon - \mathcal{R}$ by the triangle inequality. We have proved that, for any integer $N(\varepsilon)$ satisfying (2.25):

$$\|\mathcal{R}_\varepsilon - \mathcal{R}\|_{\mathcal{L}(L^2(\Omega))} \leq C \left(\sqrt{\varepsilon} \left(\sum_{n=0}^{N(\varepsilon)-1} \frac{\alpha_n}{\left(2\beta^{1/d}\right)^n} \right)^{1/2} + \sum_{n=N(\varepsilon)}^{\infty} \frac{\alpha_n}{2^n} \right). \tag{2.32}$$

Convergence of $\mathcal{R}_\varepsilon$ We are now in a position to investigate the convergence of the resistance operators. The idea is to choose $N(\varepsilon)$ so that both terms in (2.32) converge to zero while satisfying the condition (2.25). By construction, this last condition is satisfied if in every subdomain $\Omega_{n,k}$ for $n \leq N(\varepsilon)$, there lies at least one point of the uniform array $\mathcal{G}^\varepsilon$. We recall that the subdomains of the approximable decomposition $\mathcal{O}$ satisfy a uniform cone condition (see Definition 2.1.6). We can fit a ball inside a cone, so the radius of the largest ball inscribed in the subdomain $\Omega_{n,k}$ is bounded from below by $C\beta^{n/d}$. Now if this inscribed ball is large enough, it will contain a point of the uniform array $\mathcal{G}^\varepsilon$, so there exists a constant $C_\mathcal{O} > 0$ such that

$$\beta^{N(\varepsilon)} \geq C_\mathcal{O}\varepsilon^d \tag{2.33}$$

is a sufficient condition for (2.25) to be satisfied.

First, we only suppose that the series $\sum_{n\geq 0}\alpha_n$ is absolutely convergent as in (2.20). In view of (2.32), a suitable choice of $N(\varepsilon)$ is one that satisfies the condition:

$$N(\varepsilon) \to \infty \text{ and } \varepsilon \left(\beta^{-1/d}\right)^{N(\varepsilon)} \to 0 \text{ as } \varepsilon \to 0.$$

Hence, a possible choice is:

$$N(\varepsilon) = \text{Int}\left(\frac{s}{\ln\left(\beta^{1/d}\right)} \ln(\varepsilon) \right), \quad \text{with } 0 < s < 1. \tag{2.34}$$

Let us check that this choice also satisfies (2.33). Taking the logarithm, we want $N(\varepsilon)$ to be small enough that the following condition holds true:

$$N(\varepsilon) \leq \frac{\ln\left(C_\mathcal{O}\varepsilon^d\right)}{\ln(\beta)} = \frac{\ln(\varepsilon) + \ln(C_\mathcal{O})/d}{\ln(\beta^{1/d})}.$$

Clearly, this condition is satisfied for ε small enough given the choice (2.34), for any $0 < s < 1$. Moreover, this choice ensures the convergence of $\mathcal{R}_\varepsilon$ to $\mathcal{R}$. To check this, we compute from (2.32), using the formula (2.34):

$$\begin{aligned}\|\mathcal{R}_\varepsilon - \mathcal{R}\|_{\mathcal{L}(L^2(\Omega))} &\leq C\left(\sqrt{\varepsilon}\left(\left(\frac{1}{\beta^{1/d}}\right)^{N(\varepsilon)}\sum_{n=0}^{N(\varepsilon)}\frac{\alpha_n}{2^n}\right)^{1/2} + \sum_{n=N(\varepsilon)}^{\infty}\frac{\alpha_n}{2^n}\right)\\ &\leq C\left(\varepsilon^{(1-s)/2}\left(\sum_{n=0}^{\infty}\frac{\alpha_n}{2^n}\right)^{1/2} + \sum_{n=N(\varepsilon)}^{\infty}\frac{\alpha_n}{2^n}\right).\end{aligned}$$

Since the series of general term $(\alpha_n/2^n)$ is absolutely convergent, the second term converges to zero, and we have proved that $\mathcal{R}_\varepsilon$ converges strongly to $\mathcal{R}$ in $\mathcal{L}(L^2(\Omega))$.

Geometric case We can obtain estimates on the rate of convergence in case the resistances of the tree satisfy the geometric condition (2.21). In this case, we can explicitly estimate the remainder of the series of general term $\left(\frac{\alpha_n}{2^n}\right)$:

$$\sum_{n=N(\varepsilon)}^{\infty}\frac{\alpha_n}{2^n} \leq \frac{C_\alpha}{1-\alpha/2}\left(\frac{\alpha}{2}\right)^{N(\varepsilon)}.$$

From (2.32), we write the following estimate:

$$\|\mathcal{R}_\varepsilon - \mathcal{R}\|_{\mathcal{L}(L^2(\Omega))} \leq C\left(\sqrt{\varepsilon}\left(\sum_{n=0}^{N(\varepsilon)-1}\left(\frac{\alpha}{2\beta^{1/d}}\right)^n\right)^{1/2} + \frac{C_\alpha}{1-\alpha/2}\left(\frac{\alpha}{2}\right)^{N(\varepsilon)}\right).$$

We are going to detail the three cases where $\alpha/(2\beta^{1/d})$ is respectively smaller, equal and greater than 1. First, let us consider the case where $\alpha < 2\beta^{1/d}$. Then, we have the estimate:

$$\|\mathcal{R}_\varepsilon - \mathcal{R}\|_{\mathcal{L}(L^2(\Omega))} \leq C\left(\sqrt{\varepsilon} + \left(\frac{\alpha}{2}\right)^{N(\varepsilon)}\right).$$

Hence, the best rate of convergence will be achieved for the largest $N(\varepsilon)$ satisfying the condition (2.33), so we consider the choice

$$\text{or } N(\varepsilon) = \text{Int}\left(\frac{\ln(\varepsilon)}{\ln(\beta^{1/d})}\right) - \text{Int}\left(\frac{\ln(C_{\mathcal{O}})}{\ln(\beta^{-1})}\right),$$

so that $\beta^{N(\varepsilon)} \approx C_{\mathcal{O}}\varepsilon^d$. Clearly, $N(\varepsilon)$ is well–defined for ε small enough. Then, to estimate the rate of convergence, we compute:

$$\left(\frac{\alpha}{2}\right)^{N(\varepsilon)} \leq C\varepsilon^p \quad \text{with } p = \frac{\ln(\alpha/2)}{\ln(\beta^{1/d})}.$$

Now, we have assumed that $\alpha/2 < \beta^{1/d}$ and $\beta < 1$, so $0 < -\ln\left(\beta^{1/d}\right) < -\ln(\alpha/2)$. Therefore, the exponent p is greater than 1. Since $p > 1/2$, we obtain a convergence rate of $1/2$ because of the term in $\sqrt{\varepsilon}$ in (2.32).

$$\|\mathcal{R}_\varepsilon - \mathcal{R}\|_{\mathcal{L}(L^2(\Omega))} \leq C\varepsilon^q \text{ with } q = 1/2 \text{ under the condition } \alpha < 2\beta^{1/d}. \tag{2.35}$$

Next, suppose that $\alpha = 2\beta^{1/d}$. In this case, we write:

$$\|\mathcal{R}_\varepsilon - \mathcal{R}\|_{\mathcal{L}(L^2(\Omega))} \leq C\left(\sqrt{\varepsilon}N(\varepsilon) + \left(\frac{\alpha}{2}\right)^{N(\varepsilon)}\right).$$

Choosing $N(\varepsilon)$ as previously, we obtain for the same reasons convergence of the remainder $\left(\frac{\alpha}{2}\right)^{N(\varepsilon)}$ faster than the term in $\sqrt{\varepsilon}$. Hence:

$$\|\mathcal{R}_\varepsilon - \mathcal{R}\|_{\mathcal{L}(L^2(\Omega))} \leq C\varepsilon^q |\ln(\varepsilon)| \text{ with } q = 1/2 \text{ under the condition } \alpha = 2\beta^{1/d}. \tag{2.36}$$

Finally, if we suppose that $\alpha > 2\beta^{1/d}$, we obtain:

$$\|\mathcal{R}_\varepsilon - \mathcal{R}\|_{\mathcal{L}(L^2(\Omega))} \leq C\left(\left(\varepsilon\frac{\left(\alpha/(2\beta^{1/d})\right)^{N(\varepsilon)} - 1}{\alpha/(2\beta^{1/d}) - 1}\right)^{1/2} + \left(\frac{\alpha}{2}\right)^{N(\varepsilon)}\right).$$

Hence we have:

$$\|\mathcal{R}_\varepsilon - \mathcal{R}\|_{\mathcal{L}(L^2(\Omega))} \leq C\left(\frac{\alpha}{2}\right)^{N(\varepsilon)/2}\left(\sqrt{\varepsilon}\left(\beta^{-1/d}\right)^{N(\varepsilon)/2} + \left(\frac{\alpha}{2}\right)^{N(\varepsilon)/2}\right).$$

Now, keeping the same choice of $N(\varepsilon)$ as before, we remark that

$$\varepsilon\beta^{-N(\varepsilon)/d} \leq C_{\mathcal{O}}^{1/d}.$$

We can estimate the rate of convergence thanks to the estimate:

$$\left(\frac{\alpha}{2}\right)^{N(\varepsilon)/2} \leq C\left(\frac{\alpha}{2}\right)^{\frac{\ln(\varepsilon)}{2\ln(\beta^{1/d})}} \leq C\exp\left(\ln(\varepsilon)\frac{d}{2}\frac{\ln(\alpha) - \ln(2)}{\ln(\beta)}\right).$$

Finally, we obtain the following estimate for the convergence of the resistance operator:

$$\|\mathcal{R}_\varepsilon - \mathcal{R}\|_{\mathcal{L}(L^2(\Omega))} \leq C\varepsilon^q \text{ with } q = \frac{d}{2}\left(\frac{\ln(2) - \ln(\alpha)}{-\ln(\beta)}\right) \text{ under the condition } \alpha > 2\beta^{1/d}. \tag{2.37}$$

The three estimates (2.35), (2.36) and (2.37) prove (2.22) and conclude the proof of the Theorem. □

Remark 2.3.10. *Note that $q \leq 1/2$ and in the limit $\alpha/(2\beta^{1/d}) \to 1$, the exponent q converges to $1/2$, since we have for $\alpha > 2\beta^{1/d}$:*

$$\frac{d}{2}\left(\frac{\ln(2) - \ln(\alpha)}{-\ln(\beta)}\right) = \frac{1}{2}\left(1 - \frac{\ln\left(\frac{\alpha}{2\beta^{1/d}}\right)}{\ln(\beta^{-1/d})}\right) < 1/2.$$

Hence, the function $(\alpha, \beta) \mapsto q$ is continuous.

Conclusion

We have presented two different geometric frameworks and described in each case how the operator representing the tree converges to a limit operator. Let us compare the respective rates of convergence we have obtained as a result. In the first case, a highly idealized square representation of the parenchyma, the portion of the parenchyma irrigated by a given airway does not change as the number of generations n changes, and the difference between the approximate operator $\mathcal{R}_n$ and the limit operator $\mathcal{R}$ lies only in the truncature of the terms corresponding to generations of the tree

higher than n, see (2.8) and (2.9). In the second case, no assumption is made on the shape of the domain. This results in another layer of approximation as the multi–scale decomposition has to be approximated for each value of $\varepsilon > 0$, and the kernel of the approximate operator $\mathcal{R}_\varepsilon$ (2.18) differs from the kernel of the limit operator $\mathcal{R}$ (2.19) both by a truncature of the terms corresponding to higher generations and the approximation of those associated to earlier generations of the tree. Technically, there is a new difficulty in this second case since the kernels K_ε does not converge to K in $L^\infty(\Omega, L^1(\Omega))$ as in the geometric case presented in previous papers [GMM06, VSM09].

Assume that the resistances of the tree are geometric. In the idealized, square case, the operators $\mathcal{R}_n$ converge to the limit operator at a geometric rate, as fast as the equivalent resistance of the finite tree to that of the limit tree. In terms of the step size of the grid, we observe (see Remark 2.2.13) the convergence rate

$$\|\mathcal{R} - \mathcal{R}_n\|_{\mathcal{L}(L^2(\Omega))} \leq C\varepsilon^q \quad \text{with } q = d\left(1 - \frac{\ln(\alpha)}{\ln(2)}\right).$$

In the second, approximated case, given a balanced multi–scale decomposition ($\beta = 1/2$), the rate of convergence q deteriorates to (see (2.22)):

$$q = \begin{cases} \dfrac{d}{2}\left(1 - \dfrac{\ln(\alpha)}{\ln(2)}\right) & \text{if } \alpha > 2^{\frac{d-1}{d}}, \\ 1/2 & \text{if } \alpha \leq 2^{\frac{d-1}{d}}. \end{cases}$$

We observe that the rate of convergence is divided by at least 2 compared to the idealized case. The reason is that the convergence of $\mathcal{R}_\varepsilon$ takes place in the operator norm in $L^2(\Omega)$ and we lose the convergence of the kernels in the $L^\infty(\Omega, L^1(\Omega))$ norm. We also observe an upper limit for the convergence rate at $1/2$. This is expected because of the interior boundary errors induced by the approximation of $\mathcal{O}$ with the finite multi–scale decompositions $\mathcal{O}_\varepsilon$, which is of first order in the parameter ε.

Finally, the sufficient condition for the convergence of the operators in Theorem 2.3.5 is an exemple of an interesting fact concerning the construction of a real, three–dimensional self–similar branching tree: to converge from the point of view of the resistance to the airflow, the tree must diverge from a geometrical point of view, i.e. its volume must go to infinity (actually, the branches of the tree start to overlap.) Indeed, recall the value of the resistance from Poiseuille's law:

$$r = \frac{8\nu L}{\pi R^4}.$$

Assuming that the branches are homothetical, the volume of the branch is then proportional to the inverse of the resistance. Hence, the condition (2.21)

$$|\Omega_{n,k}| \leq C_\alpha \left(\frac{\alpha}{2}\right)^n (r_{n,k})^{-1}$$

implies that the volume of all the branches at generation n grows exponentially compared to the volume of the whole domain. This means, as it was already observed in the case of a purely geometric tree (Definition 2.2.9), that the actual construction of a three–dimensional infinite bronchial tree is impossible, since its resistance must be finite to deliver air to the alveoli.

2.A Annex

This annex is devoted to the proof of the Proposition 2.3.3, which we recall here. We remind the assumptions used in Section 2.3: $\mathcal{O}$ is a regular, approximable decomposition of the domain Ω (Definitions 2.1.3 and 2.1.6) satisfying the condition (2.5): there exists a constant β with $0 < \beta \leq 1/2$ and a constant $C > 0$, such that for all $n \geq 0$ and $k \in \{0, \dots, 2^n - 1\}$,

$$\beta|\Omega_{n,k}| \leq |\Omega_{n+1,2k}|, \ \beta|\Omega_{n,k}| \leq |\Omega_{n+1,2k+1}|. \tag{2.38}$$

Proposition 2.A.1. *Let ε small enough and $\mathcal{O}^\varepsilon$ be the finite multi–scale decomposition of Ω defined by (2.14) and (2.15). Then there exists positive constants C, C_1, $C_2 > 0$ independent of ε such that if $(n,k) \in \mathcal{I}_\varepsilon \cup \mathcal{E}_\varepsilon$ then:*

$$\left|\Omega^\varepsilon_{n,k} \Delta \Omega_{n,k}\right| \leq C\varepsilon \ |\Omega_{n,k}|^{\frac{d-1}{d}}, \tag{2.39}$$

and

$$C_1 \left|\Omega_{n,k}\right| \leq \left|\Omega^\varepsilon_{n,k}\right| \leq C_2 \left|\Omega_{n,k}\right|. \tag{2.40}$$

The proof, which is mostly technical, relies on a Lemma which we state and prove first in Section 2.A.1.

2.A.1 A geometric Lemma

Lemma 2.A.2. *Let D be an open, bounded domain with boundary E, with characteristic function χ_D, and such that*

- *There exists a constant $\kappa > 0$ such that for all $\mathbf{h}$ in $\mathbb{R}^d$,*

$$\|\tau_h \chi_D - \chi_D\|_{L^1(\Omega)} = |(\tau_{\mathbf{h}} D) \, \Delta D| \leq \kappa |\mathbf{h}|, \qquad \forall \mathbf{h} \in \mathbb{R}^d, \tag{2.41}$$

  where $\tau_{\mathbf{h}}$ is the operator of translation by the vector $\mathbf{h}$.

- *There exists two constants $\delta > 0$ and $\theta \in (0, \pi/2)$ such that D and $\mathbb{R}^d \setminus D$ satisfy an uniform interior cone condition with parameters δ, θ.*

Then, there exists a constant $C > 0$ depending only on the dimension d and on θ such that:

$$|E + B(0,\varepsilon)| \leq C\varepsilon \max\left(\kappa, \frac{|D|}{\delta^d}\varepsilon^{d-1}\right). \tag{2.42}$$

An illustration of the geometric meaning of the estimate (2.42) is proposed in Figure 2.7, knowing that κ is an estimate of the (d-1)–volume of E and the second quantity in the max on the right–hand side of (2.42) is an estimate only used when ε is large compared to the parameter δ.

Remark 2.A.3. *The estimate given by Lemma 2.A.2 is intuitive from a geometric point of view and connected to classical properties of compact sets in $\mathbb{R}^d$. Given $r > 0$ and a non–empty compact set A in $\mathbb{R}^d$, we can define its r–parallel set A_r and its $(d-1)$–Minkowski content $M^{d-1}(A)$, if it exists, by:*

$$A_r = A + B(0,r) \text{ and } M(A) = \lim_{r \to 0} \frac{|A_r|}{2r}.$$

The quantity on the left–hand side of (2.42) is the volume of the ε–parallel set of $E = \partial D$. It is well–known that the quantity $M^{d-1}(A)$, if it exists, is a measure of the (d-1)–volume of A, see e.g. [Sta76, RW10] and the references therein.

In particular, a theorem of Sz–Nagy [SN59] states that given an arbitrary compact set G in the plane with k components, if G_r denotes the parallel set of G of radius r then the function $|G_r| - \pi k r^2$

is concave on $(0, +\infty)$. *This result implies our weaker estimate* (2.42) *if the compact set* E *admits a Minkowski content, since in this case* $M^{d-1}(E)$ *is the derivative at* $r = 0$ *of the parallel set volume function* $|E + B(0, \varepsilon)|$. *However, this result does not extend to the dimension* $d = 3$, *which is why we need the uniform cone condition to hold for the subdomains* $\Omega_{n,k}$ *in Definition 2.1.6.*

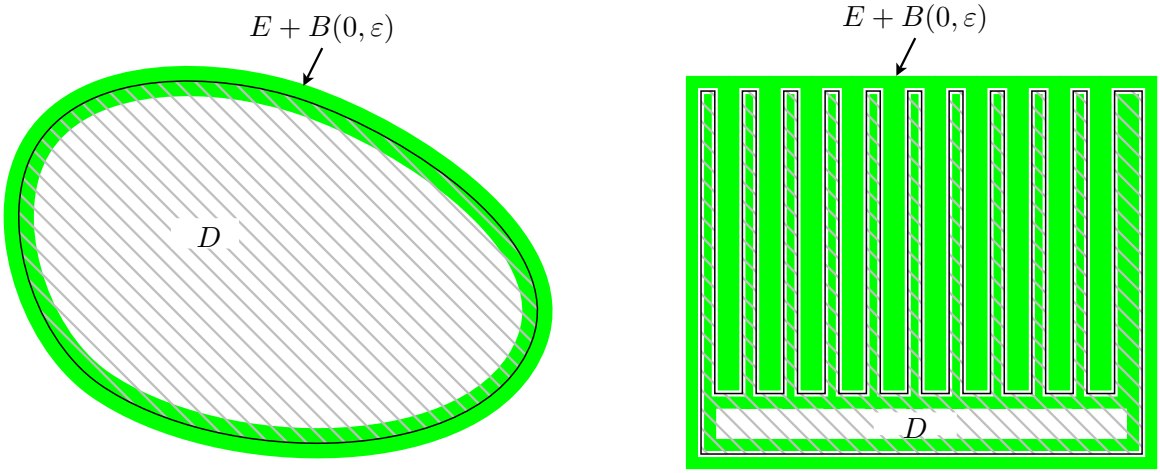

(a) A smooth subdomain (b) A rough subdomain

Figure 2.7 – Comparison between the areas of an ε–neighborhood of the boundary (in green) and the volume of the subdomain (in grey hatches) for two different shapes.

Proof of Lemma 2.A.2. Let $\varepsilon > 0$. We want to compute the measure of the ε–parallel set of $E = \partial D$, noted E_ε and defined by:

$$E_\varepsilon = E + B(0, \varepsilon) = \{\mathbf{x} + \mathbf{h} \mid \mathbf{x} \in E, \quad \mathbf{h} \in B(0, \varepsilon)\}.$$

The idea is to "integrate" the translations over $B(0, 2\varepsilon)$ to bound the volume of E_ε. Let ω_d be the volume of the unit ball in $\mathbb{R}^d$. We define the function F on Ω by:

$$F : \mathbf{x} \mapsto \frac{1}{\omega_d (2\varepsilon)^d} \int_{B(0,2\varepsilon)} |\chi_D(\mathbf{x} + \mathbf{h}) - \chi_D(\mathbf{x})| \mathrm{d}\mathbf{h} \geq 0.$$

Now, we use the estimate (2.41): for any $\mathbf{h} \in B(0, 2\varepsilon)$, $\|\tau_{\mathbf{h}} \chi_D - \chi_D\|_{L^1(\Omega)} \leq \min(2\kappa\varepsilon, 2|D|)$. By an application of Fubini's theorem, we obtain then:

$$\int_\Omega F(\mathbf{x}) \mathrm{d}\mathbf{x} \leq 2 \min(\kappa\varepsilon, |D|). \tag{2.43}$$

If we can bound F from below on E_ε, the estimate (2.43) will yield an upper bound for its measure. To prove this, we use the properties of the characteristic function of $(\tau_{\mathbf{h}} D) \Delta D$, which can be decomposed as follows. Given $\mathbf{x}$ in $\mathbb{R}^d$ and $\mathbf{h}$ in $\mathbb{R}^d$, we write:

$$|\chi_D(\mathbf{x} + \mathbf{h}) - \chi_D(\mathbf{x})| = \chi_D(\mathbf{x} + \mathbf{h})(1 - \chi_D(\mathbf{x})) + \chi_D(\mathbf{x})(1 - \chi_D(\mathbf{x} + \mathbf{h})).$$

Now, let us study the functions F_1 and F_2, defined on $\mathbb{R}^d$ by:

$$F_1 : \mathbf{x} \mapsto \int_{B(0,2\varepsilon)} \chi_D(\mathbf{x} + \mathbf{h})(1 - \chi_D(\mathbf{x})) \mathrm{d}\mathbf{h} = |B(\mathbf{x}, 2\varepsilon) \cap D| (1 - \chi_D(\mathbf{x})),$$

$$F_2 : \mathbf{x} \mapsto \int_{B(0,2\varepsilon)} \chi_D(\mathbf{x})(1 - \chi_D(\mathbf{x} + \mathbf{h})) \mathrm{d}\mathbf{h} = |B(\mathbf{x}, 2\varepsilon) \setminus D| \chi_D(\mathbf{x}).$$

The supports of the functions F_1 and F_2 are constained respectively in the sets $\mathbb{R}^d \setminus D$ and D. Let us consider $\mathbf{x}$ in E_ε and $\mathbf{x}_\perp$ in E such that $d(\mathbf{x}, \mathbf{x}_\perp) < \varepsilon$. Depending on the position of $\mathbf{x}$ relatively to D, we are going to use the exterior or interior cone condition on the boundary ∂D to bound $F_1(\mathbf{x})$ or $F_2(\mathbf{x})$ from below.

Suppose that $\mathbf{x} \in E_\varepsilon \setminus D$. Then, we know that there exists a unit vector $\mathbf{m}$ such that the cone $C(\mathbf{m})$, parameterized by θ, satisfies:

$$(\mathbf{x}_\perp + C(\mathbf{m})) \cap B(\mathbf{x}_\perp, \delta) \quad \subset D.$$

Now, thanks to the triangle inequality, this means that:

$$(\mathbf{x}_\perp + C(\mathbf{m})) \cap B\left(\mathbf{x}_\perp, \min(\delta,\ \varepsilon)\right) \quad \subset B(\mathbf{x}, 2\varepsilon) \cap D.$$

Hence, we can bound from below the value of $F(\mathbf{x})$, since:

$$F_1(\mathbf{x}) \geq C_d(\theta) \min(\delta^d,\ \varepsilon^d),$$

where $C_d(\theta) > 0$ depends only on θ and the dimension d with $C_d(\theta) = \frac{\theta}{2}$ for $d = 2$ and $C_d(\theta) = \frac{2\pi}{3}(1 - \cos(\theta))$ for $d = 3$. If $\mathbf{x} \in E_\varepsilon \cap D$, then by the same argument, we obtain:

$$F_2(\mathbf{x}) \geq C_d(\theta) \min(\delta^d,\ \varepsilon^d).$$

Hence, we have obtained that F is bounded from below on E_ε by $C_\theta \min(\delta^d,\ \varepsilon^d)$. Therefore, integrating F over E_ε we obtain:

$$\frac{C_d(\theta)}{\omega_d} \frac{\min(\delta^d,\ \varepsilon^d)|E_\varepsilon|}{\varepsilon^d} \leq 2 \min\left(\kappa\varepsilon, |D|\right).$$

If $\delta \geq \varepsilon$, we obtain the estimate:

$$|E_\varepsilon| \leq \frac{2\omega_d}{C_d(\theta)} \kappa\varepsilon.$$

On the other hand, if $\delta \leq \varepsilon$ we can write:

$$|E_\varepsilon| \leq \frac{2\omega_d |D|}{C_d(\theta)\delta^d} \varepsilon^d.$$

Hence, we have obtained the following upper bound on E_ε:

$$|E_\varepsilon| \leq \frac{2\omega_d}{C_d(\theta)} \max\left(\kappa\varepsilon, \frac{|D|}{\delta^d}\varepsilon^d\right), \tag{2.44}$$

and the proof is finished. □

2.A.2 Proof of Proposition 2.3.3 (alias Proposition 2.A.1)

Let us begin by writing some inequalities that follow from the regularity of the multi–scale decomposition. We will designate by C any constant independent of the three parameters ε, n and k in the following computations. Thanks to the interior cone condition satisfied by the whole domain Ω, we know that for all $\varepsilon > 0$ small enough and $\mathbf{x} \in \Omega$,

$$\operatorname{dist}\left(\mathbf{x}, \mathcal{G}^\varepsilon\right) \leq C\varepsilon. \tag{2.45}$$

In addition, we know that the condition of regularity and approximability holds for $\mathcal{O}$ (see Definitions 2.1.3 and 2.1.6). Since we can fit a ball inside a cone, that leads to, for all $n \in \mathbb{N}$ and $k \in \{0, \ldots, 2^n - 1\}$,

$$C|\Omega_{n,k}|^{1/d} \leq \operatorname{inscr}(\Omega_{n,k}) \leq \operatorname{diam}(\Omega_{n,k}) \leq C'|\Omega_{n,k}|^{1/d}, \tag{2.46}$$

where $\mathrm{inscr}(\Omega_{n,k})$ is the radius of the largest ball inscribed in $\Omega_{n,k}$.

We limit now our attention to such subdomains $\Omega_{n,k}$ such that the node $X_{n,k}$ belongs to the finite tree $\mathcal{T}_\varepsilon$. We recall that $\mathcal{I}_\varepsilon$ is the set of indexes of the internal nodes of $\mathcal{T}_\varepsilon$ and $\mathcal{E}_\varepsilon$ the set of indexes of the terminal nodes of $\mathcal{T}_\varepsilon$. Since either $\Omega_{n,k}$ or its parent $\Omega_{n-1,k/2}$ contains at least two points of the uniform array $\mathcal{G}^\varepsilon$, its diameter is larger than ε. Thanks to (2.46) and the condition (2.38), we have

$$|\Omega_{n,k}| \geq C\varepsilon^d \quad \text{for all } n,k \text{ such that } X_{n,k} \in \mathcal{T}_\varepsilon. \tag{2.47}$$

We are going to make a distinction between big and small subdomains of the multi–scale decomposition $\mathcal{O}$ compared to the grid size ε.

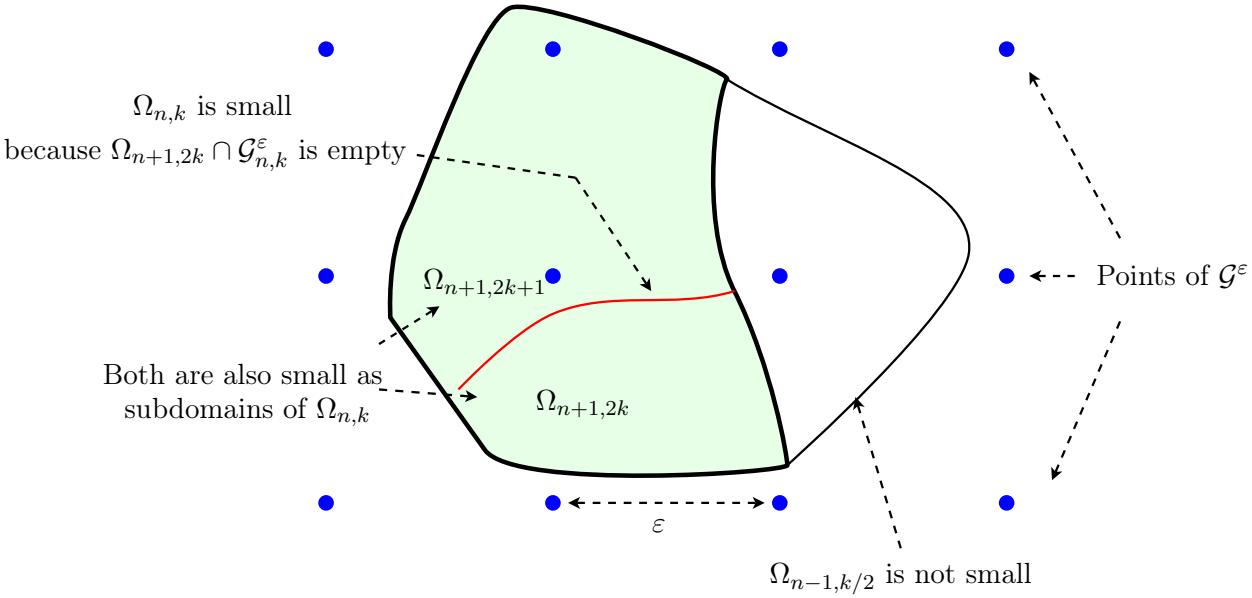

Figure 2.8 – Illustration of a small subdomain. Note that the periodic grid does not have to be square.

We define a small subdomain as:

- a subdomain $\Omega_{n,k}$ such that its portion $\mathcal{G}^\varepsilon_{n,k}$ of the uniform array $\mathcal{G}^\varepsilon$ does not intersect one of its subsets $\Omega_{n+1,2k}$ or $\Omega_{n+1,2k+1}$, so that we need to use the additional rule in the algorithm to split $\mathcal{G}^\varepsilon_{n,k}$ if it contains more than one point (see Figure 2.8),
- a subdomain $\Omega_{n,k}$ which is itself a subdomain of a member $\Omega_{m,j}$ of the previous category, which can be verified by checking that $n \geq m$ and $j = k/2^{n-m}$ where the operator / stands for the integer quotient.

Since the terminal nodes of the tree $\mathcal{T}_\varepsilon$, indexed by $\mathcal{E}_\varepsilon$, are associated with only one point of the array $\mathcal{G}^\varepsilon$, it is clear that the corresponding subdomains are small according to this definition. Formally, we will define a set of indexes $\mathcal{E}'_\varepsilon$ for the small subdomains by setting:

$$\begin{aligned}\mathcal{E}'_\varepsilon = \{&(n,k) \in \mathcal{I}_\varepsilon \cup \mathcal{E}_\varepsilon \text{ and there exists } m \leq n \text{ such that:} \\ &\mathcal{G}^\varepsilon_{m,j} \cap \overline{\Omega}_{m+1,2j} = \emptyset \text{ or } \left(\mathcal{G}^\varepsilon_{m,j} \cap \overline{\Omega}_{m+1,2j+1}\right) \setminus \overline{\Omega}_{m+1,2j} = \emptyset \text{ with } j = k/2^{n-m}\}\,.\end{aligned}$$

Study of the small subdomains. Let us bound the volume of the small subdomains by ε^d. For a given $(n,k) \in \mathcal{E}'_\varepsilon$, define

$$m = \min\{0 \le p \le n \text{ such that } \mathcal{G}^\varepsilon_{p,j} \cap \overline{\Omega}_{p+1,2j} = \emptyset \\ \text{or } \left(\mathcal{G}^\varepsilon_{p,j} \cap \overline{\Omega}_{p+1,2j+1}\right) \setminus \overline{\Omega}_{p+1,2j} = \emptyset \text{ for } j = k/2^{n-p}\},$$

and $j = k/2^{n-m}$. Without loss of generality, let us suppose that $\mathcal{G}^\varepsilon_{m,j} \cap \overline{\Omega}_{m+1,2j}$ is empty. By definition of (m,j), we know then by following the algorithm used to construct $\mathcal{G}^\varepsilon_{m,j}$ that $\mathcal{G}^\varepsilon \cap \Omega_{m+1,2j}$ is empty, see (2.11) (because the additional rule (2.12) was never used to remove a point from $\mathcal{G}^\varepsilon_{p,l}$ for $p \le m$ and $l = j/2^{m-p}$), so that the radius $\mathrm{inscr}(\Omega_{m+1,2j})$ of the largest ball inscribed in $\Omega_{n,k}$ is bounded by $C\varepsilon$ thanks to (2.45). Hence, by (2.46) we have

$$|\Omega_{m+1,2j}| \le C\varepsilon^d.$$

Then, we obtain by (2.38) that:

$$|\Omega_{n,k}| \le C\varepsilon^d \quad \text{for all } (n,k) \in \mathcal{E}'_\varepsilon. \tag{2.48}$$

Now, we show a similar set of bounds for the approximate subdomains $\Omega^\varepsilon_{n,k}$. Let $(n,k) \in \mathcal{E}_\varepsilon$, so that $X_{n,k}$ is a terminal node of $\mathcal{T}_\varepsilon$ and $\Omega^\varepsilon_{n,k}$ is given by (2.14). Then $\Omega^\varepsilon_{n,k}$ contains the cell $\mathcal{Y}^{n,k}_\varepsilon$ and, thanks to (2.45), it is contained in a ball of radius $C\varepsilon$ around the barycenter of $\mathcal{Y}^{n,k}_\varepsilon$. Hence we have the estimates

$$\varepsilon^d \le |\Omega^\varepsilon_{n,k}| \le C\varepsilon^d \text{ for all } (n,k) \in \mathcal{E}_\varepsilon.$$

Thanks to (2.47) and (2.48), we obtain that for some constants $C_1, C_2 > 0$,

$$C_1 |\Omega_{n,k}| \le \left|\Omega^\varepsilon_{n,k}\right| \le C_2 |\Omega_{n,k}| \text{ for all } (n,k) \in \mathcal{E}_\varepsilon.$$

But we have for all internal nodes $X_{n,k}$ of the tree $\mathcal{T}_\varepsilon$ the following relations:

$$|\Omega_{n+1,2k}| + |\Omega_{n+1,2k+1}| = |\Omega_{n,k}| \text{ and } |\Omega^\varepsilon_{n+1,2k}| + |\Omega^\varepsilon_{n+1,2k+1}| = |\Omega^\varepsilon_{n,k}|.$$

Hence, by recurrence on the tree we have proved the estimate (2.40):

$$C_1 |\Omega_{n,k}| \le \left|\Omega^\varepsilon_{n,k}\right| \le C_2 \left|\Omega_{n,k}\right| \text{ for all } (n,k) \in \mathcal{I}_\varepsilon \cup \mathcal{E}_\varepsilon. \tag{2.49}$$

Moreover, from (2.48), (2.49) and the well–known relation $\left|\Omega^\varepsilon_{n,k} \Delta \Omega_{n,k}\right| \le \left|\Omega^\varepsilon_{n,k}\right| + \left|\Omega_{n,k}\right|$, we have shown:

$$\left|\Omega^\varepsilon_{n,k} \Delta \Omega_{n,k}\right| \le C\varepsilon \left|\Omega_{n,k}\right|^{\frac{d-1}{d}} \text{ for } (n,k) \in \mathcal{E}'_\varepsilon. \tag{2.50}$$

Larger subdomains. For a given couple $(n,k) \in \mathcal{I}_\varepsilon \setminus \mathcal{E}'_\varepsilon$, we know by following the algorithm used to construct $\mathcal{G}^\varepsilon_{n,k}$ (see (2.11)) that

$$\mathcal{G}^\varepsilon_{n,k} \subset \overline{\Omega}_{n,k}, \quad \mathcal{G}^\varepsilon \cap \Omega_{n,k} = \mathcal{G}^\varepsilon_{n,k} \cap \Omega_{n,k}.$$

We are going to prove that $\Omega^\varepsilon_{n,k} \Delta \Omega_{n,k}$ is located around the boundary of $\Omega_{n,k}$.
First, let $\mathbf{x}$ in $\Omega^\varepsilon_{n,k} \setminus \Omega_{n,k}$. By construction, see (2.14), the center of the periodic cell $\mathcal{Y}^{n,k}_\varepsilon$ closest to $\mathbf{x}$ among the family $(\mathcal{Y}^{m,j}_\varepsilon)_{(m,j)\in\mathcal{E}_\varepsilon}$ belongs to $\overline{\Omega}_{n,k}$. Hence, thanks to (2.45), there exists $C > 0$ independent of ε such that:

$$\mathrm{dist}(\mathbf{x}, \partial\Omega_{n,k}) \le C\varepsilon.$$

Conversely, let $\mathbf{x}$ in $\Omega_{n,k} \setminus \Omega^{\varepsilon}_{n,k}$. Then, the center of the periodic cell $\mathcal{Y}^{n,k}_{\varepsilon}$ closest to $\mathbf{x}$ belongs outside of $\Omega_{n,k}$. Again, thanks to (2.45), there exists $C > 0$ independent of $\varepsilon > 0$ such that:

$$\operatorname{dist}(\mathbf{x}, \partial\Omega_{n,k}) \leq C\varepsilon.$$

Hence, the symmetric difference between $\Omega_{n,k}$ and $\Omega^{\varepsilon}_{n,k}$ satisfies:

$$\Omega^{\varepsilon}_{n,k} \Delta \Omega_{n,k} \subset \{\mathbf{x} + \mathbf{h} \in \Omega \mid \mathbf{x} \in \partial\Omega_{n,k},\ |\mathbf{h}| < C\varepsilon\}\,. \tag{2.51}$$

We recognize in the right–hand side the ε–parallel set of $\Omega_{n,k}$. Let us estimate its volume thanks to Lemma 2.A.2: the conditions of regularity and approximability of the decompositions, see Definitions 2.1.3 and 2.1.6, imply that the subdomain $\Omega_{n,k}$ satisfies the hypothesis of Lemma 2.A.2 with the constants:

$$\kappa = C_1 |\Omega_{n,k}|^{\frac{d-1}{d}}, \qquad \delta = \rho_{n,k} = r \operatorname{diam}(\Omega_{n,k}) \geq C_2 |\Omega_{n,k}|^{1/d}, \qquad \theta > 0,$$

where θ, C_1, $C_2 > 0$ are independent of ε, n and k. Hence, the following upper bound holds:

$$|(\partial\Omega_{n,k} + B(0, C\varepsilon)) \cap \Omega| \leq C\varepsilon\ \max\left(|\Omega_{n,k}|^{\frac{d-1}{d}}, \varepsilon^{d-1}\right).$$

Now we deduce from (2.51) the estimate:

$$\left|\Omega^{\varepsilon}_{n,k} \Delta \Omega_{n,k}\right| \leq C\varepsilon\ \max\left(|\Omega_{n,k}|^{\frac{d-1}{d}}, \varepsilon^{d-1}\right), \qquad \text{for all } (n,k) \in \mathcal{I}_{\varepsilon} \cup \mathcal{E}_{\varepsilon}. \tag{2.52}$$

And finally, combining (2.47), (2.52) and (2.50), we obtain

$$\left|\Omega^{\varepsilon}_{n,k} \Delta \Omega_{n,k}\right| \leq C\varepsilon\ |\Omega_{n,k}|^{\frac{d-1}{d}}, \qquad \text{for all } (n,k) \in \mathcal{I}_{\varepsilon} \cup \mathcal{E}_{\varepsilon}.$$

This finishes the proof of the Proposition. □

Chapter 3

Numerical Applications

We present in this Chapter the numerical approach we adopted to simulate a material which obeys the homogenized parenchyma models (1.81) or (1.117) we have obtained in Chapter 1. The main difficulty is the non–local operator in space which appears in the homogenized problems, as it cannot be discretized directly on the finite elements basis.

First, we introduce a mixed method based on a finite elements formulation and two algorithms based on the tree structure designed to take care efficiently of the non–local operator. Then, we show and comment some numerical results we have obtained using a mesh representing an idealized piece of parenchyma as the square example presented in Section 2.2.

Contents

3.1 Discretization of the homogenized problem 95
3.2 Numerical scheme 96
3.3 A word on the computation of the homogenized parameters. 98
3.4 Numerical results 99
3.5 Numerical study of the energy dissipation 100

3.1 Discretization of the homogenized problem

We present first the discretization scheme of the homogenized system of equations. For simplicity, the volumic force $\mathbf{f}$ and the pressure at the root of the tree p_e will be zero in this Section, and the system is driven by the pressure applied on the external boundary p_N. Keeping the notations of the homogenized problem in the compressible case, we can write the problem as a first-order mixed problem as follows.

Recall that $\mathbf{u}$ is the displacement of the homogenized material and π is a pressure variable, and let us also introduce as an additional variable the velocity, noted $\mathbf{v}$, of the homogenized material. Then $(\mathbf{u}, \mathbf{v}, \pi)$ satisfy the following formulation:

$$
\begin{cases}
\partial_t \mathbf{u} = \mathbf{v}, & \text{in } \Omega, \quad (3.1a)\\
\theta\rho\partial_t \mathbf{v} = \mathbf{div}\left(\mathcal{A}^{hom} e(\mathbf{u}) - \partial_t \pi \mathcal{B}^{hom}\right), & \text{in } \Omega, \quad (3.1b)\\
\pi + \tau_{hom}\dfrac{\partial}{\partial t}\mathcal{R}\pi = -\mathcal{R}\left(\mathcal{B}^{hom} : e(\mathbf{u})\right), & \text{in } \Omega, \quad (3.1c)\\
\left(\mathcal{A}^{hom} D(\mathbf{u}) - \partial_t \pi \mathcal{B}^{hom}\right)\mathbf{n} = -p_N \mathbf{n}, & \text{on } \Gamma_N, \quad (3.1d)\\
\mathbf{u} = \mathbf{0}, & \text{on } \Gamma_D, \quad (3.1e)\\
\mathbf{u}(0) = \mathbf{u}_0, \qquad \mathbf{u}_t(0) = \mathbf{u}_1, \qquad \pi(0) = (1-\theta)\mathcal{R}(\mathrm{div}_{\mathbf{x}}\mathbf{u}_0). & \text{in } \Omega. \quad (3.1f)
\end{cases}
$$

Remark 3.1.1. *This formulation holds also in the incompressible case, where the parameters $\mathcal{A}^{hom}$, $\mathcal{B}^{hom}$ and τ_{hom} are identified as:*

$$\mathcal{A}^{hom} = \mathcal{A}^{hom}_{inc}, \qquad \mathcal{B}^{hom} = (1-\theta)\mathrm{Id}, \qquad \tau_{hom} = 0.$$

Time discretization We introduce $\Delta t > 0$ a timestep, $t_n = n\Delta t$ and, for any vector $\mathbf{w}$, $\mathbf{w}^n(\mathbf{x}) = \mathbf{w}(t_n, \mathbf{x})$. We use a two–stage, second order singly diagonally implicit Runge-Kutta scheme (SDIRK) to discretize the system (3.1).

The properties of this method are detailed for example in [OS95]. In particular, it is only necessary to know how to solve a single implicit Euler step for the system (3.1) to apply this Runge–Kutta scheme, for which the semi–discretized variational formulation reads as follows. We write

$$\mathbf{u}^{n+1} = \mathbf{u}^n + \Delta t \mathbf{k}_u, \quad \mathbf{v}^{n+1} = \mathbf{v}^n + \Delta t \mathbf{k}_v \quad \text{and} \quad \pi^{n+1} = \pi^n + \Delta t k_\pi,$$

where $\mathbf{k}_u$, $\mathbf{k}_v \in \mathbf{V}$ and $k_\pi \in L^2(\Omega)$ solve:

$$\begin{cases} \displaystyle\int_\Omega \theta\rho \mathbf{k}_v \cdot \mathbf{w} = -\int_\Omega \mathcal{A}^{hom}\left(e(\mathbf{u}^n + \Delta t \mathbf{k}_u)\right) : e(\mathbf{w}) \\ \qquad\qquad + \displaystyle\int_\Omega k_\pi \mathcal{B}^{hom} : e(\mathbf{w}) + \int_{\Gamma_N} p_N \mathbf{w}\cdot\mathbf{n}, \qquad \text{for all } \mathbf{w} \in \mathbf{V}, & \text{(3.2a)} \\ \mathbf{k}_u = \mathbf{v}^n + \Delta t \mathbf{k}_v, & \text{(3.2b)} \\ \left(\Delta t \mathrm{Id} + \tau_{hom}\mathcal{R}\right) k_\pi = -\pi^n - \mathcal{R}\left(\mathcal{B}^{hom} : e(\mathbf{u}^n + \Delta t \mathbf{k}_u)\right). & \text{(3.2c)} \end{cases}$$

Space discretization Suppose that Ω is a polygonal domain. Given a mesh size $h > 0$, we can suppose (see Chapter 2) that we have a finite multi–scale decomposition $\mathcal{O}^h$ in which all subdomains are polygonal. We introduce the following discretization spaces for the displacement and the pressure:

- the discrete finite elements space $\mathbf{V}_h \subset \mathbf{V}$, composed of $P1$ elements based on a regular triangulation of mesh size h adapted to this multi–scale decomposition,
- the discrete pressure space M_h as the set of functions which are constant by cell on the subdomains $\Omega^h_{n,k}$ with $(n,k) \in \mathcal{E}_h$.

We approximate the resistance operator $\mathcal{R}$ by $\mathcal{R}_h$, which amounts to a truncature of the bronchial tree (see Section 2). Note that the matrix associated with $\mathcal{R}_h$ in M_h is a symmetric definite positive matrix $A^h D_h$, where A^h is the matrix associated with the resistances of the tree defined in (1.11) (see Proposition 1.1.5), and D_h is the mass matrix of M_h, which is diagonal (its entry for the basis function associated with the subdomain $\Omega_{n,k}$ is the volume $|\Omega_{n,k}|$). As a consequence, $\mathcal{R}_h$ is an isomorphism from M_h onto itself.

We now express the approximate solution as $\mathbf{u}^n_h$, $\mathbf{v}^n_h \in \mathbf{V}_h$ and $\pi^n_h \in M_h$. For any given function $\mathbf{w}$ in $\mathbf{V}_h$ or ψ in M_h, we denote by $\hat{\mathbf{w}}$ or $\hat{\psi}$ the corresponding vector of unknowns.

3.2 Numerical scheme

We propose an algorithm that enables us to solve efficiently the problem (3.2). The idea is to eliminate $\mathbf{k}_v$ and k_π and solve the resulting linear system by an iterative solver, without assembling the full matrix A^h, associated with the non–local resistance operator $\mathcal{R}_h$. From the variational formulation, we see that the non–local term can be interpreted as an additive perturbation over the original elastic FEM matrix $E_{\Delta,h}$, which is associated with the following bilinear form on $\mathbf{V}_h$:

$$(\mathbf{u}_h, \mathbf{w}_h) \mapsto \int_\Omega \theta\rho \mathbf{u}_h \cdot \mathbf{w}_h + \Delta t^2 \int_\Omega \mathcal{A}^{hom} e(\mathbf{u}_h) : e(\mathbf{w}_h).$$

Let B_h be the FEM matrix whose entries are $\int_{\Omega_{n,k}} \mathcal{B}^{hom} : e(\boldsymbol{\phi}_i)$ (where $\boldsymbol{\phi}_i$ is a FEM displacement basis function). We derive from (3.2) the following linear system:

$$\left(E_{\Delta t,h} + \Delta t B_h \left(\mathrm{Id} + \frac{\tau_{hom}}{\Delta t} A^h D_h \right)^{-1} A^h B_h^T \right) \hat{\mathbf{k}}_u = \hat{\mathbf{F}}^n, \tag{3.3}$$

where the right–hand side $\hat{\mathbf{F}}_h^n$ is the vector associated to a linear form denoting known terms corresponding to the previous timesteps:

$$\mathbf{F}_h^n(\mathbf{w}_h) = \int_\Omega \mathbf{v}_h^n \cdot \mathbf{w}_h - \Delta t \int_\Omega \mathcal{A}^{hom} e(\mathbf{u}_h^n) : e(\mathbf{w}_h) + \Delta t \int_{\Gamma_N} p_N \mathbf{w}_h \cdot \mathbf{n} + \int_\Omega \left(\left(\mathrm{Id} + \frac{\tau_{hom}}{\Delta t} \mathcal{R} \right)^{-1} \left(\pi_h^n + \mathcal{R} \left(\mathcal{B}^{hom} : e(\mathbf{u}_h^n) \right) \right) \right) \mathcal{B}^{hom} : e(\mathbf{w}_h).$$

The matrix appearing on the left–hand side of (3.3) is symmetric and positive definite. We use the conjugate gradient algorithm to solve the linear system, preconditionning by the matrix $E_{\Delta t,h}$ corresponding to the purely elastic problem. The matrix A^h is not assembled: matrix–vector products involving A^h or $\left(\mathrm{Id} + \frac{\tau_{hom}}{\Delta t} A^h D_h \right)^{-1}$ are computed by a fast algorithm thanks to the tree structure, which we describe now.

Tree-based algorithms

- First, we propose an efficient algorithm for computing the product $\mathbf{p} = A^h \mathbf{q}$, where $\mathbf{p}$ stands for the vector of pressures indexed by $\mathcal{E}_h$, the set indexing the ends of the dyadic tree $\mathcal{T}_h$, and $\mathbf{q}$ stands for a set of fluxes (see Section 1.1.3). Note that we use $\mathcal{E}_h$ as a set of indices for the degrees of freedom of M_h. Let $N_h = \max\{n \mid (n,k) \in \mathcal{E}_h\}$ be the maximum length of the tree and $\mathcal{I}_h$ be the set of indices of the interior nodes of $\mathcal{T}_h$.

Given $\mathbf{q} = (q_{n,k})_{(n,k)\in\mathcal{E}_h}$, compute $\mathbf{p} = A^h \mathbf{q}$ as follows:

1. For $n = N_h - 1, \dots, 0$, evaluate and store the fluxes for all k such that $(n,k) \in \mathcal{I}_h$ thanks to the flux conservation law:
$$q_{n,k} = q_{n+1,2k} + q_{n+1,2k+1}.$$
2. Set $p_0 = 0$ and $p_{0,0} = r_0 q_{0,0}$.
3. For $n = 1, \dots, N_h$, evaluate the pressures for all k such that $(n,k) \in \mathcal{I}_h \cup \mathcal{E}_h$, thanks to the relation:
$$p_{n,k} = p_{n-1,k/2} + r_{n,k} q_{n,k}.$$
4. Obtain the vector $\mathbf{p} = (p_{n,k})_{(n,k)\in\mathcal{E}_h}$.

Algorithm 3.1 – Pressure algorithm

- Next, we construct an efficient algorithm for computing $\mathbf{q} = \left(\mathrm{Id} + \frac{\tau_{hom}}{\Delta t} A^h D_h \right)^{-1} \mathbf{p}$ as follows. Recall that D_h is a diagonal matrix whose entries are the volumes $|\Omega_{n,k}^h|$. Given $\omega > 0$, we define the symmetric definite positive matrix $A_\omega^h = D_h^{-1} + \omega A^h$. Then, thanks to the Proposition 1.1.5, we observe that A_ω^h also represents the flux–to–pressure relation in the tree $\mathcal{T}_h$, with modified resistances $(r_{n,k}^\omega)$ defined by:

$$r_{n,k}^\omega = \omega r_{n,k} \text{ for } (n,k) \in \mathcal{I}_h, \qquad r_{n,k}^\omega = |\Omega_{n,k}|^{-1} + \omega r_{n,k} \text{ for } (n,k) \in \mathcal{E}_h.$$

Hence, we want now to compute the set of fluxes $\mathbf{q}$ exiting this modified tree for a given set of pressures $\mathbf{p}$. The idea is based on the concept of equivalent pressure and resistance of a subtree, similar to the concept of equivalent resistance in electric networks.

We define recursively the equivalent resistance $R^\omega_{n,k}$ of the subtree stemming from the edge $X_{n-1,k/2}X_{n,k}$:

- For $(n,k) \in \mathcal{E}_h$, we set $R^\omega_{n,k} = r^\omega_{n,k}$,
- For $n = N_h - 1, \dots, 0$ and k such that $(n,k) \in \mathcal{I}_h$, we set

$$R^\omega_{n,k} = r^\omega_{n,k} + \left(1/R^\omega_{n+1,2k} + 1/R^\omega_{n+1,2k+1}\right)^{-1}.$$

Given $\mathbf{p} = (p_{n,k})_{(n,k)\in\mathcal{E}_h}$, compute $\mathbf{q} = D_h^{-1}\left(A^h_\omega\right)^{-1}\mathbf{p}$ as follows:

1. Initialize the equivalent pressures at the ends of the tree as $P_{n,k} = p_{n,k}$, for $(n,k) \in \mathcal{E}_\varepsilon$.
2. For $n = N_h - 1, \dots, 0$, evaluate the equivalent pressures for all k such that $(n,k) \in \mathcal{I}_h$, defined as:
$$P_{n,k} = \frac{R^\omega_{n+1,2k+1}}{R^\omega_{n+1,2k} + R^\omega_{n+1,2k+1}} P_{n+1,2k} + \frac{R^\omega_{n+1,2k}}{R^\omega_{n+1,2k} + R^\omega_{n+1,2k+1}} P_{n+1,2k+1},$$
and store the flux deviation defined as:
$$d_{n,k} = \frac{P_{n+1,2k} - P_{n+1,2k+1}}{R^\omega_{n+1,2k} + R^\omega_{n+1,2k+1}}.$$
3. Set $\phi_{0,0} = P_{0,0}/R^\omega_{0,0}$.
4. For $n = 0, \dots, N_h - 1$ and for all k such that $(n,k) \in \mathcal{I}_h$, evaluate the fluxes $\phi_{n+1,2k}$ and $\phi_{n+1,2k+1}$ thanks to the relation:
$$\phi_{n+1,2k} = \frac{R^\omega_{n+1,2k+1}}{R^\omega_{n+1,2k} + R^\omega_{n+1,2k+1}} \phi_{n,k} + d_{n,k},$$
$$\phi_{n+1,2k} = \frac{R^\omega_{n+1,2k}}{R^\omega_{n+1,2k} + R^\omega_{n+1,2k+1}} \phi_{n,k} - d_{n,k}.$$
5. Obtain the vector $\mathbf{q} = (|\Omega^h_{n,k}|^{-1}\phi_{n,k})_{(n,k)\in\mathcal{E}_h}$.

Algorithm 3.2 – Flux algorithm

Remark 3.2.1. *These expressions simplify greatly if the tree is regular: for example, the equivalent pressure is then the average pressure and the equivalent resistances do not depend on k.*

Clearly, the cost of both algorithms and the memory requirements are linear with respect to the number N of degrees of freedom of M^h, since the tree $\mathcal{T}_h$ contains at most $2N$ vertices.

3.3 A word on the computation of the homogenized parameters.

To obtain the entries of the tensor $\mathcal{A}^{hom}$ and the matrix $\mathcal{B}^{hom}$, as well as the value of τ_{hom}, we solve numerically the elliptic cell problems (1.75) and (1.76). We refer the reader to [BGMO08] for a detailed numerical study of the homogenized coefficients as a function of the Lamé parameters. The computation of the homogenized elastic coefficients was performed on an hexagonal periodic cell for an incompressible material, with $\mu = 10^5 Pa$. The choice of an hexagonal geometry ensures that the homogenized material is isotropic, which is not the case for a square periodic cell, and is also a better fit to the geometry of the alveoli. Figure 3.1 shows the values taken by the correctors $\boldsymbol{\chi}^{1,1}$ and $\boldsymbol{\chi}^{1,2}$.

The corresponding homogenized values of the Lamé parameters were found to be respectively $\lambda_{hom} = 2820$ and $\mu_{hom} = 637$.

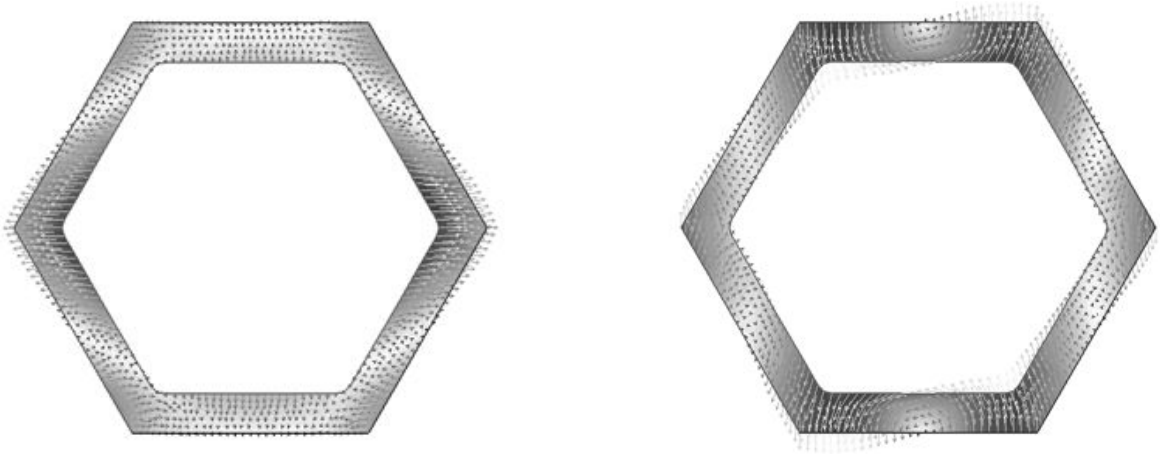

Figure 3.1 – Periodic correctors, $\boldsymbol{\chi}^{1,1}$ (left) and $\boldsymbol{\chi}^{1,2}$ (right)

3.4 Numerical results

We present a few numerical results obtained in the case of normal respiration simulations in a two–dimensional square domain with a side measuring $20cm$, connected to a geometric resistive tree with 12 generations as described in section 2.2. The geometric parameter is taken to be $\alpha = 1.63$ and the resistance at the root of the tree is $r_0 = 8020Pa \cdot s/m^3$. We apply a periodic smoothed pulse force of period $T = 4s$, with $p_{max} = 1.5 \times 10^3 Pa$ and $p_{min} = 0Pa$ on all sides of the square through Neumann conditions. For our first experiment, which simulates to normal breathing, we chose a relatively smooth profile described by the complicated expression:

$$p(t) = 750 \left(1 + \tanh\left(7 \cos\left(\frac{\pi}{2}t\right) - 3.5\right)\right).$$

Figure 3.2 shows the variation in area (in cm^2) versus time t (in s) and the air flow (in $cm^2 \cdot s^{-1}$) through the root of the bronchial tree versus time t, for a tree with 12 generations. We used the finite element software FreeFem++ [Hec12] to perform the computations.

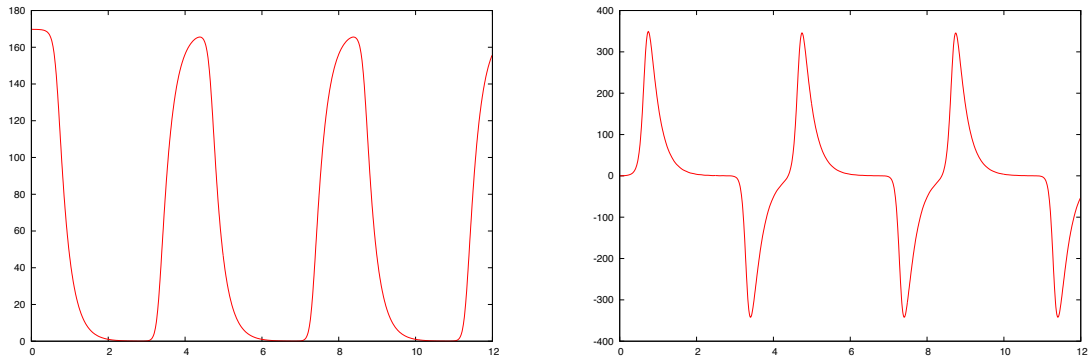

Figure 3.2 – Area change (left) and air flow (right) versus time

For a second experiment, we tried to investigate a sharper profile, closer to a forced breathing test:

$$p(t) = 750 \left(1 + \tanh\left(20 \cos\left(\frac{\pi}{2}t\right) - 5.\right)\right).$$

The corresponding medical test would run as follows.

- At time $t = 0$s, we start from a state of inspiration where the patient's lung is inflated and in equilibrium with the downwards force exerted at the diaphragm.
- After a short while, the patient lets go and the pleural pressure goes suddenly to zero. The lung returns progressively to an equilibrium position and the air exits through the bronchial tree.
- After around 2.5 seconds, the pressure increases again, the lung reinflates, air comes in the lung through the bronchial tree and we continue the cycle.

Traditionnally, the quantities measured while performing such a test would be the volume expired by the patient and the air flow blown out at the mouth.

The curves in Figure 3.2 agree very closely with the results obtained with a simple linear one–compartment model for the lung, see [Bat09]. This is a consequence of the perfect symmetry of the domain and tree used in the computations, modeling a perfectly homogeneous lung. The model also allows us to investigate the influence of local perturbations on this experiment, inducing an imbalance in the alveolar pressure across the lungs. For example, we present the variations in the phase diagram induced by a unilateral ten–fold increase of the distal resistances or a doubling of the stiffness in one half of the domain in Figure 3.3. This phase diagram, obtained by medical doctors with a device called a spirometer, can be studied to diagnose a number of respiratory pathologies. On Figure 3.3, we observe that the asymmetry introduces a concave profile because each side empties or fills at a different rate. Such examples show that this model could be useful in reproducing some spatially localized pathological features (emphysema, bronchitis, tumors...)

Remark 3.4.1. *It is not possible, with our linear model, to study a profile of maximal expiration as it is determined by the spirometer. To extend our model so that we could study this experiment, it would at least be necessary to solve the full Navier–Stokes equations in a geometry corresponding to the first generations of the bronchial tree to capture the nonlinearity due to inertial effects at such high Reynolds numbers.*

Let us explain a few particularities found on the curves shown in Figure 3.3.

- On the first set of curves (a), we observe that the loop corresponding to the increased resistances case is not closed, while all the other loops in the experiment are closed. This is due to the proportional ten–fold increase one of the relaxation times of the material (see Remark 2.2.12) associated with the ten–fold increase of the resistances on one side. Hence while, in all other cases, the system had time to relax to the starting position which was at equilibrium with the maximum pressure, this is not the case when the resistances are increased by a large enough factor.
- On the second set of curves (b), we start from a different volume of the lung depending on the stiffness. This is because we start from a state of equilibrium with the maximum inflating pressure, and the degree of inflation of the material in this state depends on its elastic stiffness. As a result, total expired volume is less at maximum expiration.

3.5 Numerical study of the energy dissipation

We have seen that the tree introduces a dissipation of energy in the material modeling the viscous effects of the airflow through the bronchial tree. An interesting question is the asymptotic behavior of the system relaxing freely from a stressed state. The pressure term corresponding to the viscous dissipation of energy in the homogenized model (3.1) by the bronchial tree is not coercive in $\mathbf{H}^1$ except in 1D, and it is unknown if it is coercive in $\mathbf{L}^2$ in a multi–dimensional setting. Coercivity

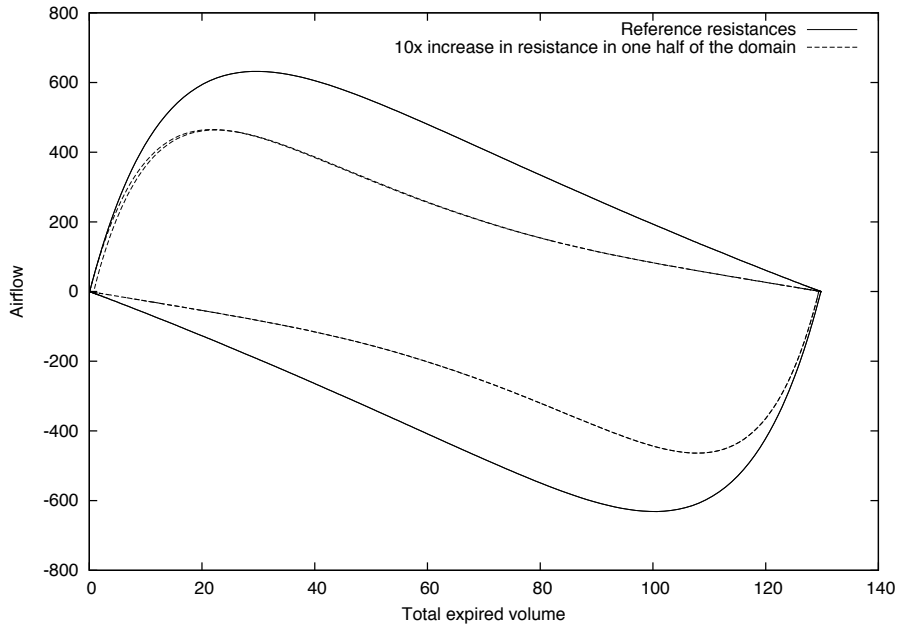

(a) Increase of the distal resistances

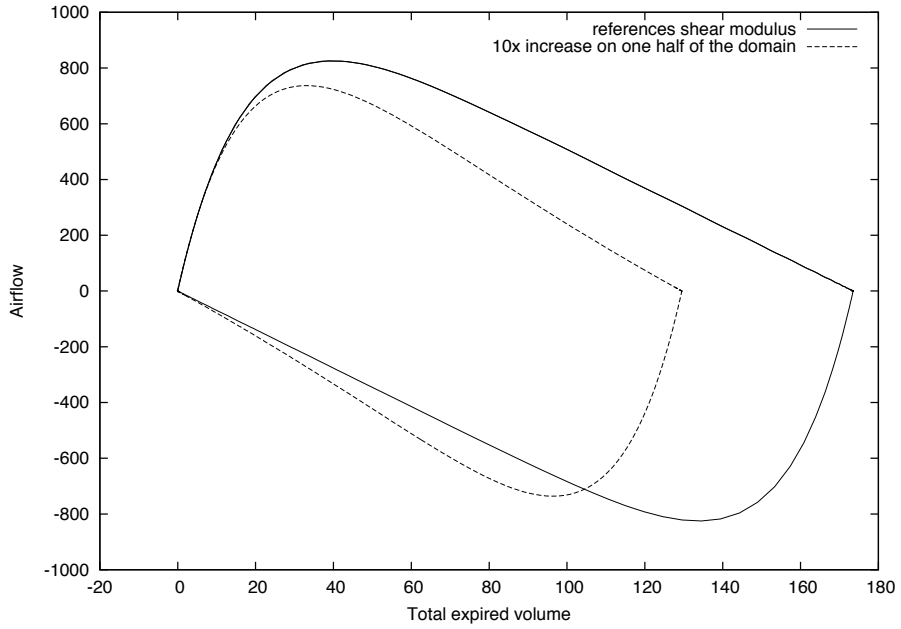

(b) Increase of the material stiffness

Figure 3.3 – Flow–Volume loops. The origin on the x axis was moved so that the curves start from a zero total expired volume.

of the viscous term is usually an essential argument to prove that the energy goes to zero in the limit where the time t goes to infinity by Hille–Yosida theory. For example, in the incompressible case the variational form corresponding to the viscous term writes, see the problem (1.117):

$$(1-\theta)\int_\Omega \partial_t \mathcal{R}\,(\mathrm{div}\mathbf{u})\,\mathrm{div}\mathbf{v}.$$

This fact suggests that the following open problems may not have an easy solution:

- **does the energy of the system reduce to zero as time goes to infinity?**
- **if the energy does go to zero, what is the profile (exponential, polynomial, fractional) of this decay ?**

A few answers to this problem were given by C. Vannier in [Van09]. In a similar 1D model connected to a geometric tree (see Section 2.2.2), the system was shown to relax eventually to the rest state for all values of the scale parameter α of the geometric law governing the airway resistances with $0 < \alpha < 2$. The energy dissipation rate was also proved to be exponential for $1 < \alpha < 2$. However, these results depend on the fact that the viscous term corresponding to the tree is coercive in 1D and the analysis cannot be extended to higher dimensions. In addition, simulations also presented in [Van09] for the relaxation from a stressed state of a bidimensional domain with four holes, using the model (1.15), show a sub–exponential rate of energy decay which becomes closer to an exponential curve as the value of α grows.

For the homogenized model in a multi–dimensional setting, this is an open question. Numerical simulations can provide some intuition into this theoretical issue, and using the numerical strategy previously described, we have computed numerically the energy decay for our homogenized model when the material is allowed to relax freely from a stressed state. Using the same computational domain connected with a 12–generation geometric tree and homogenized elastic parameters for the material as in Section 3.4, the parameter α is allowed to vary, taking a few values between 0.5 and 1.9. As α varies, we keep the value of the resistance at the root of the tree fixed at $r_0 = 4000$. We impose Dirichlet boundary conditions on all sides of Ω. The velocity of the homogenized parenchyma is chosen identically zero at the initial time of the simulation, while the initial displacement $\mathbf{u}_0$ is the solution of the static linearized elasticity problem

$$\begin{cases} \mathbf{div}\left(\mathcal{A}^{hom}_{inc} e(\mathbf{u}_0)\right) = -\nabla p_0, & \text{in } \Omega, \qquad (3.4a)\\ \mathbf{u}_0 = \mathbf{0}, & \text{on } \Gamma_D \cup \Gamma_N, \qquad (3.4b) \end{cases}$$

where p_0 takes the value 1 on the subdomain $\Omega_{4,3}$ and 0 elsewhere. This amounts to inflating this particular subdomain of the parenchyma before letting go suddenly at time $t = 0$, as shown in Figure 3.4.

The results are shown in Figure 3.5 in a logarithmic scale for the values of the total energy of the system. Straight lines denote an exponential decrease. None of the values of α shows a true exponential decrease for the whole time range, but as α increases, the energy dissipation shows a more piecewise exponential behavior.

Remark 3.5.1. *We show the whole range of values obtained numerically, but it should be noted that, due to numerical errors, the results tend to lose their validity once we dip below the .1 mark. For this numerical simulation, we set $\Delta t = 1e-3$, so since the time–stepping method is of second–order the precision does not allow us to consider the results as significant below $1e-5$ or $1e-6$, at best and without taking into account the spatial errors.*

For $\alpha = 0.7$, the rate of energy dissipation decreases smoothly along the time range considered, so that the energy dissipated over a long time period is by far the least among the values of α

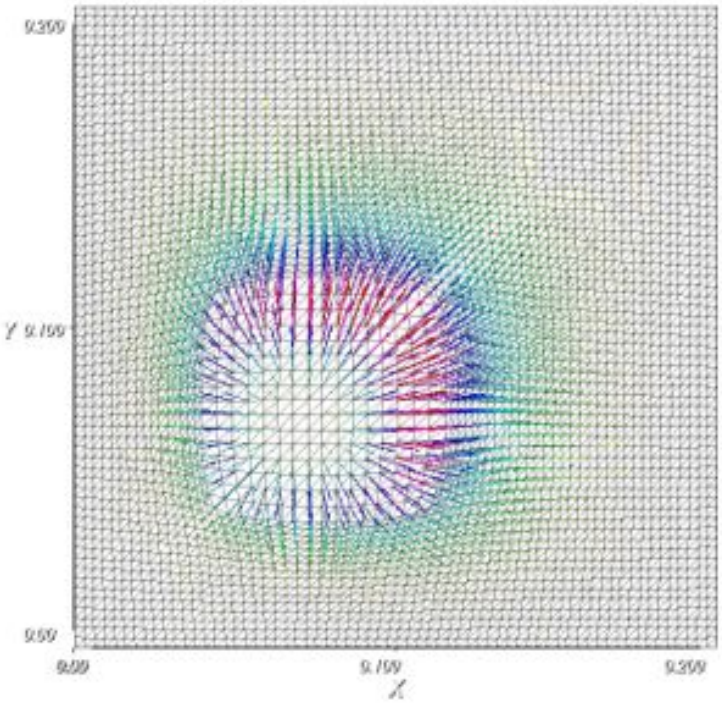

Figure 3.4 – Initial position of the parenchyma

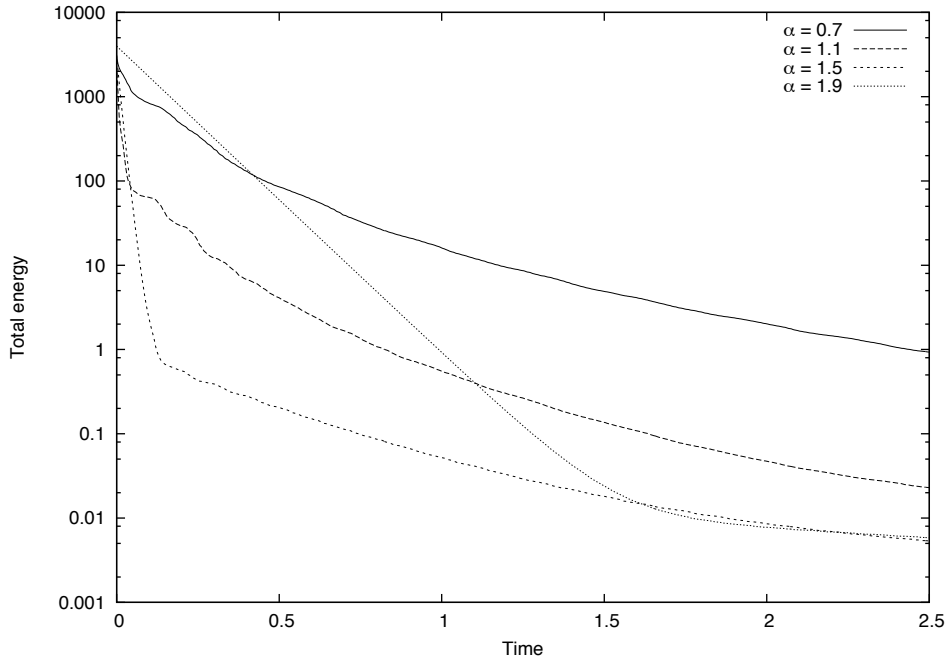

Figure 3.5 – Total energy as a function of time for a few values of α, in logarithmic scale

considered. Longer runs of the simulation do not clarify if the curve goes to zero in the end. The intermediate value $\alpha = 1.5$, which is closest to the true physiological value, seems to yield the most efficient system from a dissipation point of view. The initial energy drop during the first 0.6s is the largest of the group, and almost all the initial energy has been dissipated at time $t = .3s$. It is also the largest over the duration of the simulation, although we cannot trust this result due to numerical precision considerations. Finally, for $\alpha = 1.9$, we observe a comparatively slow exponential decrease from the start, which is not the case for the other values of α. There seems to be a sharp transition between two constant exponential rates of dissipation around $t = 1.6s$, although this may be a numerical artifact as the second line is below the numerical precision. The initial rate of decrease is by far the slowest of the group, due to over–dampening, but over the long run it seems that the corresponding tree is more efficient at completely dissipating the system's energy than for lower values of α.

Conclusion

The proposed multi–scale model enables us to describe the motion of the parenchyma taking into account the non–local viscous dissipation of energy by the air flow through the bronchial tree, and possibly nonhomogeneous properties of the parenchyma. We have studied how to construct the resistance operator for general three–dimensional structures. To model realistic situations, and in particular forced respiration situations, this approach has to be extended to non–linear problems and integrate for example non–linear elastic or viscoelastic effects due to the complex nature of the lung tissue, or simulations of the full Navier–Stokes equations in the first few generations of the bronchial tree to correctly model the flow of air.

Part II

Modelling the Sound Propagation through the Parenchyma

Chapter 4

Sound Modelling in the Parenchyma

Contents

4.1 Introduction and motivation . . . 107
4.2 Description of the coupling of the elastic and acoustic equations in a perforated domain . . . 109
4.2.1 Geometric setting . . . 109
4.2.2 Acoustic–Elastic interaction . . . 111
4.2.3 A few useful definitions and results . . . 115
4.2.4 Gårding's inequality and well–posedness . . . 118
4.2.5 Energy estimates . . . 120
4.3 Two–scale homogenization of the coupled model . . . 121
4.3.1 Two–scale problem identification . . . 122
4.3.2 Proof of the *a priori* bounds and Theorem 4.3.1 . . . 131
4.3.3 Convergence Theorem and homogenized problem . . . 133
4.4 Conclusion . . . 133
4.5 Annex . . . 134

4.1 Introduction and motivation

Lung sounds provide a cheap, non–invasive, widely used diagnostic technique which is of great interest for the detection of some pathologies in the lungs [PKW97, RHD+10]. Some diseases are associated with changes in the structure of the lung at various scales. Medical doctors have developed a good empirical understanding of the relation between the characteristics of the lung sounds they can hear, for example thanks to the stethoscope, and the underlying pathologies of a patients' lung; but researchers lack a precise physical understanding of the generation and propagation of sound waves through the respiratory system and the lung tissue, as well as of the changes in acoustic properties associated with underlying lung diseases. Another factor of interest is the need for understanding the propagation of pressure waves due to explosions or high–velocity impacts on the chest, thought to be responsible for lung contusions [GWN02].

The lung is a very complex structure. The acoustic properties of the lungs' material (called the parenchyma) are the consequence of a very complex, porous microstructure, similar to a foam. The lungs contain up to 300 million air pockets called the alveoli, connected by a bifurcating network of airways and embedded in an elastic matrix of connective tissue. It is hard to deduce accurately the macroscopic properties of such porous media, and macroscopic models of reduced complexity are used in practice. Models based on detailed tissue mechanics and geometry are expected to further improve the understanding of experimental studies [PKW97].

Current models for the acoustic properties of the lung parenchyma are usually simple and based on the work by Rice [Ric83], modelling the parenchyma as a homogeneous mixture of non–communicating air bubbles and tissue. When the sound wavelength is greatly superior to the size of the air bubbles, averaging the properties of the medium over volume leads to consider the porous medium as an elastic continuum. In this case, the speed of sound is independent of frequency and given by $c = (K/\rho)^{1/2}$, where K is the effective volumetric stiffness of the medium and ρ is the average density. This expression is usually called Wood's formula. When the volumetric proportion of the tissue phase is h, Rice argues that the effective stiffness under adiabatic conditions is found using the formula

$$\frac{1}{K} = \frac{1-h}{\gamma P} + \frac{h}{K_s},$$

where γ is the ratio of specific heats of the air, P is the gas pressure and K_t is the stiffness of the tissue structure. The average density is given by

$$\rho = (1-h)\rho_g + h\rho_s,$$

where ρ_g is the density of the air phase and ρ_s the density of the tissue phase. Experimental measurements of the speed of sound in the low–frequency range (100 Hz to 1000 Hz) presented in [Ric83, Kra83] show a good agreement with Woods' formula. We note also the one–dimensional study by Grimal et al. [GWN02] which shows, in particular, the limits of the homogeneous elastic representation as the frequency increases and the wavelength approaches the size of the alveoli.

Other acoustic models of the lung's parenchyma have been proposed, mainly to study the effects of air communication between alveoli, which is a factor at very low frequencies [BLD87]. The main wave propagation models for such porous media go back to the work of Biot [Bio56a, Bio56b]. Biot's equations were first introduced rather heuristically to characterize the flow of a viscous fluid through a porous elastic frame as well as the associated acoustic phenomena [Bio62]. Several authors have sought to derive this model using general homogenization theory [Aur80, BK82, SP80]. More recently, the subject has been revisited rigorously [All89, GM00] using two–scale homogenization theory [Ngu89, All92] with the additional assumption of periodicity. This approach has been applied to the lung by Owen and Lewis [OL01] to study high–frequency ventilation, and Siklosi et al. [SJTL08] to study the lungs of fetal sheep.

Here, we propose to revisit rigorously the non–dissipative model proposed by Rice [Ric83] for the propagation of low–frequency sound in a domain Ω modeling the parenchyma. This domain is occupied by an elastic deformable structure (the lung tissue [SIS+05]) and closed pockets filled with a compressible inviscid fluid (the air). We assume that the size of the alveoli is small compared to the wavelength, i.e. that the macroscale and microscale are well separated, and we use the two–scale homogenization technique in order to investigate the asymptotic behavior of this medium. In [FM03], the two–scale homogenization of an elastic structure is coupled with an inviscid, incompressible fluid satisfying the linearized incompressible Euler equations. Note that when the model includes a viscous fluid, the effective material obtained by homogenization usually depends strongly upon the contrast of property between the viscosity of the fluid and the elasticity of the structure, ranging from a viscoelastic material when this contrast is small to material with a diphasic macroscopic behavior when the contrast is strong [GM00]. Here, because the viscosity vanishes, the main difficulty is the absence of space derivatives of the fluid velocity in the linearized compressible Euler equations. Thus the result depends strongly upon the geometry of the micro–structure and specifically the connectedness of the fluid part. In this work, we assume that the alveoli are disconnected. This is based on the common assumption [Ric83, GWN02] that air does not communicate freely between neighbouring alveoli at frequencies above a few hundred hertz under normal circumstances. This hypothesis has been validated by a number of experimental studies, see e.g. [Kra83, BLD87]. The space repetition of the alveoli suggests us to consider an idealized medium containing a periodic arrangement of disconnected pores with a small period $\varepsilon > 0$.

The material we study behaves like a closed foam. Such a material was studied in the static case in [BGMO08], and we will see that we recover the same model in the vanishing frequency limit. We consider time–harmonic solutions to understand the behavior of the material in response to a harmonic forcing. To obtain a homogenized system, we pass to the limit as ε goes to zero and we use the two–scale convergence theory. In the dissipative case, this problem was tackled in [AAGM12]. The harmonic non–dissipative case brings a few specific difficulties since the problem set in the frequency domain, of a Helmhotz nature, is not coercive. This means that the standard two–scale homogenization procedure cannot be applied directly and we have to use some non–standard methods to study the convergence.

In the limit, we obtain a homogeneous, non dispersive elastic medium, as expected [PKW97]. We recover the effective coefficients by computing the solutions of cell problems. Interestingly, averaging effects on the fluid pressure give rise to a non–local term in the formulation of the cell problems, and we obtain the same elastic tensor as in [BGMO08]. We can perform a physical interpretation of the homogenized problem: the macroscopic effect of the gaseous bubbles is mainly a modification of the bulk modulus (compressibility) of the limit material.

The paper is organized as follows. First, we detail the geometry and derive the equations of the model. Then, we study the well–posedness of the coupled elastic–acoustic problem for a fixed value of the micro–scale parameter ε and show that it verifies a Fredholm Alternative Principle (Proposition 4.2.11). In section 4.3.1, we analyze the asymptotic behavior of the displacement field, using homogenization techniques and an argument by contradiction. The main result of the paper is the convergence Theorem 4.3.19, which describes both the two–scale convergence of the displacement field and the homogenized problem (4.74).

4.2 Description of the coupling of the elastic and acoustic equations in a perforated domain

4.2.1 Geometric setting

For the modelisation, we consider a volume Ω of lung parenchyma, filled homogeneously with a porous medium modeling the air–filled alveoli embedded in the elastic structural matrix. We suppose that Ω is a smooth, open domain in $\mathbb{R}^d$ with $d = 2$ or 3. We describe our periodically perforated material indexed by the small length scale ε, under the hypothesis of separation of the macroscopic and microscopic scales, by defining an open periodic unit cell $\mathcal{Y}$ representing the geometry of an alveolus. By rescaling, we normalize $\mathcal{Y}$ so that $|\mathcal{Y}| = 1$ and we define the associated periodic array $\mathbf{Z}$ of $\mathbb{R}^d$, which is the discrete set of translation vectors such that $\mathcal{Y} + \mathbf{Z}$ is a tiling of the whole space. The standard example is $\mathcal{Y} = (-1/2, 1/2)^d$ and $\mathbf{Z} = \mathbb{Z}^d$, we can also study for example a honeycomb as presented in Figure 4.1, where $\mathcal{Y}$ is an hexagon with side $a > 0$ such that its volume is 1 and $\mathbf{Z}$ the discrete lattice with basis $(0, a)$ and $\left(\sqrt{3}a/2, a/2\right)$ in $\mathbb{R}^2$, or a paving based on the truncated octahedron in $3D$ which is a standard representation of the alveoli [DMS80]. This provides a reference framework to study the asymptotic behavior when ε goes to zero. The reference unit cell is supposed to be divided between an elastic and a fluid (acoustic) part $\mathcal{Y}_S$ and $\mathcal{Y}_F$, where $\overline{\mathcal{Y}_F} \subset \mathring{\mathcal{Y}}$ is smooth, simply connected, and locally lies on one side only of its boundary. The boundary $\Gamma_F = \partial\mathcal{Y}_F$ is the interface between the two components of $\mathcal{Y}$. For convenience later in the paper, we suppose that the barycenter of $\mathcal{Y}_F$ is at the origin of $\mathbb{R}^d$.

More precisely, for any given small parameter $\varepsilon > 0$, we introduce the following notations.

- For a given a multi–index $\mathbf{k} \in \mathbf{Z}$, let

$$\mathcal{Y}_\varepsilon^{\mathbf{k}} = \varepsilon(\mathcal{Y} + \mathbf{k}), \quad \mathcal{Y}_{F,\varepsilon}^{\mathbf{k}} = \varepsilon(\mathcal{Y}_F + \mathbf{k}), \quad \mathcal{Y}_{S,\varepsilon}^{\mathbf{k}} = \varepsilon(\mathcal{Y}_S + \mathbf{k}), \quad \Gamma_{F,\varepsilon}^{\mathbf{k}} = \varepsilon(\Gamma_F + \mathbf{k}), \tag{4.1}$$

  that is, a translation by $\mathbf{k}$ and a rescaling by ε of the unit cell $\mathcal{Y}$.

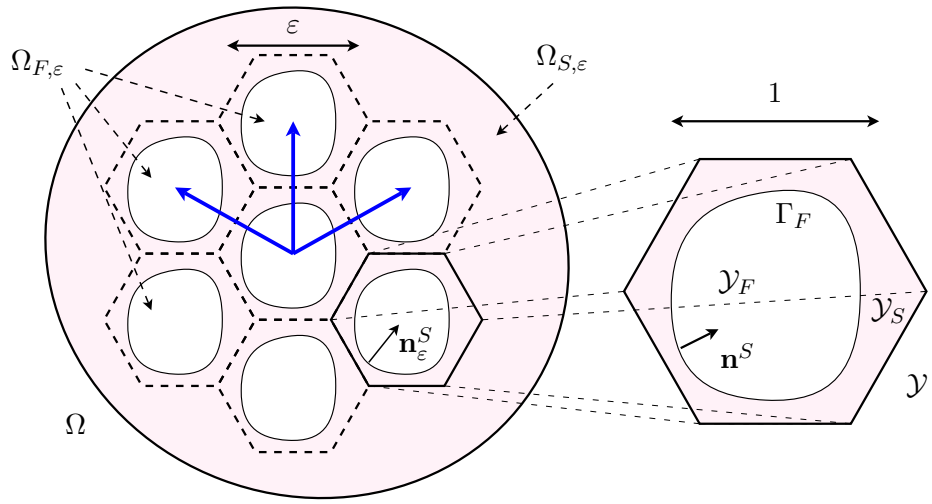

Figure 4.1 – Domain Ω and reference cell $\mathcal{Y}$

- Introducing the multi–index set

$$\mathbf{Z}_\varepsilon^\Omega = \{\mathbf{k} \in \mathbf{Z} | \overline{\mathcal{Y}_\varepsilon^{\mathbf{k}}} \subset \Omega\},$$

  we define the periodically perforated structure domain, the fluid domain and the interior interface respectively as

$$\Omega_{S,\varepsilon} = \Omega \setminus \bigcup_{\mathbf{k}\in\mathbf{Z}_\varepsilon^\Omega} \overline{\mathcal{Y}_F{}^{\mathbf{k}}}, \qquad \Omega_{F,\varepsilon} = \bigcup_{\mathbf{k}\in\mathbf{Z}_\varepsilon^\Omega} \mathcal{Y}_{F,\varepsilon}^{\mathbf{k}}, \qquad \Gamma_\varepsilon^I = \bigcup_{\mathbf{k}\in\mathbf{Z}_\varepsilon^\Omega} \Gamma_{F,\varepsilon}^{\mathbf{k}}. \tag{4.2}$$

- Let $\mathbf{n}^S$ and $\mathbf{n}_\varepsilon^S$ be unit normal vectors on the fluid–structure cell interface Γ_F and interior interface Γ_ε^I respectively, pointing in each case to the exterior of the structure represented respectively by $\mathcal{Y}_S$ and $\Omega_{S,\varepsilon}$.
- Let χ_F, χ_S be the characteristic functions of $\mathcal{Y}_F$ and $\mathcal{Y}_S$ respectively, and $\chi_{F,\varepsilon}$, $\chi_{S,\varepsilon}$, $\chi_{F,\varepsilon}^{\mathbf{k}}$, $\chi_{S,\varepsilon}^{\mathbf{k}}$ the characteristic functions of $\Omega_{F,\varepsilon}$, $\Omega_{S,\varepsilon}$, $\mathcal{Y}_{F,\varepsilon}^{\mathbf{k}}$ and $\mathcal{Y}_{S,\varepsilon}^{\mathbf{k}}$ respectively.
- The subscript # on the functional spaces' name will denote the property of periodicity with respect to $\mathbf{Z}$, in the sense that $C_\#^\infty(\mathcal{Y})$ is the space of $\mathbf{Z}$–periodic functions on $\mathbb{R}^d$ indefinitely differentiable on $\mathbb{R}^d$, and $H_\#^1(\mathcal{Y})$ and $L_\#^2(\mathcal{Y})$ are the closure of $C_\#^\infty(\mathcal{Y})$ respectively in the H^1– and the L^2–norm. Moreover, $H_\#^1(\mathcal{Y}_S)$ and $L_\#^2(\mathcal{Y}_S)$ are defined as the restrictions of functions in $H_\#^1(\mathcal{Y})$ and $L_\#^2(\mathcal{Y})$ to $\mathcal{Y}_S + \mathbf{Z}$.

Note that due to the choice of $\mathbf{Z}_\varepsilon^\Omega$, no hole intersects the exterior boundary of Ω. For this reason, $\partial\Omega_{S,\varepsilon} = \partial\Omega$ does not depend on ε. This will make the homogenization process, as ε goes to zero, more convenient but not fundamentally different from a case where the holes are allowed to sometimes intersect the exterior boundary.

As the material presents two characteristic length scales (macroscopic and microscopic), we introduce finally two sets of spatial variables: the ordinary position vector $\mathbf{x} \in \Omega$, and the position vector in a stretched coordinate system $\mathbf{y} = \varepsilon^{-1}\mathbf{x}$. The variable $\mathbf{x}$ will be called *slow variable* and the variable $\mathbf{y}$ *fast variable*, and as ε goes to zero we expect the two sets of variables to become independent. To make a difference between differentiation with respect to either set of variables $\mathbf{x}$ or $\mathbf{y}$, we will use a subscript as in $\nabla_\mathbf{x}$ or $\mathrm{div}_\mathbf{y}$ when there is a doubt. When necessary, we will use the Einstein convention of repeated indexes to write summations.

4.2.2 Acoustic–Elastic interaction

Following [HKR00], we write the model equations for the propagation of sound waves through our perforated material. As a first step, let us describe the equations governing this propagation in the time domain for a given parameter ε. As we are studying sound waves, the perturbation or displacement from rest of the structure or air is the relevant variable to consider. This perturbation is supposed to be small, so it is enough to consider the linearized behavior of both structure and air parts of the material to understand the wave propagation. The signal is then represented by a harmonic superposition of monochromatic waves, for which every excitation source and every variable obeys a harmonic dependence of frequency ω. Our goal is then to obtain a homogenized system in the asymptotic limit where ε goes to zero, describing the effective equation satisfied by the pressure wave for each value of ω.

Let us start to write the equations describing the mechanical behavior of the material. For simplicity, we adopt a Lagrangian point of view and denote $\mathbf{U}_\varepsilon$ the time–dependent displacement field throughout the structure and air parts of the domain Ω. We begin by modeling the elastic structure. Assuming that the wall material behaves like a linearized elastic medium, the stress tensor satisfies Hooke's law:

$$\sigma_\varepsilon(\mathbf{U}_\varepsilon) = \lambda\left(\mathbf{x}, \frac{\mathbf{x}}{\varepsilon}\right) \mathrm{div}(\mathbf{U}_\varepsilon)\mathrm{Id} + \mu\left(\mathbf{x}, \frac{\mathbf{x}}{\varepsilon}\right) e(\mathbf{U}_\varepsilon),$$

where $\lambda > 0$, $\mu > 0$ are the Lamé parameters, Id the identity matrix, and $e(\mathbf{U}_\varepsilon)$ is the linearized Cauchy strain tensor:

$$e(\mathbf{U}_\varepsilon) = \frac{1}{2}\left(\nabla \mathbf{U}_\varepsilon +^T \nabla \mathbf{U}_\varepsilon\right).$$

Note that we allow λ and μ to vary through the domain, for example to model a pathology where the parenchyma is locally rigidified. To model variations both at the macroscopic level and at the alveolar, microscopic level, we allow a dependence on both the slow variable $\mathbf{x}$ and the fast variable $\mathbf{y} = \varepsilon^{-1}\mathbf{x}$. We assume that λ and μ are essentially bounded, continuous in the x variable on $\overline{\Omega}$ and periodic in the $\mathbf{y}$ variable (this is the right regularity for the two–scale convergence method, and continuity in at least one variable is necessary for $\mathbf{x} \mapsto \mu(\mathbf{x}, \varepsilon^{-1}\mathbf{x})$ to be measurable, see [All92]). Moreover, μ is supposed to be uniformly bounded away from 0: there exists a constant $\mu_0 > 0$ independent of $(\mathbf{x}, \mathbf{y})$ such that:

$$\forall \mathbf{x} \in \Omega,\ \forall \mathbf{y} \in \mathcal{Y},\ \mu(\mathbf{x}, \mathbf{y}) \geq \mu_0 > 0. \tag{4.3}$$

Suppose that the material reacts to a volumic force $\mathbf{F}_\varepsilon$. The Newton action–reaction law then yields the equations for the linearized elastic material, with ρ_S denoting the density:

$$\rho_S \frac{\partial^2 \mathbf{U}_\varepsilon}{\partial t^2} - \mathrm{div}(\sigma_\varepsilon(\mathbf{U}_\varepsilon)) = \mathbf{F}_\varepsilon, \qquad \text{in } \Omega_{S,\varepsilon}. \tag{4.4}$$

We impose homogeneous Dirichlet boundary conditions on the outer boundary $\partial\Omega$:

$$\mathbf{U}_\varepsilon = \mathbf{0}, \qquad \text{on } \partial\Omega. \tag{4.5}$$

We consider now the fluid domain $\Omega_{F,\varepsilon}$. This domain is filled with air considered as an inviscid, irrotational, compressible perfect gas. We consider only small perturbations with respect to a reference equilibrium state in each hole, with the reference pressure being the atmospheric pressure P_0 and a constant equilibrium density ρ_0, under a potential volumic excitation force ∇G_ε. Following [HKR00], a complete description of the behavior of the gas is given by two conservation laws and an appropriate state law of the gas, using three variables: the displacement $\mathbf{U}_\varepsilon$, the absolute

pressure P_ε and the gas density ρ_ε.
The conservation law for momentum in this inviscid, irrotational gas writes:

$$\rho_\varepsilon \frac{\partial^2 \mathbf{U}_\varepsilon}{\partial t^2} + \nabla P_\varepsilon = \nabla G_\varepsilon, \qquad \text{in } \Omega_{F,\varepsilon}. \tag{4.6}$$

The continuity equation, or mass conservation law, writes:

$$\frac{\partial \rho_\varepsilon}{\partial t} + \operatorname{div}\left(\rho_\varepsilon \frac{\partial \mathbf{U}_\varepsilon}{\partial t}\right) = 0, \qquad \text{in } \Omega_{F,\varepsilon}. \tag{4.7}$$

To close the system, we make the assumption that the air compression associated with the propagation of sound waves is an adiabatic process. This is an usual assumption regarding sound propagation, and is motivated by the difference in characteristic times between the heat dissipation process and the short timescale associated with the propagating waves. Pressure and density are then linked by the following relation:

$$P_\varepsilon = P_0 \left(\frac{\rho_\varepsilon}{\rho_0}\right)^\gamma, \qquad \text{in } \Omega_{F,\varepsilon}, \tag{4.8}$$

where γ is the adiabatic index of the air ($\gamma \approx 1.4$). Let us now linearize the equations (4.6), (4.7), (4.8) around the reference state following our assumption of small perturbation from rest:

$$\rho_0 \frac{\partial^2 \mathbf{U}_\varepsilon}{\partial t^2} + \nabla P_\varepsilon = \nabla G_\varepsilon \qquad \text{in } \Omega_{F,\varepsilon}, \tag{4.9a}$$

$$\frac{\partial \rho_\varepsilon}{\partial t} + \rho_0 \operatorname{div}\left(\frac{\partial \mathbf{U}_\varepsilon}{\partial t}\right) = 0 \qquad \text{in } \Omega_{F,\varepsilon}. \tag{4.9b}$$

$$P_\varepsilon - P_0 = c^2(\rho_\varepsilon - \rho_0) \qquad \text{in } \Omega_{F,\varepsilon}, \tag{4.9c}$$

where we have introduced $c = \sqrt{\gamma \frac{P_0}{\rho_0}}$, the sound speed in the air. We eliminate the density ρ_ε by combining (4.9b) and (4.9c), and we find that the displacement and pressure in the fluid are solution to the system of equations:

$$\rho_0 \frac{\partial^2 \mathbf{U}_\varepsilon}{\partial t^2} + \nabla P_\varepsilon = \nabla G_\varepsilon, \qquad \text{in } \Omega_{F,\varepsilon}. \tag{4.10a}$$

$$\frac{1}{c^2}\frac{\partial P_\varepsilon}{\partial t} + \rho_0 \operatorname{div}\left(\frac{\partial \mathbf{U}_\varepsilon}{\partial t}\right) = 0, \qquad \text{in } \Omega_{F,\varepsilon}. \tag{4.10b}$$

Let us now describe the coupling conditions between the fluid and the structure. The first condition expresses the continuity of the the normal component of the strain tensor at the interface:

$$-P_\varepsilon \mathbf{n}_\varepsilon^S = \sigma_\varepsilon(\mathbf{U}_\varepsilon|_{\Omega_{S,\varepsilon}})\mathbf{n}_\varepsilon^S \qquad \text{on } \Gamma_\varepsilon^I. \tag{4.11}$$

Moreover, because the air is inviscid, there is no constraint on the tangential component of the trace of the velocity at the interface. Rather, we have slip boundary conditions, meaning that the normal component of the displacement is continuous:

$$\mathbf{U}_\varepsilon|_{\Omega_{S,\varepsilon}} \cdot \mathbf{n}_\varepsilon^S = \mathbf{U}_\varepsilon|_{\Omega_{F,\varepsilon}} \cdot \mathbf{n}_\varepsilon^S \qquad \text{on } \Gamma_\varepsilon^I. \tag{4.12}$$

Together, equations (4.4), (4.10) and the boundary conditions (4.5), (4.11) and (4.12) complemented with initial conditions form the system of time–dependent equations of our model. By construction,

the model is now linear and, as is standard, its behavior can be understood by harmonic superposition technique. We thus assume that both G_ε, $\mathbf{F}_\varepsilon$ and the initial conditions are coherent with a time–harmonic forcing along the mode $e^{i\omega t}$. This leads to assume the expansion

$$\begin{aligned} \mathbf{U}_\varepsilon(\mathbf{x},t) &= \mathbf{u}_\varepsilon(\mathbf{x})e^{i\omega t} && \text{in } \Omega, & P_\varepsilon(\mathbf{x},t) &= p_\varepsilon(\mathbf{x})e^{i\omega t} && \text{in } \Omega_{F,\varepsilon}, \\ \mathbf{F}_\varepsilon(\mathbf{x},t) &= \mathbf{f}_\varepsilon(\mathbf{x})e^{i\omega t} && \text{in } \Omega, & g_\varepsilon(\mathbf{x},t) &= G_\varepsilon(\mathbf{x})e^{i\omega t} && \text{in } \Omega. \end{aligned}$$

Note that the fields $\mathbf{u}_\varepsilon$, p_ε, $\mathbf{f}_\varepsilon$, g_ε will be complex–valued in what follows, in particular the Hilbert spaces we consider will be complex–valued spaces unless it is otherwise specified. We denote by $\mathrm{Re}\,(\cdot)$ and $\mathrm{Im}\,(\cdot)$ respectively the real and imaginary part of a complex argument.

Harmonic formulation Taking into account this time dependency, the behavior of the coupled fluid and structure for some frequency ω is described by the complex displacement / pressure field $(\mathbf{u}_\varepsilon, p_\varepsilon)$ solving the following system:

$$\begin{cases} -\rho_S\omega^2\mathbf{u}_\varepsilon - \mathrm{div}\sigma_\varepsilon(\mathbf{u}_\varepsilon) = \mathbf{f}_\varepsilon & \text{in } \Omega_{S,\varepsilon}, \quad (4.13a) \\ -\rho_0\omega^2\mathbf{u}_\varepsilon + \nabla p_\varepsilon = \nabla g_\varepsilon & \text{in } \Omega_{F,\varepsilon}, \quad (4.13b) \\ \frac{1}{c^2}p_\varepsilon + \rho_0\mathrm{div}(\mathbf{u}_\varepsilon) = 0 & \text{in } \Omega_{F,\varepsilon}, \quad (4.13c) \\ -p_\varepsilon\mathbf{n}_\varepsilon^S = \sigma_\varepsilon(\mathbf{u}_\varepsilon)\mathbf{n}_\varepsilon^S & \text{on } \Gamma_\varepsilon^I, \quad (4.13d) \\ \mathbf{u}_\varepsilon|_{\Omega_{S,\varepsilon}}\cdot\mathbf{n}_\varepsilon^S = \mathbf{u}_\varepsilon|_{\Omega_{F,\varepsilon}}\cdot\mathbf{n}_\varepsilon^S & \text{on } \Gamma_\varepsilon^I, \quad (4.13e) \\ \mathbf{u}_\varepsilon = \mathbf{0} & \text{on } \partial\Omega. \quad (4.13f) \end{cases}$$

Remember that we have assumed that $\mathbf{u}_\varepsilon$ is irrotational in $\Omega_{F,\varepsilon}$, this has lead to (4.13b). To write this system in a more suitable form for further analysis, let us introduce a velocity potential ϕ_ε defined up to a constant in each hole, such that

$$\nabla\phi_\varepsilon = i\omega\mathbf{u}_\varepsilon. \tag{4.14}$$

We choose to work with the potential that has zero mean in each hole to fix the constant. By combining the three relations (4.13b), (4.13c) and (4.14), we see that:

$$\nabla\left(-\omega^2\phi_\varepsilon - c^2\Delta\phi_\varepsilon - i\omega g_\varepsilon/\rho_0\right) = 0.$$

To get rid of the gradient in this equation we need to introduce a constant $C_\varepsilon^{\mathbf{k}}$ on each connected component of $\Omega_{F,\varepsilon}$, depending only on the hole index $\mathbf{k}$. This leads to the following Hehlmoltz equation set on $\Omega_{F,\varepsilon}$:

$$-\omega^2\phi_\varepsilon - c^2\Delta\phi_\varepsilon = i\omega\frac{g_\varepsilon + C_\varepsilon^{\mathbf{k}}}{\rho_0}. \tag{4.15}$$

Moreover, the boundary condition (4.13e) together with (4.14) imply that the following compatibility condition is satisfied:

$$\int_{\mathcal{Y}_{F,\varepsilon}^{\mathbf{k}}}\left(i\omega\frac{g_\varepsilon + C_\varepsilon^{\mathbf{k}}}{\rho_0}\right) = c^2\int_{\Gamma_{F,\varepsilon}^{\mathbf{k}}}\frac{\partial\phi_\varepsilon}{\partial\mathbf{n}_\varepsilon^S} = i\omega c^2\int_{\Gamma_{F,\varepsilon}^{\mathbf{k}}}\mathbf{u}_\varepsilon\cdot\mathbf{n}_\varepsilon^S. \tag{4.16}$$

This determines the constant appearing in equation (4.15) and gives the identity:

$$C_\varepsilon^{\mathbf{k}} = \frac{1}{|\mathcal{Y}_{F,\varepsilon}^{\mathbf{k}}|}\left(\rho_0 c^2\int_{\Gamma_{F,\varepsilon}^{\mathbf{k}}}\mathbf{u}_\varepsilon\cdot\mathbf{n}_\varepsilon^S - \int_{\mathcal{Y}_{F,\varepsilon}^{\mathbf{k}}}g_\varepsilon\right). \tag{4.17}$$

We next define a function C_ε of $L^2(\Omega)$, constant in each cell $\mathcal{Y}_\varepsilon^{\mathbf{k}}$ by

$$C_\varepsilon(\mathbf{x}) = \begin{cases} C_\varepsilon^{\mathbf{k}} & \text{if } \mathbf{x} \in \mathcal{Y}_\varepsilon^{\mathbf{k}} \text{ for some } \mathbf{k} \in \mathbf{Z}_\varepsilon^\Omega, \\ 0 & \text{else.} \end{cases} \tag{4.18}$$

We can now eliminate the fluid pressure from the equations. From (4.13c) and (4.14) we derive

$$i\omega p_\varepsilon = -\rho_0 c^2 \Delta \phi_\varepsilon,$$

which combines with (4.15) to yield

$$p_\varepsilon = -i\omega\rho_0\phi_\varepsilon + g_\varepsilon + C_\varepsilon. \tag{4.19}$$

Bringing together (4.15), (4.17) and (4.19), we write a new, equivalent system of equations describing the behavior of our coupled fluid–structure material. The new unknowns are the structure displacement and the fluid velocity potential $(\mathbf{u}_\varepsilon, \phi_\varepsilon)$. Note that the displacement field $\mathbf{u}_\varepsilon$ is defined only on $\Omega_{S,\varepsilon}$ from now on.

$$\begin{cases} -\rho_S\omega^2\mathbf{u}_\varepsilon - \mathrm{div}\sigma_\varepsilon(\mathbf{u}_\varepsilon) = \mathbf{f}_\varepsilon & \text{in } \Omega_{S,\varepsilon}, \quad (4.20a) \\ -\omega^2\phi_\varepsilon - c^2\Delta\phi_\varepsilon = i\omega\dfrac{g_\varepsilon + C_\varepsilon}{\rho_0} & \text{in } \Omega_{F,\varepsilon}, \quad (4.20b) \\ \sigma_\varepsilon(\mathbf{u}_\varepsilon)\mathbf{n}_\varepsilon^S = -\left(-i\omega\rho_0\phi_\varepsilon + g_\varepsilon + C_\varepsilon\right)\mathbf{n}_\varepsilon^S & \text{on } \Gamma_\varepsilon^I, \quad (4.20c) \\ i\omega\mathbf{u}_\varepsilon \cdot \mathbf{n}_\varepsilon^S = \dfrac{\partial\phi_\varepsilon}{\partial\mathbf{n}_\varepsilon^S} & \text{on } \Gamma_\varepsilon^I, \quad (4.20d) \\ \mathbf{u}_\varepsilon = \mathbf{0} & \text{on } \partial\Omega, \quad (4.20e) \end{cases}$$

with C_ε defined by (4.18).

Now we are going to write the variational formulation of this problem. Let us define the complex Hilbert spaces (bold face letters indicate spaces of vector–valued functions):

$$\mathbf{H}_0^1(\Omega_{S,\varepsilon}) = \left\{\mathbf{v}_\varepsilon \in \mathbf{H}^1(\Omega_{S,\varepsilon}), \mathbf{v}_\varepsilon|_{\partial\Omega} = \mathbf{0}\right\},$$

$$H^1_{mean}(\Omega_{F,\varepsilon}) = \left\{\psi \in H^1(\Omega_{F,\varepsilon}), \forall \mathbf{k} \in \mathbf{Z}_\varepsilon^\Omega, \int_{\mathcal{Y}_{F,\varepsilon}^{\mathbf{k}}} \psi = 0\right\}.$$

Let us also define the projector Π_ε from $L^2(\Omega)$ onto the functions that are constant on each cell $\mathcal{Y}_{F,\varepsilon}^{\mathbf{k}}$, by

$$\Pi_\varepsilon(\phi) = \sum_{\mathbf{k}\in\mathbf{Z}_\varepsilon^\Omega} \frac{1}{|\mathcal{Y}_\varepsilon^{\mathbf{k}}|}\left(\int_{\mathcal{Y}_\varepsilon^{\mathbf{k}}} \phi\right)\chi_{\mathcal{Y}_\varepsilon^{\mathbf{k}}}. \tag{4.21}$$

Using the operator Π_ε and (4.17), we can rewrite the L^2 function C_ε introduced in (4.18) as:

$$C_\varepsilon = \rho_0 c^2 \sum_{\mathbf{k}\in\mathbf{Z}_\varepsilon^\Omega} \frac{1}{\varepsilon^d|\mathcal{Y}_F|}\left(\int_{\Gamma_{F,\varepsilon}^{\mathbf{k}}} \mathbf{u}_\varepsilon \cdot \mathbf{n}_\varepsilon^S\right)\chi_{\mathcal{Y}_\varepsilon^{\mathbf{k}}} - \frac{1}{|\mathcal{Y}_F|}\Pi_\varepsilon\left(\chi_{F,\varepsilon} g_\varepsilon\right).$$

We can now finally conclude this preparatory work by introducing rigorously the problem we will study mathematically in the remainder of this paper, in particular to understand the behavior of its solutions as the small parameter ε goes to zero. We establish a weak formulation for the system (4.20) by taking a couple of test functions $(\mathbf{v}, \psi)$ in $\mathbf{H}_0^1(\Omega_{S,\varepsilon}) \times H^1_{mean}(\Omega_{F,\varepsilon})$ and using $\mathbf{v}$ as a test function in equation (4.20a) and ψ in equation (4.20b). The problem then reads as

follows: for $\mathbf{f}_\varepsilon \in \mathbf{L}^2(\Omega)$ and $g_\varepsilon \in H^1(\Omega)$, find $(\mathbf{u}_\varepsilon, \phi_\varepsilon) \in \mathbf{H}^1_0(\Omega_{S,\varepsilon}) \times H^1_{mean}(\Omega_{F,\varepsilon})$ such that for any $(\mathbf{v}, \psi) \in H^1_0(\Omega)^d \times H^1_{mean}(\Omega_{F,\varepsilon})$,

$$\left\{\begin{aligned} &\int_{\Omega_{S,\varepsilon}} -\rho_S\omega^2\mathbf{u}_\varepsilon\cdot\overline{\mathbf{v}} + \sigma_\varepsilon(\mathbf{u}_\varepsilon) : \overline{e(\mathbf{v})} + \rho_0 c^2 \sum_{\mathbf{k}\in\mathbf{Z}^\Omega_\varepsilon} \frac{1}{\varepsilon^d|\mathcal{Y}_F|}\left(\int_{\Gamma^{\mathbf{k}}_{F,\varepsilon}} \mathbf{u}_\varepsilon\cdot\mathbf{n}^S_\varepsilon\right)\overline{\left(\int_{\Gamma^{\mathbf{k}}_{F,\varepsilon}} \mathbf{v}\cdot\mathbf{n}^S_\varepsilon\right)} \\ &\qquad + \rho_0\int_{\Omega_{F,\varepsilon}} -\frac{\omega^2}{c^2}\phi_\varepsilon\overline{\psi} + \nabla\phi_\varepsilon\cdot\overline{\nabla\psi} + \rho_0\int_{\Gamma^I_\varepsilon} i\omega\left(\overline{\psi}\mathbf{u}_\varepsilon\cdot\mathbf{n}^S_\varepsilon - \phi_\varepsilon\overline{\mathbf{v}\cdot\mathbf{n}^S_\varepsilon}\right) \\ &= \int_{\Omega_{S,\varepsilon}} \mathbf{f}_\varepsilon\cdot\overline{\mathbf{v}} - \int_{\Gamma^I_\varepsilon}\left(g_\varepsilon - \frac{|\mathcal{Y}|}{|\mathcal{Y}_F|}\Pi_\varepsilon(\chi_{F,\varepsilon}g_\varepsilon)\right)\overline{\mathbf{v}\cdot\mathbf{n}^S_\varepsilon} + \int_{\Omega_{F,\varepsilon}}\frac{i\omega}{c^2}\left(g_\varepsilon - \frac{|\mathcal{Y}|}{|\mathcal{Y}_F|}\Pi_\varepsilon(\chi_{F,\varepsilon}g_\varepsilon)\right)\overline{\psi}. \end{aligned}\right. \tag{4.22}$$

Remark 4.2.1. *If we take the frequency ω to be zero, we recover precisely the static model studied in detail in the paper [BGMO08].*

Remark 4.2.2. *The presence of the interesting term*

$$\sum_{\mathbf{k}\in\mathbf{Z}^\Omega_\varepsilon} \frac{1}{\varepsilon^d|\mathcal{Y}_F|}\left(\int_{\Gamma^{\mathbf{k}}_{F,\varepsilon}} \mathbf{u}_\varepsilon\cdot\mathbf{n}^S_\varepsilon\right)\overline{\left(\int_{\Gamma^{\mathbf{k}}_{F,\varepsilon}} \mathbf{v}\cdot\mathbf{n}^S_\varepsilon\right)},$$

which first appeared in the model of [BGMO08] and is local at the macroscopic scale and nonlocal at the microscopic (alveolar) scale, is a consequence of the pressure term in each hole that mathematically was expressed by the compatibility condition (4.16).

4.2.3 A few useful definitions and results

Let us describe here a few definitions and results we will use frequently in the framework of two–scale homogenization laid out by G. Nguetseng [Ngu89] and G. Allaire [All92]. These are associated with some extension operators from functions defined on the domains $\Omega_{S,\varepsilon}$ or $\Omega_{F,\varepsilon}$ to functions defined on the whole domain Ω, their norms, and some *a priori* estimates on the solution to our problem. In this respect, we have to pay special attention to the dependency of the various constants involved in the bounds with respect to ε: it is indeed crucial to get uniform bounds in order to use the compactness properties of the weak or two–scale topologies.

Extension operators As is standard when dealing with porous multiscale domains, we need extension operators from $\Omega_{S,\varepsilon}$ and $\Omega_{F,\varepsilon}$ onto Ω since convergence cannot be described in parameter dependent domains. We define two extension operators:

- An extension operator in $\mathcal{L}\left(\mathbf{H}^k(\Omega_{S,\varepsilon}), \mathbf{H}^k(\Omega)\right)$ for $k = 0, 1$, denoted by $\widehat{\cdot}$, such that for some $C > 0$ independent of ε and depending only on Ω and $\mathcal{Y}$, for all $\mathbf{u}_\varepsilon \in \mathbf{H}^1(\Omega_{S,\varepsilon})$,

$$\begin{aligned} \widehat{\mathbf{u}_\varepsilon} &= \mathbf{u}_\varepsilon \text{ in } \Omega_{S,\varepsilon}, \\ \|\widehat{\mathbf{u}_\varepsilon}\|_{\mathbf{L}^2(\Omega)} \le C\|\mathbf{u}_\varepsilon\|_{\mathbf{L}^2(\Omega_{S,\varepsilon})}, &\quad \|\nabla\widehat{\mathbf{u}_\varepsilon}\|_{\mathbf{L}^2(\Omega)} \le C\|\nabla\mathbf{u}_\varepsilon\|_{\mathbf{L}^2(\Omega_{S,\varepsilon})}. \end{aligned} \tag{4.23}$$

  The construction of such an operator can be found e.g. in [CD89] or [Con85].
- An extension still denoted by $\widehat{\cdot}$: $H^1_{mean}(\Omega_{F,\varepsilon}) \to H^1_0(\Omega)$ that we are going to construct in the following Lemma.

Lemma 4.2.3. *There exists an extension operator $\widehat{\cdot}$: $H^1_{mean}(\Omega_{F,\varepsilon}) \mapsto H^1_0(\Omega)$ for every $\varepsilon > 0$, such that $\forall\phi_\varepsilon \in H^1_{mean}(\Omega_{F,\varepsilon})$ we have the property*

$$|\widehat{\phi_\varepsilon}|_{H^1(\Omega)} \le C|\phi_\varepsilon|_{H^1(\Omega_{F,\varepsilon})},$$

where the constant C depends only on $\mathcal{Y}$ and not on ε.

Proof. First of all, let us consider a linear continuous extension operator from $H^1_{mean}(\mathcal{Y}_F)$ (defined as the set of functions in $H^1(\mathcal{Y}_F)$ with zero average) to the space $H^1_0(\mathcal{Y})$. As an example, we define for any $\phi \in H^1_{mean}(\mathcal{Y}_F)$ its harmonic extension $E(\phi) \in H^1_0(\mathcal{Y})$ by solving the Poisson problem

$$\begin{cases} -\Delta\psi = 0 & \text{in } \mathcal{Y}_S \\ \psi = \phi|_{\Gamma_F} & \text{on } \Gamma_F. \end{cases}$$

It is well–known that for some C depending only on of $\mathcal{Y}_S$,

$$\|\psi\|_{H^1(\mathcal{Y}_S)} \leq C\|\phi\|_{H^{1/2}(\Gamma)}.$$

Thanks to both the trace inequality and the Poincaré–Wirtinger inequality in $H^1_{mean}(\mathcal{Y}_F)$, we have

$$\|\psi\|_{H^1(\mathcal{Y}_S)} \leq C\|\phi\|_{H^1(\mathcal{Y}_F)} \leq C|\phi|_{H^1(\mathcal{Y}_F)},$$

where C depends only on $\mathcal{Y}$, $\mathcal{Y}_F$, $\mathcal{Y}_S$. The function $E(\phi)$ on $\mathcal{Y}$ defined as

$$E(\phi)(\mathbf{x}) = \begin{cases} \phi(\mathbf{x}) & \text{if } \mathbf{x} \in \mathcal{Y}_F, \\ \psi(\mathbf{x}) & \text{if } \mathbf{x} \in \mathcal{Y}_S, \end{cases}$$

belongs to $H^1_0(\mathcal{Y})$ and the following estimate holds for some constant C, depending only on $\mathcal{Y}$, $\mathcal{Y}_S$ and $\mathcal{Y}_F$:

$$|E(\phi)|_{H^1(\mathcal{Y})} \leq C|\phi|_{H^1(\mathcal{Y}_F)}. \tag{4.24}$$

Now let $\phi_\varepsilon \in H^1_{mean}(\Omega_{F,\varepsilon})$. For each $\mathbf{k} \in \mathbf{Z}^\Omega_\varepsilon$, we have $\phi_\varepsilon|_{\mathcal{Y}^{\mathbf{k}}_{F,\varepsilon}}(\varepsilon\cdot + \mathbf{k}) \in H^1_{mean}(\mathcal{Y}_F)$. Let us define:

$$\widehat{\phi_\varepsilon}(\mathbf{x}) = \begin{cases} E\left(\phi_\varepsilon|_{\mathcal{Y}^{\mathbf{k}}_{F,\varepsilon}}(\varepsilon\cdot + \mathbf{k})\right)(\varepsilon^{-1}(\mathbf{x}-\mathbf{k})) & \text{if } \mathbf{x} \in \mathcal{Y}^{\mathbf{k}}_\varepsilon,\ \mathbf{k} \in \mathbf{Z}^\Omega_\varepsilon, \\ 0 & \text{otherwise.} \end{cases}$$

Because the traces of $\widehat{\phi}$ coincide on each side of $\partial\mathcal{Y}^{\mathbf{k}}_\varepsilon$ with 0, $\widehat{\phi_\varepsilon}$ belongs globally to $H^1_0(\Omega)$. We have the estimate:

$$\begin{aligned} |\widehat{\phi_\varepsilon}|^2_{H^1(\Omega)} &= \sum_{\mathbf{k}\in\mathbf{Z}^\Omega_\varepsilon} \int_{\mathcal{Y}^{\mathbf{k}}_{F,\varepsilon}} |\nabla\widehat{\phi_\varepsilon}|^2 \\ &= \sum_{\mathbf{k}\in\mathbf{Z}^\Omega_\varepsilon} \varepsilon^d \int_{\mathcal{Y}} |\varepsilon^{-1}\nabla\left(E\left\{\phi_\varepsilon(\varepsilon\cdot+\mathbf{k})\right\}(\mathbf{y})\right)|^2 \\ &= \varepsilon^{d-2} \sum_{\mathbf{k}\in\mathbf{Z}^\Omega_\varepsilon} |E\left\{\phi_\varepsilon(\varepsilon\cdot+\mathbf{k})\right\}|^2_{H^1_0(\mathcal{Y})} \\ &\leq C^2\varepsilon^{d-2} \sum_{\mathbf{k}\in\mathbf{Z}^\Omega_\varepsilon} |\phi_\varepsilon(\varepsilon\cdot+\mathbf{k})|^2_{H^1_0(\mathcal{Y}_F)} \\ &\leq C^2|\phi_\varepsilon|^2_{H^1(\Omega_{F,\varepsilon})}, \end{aligned} \tag{4.25}$$

where C is the same constant as in (4.24) and thus is independent of ε. This concludes the proof of the Lemma. □

Korn and Poincaré inequalities The L^2–norm of the Cauchy stress tensor $e(\mathbf{u})$ will appear naturally when we compute energy bounds for our solutions. To deduce H^1 bounds, we need the Korn inequality. This result is well known in the case of a bounded open set Ω with Dirichlet boundary conditions. Again, here we pay special attention to the dependency of the constants on

ε. It is well–known that the Korn inequality holds on Ω [Cia88]: there exists $K > 0$ depending only on Ω, such that

$$\|e(\mathbf{u})\|_{\mathbf{L}^2(\Omega)} \geq K_1 |\mathbf{u}|_{\mathbf{H}^1(\Omega)}, \qquad \forall \mathbf{u} \in \mathbf{H}^1_0(\Omega). \tag{4.26}$$

The Poincaré inequality also holds on Ω: there exists $K_2 > 0$ depending only on Ω, such that

$$\|\mathbf{u}\|_{\mathbf{H}^1(\Omega)} \leq K_2 |\mathbf{u}|_{\mathbf{H}^1(\Omega)}, \qquad \forall \mathbf{u} \in \mathbf{H}^1_0(\Omega). \tag{4.27}$$

Using the extension operator $\mathbf{u} \mapsto \widehat{\mathbf{u}}$ we can easily extend, uniformly with respect to ε, the Korn and the Poincaré inequality to $\Omega_{S,\varepsilon}$ using the property (4.2.3):

Lemma 4.2.4. *(Korn inequality on $\Omega_{S,\varepsilon}$) There exists a constant α, depending only on Ω and $\mathcal{Y}$, such that:*

$$\forall \varepsilon > 0, \quad \forall \mathbf{u}_\varepsilon \in \mathbf{H}^1_0(\Omega_{S,\varepsilon}) \quad \|e(\mathbf{u}_\varepsilon)\|_{\mathbf{L}^2(\Omega_{S,\varepsilon})} \geq \alpha |\mathbf{u}_\varepsilon|_{\mathbf{H}^1(\Omega_{S,\varepsilon})}. \tag{4.28}$$

Lemma 4.2.5. *(Poincaré inequality on $\Omega_{S,\varepsilon}$) There exists a constant β, depending only on Ω and $\mathcal{Y}$, such that:*

$$\forall \varepsilon > 0, \quad \forall \mathbf{u}_\varepsilon \in \mathbf{H}^1_0(\Omega_{S,\varepsilon}) \quad \|\mathbf{u}_\varepsilon\|_{\mathbf{H}^1(\Omega_{S,\varepsilon})} \leq \beta |\mathbf{u}_\varepsilon|_{\mathbf{H}^1(\Omega_{S,\varepsilon})}. \tag{4.29}$$

Remark 4.2.6. *To sum things up, $|\cdot|_{\mathbf{H}^1_0(\Omega_{S,\varepsilon})}$, $\|\cdot\|_{\mathbf{H}^1_0(\Omega_{S,\varepsilon})}$, $\|e(\,\cdot\,)\|_{\mathbf{L}^2(\Omega_{S,\varepsilon})}$, $|\widehat{\cdot}\,|_{\mathbf{H}^1_0(\Omega)}$, $\|\widehat{\cdot}\,\|_{\mathbf{H}^1_0(\Omega)}$, $\|e(\widehat{\cdot}\,)\|_{\mathbf{L}^2(\Omega)}$ are all equivalent norms on $\mathbf{H}^1_0(\Omega_{S,\varepsilon})$, uniformly with respect to ε.*

On $H^1_{mean}(\Omega_{F,\varepsilon})$, we also have a Poincaré estimate: by rescaling each $\mathcal{Y}^{\mathbf{k}}_\varepsilon$ to $\mathcal{Y}$ and applying the Poincaré inequality for $E\left(\phi_\varepsilon(\varepsilon\,\cdot + \mathbf{k})\right) \in H^1_0(\mathcal{Y})$, for each $\phi_\varepsilon \in H^1_{mean}(\Omega_{F,\varepsilon})$,

$$\begin{aligned}
\|\phi_\varepsilon\|^2_{L^2(\mathcal{Y}^{\mathbf{k}}_{F,\varepsilon})} \leq \|\widehat{\phi_\varepsilon}\|^2_{L^2(\mathcal{Y}^{\mathbf{k}}_\varepsilon)} &= \varepsilon^d \|E\left(\phi_\varepsilon(\varepsilon\,\cdot + \mathbf{k})\right)\|^2_{L^2(\mathcal{Y})} \\
&\leq C\varepsilon^d \left\|\nabla\left(\phi_\varepsilon(\varepsilon\,\cdot + \mathbf{k})\right)\right\|^2_{L^2(\mathcal{Y}_F)} \\
&\leq C\varepsilon^{d+2} \left\|(\nabla\phi_\varepsilon)(\varepsilon\,\cdot + \mathbf{k})\right\|^2_{H^1(\mathcal{Y})} \leq C\varepsilon^2 |\phi_\varepsilon|^2_{H^1(\mathcal{Y}^{\mathbf{k}}_{F,\varepsilon})},
\end{aligned}$$

where the constant C depends only on $\mathcal{Y}$, $\mathcal{Y}_F$, $\mathcal{Y}_S$, using (4.25). Summing these over $\mathbf{k}$ we get

Lemma 4.2.7. *(Poincaré inequality on $\Omega_{F,\varepsilon}$) There exists a constant γ depending only on $\mathcal{Y}$ such that:*

$$\forall \varepsilon > 0, \quad \forall \phi_\varepsilon \in H^1_{mean}(\Omega_{F,\varepsilon}) \quad \|\phi_\varepsilon\|_{L^2(\Omega_{F,\varepsilon})} \leq \|\widehat{\phi_\varepsilon}\|_{L^2(\Omega)} \leq \gamma\varepsilon |\phi_\varepsilon|_{H^1(\Omega_{F,\varepsilon})}. \tag{4.30}$$

Two–scale convergence Our objective in this paper is the study of the behavior of the solutions $\mathbf{u}_\varepsilon$ and ϕ_ε of the problem (4.22) as the parameter ε tends to zero. The main tool is two–scale homogenization and for the sake of completeness, we recall here the definition of two–scale convergence, see [All92] and [Ngu89] for complete references. We could also use the closely related periodic unfolding method, see [CDG08].

Definition 4.2.8. *We say that a sequence $\{u_\varepsilon\} \subset L^2(\Omega)$ two–scale converges to some function $u \in L^2(\Omega; L^2_\#(\mathcal{Y}))$, and we note $u_\varepsilon \twoheadrightarrow u$, if for all admissible test functions $v \in L^2(\Omega, C_\#(\mathcal{Y}))$,*

$$\lim_{\varepsilon\to 0} \int_\Omega u_\varepsilon(\mathbf{x}) v\left(\mathbf{x}, \frac{\mathbf{x}}{\varepsilon}\right) d\mathbf{x} = \int_\Omega \int_\mathcal{Y} u(\mathbf{x}, \mathbf{y}) v(\mathbf{x}, \mathbf{y}) d\mathbf{y} d\mathbf{x}. \tag{4.31}$$

This definition can be extended in an obvious way to complex, vector– and tensor–valued functions in $L^2(\Omega)$, $\mathbf{L}^2(\Omega)$ or $L^2(\Omega)^{d\times d}$ by changing the product to the sesquilinear scalar product in $\mathbb{C}$, the scalar product for vectors, the tensorial product for matrices respectively.

Remark 4.2.9. *The question of determining which test functions are admissible is a delicate one and has been adressed on [All92]. In particular, some amount of continuity in one variable or the other is necessary to ensure the measurability of* $\mathbf{x} \mapsto v(\mathbf{x}, \mathbf{x}/\varepsilon)$. *For example, any* $v \in L^2_\#(\mathcal{Y}, C(\overline{\Omega}))$, *such as* $1_{\overline{\Omega}}(\mathbf{x})\chi_F(\mathbf{y})$, *is an admissible test function for the two–scale convergence.*

The two–scale homogenization method relies on the following Proposition, see [All92] for proofs:

Proposition 4.2.10. *1. Let* u_ε *be a bounded sequence in* $L^2(\Omega)$, *there exists* $u(\mathbf{x}, \mathbf{y}) \in L^2(\Omega \times \mathcal{Y})$ *such that up to a subsequence still denoted by* u_ε, $u_\varepsilon \twoheadrightarrow u$.

2. Let u_ε *be a bounded sequence in* $H^1(\Omega)$ *that converges weakly to a limit* u *in* $H^1(\Omega)$. *Then,* u_ε *two–scale converges to* $u(\mathbf{x})$ *and there exists a function* $u^1(\mathbf{x}, \mathbf{y})$ *in* $L^2(\Omega; H^1_\#(\mathcal{Y})/\mathbb{R})$ *such that up to a subsequence,* ∇u_ε *two–scale converges to* $\nabla_x u(\mathbf{x}) + \nabla_y u^1(\mathbf{x}, \mathbf{y})$.

3. Let u_ε *and* $\varepsilon \nabla u_\varepsilon$ *be two bounded sequences in* $L^2(\Omega)$. *Then, there exists a function* $u(\mathbf{x}, \mathbf{y})$ *in* $L^2(\Omega; H^1_\#(\mathcal{Y}))$ *such that up to a subsequence,* $u_\varepsilon \twoheadrightarrow u(\mathbf{x}, \mathbf{y})$ *and* $\varepsilon \nabla u_\varepsilon \twoheadrightarrow \nabla_y u(\mathbf{x}, \mathbf{y})$.

4.2.4 Gårding's inequality and well–posedness

Let us now study the variational problem (4.22) more in depth. As is standard in the litterature about linear elasticity, using the fact that $\lambda \geq 0$, property (4.3) on μ and Korn's inequality (Lemma 4.2.4), we obtain:

$$\forall \mathbf{v}_\varepsilon \in \mathbf{H}^1_0(\Omega_{S,\varepsilon}), \quad \int_{\Omega_{S,\varepsilon}} \sigma_\varepsilon(\mathbf{v}_\varepsilon) : e(\mathbf{v}_\varepsilon) \geq \mu_0 \|e(\mathbf{v}_\varepsilon)\|^2_{\mathbf{H}^1(\Omega_{S,\varepsilon})} \geq \mu_0 \alpha^2 |\mathbf{v}_\varepsilon|^2_{\mathbf{H}^1(\Omega_{S,\varepsilon})}. \tag{4.32}$$

We define the sesquilinear form on $\mathbf{H}^1_0(\Omega_{S,\varepsilon}) \times H^1_{mean}(\Omega_{F,\varepsilon})$ appearing in the left–hand side of (4.22):

$$\begin{aligned} a^\omega_\varepsilon\left((\mathbf{u}_\varepsilon, \phi_\varepsilon); (\mathbf{v}, \psi)\right) = &\int_{\Omega_{S,\varepsilon}} -\rho_S \omega^2 \mathbf{u}_\varepsilon \cdot \overline{\mathbf{v}} + \sigma_\varepsilon(\mathbf{u}_\varepsilon) : \overline{e(\mathbf{v})} \\ &+ \rho_0 c^2 \sum_{\mathbf{k} \in \mathbf{Z}^\Omega_\varepsilon} \frac{1}{\varepsilon^d |\mathcal{Y}_F|} \left(\int_{\Gamma^{\mathbf{k}}_{F,\varepsilon}} \mathbf{u}_\varepsilon \cdot \mathbf{n}^S_\varepsilon \right) \overline{\left(\int_{\Gamma^{\mathbf{k}}_{F,\varepsilon}} \mathbf{v} \cdot \mathbf{n}^S_\varepsilon \right)} \\ &+ \rho_0 \int_{\Omega_{F,\varepsilon}} -\frac{\omega^2}{c^2} \phi_\varepsilon \overline{\psi} + \nabla \phi_\varepsilon \cdot \overline{\nabla \psi} + \rho_0 \int_{\Gamma^I_\varepsilon} i\omega \left(\overline{\psi} \mathbf{u}_\varepsilon \cdot \mathbf{n}^S_\varepsilon - \phi_\varepsilon \overline{\mathbf{v} \cdot \mathbf{n}^S_\varepsilon} \right). \end{aligned} \tag{4.33}$$

The analysis proceeds by the use of the Fredholm alternative to obtain a criterium for the well–posedness of the variational problem (4.22). We show that the alternative holds by proving in the following Lemma that the sesquilinear form a^ω_ε defined by (4.33) satisfies Gårding's inequality, which is known to be a sufficient condition for the alternative to hold (see [Fri69]).

Lemma 4.2.11. *The sesquilinear form* $a^\omega_\varepsilon(\cdot, \cdot)$ *verifies Gårding's inequality on the space* $\mathbf{H}^1_0(\Omega_{S,\varepsilon}) \times H^1_{mean}(\Omega_{F,\varepsilon})$: *for all* $\omega \geq 0$, *there exists constants* C, $\gamma > 0$, *both independent on* ε *but dependent on* ω, *such that for any* $\varepsilon > 0$ *and* $(\mathbf{v}, \psi) \in \mathbf{H}^1_0(\Omega_{S,\varepsilon}) \times H^1_{mean}(\Omega_{F,\varepsilon})$,

$$\begin{aligned} \mathrm{Re}\left(a^\omega_\varepsilon\left((\mathbf{v}_\varepsilon, \psi_\varepsilon); (\mathbf{v}_\varepsilon, \psi_\varepsilon)\right)\right) + C \left(\|\mathbf{v}_\varepsilon\|^2_{\mathbf{L}^2(\Omega_{S,\varepsilon})} + \|\psi_\varepsilon\|^2_{L^2(\Omega_{F,\varepsilon})} \right) \\ \geq \gamma \left(\|\mathbf{v}_\varepsilon\|^2_{\mathbf{H}^1(\Omega_{S,\varepsilon})} + \|\psi_\varepsilon\|^2_{H^1(\Omega_{F,\varepsilon})} \right). \end{aligned} \tag{4.34}$$

Proof. We follow the same steps as in [Cum01], pp 63–64 for the proof of this inequality. Let $\varepsilon > 0$, $\omega \in \mathbb{R}$, $\mathbf{v}_\varepsilon \in \mathbf{H}^1_0(\Omega_{S,\varepsilon})$ and $\psi_\varepsilon \in H^1_{mean}(\Omega_{F,\varepsilon})$. We compute from (4.33):

$$\begin{aligned} a^\omega_\varepsilon\left((\mathbf{v}_\varepsilon, \psi_\varepsilon); (\mathbf{v}_\varepsilon, \psi_\varepsilon)\right) = &\int_{\Omega_{S,\varepsilon}} -\rho_S \omega^2 |\mathbf{v}_\varepsilon|^2 + \sigma_\varepsilon(\mathbf{v}_\varepsilon) : \overline{e(\mathbf{v}_\varepsilon)} + \rho_0 c^2 \sum_{\mathbf{k} \in \mathbf{Z}^\Omega_\varepsilon} \frac{1}{\varepsilon^d |\mathcal{Y}_F|} \left| \int_{\Gamma^{\mathbf{k}}_{F,\varepsilon}} \mathbf{v}_\varepsilon \cdot \mathbf{n}^S_\varepsilon \right|^2 \\ &+ \rho_0 \int_{\Omega_{F,\varepsilon}} -\frac{\omega^2}{c^2} |\psi_\varepsilon|^2 + |\nabla \psi_\varepsilon|^2 + \rho_0 \int_{\Gamma^I_\varepsilon} i\omega \left(\overline{\psi_\varepsilon} \mathbf{v}_\varepsilon \cdot \mathbf{n}^S_\varepsilon - \psi_\varepsilon \overline{\mathbf{v}_\varepsilon \cdot \mathbf{n}^S_\varepsilon} \right). \end{aligned}$$

Taking the real part and using the coercivity of the stress tensor operator (4.32), it follows that:

$$\begin{aligned}\mathrm{Re}\left(a_\varepsilon^\omega\left((\mathbf{v}_\varepsilon,\psi_\varepsilon);(\mathbf{v}_\varepsilon,\psi_\varepsilon)\right)\right)+\left(\mu_0\alpha^2+\rho_S\omega^2\right)\|\mathbf{v}_\varepsilon\|^2_{\mathbf{L}^2(\Omega_{S,\varepsilon})}+\rho_0\left(\frac{\omega^2}{c^2}+1\right)\|\psi_\varepsilon\|^2_{\mathbf{L}^2(\Omega_{F,\varepsilon})}\\ \geq \mu_0\alpha^2\|\mathbf{v}_\varepsilon\|^2_{\mathbf{H}^1(\Omega_{S,\varepsilon})}+\rho_0\|\psi_\varepsilon\|^2_{\mathbf{H}^1(\Omega_{F,\varepsilon})}-2\rho_0\omega\left|\int_{\Gamma_\varepsilon^I}\overline{\psi_\varepsilon}\mathbf{v}_\varepsilon\cdot\mathbf{n}_\varepsilon^S\right|.\end{aligned}$$

If ω is equal to zero, we have proved the Gårding inequality (4.34). Else, we bound the last term as follows. Using the divergence theorem, the Cauchy-Schwartz inequality and the extension operator properties, see (4.2.3), we have

$$\begin{aligned}\left|\int_{\Gamma_\varepsilon^I}\overline{\psi_\varepsilon}\,\widehat{\mathbf{v}_\varepsilon}\cdot\mathbf{n}_\varepsilon^S\right|&=\left|\int_{\Omega_{F,\varepsilon}}\mathrm{div}(\widehat{\mathbf{v}_\varepsilon})\,\overline{\psi_\varepsilon}+\int_{\Omega_{F,\varepsilon}}\nabla\overline{\psi_\varepsilon}\cdot\widehat{\mathbf{v}_\varepsilon}\right|\\ &\leq C\left(|\mathbf{v}_\varepsilon|_{\mathbf{H}^1(\Omega_{S,\varepsilon})}\|\psi_\varepsilon\|_{L^2(\Omega_{F,\varepsilon})}+|\psi_\varepsilon|_{H^1(\Omega_{F,\varepsilon})}\|\mathbf{v}_\varepsilon\|_{\mathbf{L}^2(\Omega_{S,\varepsilon})}\right),\end{aligned}$$

where C is a constant independent of ε and ω. Hence, by Young's inequality, we get for any constants $\delta_1,\delta_2>0$:

$$2\rho_0\omega\left|\int_{\Gamma_\varepsilon^I}\overline{\psi_\varepsilon}\,\widehat{\mathbf{v}_\varepsilon}\cdot\mathbf{n}_\varepsilon^S\right|\leq\rho_0C\omega\left(\delta_1|\mathbf{v}_\varepsilon|^2_{\mathbf{H}^1(\Omega_{S,\varepsilon})}+\delta_1^{-1}\|\psi_\varepsilon\|^2_{L^2(\Omega_{F,\varepsilon})}+\delta_2|\psi_\varepsilon|^2_{H^1(\Omega_{F,\varepsilon})}+\delta_2^{-1}\|\mathbf{v}_\varepsilon\|^2_{\mathbf{L}^2(\Omega_{S,\varepsilon})}\right),$$

and choosing respectively $\delta_1=\frac{\mu_0\alpha^2}{2\rho_0C\omega}$ and $\delta_2=\frac{1}{2C\omega}$ we obtain

$$\begin{aligned}2\rho_0\omega\left|\int_{\Gamma_\varepsilon^I}\overline{\psi_\varepsilon}\mathbf{v}_\varepsilon\cdot\mathbf{n}_\varepsilon^S\right|&\leq\frac{\mu_0\alpha^2}{2}|\mathbf{v}_\varepsilon|^2_{\mathbf{H}^1(\Omega_{F,\varepsilon})}+\frac{2\rho_0^2C^2\omega^2}{\mu_0\alpha^2}\|\psi_\varepsilon\|^2_{L^2(\Omega_{F,\varepsilon})}\\ &\quad+\frac{\rho_0}{2}|\psi_\varepsilon|^2_{H^1(\Omega_{F,\varepsilon})}+2\rho_0C^2\omega^2\|\mathbf{v}_\varepsilon\|^2_{\mathbf{L}^2(\Omega_{S,\varepsilon})}.\end{aligned}$$

Finally we have the estimate:

$$\begin{aligned}&\mathrm{Re}\left(a_\varepsilon^\omega\left((\mathbf{v}_\varepsilon,\psi_\varepsilon);(\mathbf{v}_\varepsilon,\psi_\varepsilon)\right)\right)+\left(\mu_0\alpha^2+\rho_S\omega^2\right)\|\mathbf{v}_\varepsilon\|^2_{\mathbf{L}^2(\Omega_{S,\varepsilon})}+\rho_0\left(\frac{\omega^2}{c^2}+1\right)\|\psi_\varepsilon\|^2_{\mathbf{L}^2(\Omega_{F,\varepsilon})}\\ &\quad+2\rho_0C^2\omega^2\left(\|\mathbf{v}_\varepsilon\|^2_{\mathbf{L}^2(\Omega_{S,\varepsilon})}+\frac{\rho_0}{\mu_0\alpha^2}\|\psi_\varepsilon\|^2_{L^2(\Omega_{F,\varepsilon})}\right)\\ &\quad\geq\frac{\mu_0\alpha^2}{2}\|\mathbf{v}_\varepsilon\|^2_{\mathbf{H}^1(\Omega_{S,\varepsilon})}+\frac{\rho_0}{2}\|\psi_\varepsilon\|^2_{\mathbf{H}^1(\Omega_{F,\varepsilon})}.\end{aligned}$$

We have proved that a_ε^ω satisfies (4.34) for all $\omega\geq0$. □

Gårding's inequality (4.34) is then a sufficient condition for the Fredholm Alternative Principle to hold for the problem (4.22) (see [Fri69]):

Proposition 4.2.12. *Either the problem (4.22) is well–posed, or there exists a nonzero solution $(\mathbf{u}_\varepsilon,\phi_\varepsilon)$ to the homogeneous adjoint problem:*

$$\overline{a_\varepsilon^\omega}\left((\mathbf{v}_\varepsilon,\psi_\varepsilon);(\mathbf{u}_\varepsilon,\phi_\varepsilon)\right)=0\quad\forall(\mathbf{v}_\varepsilon,\psi_\varepsilon)\in\mathbf{H}_0^1(\Omega_{S,\varepsilon})\times H^1_{mean}(\Omega_{F,\varepsilon}).$$

Remark 4.2.13. *Note that the existence of nonzero solutions $(\mathbf{u}_\varepsilon,\phi_\varepsilon)$ is effective since this is the case when, e.g., ω is an eigenvalue for the elasticity problem in $\Omega_{S,\varepsilon}$ with the boundary conditions $\sigma_\varepsilon(\mathbf{u}_\varepsilon)\cdot\mathbf{n}_\varepsilon^S=0$ such that the associated eigenmode $\mathbf{u}_\varepsilon$ satisfies at the same time $\mathbf{u}_\varepsilon\cdot\mathbf{n}_\varepsilon^S=\mathbf{0}$ on Γ_ε^I, hence is traction–free on the fluid–structure interface, see [HKR00, Cum01]. We cannot control the apparition of these eigensystems as ε varies, so we will have to deal carefully about the well–posedness of (4.22).*

4.2.5 Energy estimates

Let us assume that a solution $(\mathbf{u}_\varepsilon, \phi_\varepsilon)$ to the problem (4.22) exists and has enough regularity, meaning that $\mathbf{u}_\varepsilon \in \mathbf{H}^1_0(\Omega_{S,\varepsilon})$, $\phi_\varepsilon \in H^1(\Omega_{S,\varepsilon})$. It is not possible to obtain directly *a priori* estimates uniform in ε for $\mathbf{u}_\varepsilon$ and ϕ_ε because ω could be an eigenvalue for the harmonic problem (4.22), see e.g. Remark 4.2.13.

Lemma 4.2.14. *Let $(\mathbf{u}_\varepsilon, \phi_\varepsilon)$ be solutions of problem (4.22). There exists a constant $C(\omega) > 0$, independent of ε (but depending on ω) such that:*

$$\|\mathbf{u}_\varepsilon\|^2_{\mathbf{H}^1(\Omega_{S,\varepsilon})} + \|\phi_\varepsilon\|^2_{H^1(\Omega_{F,\varepsilon})} \leq C(\omega)\left(\|\mathbf{u}_\varepsilon\|^2_{\mathbf{L}^2(\Omega_{S,\varepsilon})} + \|\phi_\varepsilon\|^2_{L^2(\Omega_{F,\varepsilon})} + \|\mathbf{f}_\varepsilon\|^2_{\mathbf{L}^2(\Omega)} + \|g_\varepsilon\|^2_{H^1(\Omega)}\right). \tag{4.35}$$

Proof. These estimates are obtained, as is standard, by choosing $\mathbf{u}_\varepsilon$ and ϕ_ε as test functions in the variational formulation (4.22). This leads to:

$$\begin{aligned} a^\omega_\varepsilon\left((\mathbf{u}_\varepsilon, \phi_\varepsilon); (\mathbf{u}_\varepsilon, \phi_\varepsilon)\right) = \int_{\Omega_{S,\varepsilon}} \mathbf{f}_\varepsilon \cdot \overline{\mathbf{u}_\varepsilon} - \int_{\Gamma^I_\varepsilon} \left(g_\varepsilon - \frac{|\mathcal{Y}|}{|\mathcal{Y}_F|}\Pi_\varepsilon(\chi_{F,\varepsilon} g_\varepsilon)\right) \overline{\mathbf{u}_\varepsilon} \cdot \mathbf{n}^S_\varepsilon \\ + \frac{i\omega}{c^2}\int_{\Omega_{F,\varepsilon}} \left(g_\varepsilon - \frac{|\mathcal{Y}|}{|\mathcal{Y}_F|}\Pi_\varepsilon(\chi_{F,\varepsilon} g_\varepsilon)\right) \cdot \overline{\phi_\varepsilon}. \end{aligned}$$

Denote by g^0_ε the function in $L^2(\Omega)$ defined by:

$$g^0_\varepsilon = g_\varepsilon - \frac{|\mathcal{Y}|}{|\mathcal{Y}_F|}\Pi_\varepsilon(\chi_{F,\varepsilon} g_\varepsilon).$$

Note that $\nabla g_\varepsilon = \nabla g^0_\varepsilon$ almost everywhere, and

$$\|g^0_\varepsilon\|_{L^2(\Omega)} \leq \left(1 + \frac{|\mathcal{Y}|}{|\mathcal{Y}_F|}\right)\|g_\varepsilon\|_{L^2(\Omega)}. \tag{4.36}$$

Thanks to Proposition 4.2.11, there exists two constants $C, \gamma > 0$, independent of ε and such that

$$\begin{aligned} \mathrm{Re}\left(\int_{\Omega_{S,\varepsilon}} \mathbf{f}_\varepsilon \cdot \overline{\mathbf{u}_\varepsilon} - \int_{\Gamma^I_\varepsilon} g^0_\varepsilon \overline{\mathbf{u}_\varepsilon} \cdot \mathbf{n}^S_\varepsilon + \frac{i\omega}{c^2}\int_{\Omega_{F,\varepsilon}} g^0_\varepsilon \cdot \overline{\phi_\varepsilon}\right) + C\left(\|\mathbf{u}_\varepsilon\|^2_{\mathbf{L}^2(\Omega_{S,\varepsilon})} + \|\phi_\varepsilon\|^2_{L^2(\Omega_{F,\varepsilon})}\right) \\ \geq \gamma\left(\|\mathbf{u}_\varepsilon\|^2_{\mathbf{H}^1(\Omega_{S,\varepsilon})} + \|\phi_\varepsilon\|^2_{H^1(\Omega_{F,\varepsilon})}\right). \end{aligned} \tag{4.37}$$

To control the first term of estimate (4.37), we use the Cauchy–Schwartz and Young inequalities. We obtain first:

$$\left|\int_{\Omega_{S,\varepsilon}} \mathbf{f}_\varepsilon \cdot \overline{\mathbf{u}_\varepsilon}\right| \leq \frac{1}{2}\left(\|\mathbf{u}_\varepsilon\|^2_{\mathbf{L}^2(\Omega_{S,\varepsilon})} + \|\mathbf{f}_\varepsilon\|^2_{\mathbf{L}^2(\Omega)}\right), \tag{4.38}$$

$$\left|\frac{i\omega}{c^2}\int_{\Omega_{F,\varepsilon}} g^0_\varepsilon \cdot \overline{\phi_\varepsilon}\right| \leq \frac{\omega}{2c^2}\left(\|\phi_\varepsilon\|^2_{L^2(\Omega_{F,\varepsilon})} + \|g^0_\varepsilon\|^2_{L^2(\Omega)}\right), \tag{4.39}$$

and also, for all $\delta > 0$:

$$\begin{aligned} \left|\int_{\Gamma^I_\varepsilon} g^0_\varepsilon \overline{\mathbf{u}_\varepsilon} \cdot \mathbf{n}^S_\varepsilon\right| &= \left|\int_{\Omega_{F,\varepsilon}} g^0_\varepsilon \,\overline{\mathrm{div}\widehat{\mathbf{u}_\varepsilon}} + \nabla g^0_\varepsilon \cdot \overline{\widehat{\mathbf{u}_\varepsilon}}\right| \\ &\leq \frac{1}{2}\left(\delta\|\widehat{\mathbf{u}_\varepsilon}\|^2_{\mathbf{H}^1(\Omega_{F,\varepsilon})} + \delta^{-1}\|g^0_\varepsilon\|^2_{L^2(\Omega_{F,\varepsilon})} + \delta^{-1}\|\nabla g^0_\varepsilon\|^2_{L^2(\Omega_{F,\varepsilon})}\right). \end{aligned}$$

Thanks to the properties of the extension operator (Lemma 4.2.3) and to (4.36), there exists a constant C_1 independent of ε and ω such that

$$\left| \int_{\Gamma_\varepsilon^I} g_\varepsilon^0 \overline{\mathbf{u}_\varepsilon} \cdot \mathbf{n}_\varepsilon^S \right| \leq \frac{C_1}{2} \left(\delta \|\mathbf{u}_\varepsilon\|^2_{\mathbf{H}^1(\Omega_{S,\varepsilon})} + \delta^{-1} \|g_\varepsilon\|^2_{L^2(\Omega_{F,\varepsilon})} + \delta^{-1} \|\nabla g_\varepsilon\|^2_{L^2(\Omega_{F,\varepsilon})} \right).$$

Hence choosing $\delta = \gamma/C_1$ we get the estimate

$$\left| \int_{\Gamma_\varepsilon^I} g_\varepsilon^0 \overline{\mathbf{u}_\varepsilon} \cdot \mathbf{n}_\varepsilon^S \right| \leq \frac{\gamma}{2} \|\mathbf{u}_\varepsilon\|^2_{\mathbf{H}^1(\Omega_{S,\varepsilon})} + \frac{C_1^2}{2\gamma} \|g_\varepsilon\|^2_{H^1(\Omega_{F,\varepsilon})}. \tag{4.40}$$

Combining finally (4.37), (4.38), (4.39) and (4.40) we can conclude that for some constant $C > 0$ independent of ε (but depending on ω), the following estimate holds true:

$$\frac{\gamma}{2} \left(\|\mathbf{u}_\varepsilon\|^2_{\mathbf{H}^1(\Omega_{S,\varepsilon})} + \|\phi_\varepsilon\|^2_{H^1(\Omega_{F,\varepsilon})} \right) \leq C \left(\|\mathbf{u}_\varepsilon\|^2_{\mathbf{L}^2(\Omega)} + \|\phi_\varepsilon\|^2_{L^2(\Omega_{F,\varepsilon})} + \|\mathbf{f}_\varepsilon\|^2_{\mathbf{L}^2(\Omega)} + \|g_\varepsilon\|^2_{H^1(\Omega)} \right).$$

This ends the proof of estimate (4.35). □

4.3 Two–scale homogenization of the coupled model

Note here that the standard scheme to obtain the homogenized limit as ε goes to zero does not apply. Indeed, usually we follow the steps:

- existence of a solution for a given ε,
- *a priori* bounds, independent of ε,
- two–scale convergence up to a subsequence by the use of Proposition 4.2.10,
- identification of the two–scale homogenized problem.

However the problem presented here satisfies neither the first point, because of the two valid statements in the Fredholm alternative, nor the second point since we only have a Gårding inequality and not a coercivity property. In fact, it so happens that for some values of the frequency ω, depending on ε, our problem is not well–posed due to the occurence of so–called traction–free oscillations as was explained in Remark 4.2.13.

A way to cope with this difficulty is to make the hypothesis that the required well–posedness and boundedness results are true for a small enough ε, and proceed to homogenize according to the usual theory. Then, by studying the resulting homogenized problem, it is possible to get a better understanding of the Fredholm alternative for the coupled problem (4.22) as ε goes to zero. In fact, we show that away from the discrete set of eigenvalues of the homogenized problem, the coupled problem (4.22) is well–posed for ε small enough. Moreover, when the homogenized problem has a unique solution and due to the linear character of the system, the solutions of the problem (4.22) also satisfy *a priori* bounds uniform in ε. This allows us to prove the initial assumption for all values of ω distinct from the spectrum of the homogenized problem. This kind of proof was, up to our knowledge, initiated in [BF04] for Helmholtz problems and further used to study various homogenization problems in [BBDDG05, AGMR08, AAGM12].

Let us now present the main result of the section, which will allow us to pass to the limit and obtain, as the main conclusion to the paper, the homogenized behavior of the material.

Theorem 4.3.1. *There is a discrete set Λ, such that for any $\omega \in \mathbb{R} \setminus \Lambda$, there exists $\varepsilon_0(\omega)$ and $C(\omega)$ in $\mathbb{R}_+^*$ such that for any $0 < \varepsilon < \varepsilon_0$, the problem (4.22) is well–posed for any data $(\mathbf{f}_\varepsilon, g_\varepsilon) \in \mathbf{L}^2(\Omega) \times H^1(\Omega)$, and its solution $(\mathbf{u}_\varepsilon, \phi_\varepsilon)$ satisfies the a priori bounds:*

$$\|\mathbf{u}_\varepsilon\|^2_{\mathbf{H}^1(\Omega_{S,\varepsilon})} + \|\phi_\varepsilon\|^2_{H^1(\Omega_{F,\varepsilon})} \leq C(\omega) \left(\|\mathbf{f}_\varepsilon\|^2_{\mathbf{L}^2(\Omega)} + \|g_\varepsilon\|^2_{H^1(\Omega)} \right). \tag{4.41}$$

The proof of this result is detailed in Section 4.3.2, but we need to identify and study the homogenized problem first.

4.3.1 Two–scale problem identification

In this whole section, we fix $\omega \in \mathbb{R}$ and a sequence of data $(\mathbf{f}_\varepsilon, g_\varepsilon)_{\varepsilon>0} \subset \mathbf{L}^2(\Omega) \times H^1(\Omega)$, indexed by $\varepsilon > 0$, that converges strongly to $(\mathbf{f}, g) \in \mathbf{L}^2(\Omega) \times H^1(\Omega)$. We assume that there exists $C > 0$ such that for ε small enough the variational problem (4.22) with data $(\mathbf{f}_\varepsilon, g_\varepsilon)$ has at least one solution $(\mathbf{u}_\varepsilon, \phi_\varepsilon)$, such that the following bound holds uniformly in ε:

$$\|\mathbf{u}_\varepsilon\|^2_{\mathbf{H}^1(\Omega_{S,\varepsilon})} + \|\phi_\varepsilon\|^2_{H^1(\Omega_{F,\varepsilon})} \leq C \left(\|\mathbf{f}_\varepsilon\|^2_{\mathbf{L}^2(\Omega)} + \|g_\varepsilon\|^2_{H^1(\Omega)} \right). \tag{4.42}$$

Remark 4.3.2. *Note that these assumptions reflect the conclusions of Theorem 4.3.1, which we prove later on in Section 4.3.2.*

Using the two–scale convergence framework, we are going to investigate the asymptotics of problem (4.22) and identify the homogenized two–scale problem. Since the sequence $(\mathbf{f}_\varepsilon, g_\varepsilon)_{\varepsilon>0}$ converges strongly in $\mathbf{L}^2(\Omega) \times H^1(\Omega)$ it is bounded uniformly in ε, so that from (4.42), for some $C > 0$ independent of ε,

$$\|\mathbf{u}_\varepsilon\|^2_{\mathbf{H}^1(\Omega_{S,\varepsilon})} + \|\phi_\varepsilon\|^2_{H^1(\Omega_{F,\varepsilon})} \leq C.$$

Thanks to the properties of the extension operators introduced in section 4.2.3 with (4.30), we have then for some constant $C > 0$:

$$\|\widehat{\mathbf{u}_\varepsilon}\|^2_{\mathbf{H}^1(\Omega)} + \frac{1}{\varepsilon^2}\|\widehat{\phi_\varepsilon}\|^2_{L^2(\Omega)} + |\widehat{\phi_\varepsilon}|^2_{H^1(\Omega)} \leq C. \tag{4.43}$$

Thanks to Proposition 4.2.10, we know that there exists a subsequence, still indexed by ε for simplicity, and three functions: $\mathbf{u} \in \mathbf{H}^1_0(\Omega)$, $\mathbf{u}^1 \in \mathbf{L}^2(\Omega; H^1_\#(\mathcal{Y}))$ and $\phi \in L^2(\Omega; H^1_\#(\mathcal{Y})/\mathbb{C})$, such that $\widehat{\mathbf{u}_\varepsilon}$, $\widehat{\phi_\varepsilon}$ and their gradients two–scale converge:

$$\begin{aligned} &\widehat{\mathbf{u}_\varepsilon} \twoheadrightarrow \mathbf{u} \text{ in } \mathbf{L}^2(\Omega \times \mathcal{Y}), && \nabla\widehat{\mathbf{u}_\varepsilon} \twoheadrightarrow \nabla_x \mathbf{u} + \nabla_{\mathbf{y}} \mathbf{u}^1 \text{ in } L^2(\Omega \times \mathcal{Y})^{d\times d}, \\ &\widehat{\phi_\varepsilon} \twoheadrightarrow 0 \text{ in } L^2(\Omega \times \mathcal{Y}), && \nabla\widehat{\phi_\varepsilon} \twoheadrightarrow \nabla_{\mathbf{y}} \phi \text{ in } \mathbf{L}^2(\Omega \times \mathcal{Y}). \end{aligned} \tag{4.44}$$

We are now going to identify the homogenized problem, satisfied by $\mathbf{u}$, $\chi_S \mathbf{u}^1$ and $\chi_F \phi$.

Identification of the homogenized problem To pass to the limit in the variational formulation we shall use well chosen test functions:

- $\mathbf{v}_\varepsilon(\mathbf{x}, \mathbf{x}/\varepsilon) = \mathbf{v}(\mathbf{x}) + \varepsilon \mathbf{v}^1(\mathbf{x}, \mathbf{x}/\varepsilon)$ with $\mathbf{v} \in \boldsymbol{\mathcal{D}}(\Omega)$ and $\mathbf{v}^1 \in \boldsymbol{\mathcal{D}}(\Omega, C^\infty_\#(\mathcal{Y}))$, and
- $\psi_\varepsilon(\mathbf{x}, \mathbf{x}/\varepsilon) = \varepsilon \psi(\mathbf{x}, \mathbf{x}/\varepsilon)$ with $\psi \in \mathcal{D}\left(\Omega, C^\infty(\mathcal{Y}_F) \cap H^1_{mean}(\mathcal{Y}_F)\right)$.

We can then pass to the limit as ε goes to zero in problem (4.22), which writes:

$$\begin{aligned} &\int_{\Omega_{S,\varepsilon}} -\rho_S \omega^2 \mathbf{u}_\varepsilon \cdot \overline{\mathbf{v}_\varepsilon} + \sigma_\varepsilon(\mathbf{u}_\varepsilon) : \overline{e(\mathbf{v}_\varepsilon)} + \rho_0 c^2 \sum_{\mathbf{k} \in \mathbf{Z}^\Omega_\varepsilon} \frac{1}{\varepsilon^d |\mathcal{Y}_F|} \left(\int_{\Gamma^{\mathbf{k}}_{F,\varepsilon}} \mathbf{u}_\varepsilon \cdot \mathbf{n}^S_\varepsilon \right) \overline{\left(\int_{\Gamma^{\mathbf{k}}_{F,\varepsilon}} \mathbf{v}_\varepsilon \cdot \mathbf{n}^S_\varepsilon \right)} \\ &+\rho_0 \int_{\Omega_{F,\varepsilon}} -\frac{\omega^2}{c^2} \phi_\varepsilon \overline{\psi_\varepsilon} + \nabla\phi_\varepsilon \cdot \overline{\nabla\psi_\varepsilon} + \rho_0 \int_{\Gamma^I_\varepsilon} i\omega \left(\overline{\psi_\varepsilon} \mathbf{u}_\varepsilon \cdot \mathbf{n}^S_\varepsilon - \phi_\varepsilon \overline{\mathbf{v}_\varepsilon} \cdot \mathbf{n}^S_\varepsilon \right) \\ &= \int_{\Omega_{S,\varepsilon}} \mathbf{f}_\varepsilon \cdot \overline{\mathbf{v}_\varepsilon} + \int_{\Omega_{F,\varepsilon}} \nabla g_\varepsilon \cdot \overline{\mathbf{v}_\varepsilon} + \int_{\Omega_{F,\varepsilon}} \left(g_\varepsilon - \frac{|\mathcal{Y}|}{|\mathcal{Y}_F|} \Pi_\varepsilon(\chi_{F,\varepsilon} g_\varepsilon) \right) \overline{\left(\operatorname{div}(\mathbf{v}_\varepsilon) - \frac{i\omega}{c^2} \psi_\varepsilon \right)}. \end{aligned} \tag{4.45}$$

It is straightforward to pass to the limit in most terms of the identity. For instance, $\chi_{S,\varepsilon}\sigma_\varepsilon(\mathbf{v}_\varepsilon)$ is an admissible test function in the sense of two–scale convergence, so

$$\int_{\Omega_{S,\varepsilon}} \sigma_\varepsilon(\mathbf{u}_\varepsilon) : e(\mathbf{v}_\varepsilon) = \int_{\Omega_{S,\varepsilon}} e(\mathbf{u}_\varepsilon) : \sigma_\varepsilon(\mathbf{v}_\varepsilon) \to \int_\Omega \int_{\mathcal{Y}_S} \left(e_{\mathbf{x}}(\mathbf{u}) + e_{\mathbf{y}}(\mathbf{u}^1)\right) : \left(\sigma_{\mathbf{x}}(\mathbf{v}) + \sigma_{\mathbf{y}}(\mathbf{v}^1)\right)$$
$$= \int_\Omega \int_{\mathcal{Y}_S} \left(\sigma_{\mathbf{x}}(\mathbf{u}) + \sigma_{\mathbf{y}}(\mathbf{u}^1)\right) : \left(e_{\mathbf{x}}(\mathbf{v}) + e_{\mathbf{y}}(\mathbf{v}^1)\right),$$

where we denote by $\sigma_{\mathbf{x}}(\cdot)$ and $\sigma_{\mathbf{y}}(\cdot)$ respectively the tensor–valued operators:

$$\sigma_{\mathbf{x}}(\mathbf{u}) : \ (\mathbf{x},\ \mathbf{y}) \mapsto \lambda(\mathbf{x},\mathbf{y})\mathrm{div}_{\mathbf{x}}(\mathbf{u})(\mathbf{x},\mathbf{y})\mathrm{Id} + \mu(\mathbf{x},\mathbf{y})e_{\mathbf{x}}(\mathbf{u})(\mathbf{x},\mathbf{y}) \text{ for } \mathbf{u} \in \mathbf{H}^1(\Omega, L^2_\#(\mathcal{Y})), \tag{4.46a}$$
$$\sigma_{\mathbf{y}}(\mathbf{u}) : \ (\mathbf{x},\ \mathbf{y}) \mapsto \lambda(\mathbf{x},\mathbf{y})\mathrm{div}_{\mathbf{y}}(\mathbf{u})(\mathbf{x},\mathbf{y})\mathrm{Id} + \mu(\mathbf{x},\mathbf{y})e_{\mathbf{y}}(\mathbf{u})(\mathbf{x},\mathbf{y}) \text{ for } \mathbf{u} \in \mathbf{H}^1_\#(\mathcal{Y}, L^2(\Omega)). \tag{4.46b}$$

The main difficulty consists in dealing with the nonstandard terms supported by the interior boundary Γ^I_ε, which are:

$$\rho_0 c^2 \sum_{\mathbf{k}\in\mathbf{Z}^\Omega_\varepsilon} \frac{1}{\varepsilon^d |\mathcal{Y}_F|} \left(\int_{\Gamma^{\mathbf{k}}_{F,\varepsilon}} \mathbf{u}_\varepsilon \cdot \mathbf{n}^S_\varepsilon\right) \overline{\left(\int_{\Gamma^{\mathbf{k}}_{F,\varepsilon}} \mathbf{v}_\varepsilon \cdot \mathbf{n}^S_\varepsilon\right)} + \rho_0 \int_{\Gamma^I_\varepsilon} i\omega \left(\overline{\psi_\varepsilon}\mathbf{u}_\varepsilon \cdot \mathbf{n}^S_\varepsilon - \phi_\varepsilon \overline{\mathbf{v}_\varepsilon} \cdot \mathbf{n}^S_\varepsilon\right),$$

and also with the term

$$\int_{\Omega_{F,\varepsilon}} \left(g_\varepsilon - \frac{|\mathcal{Y}|}{|\mathcal{Y}_F|}\Pi_\varepsilon(\chi_{F,\varepsilon} g_\varepsilon)\right) \overline{\left(\mathrm{div}(\mathbf{v}_\varepsilon) - \frac{i\omega}{c^2}\psi_\varepsilon\right)}.$$

First, we consider the product of integrals on the boundary of the holes as in [BGMO08] and [Con85]. We write:

$$\sum_{\mathbf{k}\in\mathbf{Z}^\Omega_\varepsilon} \varepsilon^{-d} \left(\int_{\Gamma^{\mathbf{k}}_{F,\varepsilon}} \mathbf{u}_\varepsilon \cdot \mathbf{n}^S_\varepsilon\right) \overline{\left(\int_{\Gamma^{\mathbf{k}}_{F,\varepsilon}} \mathbf{v}_\varepsilon \cdot \mathbf{n}^S_\varepsilon\right)} = \sum_{\mathbf{k}\in\mathbf{Z}^\Omega_\varepsilon} \int_{\mathcal{Y}_{F^{\varepsilon,\mathbf{k}}}} \mathrm{div}\ \widehat{\mathbf{u}_\varepsilon}(\mathbf{x}) \overline{\left(\varepsilon^{-d} \int_{\mathcal{Y}_{F^{\varepsilon,\mathbf{k}}}} \mathrm{div}\ \mathbf{v}_\varepsilon(\mathbf{x}')d\mathbf{x}'\right)} d\mathbf{x}$$
$$= \int_\Omega \chi_{F,\varepsilon}\ \mathrm{div}\ \widehat{\mathbf{u}_\varepsilon}\ \ \overline{\Pi_\varepsilon(\chi_{F,\varepsilon}\mathrm{div}\ \mathbf{v}_\varepsilon)},$$

where Π_ε is defined by (4.21). To study the convergence of this product involving the projector Π_ε, we need the following strong convergence result, which is proved in [AGMR08] or [BGMO08]:

Lemma 4.3.3. *Let $\phi \in C^\infty(\overline{\Omega}; C^\infty_\#(\mathcal{Y}))$, then*

$$\Pi_\varepsilon\left(\phi\left(\cdot, \frac{\cdot}{\varepsilon}\right)\chi^\varepsilon_F\right) \to \frac{1}{|\mathcal{Y}|}\int_{\mathcal{Y}_F} \phi(\cdot,\mathbf{y})d\mathbf{y} \qquad \textit{strongly in } L^2(\Omega).$$

As a first consequence of Lemma 4.3.3, we obtain that $\int_{\mathcal{Y}_F}\phi = 0$ a.e. $\mathbf{x} \in \Omega$, because $\Pi_\varepsilon\left(\widehat{\phi_\varepsilon}\chi_{F,\varepsilon}\right) = 0$ in Ω. Next, since $\mathrm{div}\ \mathbf{v}_\varepsilon = \mathrm{div}_{\mathbf{x}}\mathbf{v} + \varepsilon\mathrm{div}_{\mathbf{y}}\mathbf{v}^1 + \mathrm{div}_{\mathbf{x}}\mathbf{v}^1$, we obtain immediately:

$$\Pi_\varepsilon(\chi_{F,\varepsilon}\mathrm{div}\ \mathbf{v}_\varepsilon) \to \int_{\mathcal{Y}_F} \mathrm{div}_{\mathbf{x}}\mathbf{v} + \mathrm{div}_{\mathbf{y}}\mathbf{v}^1 \qquad \text{strongly in } L^2(\Omega).$$

Moreover, for any $w \in \mathcal{D}(\Omega)$, the function

$$\chi_F(\mathbf{y})w(\mathbf{x}) \in C(\overline{\Omega}, L^2_\#(\mathcal{Y}))$$

is an admissible test function, see Remark 4.2.9. Hence, by definition of two–scale convergence we obtain

$$\chi_{F,\varepsilon}\text{div } \widehat{\mathbf{u}_\varepsilon} \rightharpoonup \int_{\mathcal{Y}_F} \text{div}_{\mathbf{x}}\mathbf{u} + \text{div}_{\mathbf{y}}\mathbf{u}^1 \qquad \text{weakly in } L^2(\Omega).$$

Combining these two results, we see that $\int_\Omega \left(\chi_{F,\varepsilon}\text{ div }\widehat{\mathbf{u}_\varepsilon}\ \overline{\Pi_\varepsilon(\chi_{F,\varepsilon}\text{ div }\mathbf{v}_\varepsilon)}\right)$ converges to

$$\frac{1}{|\mathcal{Y}_F|}\int_\Omega \left(\int_{\mathcal{Y}_F} \text{div}_{\mathbf{x}}\mathbf{u} + \text{div}_{\mathbf{y}}\mathbf{u}^1 d\mathbf{y}\right)\overline{\left(\int_{\mathcal{Y}_F} \text{div}_{\mathbf{x}}\mathbf{v} + \text{div}_{\mathbf{y}}\mathbf{v}^1 d\mathbf{y}'\right)}.$$

Another nonstandard term corresponds to the integral over the interior boundary. This one is easier to deal with since it can be rewritten as a standard bilinear form using the Stokes formula. Indeed, we obtain:

$$\int_{\Gamma_\varepsilon^I} \overline{\psi}\mathbf{u}_\varepsilon\cdot\mathbf{n}_\varepsilon^S - \phi_\varepsilon\overline{\mathbf{v}_\varepsilon}\cdot\mathbf{n}_\varepsilon^S = \int_{\Omega_{F,\varepsilon}} \left(\nabla\phi_\varepsilon\cdot\overline{\mathbf{v}_\varepsilon} + \phi_\varepsilon\text{div }\mathbf{v}_\varepsilon - \overline{\nabla\psi_\varepsilon}\cdot\mathbf{u}_\varepsilon - \overline{\psi_\varepsilon}\text{div }\mathbf{v}_\varepsilon\right).$$

Because $\widehat{\phi_\varepsilon}$ and ψ_ε converge strongly to 0 in $L^2(\Omega)$, see (4.44), passing to the two–scale limit yields:

$$\lim_{\varepsilon\to 0}\int_{\Gamma_\varepsilon^I} \overline{\psi}\mathbf{u}_\varepsilon\cdot\mathbf{n}_\varepsilon^S - \phi_\varepsilon\overline{\mathbf{v}}\cdot\mathbf{n}_\varepsilon^S = \int_\Omega\int_{\mathcal{Y}_F} \nabla_{\mathbf{y}}\phi\cdot\overline{\mathbf{v}} - \overline{\nabla_{\mathbf{y}}\psi}\cdot\mathbf{u}.$$

Finally, let us compute the limit of the term:

$$\int_{\Omega_{F,\varepsilon}} \left(g_\varepsilon - \frac{|\mathcal{Y}|}{|\mathcal{Y}_F|}\Pi_\varepsilon(\chi_{F,\varepsilon}g_\varepsilon)\right)\overline{\left(\text{div}(\mathbf{v}_\varepsilon) - \frac{i\omega}{c^2}\psi_\varepsilon\right)}.$$

Let $g_\varepsilon^0 = \left(g_\varepsilon - \frac{|\mathcal{Y}|}{|\mathcal{Y}_F|}\Pi_\varepsilon(g_\varepsilon\chi_{F,\varepsilon})\right)$ in $L^2(\Omega_{F,\varepsilon})$. This function has zero mean over each pore $\mathcal{Y}_{F,\varepsilon}^{\mathbf{k}}$ in the domain $\Omega_{F,\varepsilon}$, so from Lemma 4.2.7, we deduce that for some $C>0$ independant of ε,

$$\|\widehat{g_\varepsilon^0}\|_{L^2(\Omega_{F,\varepsilon})} \le C\varepsilon|g_\varepsilon^0|_{H^1(\Omega_{F,\varepsilon})} \le C\varepsilon\|\nabla g_\varepsilon\|_{\mathbf{L}^2(\Omega)}.$$

Since the sequence (g_ε) is strongly convergent in $H^1(\Omega)$, $\|\nabla g_\varepsilon\|_{\mathbf{L}^2(\Omega)}$ is bounded independently of ε. Thus $\widehat{g_\varepsilon^0}$ converges strongly to 0 in $L^2(\Omega)$. Hence

$$\lim_{\varepsilon\to 0}\int_{\Omega_{F,\varepsilon}} g_\varepsilon^0\overline{\left(\text{div}(\mathbf{v}_\varepsilon) - \frac{i\omega}{c^2}\psi_\varepsilon\right)} = \lim_{\varepsilon\to 0}\int_\Omega \chi_{F,\varepsilon}\widehat{g_\varepsilon^0}\overline{\left(\text{div}(\mathbf{v}_\varepsilon) - \frac{i\omega}{c^2}\psi_\varepsilon\right)} = 0.$$

We can now pass to the two–scale limit in every term of identity (4.45). We deduce that $\mathbf{u}$, $\mathbf{u}^1$ and ϕ are solutions of the following two–scale variational formulation: for all $\mathbf{v}\in\boldsymbol{\mathcal{D}}(\Omega)$, $\mathbf{v}^1(\mathbf{x},\mathbf{y})\in\boldsymbol{\mathcal{D}}(\Omega, C^\infty_\#(\mathcal{Y}))$ and $\psi\in\mathcal{D}\left(\Omega, C^\infty(\mathcal{Y}_F)\cap H^1_{mean}(\mathcal{Y}_F)\right)$,

$$\begin{aligned}
&\int_\Omega\int_{\mathcal{Y}_S} -\rho_S\omega^2\mathbf{u}\cdot\overline{\mathbf{v}} + \left(\sigma_{\mathbf{x}}(\mathbf{u}) + \sigma_{\mathbf{y}}(\mathbf{u}^1)\right) : \overline{\left(e_{\mathbf{x}}(\mathbf{v}) + e_{\mathbf{y}}(\mathbf{v}^1)\right)} \\
&\quad + \frac{\rho_0 c^2}{|\mathcal{Y}_F|}\int_\Omega \left(\int_{\mathcal{Y}_F} (\text{div}_{\mathbf{x}}\mathbf{u} + \text{div}_{\mathbf{y}}\mathbf{u}^1)d\mathbf{y}\right)\overline{\left(\int_{\mathcal{Y}_F} (\text{div}_{\mathbf{x}}\mathbf{v} + \text{div}_{\mathbf{y}}\mathbf{v}^1)d\mathbf{y}'\right)}d\mathbf{x} \qquad (4.47)\\
&\quad + \rho_0\int_\Omega\int_{\mathcal{Y}_F} \nabla_{\mathbf{y}}\phi\cdot\overline{\nabla_{\mathbf{y}}\psi} + \rho_0 i\omega\int_\Omega\int_{\mathcal{Y}_F} \left(\nabla_{\mathbf{y}}\phi\cdot\overline{\mathbf{v}} - \overline{\nabla_{\mathbf{y}}\psi}\cdot\mathbf{u}\right) \\
&\quad = \int_\Omega\int_{\mathcal{Y}} (\mathbf{f}\chi_S + \nabla g\chi_F)\cdot\overline{\mathbf{v}}.
\end{aligned}$$

Remark 4.3.4. *Let us make a few comments on the homogenized model described by the system (4.47). At first glance, the only remaining inertia term seems to be $\rho_S\omega^2\mathbf{u}$, so it seems that there is no added mass effect from the fluid on the structure. However, we will see that we have the relationship*

$$\nabla_{\mathbf{y}}\phi_\varepsilon = i\omega\mathbf{u},$$

so the effective density is equal to the average density of the mixture.

On the other hand, there is no impact from the micro–structure geometry on the effective density of the homogenized material because $\mathbf{u}^1$ does not appear in the inertia terms. This means, for example, that there is no possibility of a band gap effect as in [AGMR08] as the mass does not depend on the frequency ω.

Remark 4.3.5. *When ω is zero, the fluid and the structure decouple and we find $\phi = 0$. Our homogenized model then reduces to the same homogenized two–scale system found in the static case in [BGMO08].*

The next step is to decompose this two–scale problem on $\Omega \times \mathcal{Y}$ into cell problems for ϕ and $\mathbf{u}^1$ where we use the macroscopic displacement $\mathbf{u}$ as a slow–varying parameter, and an effective homogenized problem on $\mathbf{u}$. Solving the cell problems yields explicit corrector functions, which can be reinjected in (4.47) to write the homogenized coefficients for the macroscopic problem.

Fluid cell problem Choosing $\mathbf{v} = \mathbf{0}$ and $\mathbf{v}^1 = \mathbf{0}$, we recover the following variational problem for the homogenized fluid velocity potential ϕ. The restriction $\phi|_{\mathcal{Y}_F} \in L^2(\Omega, H^1_{mean}(\mathcal{Y}_F))$ verifies:

$$\rho_0 \int_\Omega \int_{\mathcal{Y}_F} \nabla_{\mathbf{y}}\phi \cdot \overline{\nabla_{\mathbf{y}}\psi} = \rho_0 i\omega \int_\Omega \int_{\mathcal{Y}_F} \overline{\nabla_{\mathbf{y}}\psi} \cdot \mathbf{u} \quad \forall \psi \in \mathcal{D}\left(\Omega, C^\infty(\mathcal{Y}_F) \cap H^1_{mean}(\mathcal{Y}_F)\right).$$

Since $\mathbf{u}$ does not depend on the $\mathbf{y}$ variable and $\mathcal{Y}_F$ is strictly included in $\mathcal{Y}$, it implies that $\nabla_{\mathbf{y}}\phi = i\omega\mathbf{u}$ a.e. in $\Omega \times \mathcal{Y}_F$. This determines uniquely $\phi|_{\mathcal{Y}_F}$ as a function of $\mathbf{u}$. Remember that we have chosen originally the origin as the barycenter of $\mathcal{Y}_F$, hence this yields

$$\phi = i\omega\mathbf{y}\cdot\mathbf{u} \quad \text{and} \quad \nabla_{\mathbf{y}}\phi = i\omega\mathbf{u}, \qquad \text{on } \Omega \times \mathcal{Y}_F. \tag{4.48}$$

Remark 4.3.6. *We see that the velocity of the fluid coincides locally with the velocity of the structure. This result is a consequence of the completely disconnected geometry of the fluid domain: since the pores are closed, there is no independent motion of the gas with respect to the structure.*

Elastic cell problem From (4.47), by taking $\mathbf{v} = \mathbf{0}$ and $\psi = 0$ we obtain that a.e. $\mathbf{x} \in \Omega$ and for all $\mathbf{v}^1 \in \boldsymbol{C}^\infty_\#(\mathcal{Y})$,

$$\int_{\mathcal{Y}_S} \left(\sigma_{\mathbf{x}}(\mathbf{u}) + \sigma_{\mathbf{y}}(\mathbf{u}^1)\right) : \overline{e_{\mathbf{y}}(\mathbf{v}^1)} = \frac{\rho_0 c^2}{|\mathcal{Y}_F|}\left(\int_{\mathcal{Y}_F} \mathrm{div}_{\mathbf{x}}\mathbf{u} + \mathrm{div}_{\mathbf{y}}\mathbf{u}^1 d\mathbf{y}\right)\overline{\left(\int_{\Gamma_F} \mathbf{v}^1 \cdot \mathbf{n}_S\right)}. \tag{4.49}$$

The strong formulation associated with (4.49) is

$$\begin{cases} -\mathbf{div}_{\mathbf{y}}\left(\sigma_{\mathbf{y}}(\mathbf{u}^1)\right) = \mathbf{div}_{\mathbf{y}}\left(\sigma_{\mathbf{x}}(\mathbf{u})\right), & \text{in } \mathcal{Y}_S, \\ \sigma_{\mathbf{y}}(\mathbf{u}^1)\mathbf{n}_S - \dfrac{\rho_0 c^2}{|\mathcal{Y}_F|}\left(\displaystyle\int_{\Gamma_F} \mathbf{u}^1 \cdot \mathbf{n}_S\right)\mathbf{n}_S = \rho_0 c^2 \mathrm{div}_{\mathbf{x}}(\mathbf{u})\mathbf{n}_S - \sigma_{\mathbf{x}}(\mathbf{u})\mathbf{n}_S, & \text{on } \Gamma_F, \\ \mathbf{u}^1 \text{ is } \mathcal{Y}\text{–periodic.} \end{cases}$$

Since this problem is linear, we are going to take advantage of the superposition principle to express $\mathbf{u}^1$ in terms of $\mathbf{u}$. We define the auxiliary functions $\mathbf{p}^{kl} \in \mathbf{H}^1(\mathcal{Y}_S)$ by:

$$\mathbf{p}^{kl}(\mathbf{y}) = \frac{1}{2}\left(y_k \mathbf{e}^l + y_l \mathbf{e}^k\right) \qquad \text{for } 1 \leq k, l \leq d, \tag{4.50}$$

where the vectors $\mathbf{e}^k$ for $1 \leq k \leq d$ are the unit vectors of $\mathbb{R}^d$ whose components are $\mathbf{e}^k_l = \delta_{kl}$ for $1 \leq k, l \leq d$. Now, we compute

$$e_{\mathbf{y}}(\mathbf{p}^{kl}) = \frac{1}{2}\left(\mathbf{e}^k \otimes \mathbf{e}^l + \mathbf{e}^l \otimes \mathbf{e}^k\right).$$

Therefore, the family $\left(e_{\mathbf{y}}(\mathbf{p}^{kl})\right)$ forms a basis of the set of symmetric tensors of order 2, and in particular

$$e_{\mathbf{x}}(\mathbf{u}) = e_{\mathbf{x}}(\mathbf{u})_{kl} e_{\mathbf{y}}(\mathbf{p}^{kl}).$$

Moreover, we compute:

$$\begin{aligned}
\sigma_{\mathbf{x}}(\mathbf{u}) &= \lambda \mathrm{div}(\mathbf{u})\mathrm{Id} + \mu e_{\mathbf{x}}(\mathbf{u}) \\
&= \lambda \left(e_{\mathbf{x}}(\mathbf{u})_{kl}\delta_{kl}\right)\mathrm{Id} + \mu e_{\mathbf{x}}(\mathbf{u})_{kl} e_{\mathbf{y}}(\mathbf{p}^{kl}) \\
&= e_{\mathbf{x}}(\mathbf{u})_{kl}\left(\lambda \mathrm{div}(\mathbf{p}^{kl}) + \mu e_{\mathbf{y}}(\mathbf{p}^{kl})\right) \\
&= e_{\mathbf{x}}(\mathbf{u})_{kl}\sigma_{\mathbf{y}}(\mathbf{p}^{kl}).
\end{aligned}$$

Using the superposition principle in the local problem (4.49)), we decompose $\mathbf{u}^1|_{\Omega\times\mathcal{Y}_S}$ as follows:

$$\mathbf{u}^1(\mathbf{x}, \mathbf{y}) = e_{\mathbf{x}}(\mathbf{u})_{kl}(\mathbf{x})\boldsymbol{\chi}^{kl}(\mathbf{x}, \mathbf{y}), \quad \mathbf{x} \in \Omega,\ \mathbf{y} \in \mathcal{Y}_S, \tag{4.51}$$

where the functions $\boldsymbol{\chi}^{kl} \in \mathbf{L}^\infty(\Omega, H^1_\#(\mathcal{Y}_S, \mathbb{R})/\mathbb{R})$, $1 \leq k, l \leq d$ are solutions of the cell problems

$$LP_{kl} \begin{cases} -\mathbf{div}_{\mathbf{y}}\left(\sigma_{\mathbf{y}}(\mathbf{p}^{kl} + \boldsymbol{\chi}^{kl})\right) = \mathbf{0}, & \text{in } \mathcal{Y}_S, \\ \sigma_{\mathbf{y}}(\mathbf{p}^{kl} + \boldsymbol{\chi}^{kl})\mathbf{n}_S - \dfrac{\rho_0 c^2}{|\mathcal{Y}_F|}\left(\displaystyle\int_{\Gamma_F} (\mathbf{p}^{kl} + \boldsymbol{\chi}^{kl}) \cdot \mathbf{n}_S\right)\mathbf{n}_S = \mathbf{0}, & \text{on } \Gamma_F, \\ \boldsymbol{\chi}^{kl} \text{ is } \mathcal{Y}\text{–periodic.} \end{cases} \tag{4.52}$$

Remark 4.3.7. *Note that there is no dependence on ω in the structure cell problem, so the homogenized material's elastic behavior is independent of frequency. It is, however, parameterized by the slow variable $\mathbf{x}$ if the Lamé coefficients $\lambda(\mathbf{x}, \mathbf{y})$ and $\mu(\mathbf{x}, \mathbf{y})$ depend effectively on $\mathbf{x}$.*

Remark 4.3.8. *The functions $\boldsymbol{\chi}^{kl}$ are called the correctors for the homogenized problem (4.47). The cell problems LP_{kl} have only real coefficients and data; therefore, the family of correctors $(\boldsymbol{\chi}^{kl})_{kl}$ are in fact $\mathbb{R}^d$–valued functions by opposition to the complex–valued displacement. This will be important when computing the homogenized coefficients, see Proposition 4.3.13.*

Note that the system (4.52) is parameterized by the slow variable $\mathbf{x}$ and involves a non–local boundary term.

Remark 4.3.9. *The cell problem is nonstandard as there is a non–local term in the boundary conditions, as in the static case [BGMO08].*

The compatibility condition for existence and uniqueness of solutions of LP_{kl}, or more generally for any problem of the form

$$\begin{cases} -\mathbf{div}_{\mathbf{y}}\left(\sigma_{\mathbf{y}}(\mathbf{u})\right) = \mathbf{F}, & \text{in } \mathcal{Y}_S \\ \sigma_{\mathbf{y}}(\mathbf{u})\mathbf{n}_S - \dfrac{\rho_0 c^2}{|\mathcal{Y}_F|}\left(\displaystyle\int_{\Gamma_F} \mathbf{u} \cdot \mathbf{n}_S\right)\mathbf{n}_S = \mathbf{G}, & \text{on } \Gamma_F \\ \mathbf{u} \text{ is } \mathcal{Y}\text{–periodic,} \end{cases} \tag{4.53}$$

reads, since $\int_{\Gamma_F} \mathbf{n}_S = \mathbf{0}$:

$$\int_{\mathcal{Y}_S} \mathbf{F} + \int_{\Gamma_F} \mathbf{G} = \mathbf{0}. \tag{4.54}$$

In our case, it writes:

$$\begin{aligned}\int_{\mathcal{Y}_S} \mathbf{div_y}\left(\sigma_{\mathbf{y}}(\mathbf{p}^{kl})\right) + \int_{\Gamma_F} \left(\rho_0 c^2 \mathrm{div}_{\mathbf{y}}(\mathbf{p}^{kl})\mathbf{n}_S - \sigma_{\mathbf{y}}(\mathbf{p}^{kl})\mathbf{n}_S\right) \\ = \int_{\Gamma_F} \sigma_{\mathbf{y}}(\mathbf{p}^{kl})\mathbf{n}_S - \int_{\Gamma_F} \sigma_{\mathbf{y}}(\mathbf{p}^{kl})\mathbf{n}_S = \mathbf{0}.\end{aligned}$$

Thus, the compatibility condition is satisfied, and the local problems LP_{kl} as well as (4.49) are well posed. Notice that the function $\mathbf{p}^{kl} + \boldsymbol{\chi}^{kl}$, which appears in the cell problem LP_{kl}, describes the microstructure's response to a spatially slowly varying strain. We will need the following technical result for such functions, a special version of Korn's inequality, which is proved in the annex:

Lemma 4.3.10. *Consider the space of real–valued functions on $\mathcal{Y}_S$ defined as follows:*

$$\mathbf{V} = Span\left\{(\mathbf{p}^{kl})_{1\leq k,l\leq d}\right\} + \mathbf{H}^1_{\#}(\mathcal{Y}_S,\mathbb{R})/\mathbb{R} \subset \mathbf{H}^1(\mathcal{Y}_S,\mathbb{R})/\mathbb{R}, \tag{4.55}$$

where the family $(\mathbf{p}_{kl})_{1\leq k,l\leq d}$ is defined by (4.50). Then the following Korn's inequality holds in $\mathbf{V}$: there exists $C > 0$ depending only on $\mathcal{Y}_S$ such that

$$\|\boldsymbol{\phi}\|_{\mathbf{H}^1(\mathcal{Y}_S)} \leq C\|e(\boldsymbol{\phi})\|_{L^2(\mathcal{Y}_S)} \qquad \forall \boldsymbol{\phi} \in \mathbf{V}. \tag{4.56}$$

Homogenized problem Thanks to the expressions of ϕ (4.48) and $\mathbf{u}^1$ (4.51) parameterized by $\mathbf{u}$, we can eliminate $\mathbf{u}^1$ and ϕ from the two–scale system (4.47) to obtain the homogenized variational formulation satisfied by the displacement $\mathbf{u}$: for any $\mathbf{v} \in \boldsymbol{\mathcal{D}}(\Omega)$,

$$\begin{aligned}\int_\Omega -(|\mathcal{Y}_S|\rho_S + |\mathcal{Y}_F|\rho_0)\omega^2\mathbf{u}\cdot\overline{\mathbf{v}} + \int_{\mathcal{Y}_S}\left(\sigma_{\mathbf{x}}(\mathbf{u}) + e_{\mathbf{x}}(\mathbf{u})_{kl}\int_{\mathcal{Y}_S}\sigma_{\mathbf{y}}(\boldsymbol{\chi}^{kl})\right) : \overline{e_{\mathbf{x}}(\mathbf{v})} \\ + \rho_0 c^2 \int_\Omega \left(|\mathcal{Y}_F|\mathrm{div}_{\mathbf{x}}\mathbf{u} - e_{\mathbf{x}}(\mathbf{u})_{kl}\int_{\Gamma_F}\boldsymbol{\chi}^{kl}\cdot\mathbf{n}_S\right)\overline{\mathrm{div}_{\mathbf{x}}\mathbf{v}}d\mathbf{x} \\ = \int_\Omega (|\mathcal{Y}_S|\mathbf{f} + |\mathcal{Y}_F|\nabla g)\cdot\overline{\mathbf{v}}.\end{aligned}$$

Now, this formulation motivates the introduction of the *homogenized coefficients*, respectively the homogenized density, elastic tensor and stress of the effective material:

$$\rho^* = |\mathcal{Y}_S|\rho_S + |\mathcal{Y}_F|\rho_0, \tag{4.57}$$

$$\mathcal{A}^*_{ijkl} = \int_{\mathcal{Y}_S}\left(\sigma_{\mathbf{y}}(\mathbf{p}^{kl} + \boldsymbol{\chi}^{kl})_{ij} - \rho_0 c^2\delta_{ij}\mathrm{div}_{\mathbf{y}}\boldsymbol{\chi}^{kl}\right) + \rho_0 c^2|\mathcal{Y}_F|\delta_{ij}\delta_{kl}, \tag{4.58}$$

$$\sigma^*(\mathbf{u}) = \left(\mathcal{A}^*_{ijkl}e(\mathbf{u})_{kl}\right)_{1\leq i,j\leq d} = \mathcal{A}^* e(\mathbf{u}). \tag{4.59}$$

Finally, by density of test functions $\mathbf{v} \in \boldsymbol{\mathcal{D}}(\Omega)$ in $\mathbf{H}^1_0(\Omega)$, $\mathbf{u}$ is a solution of the following variational problem on $\mathbf{H}^1_0(\Omega)$: find $\mathbf{u} \in \mathbf{H}^1_0(\Omega)$ such that for any $\mathbf{v} \in \mathbf{H}^1_0(\Omega)$,

$$\int_\Omega -\rho^*\omega^2\mathbf{u}\cdot\overline{\mathbf{v}} + \mathcal{A}^* e(\mathbf{u}) : \overline{e(\mathbf{v})} = \int_\Omega (|\mathcal{Y}_S|\mathbf{f} + |\mathcal{Y}_F|\nabla g)\cdot\overline{\mathbf{v}}. \tag{4.60}$$

Remark 4.3.11. *Let us comment on the properties of the homogenized problem (4.60), which are easier to understand than for the two–scale formulation (4.47). In particular, we can study from the definitions of the effective density (4.57) and the homogenized elastic tensor (4.58) the effects of the fluid on the structure:*

- *An added mass effect , so that the effective density (4.57) of the homogenized porous medium is also its averaged density,*
- *A mean pressure term, which is non–local in the micro–scale cell problems (4.52) and appears in the effective elastic tensor (4.58) as a contribution to the compressibility factor of the material. This is an extension to the two–scale limit of the phenomenon described in Remark 4.2.2 for finite values of ε: the pressure term in each hole results in an effect which is nonlocal at the microscopic scale, but local at the macroscopic scale. In fact, this is the same effective tensor that was found in [BGMO08] in the static case (modulo a different air compressibility factor, because we have used a different state law for the gas.)*

On the whole, the resulting homogenized model (4.60) behaves like a linearized elastic material. This is in agreement with the experimental data since low–frequency sound propagates in the lungs without much attenuation [Ric83].

Remark 4.3.12. *From a more technical point of view, notice that we may also write the elastic stress all along with an appropriate fourth–order symmetric elastic tensor, i.e.*

$$\sigma_\varepsilon(\cdot) = \mathcal{A}_\varepsilon e(\cdot).$$

The tensor $\mathcal{A}_\varepsilon$ is defined by

$$(\mathcal{A}_\varepsilon)_{ijkl}(\mathbf{x}) = \lambda(\mathbf{x}, \mathbf{x}/\varepsilon)\,\delta_{ij}\delta_{kl} + \mu(\mathbf{x}, \mathbf{x}/\varepsilon)\,(\delta_{ik}\delta_{jl} + \delta_{il}\delta_{jk}), \qquad 1 \le i, j, k, l \le d.$$

Moreover, both tensors $\mathcal{A}_\varepsilon$ and $\mathcal{A}^*$ have only real coefficients: this is obvious for $\mathcal{A}_\varepsilon$ and follows from Remark 4.3.8 and (4.58) for $\mathcal{A}^*$.

Let us study the properties of problem (4.60). The sesquilinear form that appears on the left hand side is not coercive. However, the following ellipticity properties of $\mathcal{A}^*$ show that the homogenized problem keeps much of the operator structure of linearized elasticity.

Proposition 4.3.13. *The fourth–order real–valued tensor $\mathcal{A}^*(\mathbf{x})$ defined in (4.58) has the following properties:*

1. *(Symmetry) The coefficients of $\mathcal{A}^*$ satisfy the property:*

$$\mathcal{A}^*_{ijkl} = \mathcal{A}^*_{ijlk} = \mathcal{A}^*_{klij}, \tag{4.61}$$

2. *(Strong Ellipticity) There exists $\kappa > 0$ depending only on μ_0 and the geometry of the cell $\mathcal{Y}$ such that for any $\mathbf{x} \in \Omega$ and any $d \times d$ real symmetric matrix $\underline{\xi}$,*

$$\mathcal{A}^*(\mathbf{x})\underline{\xi} : \underline{\xi} \ge \kappa \underline{\xi} : \underline{\xi}; \tag{4.62}$$

3. *(Definite positiveness)*

$$\mathcal{A}^*(\mathbf{x})\underline{\xi} : \underline{\xi} = 0 \Leftrightarrow \underline{\xi} = 0. \tag{4.63}$$

Proof. This proof follows the same lines as in [BGMO08, Con85]. Let

$$\boldsymbol{\phi}^{kl}(\mathbf{x}, \mathbf{y}) = \mathbf{p}^{kl}(\mathbf{y}) + \boldsymbol{\chi}^{kl}(\mathbf{x}, \mathbf{y}), \tag{4.64}$$

where $\mathbf{p}^{kl}$ and $\boldsymbol{\chi}^{kl}$ are defined respectively in (4.50) and as solution of system (4.52). Let $a_y^{\#}(\cdot,\cdot)$ be the bilinear form associated with the (real) local problems LP_{kl} (4.52),

$$a_y^{\#}(\boldsymbol{\phi},\boldsymbol{\chi}) = \int_{\mathcal{Y}_S} \mathcal{A}(\mathbf{x},\mathbf{y})e(\boldsymbol{\phi}) : e(\boldsymbol{\chi}) + \frac{\rho_0 c^2}{|\mathcal{Y}_F|}\left(\int_{\Gamma_F} \boldsymbol{\phi}\cdot\mathbf{n}_S\right)\left(\int_{\Gamma_F} \boldsymbol{\chi}\cdot\mathbf{n}_S\right). \tag{4.65}$$

We are going to prove that:

$$\mathcal{A}^*_{ijkl}(\mathbf{x}) = a_y^{\#}(\boldsymbol{\phi}^{ij},\boldsymbol{\phi}^{kl}). \tag{4.66}$$

Note that thanks to symmetry and bilinearity,

$$a_y^{\#}(\boldsymbol{\phi}^{ij},\boldsymbol{\phi}^{kl}) = a_y^{\#}(\boldsymbol{\phi}^{kl},\mathbf{p}^{ij}) + a_y^{\#}(\boldsymbol{\phi}^{kl},\boldsymbol{\chi}^{ij}). \tag{4.67}$$

Let us study the first term in the right–hand side of (4.67). We compute a.e. $\mathbf{x}\in\Omega$,

$$\begin{aligned} a_y^{\#}(\boldsymbol{\phi}^{kl},\mathbf{p}^{ij}) &= \int_{\mathcal{Y}_S} \mathcal{A}e(\boldsymbol{\phi}^{kl}) : e(\mathbf{p}^{ij}) + \frac{\rho_0 c^2}{|\mathcal{Y}_F|}\left(\int_{\Gamma_F} \boldsymbol{\phi}^{kl}\cdot\mathbf{n}_S\right)\left(\int_{\Gamma_F} \mathbf{p}^{ij}\cdot\mathbf{n}_S\right) \\ &= \int_{\mathcal{Y}_S} \sigma_{\mathbf{y}}(\boldsymbol{\phi}^{kl})_{ij} + \frac{\rho_0 c^2}{|\mathcal{Y}_F|}\left(\int_{\mathcal{Y}_S} \mathrm{div}_{\mathbf{y}}\boldsymbol{\chi}^{kl} - \int_{\mathcal{Y}_F} \mathrm{div}_{\mathbf{y}}\mathbf{p}^{kl}\right)\left(-\int_{\mathcal{Y}_F} \mathrm{div}_{\mathbf{y}}\mathbf{p}^{ij}\right). \end{aligned}$$

Now, we derive from the definition of $\mathbf{p}^{kl}$ (4.50):

$$e(\mathbf{p}^{kl})_{ij} = \frac{1}{2}\left(\delta_{ik}\delta_{jl} + \delta_{il}\delta_{jk}\right) \text{ and } \int_{\mathcal{Y}_F} \mathrm{div}_{\mathbf{y}}\mathbf{p}^{kl} = |\mathcal{Y}_F|\delta_{kl},$$

and using the symmetry of $\sigma_{\mathbf{y}}$, we obtain:

$$\begin{aligned} a_y^{\#}(\boldsymbol{\phi}^{kl},\mathbf{p}^{ij}) &= \int_{\mathcal{Y}_S} \left(\sigma_{\mathbf{y}}(\boldsymbol{\phi}^{kl})_{ij} - \rho_0 c^2 \mathrm{div}_{\mathbf{y}}\boldsymbol{\chi}^{kl}\delta_{ij}\right) + \rho_0 c^2 |\mathcal{Y}_F|\delta_{ij}\delta_{kl} \\ &= \mathcal{A}^*_{ijkl}. \end{aligned}$$

Next, we prove that the second term in the right–hand side of (4.67), $a_y^{\#}(\boldsymbol{\phi}^{kl},\boldsymbol{\chi}^{ij})$, is equal to zero. Using $\boldsymbol{\chi}^{ij}$ as a test function in LP_{kl} and integrating by parts, we get a.e. $\mathbf{x}\in\Omega$,

$$\begin{aligned} \int_{\mathcal{Y}_S} \sigma_{\mathbf{y}}(\boldsymbol{\phi}^{kl}) : e_{\mathbf{y}}(\boldsymbol{\chi}^{ij}) = &-\frac{\rho_0 c^2}{|\mathcal{Y}_F|}\left(\int_{\Gamma_F} \boldsymbol{\chi}^{kl}\cdot\mathbf{n}_S\right)\left(\int_{\Gamma_F} \boldsymbol{\chi}^{ij}\cdot\mathbf{n}_S\right) \\ &+ \rho_0 c^2 \int_{\Gamma_F} \mathrm{div}_{\mathbf{y}}(\mathbf{p}^{kl})\boldsymbol{\chi}^{ij}\cdot\mathbf{n}_S. \end{aligned}$$

But since $\mathbf{p}^{kl}$ is a first–order polynomial, $\mathrm{div}_{\mathbf{y}}(\mathbf{p}^{kl})$ is constant, so:

$$\mathrm{div}_{\mathbf{y}}(\mathbf{p}^{kl}) = \frac{1}{|\mathcal{Y}_F|}\int_{\mathcal{Y}_F} \mathrm{div}_{\mathbf{y}}(\mathbf{p}^{kl}) = -\frac{1}{|\mathcal{Y}_F|}\int_{\Gamma_F} \mathbf{p}^{kl}\cdot\mathbf{n}_S.$$

Therefore,

$$\int_{\mathcal{Y}_S} \sigma_{\mathbf{y}}(\boldsymbol{\phi}^{kl}) : e_{\mathbf{y}}(\boldsymbol{\chi}^{ij}) = -\frac{\rho_0 c^2}{|\mathcal{Y}_F|}\left(\int_{\Gamma_F} \boldsymbol{\phi}^{kl}\cdot\mathbf{n}_S\right)\left(\int_{\Gamma_F} \boldsymbol{\chi}^{ij}\cdot\mathbf{n}_S\right).$$

Thus $a_y^{\#}(\boldsymbol{\phi}^{kl},\boldsymbol{\chi}^{ij}) = 0$ and we have proved (4.66), $a_y^{\#}(\boldsymbol{\phi}^{kl},\boldsymbol{\phi}^{ij}) = \mathcal{A}^*_{ijkl}$.

Symmetry $a_y^{\#}$ is symmetric, so this is also true of $\mathcal{A}^*$.

Uniform coercivity Since $\mathcal{A}^*(\mathbf{x})$ is positive definite in a finite dimensional space, it is known that there exists a scalar $\kappa(\mathbf{x}) > 0$ such that $\mathcal{A}^*(\mathbf{x})\underline{\xi} : \underline{\xi} \geq \kappa(\mathbf{x})\underline{\xi} : \underline{\xi}$. However, $\kappa(\mathbf{x})$ depends both on the geometry and on the Lamé coefficient $\mu(\mathbf{x}, \mathbf{y})$, in a way that is not clear at this point. We are going to prove a uniform lower bound for $\kappa(\mathbf{x})$, independent of $\mathbf{x}$ and of the continuity properties of λ and μ, that makes these dependencies explicit. Let us define the function

$$\boldsymbol{\phi}_\xi = \xi_{ij}\boldsymbol{\phi}^{ij}.$$

We have

$$\mathcal{A}^*(\mathbf{x})\underline{\xi} : \underline{\xi} = a_y^{\#}(\boldsymbol{\phi}_\xi(\mathbf{x}), \boldsymbol{\phi}_\xi(\mathbf{x})) \geq \mu_0 \|e_{\mathbf{y}}(\boldsymbol{\phi}_\xi(\mathbf{x}))\|^2_{L^2(\mathcal{Y}_S)}. \tag{4.68}$$

Now, let $\mathbf{z}_1, \ldots, \mathbf{z}_d$, be a basis of $\mathbf{Z}$ (and $\mathbb{R}^d$) such that for d faces of the unit cell $\mathcal{Y}$, denoted by $F_1, \ldots, F_d$, the translated surfaces $F_1 + \mathbf{z}_1, \ldots, F_d + \mathbf{z}_d$ are also faces of $\mathcal{Y}_F$. Then, for $i = 1, \ldots, d$ and any $\mathbf{y} \in F_i$, by $\mathcal{Y}$–periodicity of $\boldsymbol{\chi}^{kl}$ we have

$$\underline{\xi}\mathbf{z}_i = p_\xi(\mathbf{z}_i) = \boldsymbol{\phi}_\xi(\mathbf{y} + \mathbf{z}_i) - \boldsymbol{\phi}_\xi(\mathbf{y}).$$

Because the trace operator is continuous from $\mathbf{H}^1(\mathcal{Y}_S)$ on F_i and $F_i + \mathbf{z}_i$, there exists a constant C depending on $\mathcal{Y}_S$, $\mathcal{Y}$ only such that

$$\|\underline{\xi}\mathbf{z}_i\| \leq C\|\boldsymbol{\phi}_\xi\|_{\mathbf{H}^1(\mathcal{Y}_S)}.$$

Since the $\mathbf{z}_i$ form a basis of $\mathbb{R}^d$, we have

$$\sqrt{\underline{\xi} : \underline{\xi}} < C \sup_{i=1,\ldots,d} \|\underline{\xi}\mathbf{z}_i\| \leq C\|\boldsymbol{\phi}_\xi\|_{\mathbf{H}^1(\mathcal{Y}_S)}.$$

Here, C depends on $\mathcal{Y}_S$ and $\mathcal{Y}$ only. To conclude, we need to use the special version of Korn inequality for the space on which the $\boldsymbol{\phi}_\xi$ live which is proved in the Annex, Lemma 4.3.10. This yields

$$\|\boldsymbol{\phi}_\xi\|_{\mathbf{H}^1(\mathcal{Y}_S)} \leq C\|e(\boldsymbol{\phi}_\xi)\|_{L^2(\mathcal{Y}_S)},$$

where C does not depend on $\mathbf{x}$ and depends only on $\mathcal{Y}_S$ and $\mathcal{Y}$. Combining estimates (4.68) and (4.56), we have proved that for some constant $C > 0$ depending only on $\mathcal{Y}_S$ and $\mathcal{Y}$,

$$\mathcal{A}^*(\mathbf{x})\underline{\xi} : \underline{\xi} > C\mu_0\underline{\xi} : \underline{\xi} \qquad \forall \mathbf{x} \in \Omega. \tag{4.69}$$

Positive definiteness Finally, the property (4.63) is a direct consequence from the strong ellipticity property. This ends the proof of the Proposition. □

We are going to apply the Fredholm theory to the homogenized problem to show that there is a discrete set of resonant frequencies ω for the homogenized problem. We denote by $(\,\cdot\,,\,\cdot\,)_{\mathbf{L}^2}$ the $\mathbf{L}^2$–scalar product in $\mathbf{L}^2(\Omega)$.

Definition 4.3.14. *Let B be the unbounded operator $\mathbf{L}^2(\Omega) \to \mathbf{L}^2(\Omega)$ such that:*

$$\begin{cases} D(B) = \left\{\mathbf{u} \in \mathbf{H}_0^1(\Omega), -\mathbf{div}\left(\mathcal{A}^*(\mathbf{x})e(\mathbf{u})\right) \in \mathbf{L}^2(\Omega)\right\} \\ B\mathbf{u} = -\mathbf{div}\left(\mathcal{A}^*(\mathbf{x})e(\mathbf{u})\right), \end{cases} \tag{4.70}$$

and b be the associated sesquilinear form in $\mathbf{H}^1(\Omega)$, that is

$$b(\mathbf{u}, \mathbf{v}) = \int_\Omega \mathcal{A}^*(\mathbf{x})e(\mathbf{u}) : \overline{e(\mathbf{v})} = (B\mathbf{u}, \mathbf{v})_{\mathbf{L}^2}. \tag{4.71}$$

Define the family of operators $A_\omega = B - \omega^2 I$ *with* $D(A_\omega) = D(B)$*, and the associated family of sesquilinear forms* a_ω *appearing on the left–hand side of* (4.60)*:*

$$a_\omega(\mathbf{u}, \mathbf{v}) = \int_\Omega -\rho^* \omega^2 \mathbf{u} \cdot \overline{\mathbf{v}} + \mathcal{A}^*(\mathbf{x}) e(\mathbf{u}) : \overline{e(\mathbf{v})} = (A_\omega \mathbf{u}, \mathbf{v})_{\mathbf{L}^2}. \tag{4.72}$$

Then, we have the well–known properties, since B is elliptic:

Proposition 4.3.15. *1. B is self–adjoint and has compact resolvent,*

2. *the eigenvalues of B form a sequence of nonnegative real numbers converging to $+\infty$ $(\lambda_n)_{n\geq 0}$, $0 < \lambda_0 < ... < \lambda_n < ...$*
3. *A_ω is invertible iff $\omega^2 \notin (\lambda_n)_{n\geq 0}$,*
4. *If $\omega^2 = \lambda_n$, the solutions of $A_\omega u = 0$ form a subspace $\mathbf{V}_n$ of finite dimension d_n for which there exists an orthonormal basis of eigenvectors of B, $(\boldsymbol{\phi}^k)_{1\leq k\leq d_n}$, and $A_\omega \mathbf{u} = \mathbf{f}$ is solvable iff $(\boldsymbol{\phi}^k, \mathbf{f})_{\mathbf{L}^2} = 0$ for all $1 \leq k \leq d_n$.*

Remark 4.3.16. *In the case of Neumann boundary conditions, we would have $\lambda_0 = 0$ with multiplicity $d_0 = 6$ corresponding to the rigid displacements, but everything else stands. Indeed, the homogenization process and $\mathcal{A}^*$ do not depend on the boundary conditions.*

4.3.2 Proof of the *a priori* bounds and Theorem 4.3.1

We are now going to prove Theorem 4.3.1, making good use of our knowledge of the homogenized system (4.60) and its eigenvalue set. The idea is to proceed by contradiction. Suppose that the affirmations in Theorem 4.3.1 are false for some ω for which the problem (4.60) is well–posed. Then, the following alternative holds true:

- The problem (4.22) is ill–posed for arbitrary small values of ε. In this case, there is a sequence $(\varepsilon_n)_{n\geq 0}$ converging to zero such that for all $n \geq 0$, the problem (4.22) is ill–posed. We know then by Proposition 4.2.11 that the homogeneous problem (4.22) with vanishing data $(\mathbf{f}_n, g_n) = (\mathbf{0}, 0)$ has a non–zero solution $(\mathbf{u}_n, \phi_n)$. Since the problem is linear, we can require that $(\mathbf{u}_n, \phi_n)$ is normalized, rescaling the data by $\left(\|\mathbf{u}_n\|^2_{\mathbf{H}^1(\Omega_{S,\varepsilon_n})} + \|\phi_n\|^2_{H^1(\Omega_{F,\varepsilon_n})}\right)^{-1/2}$ if necessary:

$$\|\mathbf{u}_n\|^2_{\mathbf{H}^1(\Omega_{S,\varepsilon_n})} + \|\phi_n\|^2_{H^1(\Omega_{F,\varepsilon_n})} = 1.$$

- Or the problem (4.22) is well–posed for ε small enough, but the solutions do not satisfy *a priori* bounds uniform in ε. Then, there exists a sequence $(\varepsilon_n)_{n\geq 0}$ converging to zero such that for some sequence $(\mathbf{f}_n, g_n) \in \mathbf{L}^2(\Omega) \times H^1(\Omega)$ indexed by $n \geq 0$, the sequence of solutions $(\mathbf{u}_n, \phi_n)$ of (4.22) satisfies

$$1 = \|\mathbf{u}_n\|^2_{\mathbf{H}^1(\Omega_{S,\varepsilon_n})} + \|\phi_n\|^2_{H^1(\Omega_{F,\varepsilon_n})} > n\left(\|\mathbf{f}_n\|^2_{\mathbf{L}^2(\Omega)} + \|g_n\|^2_{H^1(\Omega)}\right).$$

In either case, we have obtained a sequence $(\varepsilon_n)_{n\geq 0}$ converging to zero and a sequence of data $(\mathbf{f}_n, g_n)$ converging strongly to zero, such that the sequence $(\mathbf{u}_n, \phi_n)$ is a sequence of solutions of (4.22) and is bounded independently of n in $\mathbf{H}^1(\Omega_{S,\varepsilon}) \times H^1(\Omega_{F,\varepsilon})$:

$$\|\mathbf{u}_n\|^2_{\mathbf{H}^1(\Omega_{S,\varepsilon_n})} + \|\phi_n\|^2_{H^1(\Omega_{F,\varepsilon_n})} = 1. \tag{4.73}$$

We are going to show that $\widehat{\mathbf{u}_n}$ and $\widehat{\phi_n}$ converge strongly to zero in $L^2(\Omega)$, and then, using the estimate (4.35) we will conclude that $\widehat{\mathbf{u}_n}$ and $\widehat{\phi_n}$ converge to zero in $H^1(\Omega)$ which is absurd considering (4.73).

Thanks to (4.73), we can apply our analysis from section 4.3.1 directly. In particular, $\widehat{\mathbf{u}_n}$ and $\widehat{\phi_n}$ two–scale converge: there exists functions $\mathbf{u} \in \mathbf{H}^1_D(\Omega)$, $\mathbf{u}^1 \in \mathbf{L}^2(\Omega, H^1_\#(\mathcal{Y})/\mathbb{C})$ and $\phi \in L^2(\Omega, H^1_\#(\mathcal{Y}))$ such that

$$\widehat{\mathbf{u}_n} \rightarrow\!\!\!\!\rightarrow \mathbf{u}, \qquad \widehat{\nabla \mathbf{u}_n} \rightarrow\!\!\!\!\rightarrow \nabla_{\mathbf{x}}\mathbf{u} + \nabla_{\mathbf{y}}\mathbf{u}^1,$$
$$\widehat{\phi_n} \rightarrow\!\!\!\!\rightarrow 0, \qquad \widehat{\nabla \phi_n} \rightarrow\!\!\!\!\rightarrow \nabla_{\mathbf{y}}\phi.$$

Moreover, $(\mathbf{u}, \mathbf{u}^1|_{\Omega\times\mathcal{Y}_S}, \phi|_{\Omega\times\mathcal{Y}_F})$ satisfy the homogenized problem (4.74) with zero right hand side. We have supposed that the variational problem (4.74) is well–posed for our choice of ω. As a consequence, $\mathbf{u}$ is equal to zero and the respective restrictions of $\mathbf{u}^1$ and ϕ to $\Omega \times \mathcal{Y}_S$ and $\Omega \times \mathcal{Y}_F$ are also zero. Let us now show that this weak convergence result implies that $\widehat{\mathbf{u}_n}$ and $\widehat{\phi_n}$ converge to 0 strongly in $H^1(\Omega)$. The first difficulty is that we do not control $\mathbf{u}^1$ and ϕ on the whole domain $\Omega\times\mathcal{Y}$, and thus the two–scale limits of the gradients $\nabla\widehat{\mathbf{u}_n}$ and $\nabla\widehat{\phi_n}$ are not *a priori* uniquely defined. We prove that this is not the case for the weak H^1–limits. We know that $\nabla\widehat{\mathbf{u}_n}$ converges weakly to $\int_{\mathcal{Y}} \nabla_{\mathbf{x}}\mathbf{u} + \nabla_y\mathbf{u}^1$ so, since, $\mathbf{u} = \mathbf{0}$ and $\mathbf{u}^1|_{\mathcal{Y}_S} = \mathbf{0}$,

$$\nabla\widehat{\mathbf{u}} \rightharpoonup \int_{\mathcal{Y}_F} \nabla_y \mathbf{u}^1 \quad \text{weakly in } H^1(\Omega, \mathbb{C}^{d\times d}).$$

Then, for almost every $\mathbf{x} \in \Omega$, $\mathbf{u}^1(\mathbf{x}, \cdot)$ is zero on $\mathcal{Y}_S$ and belongs to $\mathbf{H}^1_\#(\mathcal{Y})$, so clearly $\mathbf{u}^1 = 0$ on $\Gamma_F = \partial\mathcal{Y}_F$. Integrating by parts, we obtain for any $i, j \in \{1, \dots, d\}$,

$$\int_{\mathcal{Y}_F} \partial_i u^1_j(\mathbf{x}, \mathbf{y})\mathrm{d}\mathbf{y} = \int_{\Gamma_F} u^1_j(\mathbf{x}, \mathbf{y}) n_{S,i}(\mathbf{y}) = 0.$$

In the same way, we know that $\nabla\widehat{\phi_n}$ converges weakly to $\int_{\mathcal{Y}_S} \nabla\phi$ in $\mathbf{H}^1(\Omega)$ and for any $i \in \{1, \dots, d\}$,

$$\int_{\mathcal{Y}_S} \partial_i \phi(\mathbf{x}, \mathbf{y})\mathrm{d}\mathbf{y} = \int_{\Gamma_F} \phi(\mathbf{x}, \mathbf{y}) n_{S,i}(\mathbf{y}) = 0.$$

This proves that $\widehat{\mathbf{u}_n}$ and $\widehat{\phi_n}$ converge weakly to zero in $\mathbf{H}^1(\Omega)$ and $H^1(\Omega)$ respectively. By compactness of the injection $H^1_0(\Omega) \to L^2(\Omega)$, there exists a subsequence (still denoted by n) such that $\widehat{\mathbf{u}_n}$ and $\widehat{\phi_n}$ converge strongly to 0 in $L^2(\Omega)$. We now use the estimate (4.35). Since $(\mathbf{u}_n, \phi_n)$ are solutions of (4.22), we get:

$$\|\mathbf{u}_n\|^2_{\mathbf{H}^1(\Omega_S^{\varepsilon_n})} + \|\phi_n\|^2_{H^1(\Omega_F^{\varepsilon_n})} \leq C(\omega)\left(\|\mathbf{u}_n\|^2_{\mathbf{L}^2(\Omega_S^{\varepsilon_n})} + \|\phi_n\|^2_{L^2(\Omega_F^{\varepsilon_n})} + \|\mathbf{f}_n\|^2_{\mathbf{L}^2(\Omega)} + \|g_n\|^2_{H^1(\Omega)}\right).$$

Hence since $\widehat{\mathbf{u}_n}$ and $\widehat{\phi_n}$ converge strongly to zero in $L^2(\Omega)$, we obtain

$$\lim_{n\to\infty} \|\mathbf{u}_n\|^2_{\mathbf{H}^1(\Omega_{S,\varepsilon_n})} + \|\phi_n\|^2_{H^1(\Omega_{F,\varepsilon_n})} = 0.$$

But this is in contradiction with the construction of the sequence, which ensures

$$\|\mathbf{u}_n\|^2_{\mathbf{H}^1(\Omega_{S,\varepsilon_n})} + \|\phi_n\|^2_{H^1(\Omega_{F,\varepsilon_n})} = 1.$$

Thus we have proved Theorem 4.3.1. □

We have the following Proposition, which completes Theorem 4.3.1:

Proposition 4.3.17. *Let $0 < \lambda_0 \leq \cdots < \lambda_n \leq \dots$ be the ordered sequence of eigenvalues of the homogeneous variational problem on $\mathbf{H}^1_0(\Omega)$*

$$-\rho^*\lambda^2\mathbf{u} - \mathbf{div}\left(\sigma^*(\mathbf{u})\right) = 0.$$

then, for any $\omega \in \mathbb{R} \setminus \{\lambda_n\}_{n\in\mathbb{N}}$, *there exists* $\varepsilon_0(\omega)$ *and* $C(\omega)$ *in* $\mathbb{R}_+^*$ *such that for* $0 < \varepsilon < \varepsilon_0(\omega)$, *the problem* (4.22) *is well posed and for any data* $\mathbf{f} \in \mathbf{L}^2(\Omega)$ *and* $g \in H^1(\Omega)$, *the solution* $(\mathbf{u}_\varepsilon, \phi_\varepsilon)$ *satisfies the a priori estimate:*

$$\|\mathbf{u}_\varepsilon\|^2_{H^1(\Omega_{S,\varepsilon})} + \|\phi_\varepsilon\|^2_{H^1(\Omega_{F,\varepsilon})} \leq C(\omega)\left(\|\mathbf{f}\|^2_{L^2(\Omega)} + \|g\|^2_{H^1(\Omega)}\right).$$

Remark 4.3.18. *The convergence of the resonant frequencies of the coupled problem* (4.22) *to the eigenvalues of the homogenized operator* B *defined in* (4.70) *is similar to the results of collective compactness of sequences of operators detailed e.g. in [Ans71]. These results have been used in homogenization theory, see for example [KLS12]. However we cannot apply directly these results here because the resonant frequencies for which problem* (4.22) *is not well–posed are not defined as eigenvalues of the unbounded operator on* $\mathbf{L}^2(\Omega_{S,\varepsilon}) \times L^2(\Omega_{F,\varepsilon})$ *defined variationally on the left–hand side of* (4.22), *which depends in particular on* ω *because of the boundary conditions and on* ε *by its domain of definition.*

4.3.3 Convergence Theorem and homogenized problem

Finally, we can sum up the asymptotic behavior of the solutions in our main Theorem.

Theorem 4.3.19. *Two–scale homogenization of problem* (4.22)
Let the frequency $\omega \geq 0$ *be such that* ω^2 *is in the resolvent set of* B, *then for* ε *small enough the problem* (4.22) *is well posed.*
Moreover, let the data $(\mathbf{f}_\varepsilon, g_\varepsilon)_{\varepsilon>0} \subset \mathbf{L}^2(\Omega) \times H^1(\Omega)$ *be a sequence such that* $\mathbf{f}_\varepsilon$ *and* g_ε *converge strongly to* $\mathbf{f} \in \mathbf{L}^2(\Omega)$ *and* $g \in H^1(\Omega)$, *then the solutions* $(\mathbf{u}_\varepsilon, \phi_\varepsilon)$ *of the problem* (4.22) *two–scale converge in the sense that:*

$$\chi_{S,\varepsilon}\widehat{\mathbf{u}_\varepsilon} \twoheadrightarrow \mathbf{u}\chi_S,$$
$$\widehat{\phi_\varepsilon} \twoheadrightarrow 0, \qquad \chi_{F,\varepsilon}\nabla\widehat{\phi_\varepsilon} \twoheadrightarrow \mathbf{u}\chi_F,$$

where $\mathbf{u}$ *is the solution of the homogenized problem:*

$$\begin{cases} -\rho^*\omega^2\mathbf{u} - \mathbf{div}(\sigma^*(\mathbf{u})) = |\mathcal{Y}_S|\mathbf{f} + |\mathcal{Y}_F|\nabla g & \text{on } \Omega, \\ \mathbf{u} = 0 & \text{on } \partial\Omega, \end{cases} \tag{4.74}$$

and the coefficients σ^* *and* ρ^* *can be explicitly computed using formulas* (4.57), (4.58), (4.59).

Proof. The only result in this Theorem which we have not yet proved is the two–scale convergence of the whole sequences $\chi_{S,\varepsilon}\widehat{\mathbf{u}_\varepsilon}$, $\chi_{F,\varepsilon}\widehat{\phi_\varepsilon}$, as opposed to subsequences only. This is a consequence of the uniqueness of the solution of the homogenized problem (4.74), since every subsequence then converges to the same limit. □

4.4 Conclusion

We have presented a mathematically sound way of obtaining an effective constitutive equation for the propagation of sound in the human lungs. Starting from a model coupling elastic and acoustic equations in a perforated medium, we obtain a simple homogenized, linearized elastic-like medium. In particular, we have shown that the resonances of the material do not change the homogenized model: in fact, the resonances of the real material, for $\varepsilon > 0$ finite, are shown to be close to the resonances of the homogenized material.

Obviously, this model is limited in its physical description of the lungs, but is satisfying since we recover a model which has been shown to be correct for the low–frequency range [Ric83]. However, for higher frequencies it is expected that some of the phenomena we have neglected become more

important, in particular viscous attenuation or scattering by the alveoli as the wavelength becomes smaller [GWN02]. Indeed, it is well-known that sounds of a frequency above 1kHz are quickly attenuated when propagating through the parenchyma [PKW97, RHD+10]. We propose in the next Chapter a new model showing the memory effects due to a viscoelastic micro–structure.

4.5 Annex

Let us provide here the proof of Lemma 4.3.10. We recall the definition of the functions $\mathbf{p}^{kl} \in \mathbf{H}^1(Y_S)$:

$$\mathbf{p}^{kl}(\mathbf{y}) = \frac{1}{2}\left(y_k \mathbf{e}^l + y_l \mathbf{e}^k\right) \qquad \text{for } 1 \le k, l \le d, \tag{4.75}$$

where the vectors $\mathbf{e}^k$ for $1 \le k \le d$ are the unit vectors of $\mathbb{R}^d$ whose components are $\mathbf{e}^k_l = \delta_{kl}$ for $1 \le k,\ l \le d$.

Lemma 4.5.1. *Consider the space of real–valued functions on Y_S defined as follows:*

$$\mathbf{V} = Span\left\{(\mathbf{p}^{kl})_{1\le k,l\le d}\right\} + \mathbf{H}^1_{\#}(Y_S,\mathbb{R})/\mathbb{R}^d \subset \mathbf{H}^1(Y_S,\mathbb{R})/\mathbb{R}^d, \tag{4.76}$$

where the family $(\mathbf{p}_{kl})_{1\le k,l\le d}$ is defined by (4.75). Then the following Korn's inequality holds in $\mathbf{V}$: there exists $C > 0$ depending only on the geometry of Y_S such that

$$\|\boldsymbol{\phi}\|_{H^1_{\#}(Y_S)} \le C\|e(\boldsymbol{\phi})\|_{L^2(Y_S)} \qquad \forall \boldsymbol{\phi} \in \mathbf{V}. \tag{4.77}$$

Proof. We follow the proof of Theorem 6.3–4 in [Cia88].

Step 1. We begin by showing that $\mathbf{V}$ is a closed subspace of $\mathbf{H}^1(Y_S)/\mathbb{R}^d$. $\mathbf{H}^1_{\#}(Y_S)$ is closed in $\mathbf{H}^1(Y_S)$ since it is the closure of $C^\infty_{\#}(Y_S)^d$ in $\mathbf{H}^1(Y_S)$.
Since the space of constant functions, noted $\mathbb{R}^d$ for simplicity, is a subspace of $\mathbf{H}^1_{\#}(Y_S)$ with finite dimension, it is closed both in $\mathbf{H}^1(Y_S)$ and in $\mathbf{H}^1_{\#}(Y_S)$. Identifying the quotient spaces $\mathbf{H}^1(Y_S)/\mathbb{R}^d$ and $\mathbf{H}^1_{\#}(Y_S)/\mathbb{R}^d$ with the orthogonal complement of $\mathbb{R}^d$ in each space, it is clear that $\mathbf{H}^1_{\#}(Y_S)/\mathbb{R}^d$ is a closed subspace of $\mathbf{H}^1(Y_S)/\mathbb{R}^d$.

Step 2. Let $\mathbf{M}$ be the orthogonal complement of $\mathbf{H}^1_{\#}(Y_S)/\mathbb{R}^d$ in $\mathbf{H}^1(Y_S)/\mathbb{R}^d$. For each choice of $k, l,\ 1 \le k, l \le d$, we can decompose each $\mathbf{p}^{kl}$ according to the direct sum $\mathbf{H}^1(Y_S)/\mathbb{R}^d = \mathbf{M} \oplus \mathbf{H}^1_{\#}(Y_S)/\mathbb{R}^d$:

$$\mathbf{p}^{kl} = \mathbf{p}^{kl}_0 + \boldsymbol{\psi}^{kl} \qquad \boldsymbol{p}^{kl}_0 \in \mathbf{M}, \quad \boldsymbol{\psi}^{kl} \in \mathbf{H}^1_{\#}(Y_S)/\mathbb{R}^d.$$

Let $(\boldsymbol{\phi}^n)$ be a sequence of elements in $\mathbf{V}$, such that $\boldsymbol{\phi}^n \to \phi$ in $\mathbf{H}^1(Y_S)/\mathbb{R}^d$. We have a unique decomposition

$$\boldsymbol{\phi}^n = \alpha^n_{kl}\mathbf{p}^{kl}_0 + \boldsymbol{\psi}^n, \qquad \underline{\alpha}^n \in \mathbb{R}^{d\times d}, \quad \boldsymbol{\psi}^n \in \mathbf{H}^1_{\#}(Y_S)/\mathbb{R}^d,$$

and $\|\boldsymbol{\phi}^n\|^2_{\mathbf{H}^1(Y_S)} = \|\sum_{kl}\alpha^n_{kl}\mathbf{p}^{kl}_0\|^2_{\mathbf{H}^1(Y_S)} + \|\boldsymbol{\psi}^n\|^2_{\mathbf{H}^1(Y_S)}$, so $(\alpha^n_{kl}\mathbf{p}^{kl}_0)$ is bounded. Since the space $Span\left\{(\mathbf{p}^{kl}_0)_{1\le k,l\le d}\right\}$ has a finite dimension, there exists $\mathbf{p} \in Span\left\{(\mathbf{p}^{kl}_0)_{1\le k,l\le d}\right\}$ such that up to a subsequence

$$\alpha^n_{kl}\mathbf{p}^{kl}_0 \to \mathbf{p}.$$

Then, $\boldsymbol{\psi}_n$ converges to $\boldsymbol{\psi}$ in $\mathbf{H}^1(Y_S)/\mathbb{R}^d$, so since $\mathbf{H}^1_{\#}(Y_S)/\mathbb{R}^d$ is closed in $\mathbf{H}^1(Y_S)/\mathbb{R}^d$,

$$\boldsymbol{\psi}_n \to \boldsymbol{\psi} \in \mathbf{H}^1_{\#}(Y_S)/\mathbb{R}^d.$$

Finally, $\boldsymbol{\phi} = \mathbf{p} + \boldsymbol{\psi} \in \mathbf{V}$ and $\mathbf{V}$ is closed as a subspace of $\mathbf{H}^1(Y_S)/\mathbb{R}^d$.

Step 3. Let us show that $\mathbf{V}$ contains no infinitesimal rigid displacement of a solid body. Suppose we have two vectors $\mathbf{a}, \mathbf{b} \in \mathbb{R}^d$ such that

$$\mathbf{V} \ni \mathbf{a} + \mathbf{b} \times \mathbf{y} = \underline{B}_{kl}\mathbf{p}^{kl} + \boldsymbol{\psi}, \qquad \underline{B} \in \mathbb{R}^{d\times d},\ \boldsymbol{\psi} \in \mathbf{H}^1_{\#}(Y_S).$$

Recall that $\mathbf{p}^{kl}$ is defined by (4.75). Since $\mathbf{p}^{kl}$, $\mathbf{b}\times\mathbf{y}$ and $\mathbf{a}$ are all polynomial functions in the variable $\mathbf{y}$, $\boldsymbol{\psi}$ is one too. Then $\boldsymbol{\psi}$ is a periodic polynomial function, therefore it has to be equal to a constant $\mathbf{c}$. Then $\mathbf{a}=\mathbf{c}$ because $\mathbf{p}^{kl}(0)=0$, see definition (4.75). Now, we have

$$\mathbf{b}\times\mathbf{y}=\frac{1}{2}B_{kl}y_k\mathbf{e}^l+\frac{1}{2}B_{kl}y_l\mathbf{e}^k=\frac{1}{2}(\underline{B}+\underline{B}^T)\mathbf{y}.$$

Observe that the cross product on the left can be represented only by a skew–symmetric matrix, while we have a symmetric matrix on the right of the identity. Therefore both matrices are in fact zero. This means that $\mathbf{b}=\mathbf{0}$ and since we have taken the quotient by the constants in definition (4.76), $\mathbf{V}$ contains no infinitesimal rigid displacement of a solid body aside from $\{\mathbf{0}\}$.

Step 4. Now, suppose assertion (4.77) is wrong. Then, there exists $(\boldsymbol{\phi}^n)$ a sequence of elements of $\mathbf{V}$ such that:

$$\|\boldsymbol{\phi}^n\|_{\mathbf{H}^1(Y_S)}=1 \text{ for all } n\in\mathbb{N}, \text{ and } \lim_{n\to\infty}\|e(\boldsymbol{\phi}^n)\|_{L^2(Y_S)}=0.$$

Using the Rellich–Kondrasov theorem, there exists a subsequence (still denoted by n) such that $\boldsymbol{\phi}^n$ converges strongly in $\mathbf{L}^2(\Omega)$. Since $e(\boldsymbol{\phi}^n)$ also converges strongly in $L^2(\Omega)$, we deduce that $\boldsymbol{\phi}^n$ is a Cauchy sequence with respect to the norm

$$\boldsymbol{\phi}\mapsto\sqrt{\|\boldsymbol{\phi}\|^2_{\mathbf{L}^2(Y_S)}+\|e(\boldsymbol{\phi})\|^2_{L^2(Y_S)}}.$$

By the standard Korn's inequality in $\mathbf{H}^1(Y_S)$, this norm is equivalent to the norm $\|\cdot\|_{\mathbf{H}^1(Y_S)}$ on $\mathbf{H}^1(Y_S)$. Hence, since $\mathbf{V}$ is closed and therefore complete, there exists $\boldsymbol{\phi}\in\mathbf{V}$ such that $\boldsymbol{\phi}^n$ converges to $\boldsymbol{\phi}$ strongly. Moreover, the limit $\boldsymbol{\phi}$ satisfies

$$\|e(\boldsymbol{\phi})\|_{L^2(Y_S)}=\lim_{n\to\infty}\|e(\boldsymbol{\phi}^n)\|_{L^2(Y_S)}=0.$$

Now $\boldsymbol{\phi}$ is an infinitesimal rigid dislacement of a solid body and belongs to $\mathbf{V}$, hence $\boldsymbol{\phi}=\mathbf{0}$. This is a contradiction, since $\|\boldsymbol{\phi}^n\|_{\mathbf{H}^1(Y_S)}=1$ for all $n\in\mathbb{N}$.

□

Chapter 5

Sound and Ultrasound Propagation in a Viscoelastic Model of the Lungs' Parenchyma: Theory, Numerical Simulations

Results of this chapter have been obtained in collaboration with Jan Hesthaven with the support of Brown University.

Contents

5.1 Motivation and introduction . . . 137
5.2 The viscoelastic homogenized model . . . 139
5.2.1 The microscale model . . . 139
5.2.2 The mathematical homogenization method . . . 142
5.2.3 The microcell problem . . . 145
5.2.4 Effective equation and effective relaxation modulus . . . 147
5.2.5 Effective equations in the time domain . . . 148
5.3 Numerical offline/online strategy for the global dispersive problem . . . 149
5.3.1 Evaluation of the convolution integral . . . 149
5.3.2 Computation and fitting of the dispersive curve . . . 151
5.3.3 Discontinuous Galerkin discretization . . . 152
5.3.4 Implicit–explicit time–stepping scheme . . . 153
5.4 Numerical results . . . 154
5.4.1 Effective viscoelastic modulus computation . . . 154
5.4.2 Fitting the dispersion curve . . . 156
5.4.3 Wave propagation computations . . . 160
5.4.4 Orthotropic and isotropic behavior . . . 162

5.1 Motivation and introduction

Understanding the acoustic properties of the lungs is of great interest in a range of medical domains, from the diagnostic of pathologies such as bronchitis and asthma to recently introduced imaging methods of breathing sounds. Medical doctors have been commonly using the analysis of lung sounds for the diagnostic of pathologies, mainly relying on the stethoscope, and have a good empirical understanding of the relationship between the characteristics of lung sounds and

underlying pathologies. However, far less is known about the detailed physical mechanisms of sound generation and transmission in the respiratory system. More advanced models could also explain lung contusions due to a blunt, high–velocity impact to the chest as well as exposure to explosions or, for small mammals, to medical ultrasound.

There is extensive experimental data, both *in vitro* and *in vivo*, and a relatively good theoretical understanding of the propagation through lung tissue of relatively low–frequency sound, in the audible range. In the frequency band between roughly a few Hz to 1 kHz, the two main components of the lung tissue, air and connective tissue, are acoustically strongly coupled and the resulting mixture behaves like a homogeneous material with high density of the tissue and high compressibility of the air filling. Acting as a highly dense gas, the tissue produces a very low speed of sound of less than 50 m/s. As frequency increases above 1 kHz, the wavelength approaches the size of the air pockets embedded in the lungs' tissue, called alveoli, and the absorption increases strongly such that no signal in the audible range is detectable through the human lungs above a frequency of .5–1.5 kHz. Note that this low–pass behavior is unique among human organs. By contrast, the typical speed of sound or ultrasound in soft tissue is normally much higher, around 1500 m/s, comparable to the speed of sound in water. For a review of experimental and theoretical studies on the subject, we refer to [PKW97].

On the contrary, there are very few studies on the propagation of ultrasound through the lung tissue between 10 kHz and 10 Mhz, see e.g. [Dun86]. Recently published studies indicate that the propagation properties of ultrasound through the lung are far from understood. In particular, it seems that the effective behavior for *in vivo* lung tissue is very different from the prohibitively high absorption previously measured at all ultrasound frequencies in *in vitro* lung samples. According to [RHD+10], low–frequency ultrasound may permeate the human lungs *in situ* for frequencies above 10 kHz, and propagation properties are highly dependent on the state of inflation of the lung, or on obstructive pathologies in the patients' lungs. An effective speed of sound above 1000 m/s was computed for these new ultrasound recordings, highlighting the difference in behavior with the low–frequency models developed e.g. in [Ric83]. Further development of theoretical models, possibly based on more detailed tissue mechanics, could lead to an increased understanding of these experimental observations and a better modeling of the lungs' acoustical properties.

Elastic fibers are the basic constituent of the connective tissue forming the alveolar wall. At small strain, they exhibit a predominantly elastic behavior with relatively small viscous losses. The remaining material consists of blood vessels, cells and a hydrophilic gel [SIS+05]. The mechanical properties of composite tissue depend on the relative amounts of their constituents, but also on their geometrical structure [FGX05]. In the lungs, the elastic fibers are arranged as a three–dimensional network.

In previous attempts to derive a law at the macroscopic scale fitting experimental results, the alveolar wall was modeled as an homogeneous elastic or viscoelastic medium [OL01, SJTL08, BGMO08]. Here, we change this point of view and try to investigate, theoretically and numerically, some macroscopic effects of the heterogeneity of the alveolar material at the micro–scale. Indeed, the previous discussion suggests that we model the lungs as a foamy material with microstructure, consisting of air bubbles separated by a heterogeneous viscoelastic medium which contains elastic fibers mixed with a viscous gel.

We make some simplifying modeling assumptions. First, motivated by the space repetition of the alveoli, we assume that the parenchyma consists of a periodic arrangement of pores with a small period $\varepsilon > 0$. We furthermore assume that the heterogeneous matrix constituting the connective tissue obeys the law of linearized viscoelasticity, and interacts with closed pockets filled with a compressible perfect gas modeling the air. Note that this assumes that air does not communicate freely between neighbouring alveoli. This common modeling assumption [Ric83, GWN02] has been validated by experimental studies [Kra83, BLD87] for frequencies above a few hundred hertz.

Once the model is set up, we employ a two–scale homogenization technique [Ngu89, All92] to derive effective acoustic equations for the composite tissue of the lungs by performing an asymptotic study as ε goes to zero. In this limit, we obtain equations describing a homogeneous viscoelastic medium without microstructure. The effective coefficients describing this homogenized medium are recovered from the given periodic micro–scale structure. Note that the homogenization of a similar model, in the static case, was considered in [BGMO08]. As is well–known [YPY98], the homogenization of heterogeneous viscoelastic composites, by the interaction of temporal and spatial variations of the coefficients in the differential equations of the model, gives rise to new memory effects. Even when the original models present only instantaneous memories, long–term memories are induced during the homogenization process [SP80, Tar09].

Finally, we face the problem of computing numerical simulations based on our homogenized description of the parenchyma. The appearance of the new memory effects by homogenization as a convolution term makes the equation hard to use directly. It is standard [SH10] to modify the model so that the the convolution is replaced by additional differential equations. We achieve this by approximating the viscoelastic behavior of the homogenized medium by a generalized Maxwell model with n relaxation frequencies [BW89] and then propose an efficient strategy based on a Discontinuous Galerkin method [HW08], which is a finite element method with discontinuities at the interfaces of the elements. Discontinuous Galerkin methods have been widely studied recently, as they combine many advantages, such as adaptativity to complex geometries, high parallelizability and high–order approximation. We present here a high–order Discontinuous Galerkin discretization adapted to the integration of the viscoelastic system in the time domain, with an implicit–explicit time–stepping scheme designed to minimize the computational cost of the method.

The paper is organized as follows. In Section 5.2, we describe the parenchyma model and we study theoretically this fluid–structure interaction system. In particular, we sketch the homogenization procedure, which consists of deriving the homogenized limit as ε goes to zero of the model (5.5) by the two–scale convergence framework, and we obtain a macroscopic description involving new memory effects, which depend on the micro–structure of the material.

Then, in Section 5.3, we propose a numerical method designed to efficiently solve the difficult viscoelastic problem obtained by homogenization. We introduce an efficient approximation of the memory terms by the use of Prony series and detail the discretization of the equations system by the Discontinuous Galerkin method. Finally, in Section 5.4, we illustrate this study by some numerical results in two dimensions and discuss its relevance to observations.

5.2 The viscoelastic homogenized model

5.2.1 The microscale model

Consider a system composed of a porous, inhomogeneous, incompressible viscoelastic frame perforated by gaseous bubbles. Let the tissue sample be contained in Ω, a bounded domain in $\mathbb{R}^d$, $d = 2$ or 3, which is supposed to be stress–free as the reference configuration of the composite. Assume that ε denotes a characteristic length of the pore size. We assume that the microscopic and macroscopic scale are well separated, meaning that the parameter ε is small. To deal with the two different length scales associated with variations of the variables at the micro– and macro–scale, we introduce, in addition to the global position vector $\mathbf{x}$, a local position vector $\mathbf{y}$ in a stretched coordinate system, which is related to $\mathbf{x}$ by

$$\mathbf{y} = \mathbf{x}/\varepsilon.$$

For example, if $E_\varepsilon(\mathbf{x}) = E(\mathbf{x}/\varepsilon)$ was to describe a coefficient appearing in the constitutive equations, then we could suppose that it depends on the fast variable $\mathbf{y}$ as a constant in some component of

the material and a different constant in another part of the material to describe heterogeneity of the tissue at the micro–scale.

The microscale geometry. Let us be more precise in our description of the material geometry. We restrict our attention to a periodic setting. Let $\mathbf{Z}$ be a reference periodic array in $\mathbb{R}^d$ with a reference periodicity cell $\mathcal{Y}$, normalized so that $|\mathcal{Y}| = 1$. The bounded domain $\Omega \subset \mathbb{R}^d$ is filled with periodically distributed gaseous bubbles. The viscoelastic matrix is assumed connected while the gaseous bubbles are isolated. The reference cell $\mathcal{Y}$ is therefore divided into two parts: an open simply connected bubble $\mathcal{Y}_F$, $\overline{\mathcal{Y}_F} \subset \mathring{\mathcal{Y}}$ having a smooth boundary Γ and its complement $\mathcal{Y}_S = \mathcal{Y} \backslash \overline{\mathcal{Y}_F}$ representing the viscoelastic skeleton, see Figure 5.1. Hence, the viscoelastic material occupies the domain Ω_ε obtained by ε–periodicity after excluding the bubbles strictly included in Ω:

$$\Omega_\varepsilon = \bigcup_{\mathbf{k} \in \mathbf{Z}_\varepsilon^\Omega} \varepsilon\,(\mathcal{Y}_S + \mathbf{k}), \qquad \mathbf{Z}_\varepsilon^\Omega = \{\mathbf{k} \in \mathbf{Z} : \quad \varepsilon(\mathcal{Y}_F + \mathbf{k}) \subset \Omega\}\,.$$

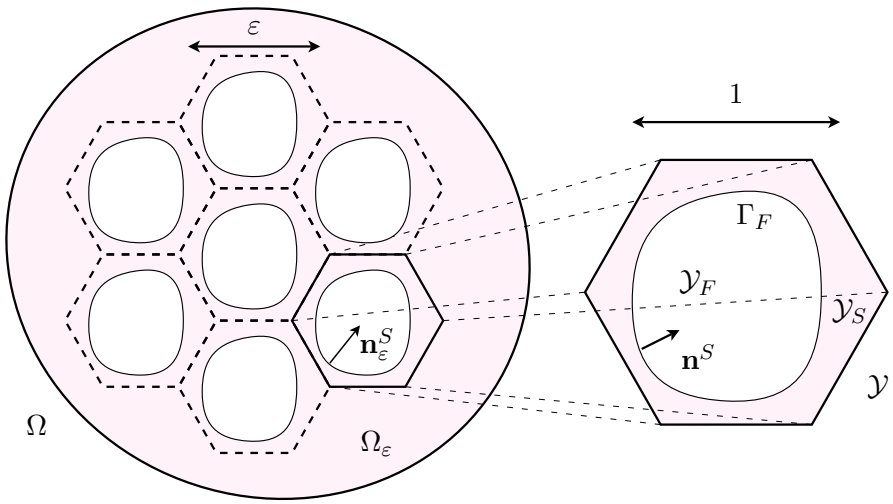

Figure 5.1 – Domain Ω_ε and unit fluid–structure cell $\mathcal{Y}$

The microscale model equations. We will consider motions of the medium small enough to be governed by linearized equations and denote the gaseous bubbles as $\mathcal{B}_\varepsilon^{\mathbf{k}} = \varepsilon(\mathcal{Y}_F + \mathbf{k})$ for $\mathbf{k} \in \mathbf{Z}_\varepsilon^\Omega$. Suppose that the closed gas bubbles behave like a perfect gas experiencing adiabatic compression, so the relation between volume $V_\varepsilon^{\mathbf{k}}(t)$ and pressure $p_\varepsilon^{\mathbf{k}}$ of the $\mathbf{k}$–bubble at time t is given by the law

$$p_\varepsilon^{\mathbf{k}}(t)\left(V_\varepsilon^{\mathbf{k}}(t)\right)^\gamma = \text{Cst.}\,,$$

where γ is the specific heat ratio for the gas (about 1.4 for air). Let $\mathbf{u}_\varepsilon$ be the (small) displacement field of the elastic media. Linearizing around an equilibrum state of atmospheric pressure p_a and volume $\left|\mathcal{B}_\varepsilon^{\mathbf{k}}\right|$, the equation governing the pressure inside the bubbles is [BGMO08]:

$$p_\varepsilon^{\mathbf{k}} - p_a \approx \frac{\gamma p_a}{|\mathcal{B}_\varepsilon^{\mathbf{k}}|} \int_{\partial \mathcal{B}_\varepsilon^{\mathbf{k}}} \mathbf{u}_\varepsilon \cdot \mathbf{n}_\varepsilon, \tag{5.1}$$

where $\mathbf{n}_\varepsilon$ is the unit normal to $\partial\Omega_\varepsilon$, pointing into the gaseous bubbles.

The equation of motion for the incompressible viscoelastic structure is given by

$$\begin{aligned} \rho_s \frac{\partial^2 \mathbf{u}_\varepsilon}{\partial t^2} &= \mathbf{div}\sigma_\varepsilon + \mathbf{f}, \\ \text{div } \mathbf{u}_\varepsilon &= 0, \end{aligned} \tag{5.2}$$

where $\rho_s > 0$ denotes the density of the alveolar wall, $\mathbf{f}$ is a volumic excitation force, and σ_ε is the stress tensor, which is related to $\nabla \mathbf{u}_\varepsilon$ by the constitutive law of the inhomogeneous wall material. We wish to study specifically the possible effects of the heterogeneity of the alveolar wall. In order to describe linear viscoelastic behavior, we recover the stress response from the strain history input as follows:

$$\sigma_\varepsilon(\mathbf{x}, t) = -p_\varepsilon(\mathbf{x}, t)\mathrm{Id} + \int_{-\infty}^{t} E_\varepsilon(\mathbf{x}, t-\tau)\frac{\partial}{\partial \tau} e(\mathbf{u}_\varepsilon(\mathbf{x}, \tau))\mathrm{d}\tau, \tag{5.3}$$

where
- σ_ε is the stress tensor,
- p_ε is a Lagrange multiplier associated with the constraint div $\mathbf{u}_\varepsilon = 0$,
- E_ε is the relaxation function, a fourth–order time–dependent tensor,
- $e(\mathbf{u}_\varepsilon) = 1/2\left(\nabla \mathbf{u}_\varepsilon + {}^T \nabla \mathbf{u}_\varepsilon\right)$ is the strain tensor of the material.

Note that p_ε is homogeneous to a pressure. At the boundary of the gaseous bubbles we have balance of the forces, that is

$$\mathbf{n}_\varepsilon \cdot \sigma_\varepsilon = (p_a - p_\varepsilon^{\mathbf{k}})\mathbf{n}_\varepsilon = -\frac{\gamma p_a}{|\mathcal{B}_\varepsilon^{\mathbf{k}}|}\left(\int_{\partial \mathcal{B}_\varepsilon^{\mathbf{k}}} \mathbf{u}_\varepsilon \cdot \mathbf{n}_\varepsilon\right)\mathbf{n}_\varepsilon \quad \text{on each } \partial\mathcal{B}_\varepsilon^{\mathbf{k}}. \tag{5.4}$$

For simplicity, we suppose that the material is initially at rest at time $t = 0$ and we impose homogeneous Dirichlet boundary conditions on the exterior boundary $\partial\Omega$. We collect the equations for the structure (5.2) and (5.3) as well as the boundary constraint describing the bubble response (5.4) to recover the following microscale description of the model:

$$\begin{cases} \rho_s \partial_{tt}\mathbf{u}_\varepsilon - \mathbf{div}\sigma_\varepsilon = \mathbf{f}, & \text{in } \Omega_\varepsilon, \\ \sigma_\varepsilon = -p_\varepsilon \mathrm{Id} + \displaystyle\int_0^t E_\varepsilon(\mathbf{x}, t-\tau)\frac{\partial}{\partial\tau} e(\mathbf{u}_\varepsilon(\mathbf{x},\tau))\mathrm{d}\tau, & \text{in } \Omega_\varepsilon, \\ \text{div } \mathbf{u}_\varepsilon = 0, & \text{in } \Omega_\varepsilon, \\ \mathbf{n}_\varepsilon \cdot \sigma_\varepsilon = -\dfrac{\gamma p_a}{\varepsilon^d |\mathcal{Y}_F|}\left(\displaystyle\int_{\partial\mathcal{B}_\varepsilon^{\mathbf{k}}} \mathbf{u}_\varepsilon \cdot \mathbf{n}_\varepsilon\right)\mathbf{n}_\varepsilon, & \text{on } \partial\mathcal{B}_\varepsilon^{\mathbf{k}},\ \forall \mathbf{k} \in \mathbf{Z}_\varepsilon^\Omega, \\ \mathbf{u}_\varepsilon = \mathbf{0} & \text{on } \partial\Omega, \end{cases} \tag{5.5}$$

$$\mathbf{u}_\varepsilon(t=0) = \mathbf{0}. \tag{5.6}$$

Heterogeneities. Following [Han05], the relaxation function writes

$$E_\varepsilon(\mathbf{x}, t) = E_\infty(\mathbf{x}/\varepsilon) + G(\mathbf{x}/\varepsilon, t) = E_\infty(\mathbf{y}) + G(\mathbf{y}, t), \tag{5.7}$$

where E_∞ represents the elastic response of the material at equilibrium, while G denotes the memory properties of the material. We suppose that $E_\infty(\mathbf{y})$ and $G(\mathbf{y}, t)$ belong respectively to $L^\infty(\mathcal{Y}, Sym)$ and $L^1(\mathbb{R}^+; L^\infty(\mathcal{Y}, Sym))$ where Sym is the set of symmetric fourth–order tensors. Furthermore,

we suppose that E_∞ is uniformly definite positive, meaning that there exists $\alpha > 0$ such that for all $\mathbf{y} \in \mathcal{Y}$ and any symmetric matrix ξ,

$$\sum_{1\leq i,j\leq d} E_{\infty,ijkl}(\mathbf{y})\xi_{ij}\xi_{kl} \geq \alpha|\xi|^2. \tag{5.8}$$

In addition, the time–dependent tensor G is positive and satisfies the weak dissipativity condition [Han05]:

$$\sum_{1\leq i,j\leq d} \int_{-\infty}^{T}\int_{-\infty}^{t} G_{ijkl}(t-s)\xi_{ij}(s)\xi_{kl}(t) \geq 0, \tag{5.9}$$

for all smooth test functions with compact support $\xi(t)$ in Sym and $T > 0$. Modeling the structure as a network of elastic fibers coated with a viscous gel representing the ground substance, we expect the elastic coefficients E_∞ to dominate in the fibers while the viscous components G dominate in the gel. Other models are also possible, such as modeling the gel as a purely Newtonian fluid and the fibers as a purely elastic medium (see e.g. [GM00]) .

5.2.2 The mathematical homogenization method

In this section, we outline the mathematical homogenization procedure to derive equations for the macroscopic motion of the medium. Clearly, it is not possible to solve (5.5) on a realistic geometry for more than a small number of alveoli, and certainly not for the millions that are contained in the parenchyma. To derive effective equations, the two–scale method of homogenization [Ngu89] is a widely used tool that has previously been applied to different models of the lung parenchyma by Owen and Lewis [OL01] as well as Siklosi et al. [SJTL08] for example. The approach consists in modeling the parenchyma as an array of periodically repeating cells, representing individual alveoli, and obtain equations governing the behavior of spatially averaged relevant quantities such as deformation and pressure by separating the variations at the micro–scale and macro–scale. It is also possible to deal with random inhomogeneities in the micro–structure [BK82], but the evaluation of the effective parameters is more complicated.

Weak formulation, existence and uniqueness. First, we study the existence and uniqueness of weak solutions to (5.5). For such viscoelastic problems this has been proved in a slightly different context [FGX05]. Define the Sobolev spaces $\mathbf{V}_\varepsilon = \mathbf{H}_0^1(\Omega_\varepsilon)$, $\mathbf{X}_\varepsilon = \mathbf{L}^2(\Omega_\varepsilon)$, $M_\varepsilon = L^2(\Omega_\varepsilon)$, and $\mathbf{V} = \mathbf{H}_0^1(\Omega)$, $\mathbf{X} = \mathbf{L}^2(\Omega)$, $M = L^2(\Omega)$. Let $T > 0$, the variational formulation associated with (5.5) is as follows.

Find $\mathbf{u}_\varepsilon$ in $L^\infty(0,T;\mathbf{V}_\varepsilon)$, $\partial_t\mathbf{u}_\varepsilon \in L^\infty(0,T;\mathbf{X}_\varepsilon)$, $q \in H^{-1}(0,T;M_\varepsilon)$ such that for all $\mathbf{v}_\varepsilon \in \mathbf{V}_\varepsilon$,

$$\begin{cases} \dfrac{\mathrm{d}}{\mathrm{d}t}\displaystyle\int_{\Omega_\varepsilon} \rho_s \partial_t\mathbf{u}_\varepsilon\cdot\mathbf{v}_\varepsilon + \dfrac{\mathrm{d}}{\mathrm{d}t}\int_{\Omega_\varepsilon}\left(\int_0^t G(\mathbf{x}/\varepsilon, t-\tau)e(\mathbf{u}_\varepsilon(\tau))\mathrm{d}\tau\right) : e(\mathbf{v}_\varepsilon) \\ \qquad -\displaystyle\int_\Omega p_\varepsilon \mathrm{div}(\mathbf{v}_\varepsilon) + \int_\Omega E_\infty(\mathbf{x}/\varepsilon)e(\mathbf{u}_\varepsilon) : e(\mathbf{v}_\varepsilon) \\ \qquad + \dfrac{\gamma p_a}{|\mathcal{Y}_F|\varepsilon^d}\displaystyle\sum_{\mathbf{k}\in\mathbf{Z}_\varepsilon^\Omega}\left(\int_{\partial\mathcal{B}_\varepsilon^{\mathbf{k}}}\mathbf{u}_\varepsilon\cdot\mathbf{n}_\varepsilon\right)\left(\int_{\partial\mathcal{B}_\varepsilon^{\mathbf{k}}}\mathbf{v}_\varepsilon\cdot\mathbf{n}_\varepsilon\right) = \displaystyle\int_{\Omega_\varepsilon}\mathbf{f}\cdot\mathbf{v}_\varepsilon, \\ \mathrm{div}\ \mathbf{u}_\varepsilon = 0, \qquad \text{a.e. in } \Omega_\varepsilon, \\ \mathbf{u}_\varepsilon(t=0) = \mathbf{0}, \qquad \text{a.e. in } \Omega_\varepsilon, \\ \partial_t\mathbf{u}_\varepsilon(t=0) = \mathbf{0}, \qquad \text{a.e. in } \Omega_\varepsilon. \end{cases} \tag{5.10}$$

This formulation has to be understood in $H^{-1}(0,T)$. Thanks to the positivity condition (5.8) we have the following result:

Proposition 5.2.1. *Assume that* $\mathbf{f} \in L^2(0,T;\mathbf{X})$.

Then, there exists a unique $\mathbf{u}_\varepsilon \in L^\infty(0,T;\mathbf{V}_\varepsilon) \cap W^{1,\infty}(0,T;\mathbf{X}_\varepsilon)$ *and* $q \in H^{-1}(0,T;M_\varepsilon)$ *which satisfies* (5.10). *Moreover, there exists a constant* C *which does not depend on* ε *such that:*

$$\|\partial_t \mathbf{u}_\varepsilon\|_{L^\infty(0,T;\mathbf{X}_\varepsilon)} + \|\mathbf{u}_\varepsilon\|_{L^\infty(0,T;\mathbf{V}_\varepsilon)} + \|p_\varepsilon\|_{H^{-1}(0,T;M_\varepsilon)} \leq C\|\mathbf{f}\|_{L^2(0,T;\mathbf{X}_\varepsilon)},$$

Proof. The proof of this proposition employs classic tools, presented in [LM68] for example. Let us sketch the main steps. First, we obtain $\mathbf{u}_\varepsilon$ as the solution of an auxiliary weak formulation without the pressure, obtained by taking divergence–free test functions and following Galerkin's method:

- Choose an orthonormal basis of $\mathbf{V}_\varepsilon^{inc} = \{\mathbf{v}_\varepsilon \in \mathbf{V}_\varepsilon : \text{div } \mathbf{v}_\varepsilon = 0 \text{ a.e. in } \Omega_\varepsilon\}$, and define finite–dimensional Galerkin spaces of approximation;
- Solve the ODE initial value problems obtained by reduction of the auxiliary weak formulation to the finite–dimensional Galerkin spaces, in which existence and uniqueness hold,
- Bound the sequence of Galerkin approximations using energy estimates to obtain their weak convergence,
- Pass to the weak limit and prove that it satisfies the variational formulation (5.10) for any divergence–free test function,
- Prove uniqueness by studying the difference between two solutions in the weak formulation.

In the end, we obtain $\mathbf{u}_\varepsilon \in L^\infty(0,T;\mathbf{V}_\varepsilon^{inc}) \cap W^{1,\infty}(0,T;\mathbf{X}_\varepsilon)$ as solution of the auxiliary variational formulation which reflects (5.10) with only divergence–free test functions. To proceed in the homogenization process, it is crucial to obtain *a priori* estimates with constants that do not depend on Ω_ε. Taking formally $\partial_t \mathbf{u}_\varepsilon$ as a test function in (5.10) (this can be rigorously justified by passing to the limit with the Galerkin approximations), we obtain the following energy estimates:

$$\begin{aligned}\frac{1}{2}\frac{\mathrm{d}}{\mathrm{d}t}\Bigg(\int_{\Omega_\varepsilon} \rho_s \partial_t \mathbf{u}_\varepsilon \cdot \partial_t \mathbf{u}_\varepsilon + \int_\Omega E_\infty(\mathbf{x}/\varepsilon) e(\mathbf{u}_\varepsilon) : e(\mathbf{u}_\varepsilon) \\ + \frac{\gamma p_a}{|\mathcal{Y}_F|\varepsilon^d} \sum_{\mathbf{k}\in\mathbf{Z}_\varepsilon^\Omega} \left(\int_{\partial\mathcal{B}_\varepsilon^{\mathbf{k}}} \mathbf{u}_\varepsilon \cdot \mathbf{n}_\varepsilon\right)\left(\int_{\partial\mathcal{B}_\varepsilon^{\mathbf{k}}} \mathbf{u}_\varepsilon \cdot \mathbf{n}_\varepsilon\right)\Bigg) \\ + \int_{\Omega_\varepsilon} \left(\int_0^t G(\mathbf{x}/\varepsilon, t-\tau) e(\partial_t \mathbf{u}_\varepsilon(\tau))\mathrm{d}\tau\right) : e(\partial_t \mathbf{u}_\varepsilon) = \int_{\Omega_\varepsilon} \mathbf{f} \cdot \partial_t \mathbf{u}_\varepsilon.\end{aligned}$$

We integrate in time and use Young's inequality and the coerciveness and dissipativity conditions (5.8), (5.9). Since the energy of the domain is zero at the initial time, we obtain a.e. $t \in [0,T]$:

$$\rho_s \|\partial_t \mathbf{u}_\varepsilon(t)\|^2_{\mathbf{X}_\varepsilon} + \alpha \|e(\mathbf{u}_\varepsilon(t))\|^2_{L^2(\Omega_\varepsilon)} \leq \int_0^t \left(\|\mathbf{f}\|^2_{\mathbf{X}_\varepsilon} + \|\partial_t \mathbf{u}_\varepsilon\|^2_{\mathbf{X}_\varepsilon}\right).$$

It is well–known that in perforated domains such as Ω_ε, the Korn and Poincaré inequality holds with a constant independent of ε (see for example [GM00, BGMO08]): there exist constants K and γ, depending only on Ω and $\mathcal{Y}_S$, such that for all $\mathbf{v}_\varepsilon \in \mathbf{V}_\varepsilon$, we have

$$\|\nabla \mathbf{u}_\varepsilon\|_{L^2(\Omega_\varepsilon)} \leq K\|e(\mathbf{u}_\varepsilon)\|_{L^2(\Omega_\varepsilon)}, \qquad \|\mathbf{u}_\varepsilon\|_{\mathbf{V}_\varepsilon} \leq \gamma \|\nabla \mathbf{u}_\varepsilon\|_{L^2(\Omega_\varepsilon)}.$$

Thus Gromwall's inequality (in the integral form) yields the estimate,

$$\|\partial_t \mathbf{u}_\varepsilon(t)\|^2_{\mathbf{X}_\varepsilon} + \|\mathbf{u}_\varepsilon(t)\|^2_{\mathbf{V}_\varepsilon} \leq C \int_0^T \|\mathbf{f}\|^2_{\mathbf{X}_\varepsilon}, \qquad \text{a.e. } t \in [0,T],$$

where C does not depend on ε. Finally, existence, uniqueness and an *a priori* estimate for the pressure p_ε are obtained from (5.10), following the proof of Theorem 1 in [BG11]. □

If the excitation force $\mathbf{f}$ satisfies a stronger regularity assumption, one obtains a better regularity for the solution:

Proposition 5.2.2. *Suppose that* $\mathbf{f} \in H^1(0,T;\mathbf{X})$. *Then, there exists* $\mathbf{u}_\varepsilon$ *in* $W^{2,\infty}(0,T;\mathbf{X}_\varepsilon) \cap W^{1,\infty}(0,T;\mathbf{V}_\varepsilon)$ *and* $p_\varepsilon \in L^\infty(0,T;M_\varepsilon)$ *which satisfies* (5.10). *Moreover, there exists a constant* C *which does not depend on* ε *such that:*

$$\|\mathbf{u}_\varepsilon\|_{W^{2,\infty}(0,T;\mathbf{X}_\varepsilon)} + \|\mathbf{u}_\varepsilon\|_{W^{1,\infty}(0,T;\mathbf{V}_\varepsilon)} + \|p_\varepsilon\|_{L^\infty(0,T;M_\varepsilon)} \leq C\|\mathbf{f}\|_{H^1(0,T;\mathbf{X}_\varepsilon)}. \tag{5.11}$$

The proof consists simply in differentiating the weak formulation in time and using the result of Proposition 5.2.1. The L^∞–bound on the pressure is obtained thanks to an *inf–sup* condition uniform in ε, see Proposition 3.1 in [BGMO08].

Asymptotic behavior. Hereafter, we suppose that $\mathbf{f} \in H^1(0,T;\mathbf{X})$ for simplicity of exposition. We now study the properties of the solution of the system as ε converges to zero. This procedure allows us to average out the microscale oscillations to understand the macroscale properties of the solution. We use here the notion of two–scale convergence introduced by Nguetseng [Ngu89] and Allaire [All92]. We denote by $\widetilde{\cdot}$ the extension by zero in $\Omega\backslash\Omega_\varepsilon$ and we adopt the following convention: the index $\#$ denotes spaces of $\mathcal{Y}$–periodic functions on Y or $\mathcal{Y}_S$ with null average, in particular we set

$$\mathbf{H}^1_\#(\mathcal{Y}_S) = \left\{ \mathbf{v}^1 \in H^1(\mathcal{Y}_S;\mathbb{R}^d), \quad \mathbf{v}^1 \text{ is } \mathcal{Y}\text{–periodic and } \int_{\mathcal{Y}_S} \mathbf{v}^1 = \mathbf{0} \right\}.$$

We extend naturally the definition of two–scale convergence to the time–dependent setting, as in [GM00] .

Definition 5.2.3. *A sequence* $(u_\varepsilon(t,\mathbf{x}))_{\varepsilon>0}$ *in* $L^2((0,T)\times\Omega)$ *two–scale converges to* $u(t,\mathbf{x},\mathbf{y})$ *in* $L^2((0,T)\times\Omega\times\mathcal{Y})$ *if for any* $v(t,\mathbf{x},\mathbf{y})$ *in* $L^2((0,T)\times\Omega, C_\#(\mathcal{Y}))$, *one has:*

$$\lim_{\varepsilon\to 0}\int_0^T\int_\Omega u_\varepsilon(t,\mathbf{x})\; v(t,\mathbf{x},\mathbf{x}/\varepsilon)\mathrm{d}\mathbf{x}\mathrm{d}t = \int_0^T\int_\Omega\int_{\mathcal{Y}} u(t,\mathbf{x},\mathbf{y})\; v(t,\mathbf{x},\mathbf{y})\mathrm{d}\mathbf{y}\mathrm{d}\mathbf{x}\mathrm{d}t.$$

Thanks to the compactness properties of the two–scale convergence (see e.g. [All92]), it is well–known that the *a priori* bounds (5.11) imply the existence of three functions $\mathbf{u}$ in $H^1(0,T;\mathbf{V}) \cap H^2(0,T;\mathbf{X})$, $\mathbf{u}^1$ in $H^1(0,T;L^2(\Omega,\mathbf{H}^1_\#(\mathcal{Y}_S)))$ and $p \in L^2((0,T)\times\Omega\times\mathcal{Y}_S)$ such that, up to a subsequence:

$$\widetilde{\mathbf{u}_\varepsilon} \to \mathbf{u}(x)\chi_S(y) \qquad \text{in the two–scale sense,} \tag{5.12a}$$

$$\widetilde{\nabla\mathbf{u}_\varepsilon} \to (\nabla_x\mathbf{u} + \nabla_y\mathbf{u}^1)\chi_S(y) \qquad \text{in the two–scale sense,} \tag{5.12b}$$

$$\widetilde{p_\varepsilon} \to p\chi_S(y) \qquad \text{in the two–scale sense,} \tag{5.12c}$$

where χ_S is the characteristic function of $\mathcal{Y}_S$.

Remark 5.2.4. *Note that the convergence results* (5.12) *are a rigorous expression of the heuristic argument that the properties of the material can be expanded as an asymptotic expansion in powers of* ε*:*

$$\mathbf{u}_\varepsilon(\mathbf{x}) \approx \mathbf{u}(\mathbf{x},\varepsilon) + \varepsilon\mathbf{u}^1(\mathbf{x},\mathbf{x}/\varepsilon) + \varepsilon^2\mathbf{u}^2(\mathbf{x},\mathbf{x}/\varepsilon) + \dots$$

We are now in a position to pass to the limit in the variational formulation (5.10). The idea is to use oscillating test functions of the form

$$\mathbf{v}_\varepsilon = \mathbf{v}(x) + \varepsilon\mathbf{v}^1(\mathbf{x},\mathbf{x}/\varepsilon).$$

Thanks to the two–scale convergences (5.12) we can pass to the limit in most terms of the weak formulation (5.10). We refer to [BGMO08] for details on the specific treatment of the term containing a non–local product of integrals in (5.10). In the end, we obtain that $\mathbf{u}$, $\mathbf{u}^1$ and p are solutions of the variational formulation, for all $\mathbf{v} \in \mathbf{V}$ and $\mathbf{v}^1 \in L^2(\Omega, H^1_\#(\mathcal{Y}_S))$:

$$\left\{\begin{array}{l} \displaystyle\int_\Omega \int_{\mathcal{Y}_S} \rho_s \partial_{tt}\mathbf{u}\cdot\mathbf{v} \\ \quad \displaystyle+ \int_\Omega \int_{\mathcal{Y}_S} \left(\int_0^t G(\mathbf{y}, t-\tau)\left(e_{\mathbf{x}}(\partial_t \mathbf{u}(\tau)) + e_{\mathbf{y}}(\partial_t \mathbf{u}^1(\tau))\right) \mathrm{d}\tau \right) : \left(e_{\mathbf{x}}(\mathbf{v}) + e_{\mathbf{y}}(\mathbf{v}^1)\right) \\ \quad \displaystyle- \int_\Omega \int_{\mathcal{Y}_S} p\left(\mathrm{div}_{\mathbf{x}}(\mathbf{v}) + \mathrm{div}_{\mathbf{y}}(\mathbf{v}^1)\right) \\ \quad \displaystyle+ \int_\Omega \int_{\mathcal{Y}_S} E_\infty(\mathbf{y})\left(e_{\mathbf{x}}(\mathbf{u}) + e_{\mathbf{y}}(\mathbf{u}^1)\right) : \left(e_{\mathbf{x}}(\mathbf{v}) + e_{\mathbf{y}}(\mathbf{v}^1)\right) \\ \quad \displaystyle+ \frac{|\mathcal{Y}|\gamma p_a}{|\mathcal{Y}_F|} \int_\Omega \mathrm{div}_{\mathbf{x}}\mathbf{u} \left(|\mathcal{Y}_F| \mathrm{div}_{\mathbf{x}}\mathbf{v} - \int_\Gamma \mathbf{v}^1\cdot\mathbf{n} \right) = \int_\Omega \int_{\mathcal{Y}_S} \mathbf{f}\cdot\mathbf{v}, \\ \mathrm{div}_{\mathbf{x}}\mathbf{u} + \mathrm{div}_{\mathbf{y}}\mathbf{u}^1 = 0, \qquad \mathbf{u}(t=0) = \mathbf{0}, \qquad \partial_t\mathbf{u}(t=0) = \mathbf{0}, \qquad \text{a.e. in } \Omega_\varepsilon. \end{array}\right. \tag{5.13}$$

Proposition 5.2.5. *The system (5.13) has a unique solution with* $\mathbf{u} \in W^{1,\infty}(0,T;\mathbf{V}) \cap W^{2,\infty}(0,T;\mathbf{X})$, $\mathbf{u}^1 \in W^{1,\infty}(0,T;L^2(\Omega,\mathbf{H}^1_\#(\mathcal{Y}_S)))$ *and* $p \in L^\infty((0,T)\times\Omega\times\mathcal{Y}_S)$. *Also, the whole sequence* $(\widetilde{\mathbf{u}_\varepsilon}, \widetilde{p_\varepsilon})_{\varepsilon>0}$ *two–scale converges to* $\mathbf{u}$, $\mathbf{u}^1$ *and* p *in the sense of (5.12).*

Proof. The proof of this result follows that of Proposition 5.2.1, given that $\|e_{\mathbf{x}}(\mathbf{u}) + e_{\mathbf{y}}(\mathbf{u}^1)\|_{L^2(\Omega\times\mathcal{Y}_S)}$ is a norm for the Hilbert space $\mathbf{V} \times L^2(\Omega;\mathbf{H}^1_\#(\mathcal{Y}_S))$ (Lemma 2.5 in [BGMO08]). Existence and uniqueness of the limit pressure p can be proved using a two–scale *inf–sup* condition (Lemma 3.6 in [BGMO08]). □

5.2.3 The microcell problem

The two–scale homogenized system is too complicated to be used directly. We are going to eliminate the micro–scale variables $\mathbf{u}^1$ and p to obtain the effective macro–scale equations. The system (5.13) is linear, and admits a unique solution. Hence, because of the superposition principle, we seek to express formally $\mathbf{u}^1(\mathbf{x},\mathbf{y},t)$ and $p(\mathbf{x},\mathbf{y},t)$ as expressions parameterized by the macro–scale displacement history $(\mathbf{u}(\mathbf{x},\tau))_{\tau\le t}$:

$$\mathbf{u}^1(t,\mathbf{x},\mathbf{y}) = \sum_{1\le i,j\le d} \int_0^t \boldsymbol{\chi}^{ij}(\mathbf{y}, t-\tau) e_{\mathbf{x}}(\mathbf{u})_{ij}(\mathbf{x},\tau)\mathrm{d}\tau, \tag{5.14}$$

$$p(t,\mathbf{x},\mathbf{y}) = \sum_{1\le i,j\le d} \int_0^t \eta^{ij}(\mathbf{y}, t-\tau) e_{\mathbf{x}}(\mathbf{u})_{ij}(\mathbf{x},\tau)\mathrm{d}\tau, \tag{5.15}$$

where $\boldsymbol{\chi}^{ij}(\mathbf{y},t)$ and $\eta^{ij}(\mathbf{y},t)$ are correctors to be determined as solutions of *cell problems* set on $\mathcal{Y}_S$. Note that $\boldsymbol{\chi}^{ij}$ and η^{ij} are in general distributions in the time domain, and obtaining their precise expression from the time–dependent two–scale problem (5.13) is possible but requires cumbersome calculations (see [GM00, FGX05] for a similar derivation). To better understand the frequency–domain behavior of the effective medium, and to simplify the analysis, we use the Fourier transform in the time variable to describe the local problems. For a given integrable or square–integrable function ψ, we denote its (complex–valued) Fourier transform $\widehat{\psi}$ defined for any $\omega \in \mathbb{R}$ as

$$\widehat{\psi}(\omega) = \frac{1}{\sqrt{2\pi}} \int_{-\infty}^{\infty} \psi(t) e^{-i\omega t}\mathrm{d}t.$$

If ψ is defined on $(0,T)$, we extend it by zero elsewhere. Taking the Fourier transform and setting $\mathbf{v}=0$ in (5.13), we obtain that the functions $\widehat{\mathbf{u}^1}$ and $\widehat{p}$ are solutions of the following variational problem parameterized by $e_{\mathbf{x}}(\widehat{\mathbf{u}})$ for any frequency ω: for all $\mathbf{v}^1 \in \mathbf{H}^1_{\#}(\mathcal{Y}_S)$,

$$\begin{cases} \displaystyle\int_{\mathcal{Y}_S} \left(E_\infty + i\omega\widehat{G}(\omega)\right)\left(e_{\mathbf{x}}(\widehat{\mathbf{u}}) + e_{\mathbf{y}}(\widehat{\mathbf{u}^1})\right) : e_{\mathbf{y}}(\mathbf{v}^1) \\ \qquad \displaystyle - \int_{\mathcal{Y}_S} \widehat{p}\,\mathrm{div}_{\mathbf{y}}(\mathbf{v}^1) - \frac{|\mathcal{Y}|\gamma p_a}{|\mathcal{Y}_F|}\mathrm{div}_{\mathbf{x}}\widehat{\mathbf{u}} \int_\Gamma \mathbf{v}^1\cdot\mathbf{n} = \mathbf{0}, \\ \qquad \mathrm{div}_{\mathbf{x}}\widehat{\mathbf{u}} + \mathrm{div}_{\mathbf{y}}\widehat{\mathbf{u}^1} = 0. \end{cases}$$

Note that, by Stokes formula, $\int_\Gamma \mathbf{v}^1\cdot\mathbf{n} = \int_{\mathcal{Y}_S} \mathrm{div}_{\mathbf{y}}\mathbf{v}^1$. Substituting the decompositions (5.14) and (5.15), we have, collecting the terms in $e_{\mathbf{x}}(\widehat{\mathbf{u}})$,

$$\begin{cases} \displaystyle\left\{\int_{\mathcal{Y}_S}\left(E_\infty + i\omega\widehat{G}(\omega)\right) e_{\mathbf{y}}\left(\mathbf{p}^{ij} + \widehat{\boldsymbol{\chi}^{ij}}(\omega)\right) : e_{\mathbf{y}}(\mathbf{v}^1)\right. \\ \qquad \displaystyle\left. - \int_{\mathcal{Y}_S}\left(\frac{|\mathcal{Y}|\gamma p_a}{|\mathcal{Y}_F|}\delta_{ij} + \widehat{\eta^{ij}}(\omega)\right)\mathrm{div}_{\mathbf{y}}(\mathbf{v}^1)\right\} e_{\mathbf{x}}(\widehat{\mathbf{u}})_{ij} = \mathbf{0}, \\ \left(\delta_{ij} + \mathrm{div}_{\mathbf{y}}\widehat{\boldsymbol{\chi}^{ij}}(\omega)\right) e_{\mathbf{x}}(\widehat{\mathbf{u}})_{ij} = 0, \end{cases}$$

where we have introduced the family of polynomials $\mathbf{p}^{ij}$, $1\le i,j\le d$ defined as:

$$\mathbf{p}^{ij}(\mathbf{y}) = \frac{1}{2}\left(y_i\mathbf{e}^j + y_i\mathbf{e}^j\right),$$

which is chosen so that the family $e_{\mathbf{y}}(\mathbf{p}^{ij}) = \frac{1}{2}\left(\mathbf{e}^i\otimes\mathbf{e}^j + \mathbf{e}^j\otimes\mathbf{e}^i\right)$ constitutes a basis of the set of symmetric tensors.

Hence, it is natural to seek $\widehat{\boldsymbol{\chi}^{ij}}(\omega,\mathbf{y})$ and $\widehat{\eta^{ij}}(\omega,\mathbf{y})$ as solutions of mixed cell problems parameterized by ω:

$$\begin{cases} -\mathbf{div}_{\mathbf{y}}\sigma_y^\omega\left(\widehat{\boldsymbol{\chi}^{ij}}(\omega),\widehat{\eta^{ij}}(\omega)\right) = \mathbf{div}_{\mathbf{y}}\sigma_y^\omega\left(\mathbf{p}^{ij}, \dfrac{|\mathcal{Y}|\gamma p_a}{|\mathcal{Y}_F|}\delta_{ij}\right), & \text{in } \mathcal{Y}_S, \\ \mathrm{div}_{\mathbf{y}}\widehat{\boldsymbol{\chi}^{ij}}(\omega) = -\delta_{ij}, & \text{in } \mathcal{Y}_S, \\ \sigma_y^\omega\left(\widehat{\boldsymbol{\chi}^{ij}}(\omega),\widehat{\eta^{ij}}(\omega)\right)\mathbf{n} = -\sigma_y^\omega\left(\mathbf{p}^{ij}, \dfrac{|\mathcal{Y}|\gamma p_a}{|\mathcal{Y}_F|}\delta_{ij}\right)\mathbf{n}, & \text{on } \Gamma, \\ \widehat{\eta^{ij}}(\omega),\ \widehat{\boldsymbol{\chi}^{ij}}(\omega)\ \mathcal{Y}\text{–periodic}, \end{cases} \tag{5.16}$$

where the local stress tensor σ_y^ω is defined for any $\omega\in\mathbb{R}$ as

$$\sigma_y^\omega(\eta,\boldsymbol{\chi}) = -\eta\mathrm{Id} + \left(E_\infty + i\omega\widehat{G}(\omega)\right)e_{\mathbf{y}}(\boldsymbol{\chi}).$$

To ensure that this problem is well–posed, we make hereafter the assumption that for any frequency ω, there exists a constant $\alpha(\omega)>0$ such that

$$\left|\left(E_\infty(\mathbf{y}) + i\omega\widehat{G}(\mathbf{y},\omega)\right)\xi : \xi\right| \ge \alpha(\omega)|\xi|^2 \qquad \text{for any } \mathbf{y}\in\mathcal{Y}_S \text{ and } \xi\in Sym. \tag{5.17}$$

Existence and uniqueness of the correctors $\widehat{\boldsymbol{\chi}^{ij}}(\omega)\in\mathbf{H}^1_{\#}(\mathcal{Y}_S)$ and $\widehat{\eta^{ij}}(\omega)\in L^2_{\#}(\mathcal{Y}_S)$ as solutions of (5.16) is then a consequence of the Lax–Milgram theorem.

Remark 5.2.6. *The quantity $E_\infty(\mathbf{y}) + i\omega\widehat{G}(\mathbf{y},\omega)$ is called the complex relaxation modulus, and is the frequency–domain equivalent of the relaxation function in the description of the viscoelastic material. Condition (5.17) is satisfied in particular if the real or imaginary part of the complex relaxation modulus is positive definite. For $\omega = 0$ we recover the condition (5.8) satisfied by any solid material. For $\omega > 0$, we know in general that the dissipation condition (5.9) implies that the imaginary part $\omega \mathrm{Re}\left(\widehat{G}(\mathbf{y},\omega)\right)$ of the complex relaxation modulus is always a positive tensor, and is positive definite for any truly dissipative viscoelastic material (see e.g. [Han05]).*

Remark 5.2.7. *It is well–known that the solutions of (5.16) depend continuously on the parameters. Since $G(\mathbf{y},t)$ belongs to $L^1(0,T)$, its Fourier transform $\widehat{G}(\mathbf{y},\omega)$ is a continuous function of ω, hence the functions $\omega \mapsto \widehat{\boldsymbol{\chi}^{ij}}(\omega)$ and $\omega \mapsto \widehat{\eta^{ij}}(\omega)$ are also continuous.*

5.2.4 Effective equation and effective relaxation modulus

We have seen that for a given $\widehat{\mathbf{u}}$, the local variables $\widehat{\mathbf{u}^1}$ and $\widehat{p}$ are determined by the formulae

$$\widehat{\mathbf{u}^1}(\mathbf{x},\mathbf{y},\omega) = \sum_{1\le i,j\le d} e_{\mathbf{x}}(\widehat{\mathbf{u}})_{ij}(\mathbf{x},\omega)\ \widehat{\boldsymbol{\chi}^{ij}}(\mathbf{y},\omega), \quad \widehat{p}(\mathbf{x},\mathbf{y},\omega) = \sum_{1\le i,j\le d} e_{\mathbf{x}}(\widehat{\mathbf{u}})_{ij}(\mathbf{x},\omega)\ \widehat{\eta^{ij}}(\mathbf{y},\omega).$$

Applying the Fourier transform to the system (5.13) and taking $\mathbf{v}^1 = 0$, we obtain

$$\begin{cases} \displaystyle\int_\Omega -\rho_s|\mathcal{Y}_S|\omega^2\mathbf{u}\cdot\mathbf{v} + \int_\Omega e_{\mathbf{x}}(\widehat{\mathbf{u}})_{ij}(\mathbf{x})\left(\int_{\mathcal{Y}_S}\left(E_\infty + i\omega\widehat{G}(\omega)\right)e_{\mathbf{y}}\left(\mathbf{p}^{ij}+\widehat{\boldsymbol{\chi}}^{ij}\right)\right) : e_{\mathbf{x}}(\mathbf{v}) \\ \quad \displaystyle -\int_\Omega e_{\mathbf{x}}(\widehat{\mathbf{u}})_{ij}(\mathbf{x})\left(\int_{\mathcal{Y}_S}\widehat{\eta^{ij}}\right)\mathrm{div}_{\mathbf{x}}(\mathbf{v}) + |\mathcal{Y}|\gamma p_a\int_\Omega \mathrm{div}_{\mathbf{x}}\widehat{\mathbf{u}}\ \mathrm{div}_{\mathbf{x}}\mathbf{v} = \int_\Omega |\mathcal{Y}_S|\widehat{\mathbf{f}}\cdot\mathbf{v}. \end{cases}$$

Hence the effective equation in the frequency domain for the displacement of the structure $\widehat{\mathbf{u}}$ takes the form

$$-\omega^2|\mathcal{Y}_S|\rho_S\widehat{\mathbf{u}} - \mathbf{div}\left(\widehat{\mathcal{G}}^{hom}e(\widehat{\mathbf{u}})\right) = |\mathcal{Y}_S|\widehat{\mathbf{f}}, \tag{5.18}$$

where the homogenized complex relaxation modulus of the material $\widehat{\mathcal{G}}^{hom}$ is obtained by averaging the correctors in $\mathcal{Y}_S$:

$$\widehat{\mathcal{G}}^{hom}_{ijkl}(\omega) = |\mathcal{Y}_S|\left(E_\infty + i\omega\widehat{G}(\omega) + \frac{|\mathcal{Y}|\gamma p_a}{|\mathcal{Y}_S|}\mathrm{Id}\right)_{ijkl} + \left(\int_{\mathcal{Y}_S}\sigma_y^\omega\left(\widehat{\boldsymbol{\chi}}^{ij}(\omega),\eta^{ij}(\omega)\right)\right)_{kl}. \tag{5.19}$$

It is easily shown (see e.g. [All92]) that $\widehat{\mathcal{G}}^{hom}$ satisfies the usual symmetry conditions, for any value of ω:

$$\widehat{\mathcal{G}}^{hom}_{ijkl} = \widehat{\mathcal{G}}^{hom}_{klij} = \widehat{\mathcal{G}}^{hom}_{ijlk}.$$

In addition, the data and coefficients in (5.16) are real when $\omega = 0$, hence $\widehat{\mathcal{G}}^{hom}(0)$ is positive definite.

Decomposition of the relaxation modulus. To come back to the time–domain, it is necessary to further decompose the complex relaxation modulus $\widehat{\mathcal{G}}^{hom}$. By analogy with (5.7), we introduce the homogenized equilibrium modulus $E^{hom}_\infty = \widehat{\mathcal{G}}^{hom}(0)$ and write

$$\widehat{\mathcal{G}}^{hom}(\omega) = E^{hom}_\infty + i\omega\widehat{G}^{hom}(\omega). \tag{5.20}$$

To compute the memory function G^{hom}, let us also decompose $\widehat{\boldsymbol{\chi}^{ij}}$ and $\widehat{\eta^{ij}}$ as

$$\widehat{\boldsymbol{\chi}^{ij}}(\omega) = \widehat{\boldsymbol{\chi}^{ij}}(0) + i\omega\widehat{\boldsymbol{\phi}^{ij}}(\omega), \qquad \widehat{\eta^{ij}}(\omega) = \widehat{\eta^{ij}}(0) + i\omega\widehat{\psi^{ij}}(\omega).$$

By substraction in (5.16), the functions $\widehat{\boldsymbol{\phi}^{ij}}(\omega)$ and $\widehat{\psi^{ij}}(\omega)$ are solutions of the mixed problem:

$$\begin{cases} -\mathbf{div_y}\sigma_y^\omega\left(\widehat{\boldsymbol{\phi}^{ij}}(\omega),\widehat{\psi^{ij}}(\omega)\right)=\mathbf{div_y}\left(\widehat{G}(\omega)\left(\mathbf{p}^{ij}+\widehat{\boldsymbol{\chi}^{ij}}(0)\right)\right) & \text{in } \mathcal{Y}_S,\\ \mathrm{div_y}\widehat{\boldsymbol{\phi}^{ij}}(\omega)=0 & \text{in } \mathcal{Y}_S,\\ \sigma_y^\omega\left(\widehat{\boldsymbol{\phi}^{ij}}(\omega),\widehat{\psi^{ij}}(\omega)\right)\mathbf{n}=-\left(\widehat{G}(\omega)e_{\mathbf{y}}\left(\mathbf{p}^{ij}+\widehat{\boldsymbol{\chi}^{ij}}(0)\right)\right)\mathbf{n} & \text{on } \Gamma,\\ \widehat{\psi^{ij}},\ \widehat{\boldsymbol{\phi}^{ij}}\ \mathcal{Y}\text{–periodic.} \end{cases} \tag{5.21}$$

Now the effective memory function G^{hom} is defined by its Fourier transform as:

$$\widehat{G}^{hom}_{ijkl}(\omega)=\int_{\mathcal{Y}_S}\widehat{G}_{ijkl}(\omega)+\left(\int_{\mathcal{Y}_S}\widehat{G}(\omega)e_{\mathbf{y}}\left(\widehat{\boldsymbol{\chi}}^{ij}(0)\right)+\sigma_y^\omega\left(\widehat{\boldsymbol{\phi}}^{ij}(\omega),\psi^{ij}(\omega)\right)\right)_{kl}. \tag{5.22}$$

5.2.5 Effective equations in the time domain

Let us now conclude this presentation of the homogenization process by describing the effective behavior of the viscoelastic porous domain as a function of time. The macroscopic displacement is described by the variable $\mathbf{u}(\mathbf{x},t)$, and combining (5.18) and (5.20), we obtain the homogenized system

$$\begin{cases} |\mathcal{Y}_S|\rho_S\partial_{tt}\mathbf{u}(t)-\mathbf{div}(\sigma^{hom}(t))=|\mathcal{Y}_S|\mathbf{f}(t), & \text{in } \Omega,\\ \sigma^{hom}(t)=E^{hom}_\infty e(\mathbf{u}(t))+\displaystyle\int_0^t G^{hom}(t-\tau)e(\partial_t\mathbf{u}(\tau))\mathrm{d}\tau, & \text{in } \Omega,\\ \mathbf{u}=\mathbf{0}, & \text{on } \partial\Omega. \end{cases} \tag{5.23}$$

Notice that the homogenized equations (5.23) have exactly the same form as the original ones (5.5) if the original moduli $E_\infty(\mathbf{x}/\varepsilon)$ and $G(\mathbf{x}/\varepsilon,t)$ are replaced by the corresponding effective moduli E^{hom}_∞ and $G^{hom}(t)$. Hence we have replaced a complicated problem, set on a perforated domain, by a classic viscoelastic problem without microstructure.

However, this simplification comes at the cost of having to compute beforehand the values of the homogenized moduli by solving cell problems. In particular, it is necessary to obtain the values of the memory function $G^{hom}(t)$ for every time t. Applying the inverse Fourier transform to (5.22) and (5.21), we recover $G^{hom}(t)$ as

$$G^{hom}_{ijkl}(t)=\begin{cases}\int_{\mathcal{Y}_S}G_{ijkl}(t)+\left(\int_{\mathcal{Y}_S}G(t)e_{\mathbf{y}}\left(\widehat{\boldsymbol{\chi}}^{ij}(0)\right)+\sigma^{ij}(t)\right)_{kl}, & \text{for } t>0,\\ 0, & \text{for } t\le 0,\end{cases}$$

where the tensor $\sigma^{ij}(t)$ is defined as a function of $\boldsymbol{\phi}^{ij}(t)$, $\psi^{ij}(t)$ which are solutions of the following quasi–static viscoelastic problem for $t>0$:

$$\begin{cases} -\mathbf{div_y}\sigma^{ij}(t)=\mathbf{div_y}\left(G(t)e_{\mathbf{y}}\left(\mathbf{p}^{ij}+\widehat{\boldsymbol{\chi}^{ij}}(0)\right)\right), & \text{in } \mathcal{Y}_S,\\ \sigma^{ij}(t)=-\psi^{ij}(t)\mathrm{Id}+E_\infty e(\boldsymbol{\phi}^{ij}(t))+\displaystyle\int_0^t G(t-\tau)e(\partial_t\boldsymbol{\phi}^{ij}(\tau))\mathrm{d}\tau, & \text{in } \mathcal{Y}_S,\\ \mathrm{div_y}\boldsymbol{\phi}^{ij}=0, & \text{in } \mathcal{Y}_S,\\ \sigma^{ij}(t)\mathbf{n}=-\left(G(t)e_{\mathbf{y}}\left(\mathbf{p}^{ij}+\widehat{\boldsymbol{\chi}^{ij}}(0)\right)\right)\mathbf{n}, & \text{on } \Gamma,\\ \psi^{ij},\ \boldsymbol{\phi}^{ij}\ \mathcal{Y}\text{–periodic.} \end{cases} \tag{5.24}$$

Memory effects. An interesting aspect of the homogenization of viscoelastic materials is the appearance of new memory effects caused by the coupling of spatial and temporal variations of the viscoelastic modulus of the material. It has been argued by Tartar [Tar09] that such long–term memory effects are induced by the spatial averaging in the solutions of hyperbolic equations with coefficients oscillating in space. In particular, long–term memory effects have been shown to appear when homogenizing two–phase media coupling an elastic matrix and a Newtonian fluid [GM00] [BG11], a Voigt body [SP80], or a Maxwell body [Suq87], even though each component exhibits only instantaneous memory.

The appearance of new memory effects depend directly on the inhomogeneity of the viscoelastic properties of the material. Indeed, suppose that the dependence on the time and space variables of the material are separable, in the sense that the relaxation function of the wall material is

$$E(\mathbf{y},t) = E_\infty(\mathbf{y})\,(1+g(t)) \qquad \text{or} \qquad G(\mathbf{y},t) = E_\infty(\mathbf{y})g(t),$$

where g belongs to $L^1(\mathbb{R}_+)$. Then, thanks to (5.16),

$$\mathbf{div_y}\left(E_\infty e_{\mathbf{y}}\left(\mathbf{p}^{ij} + \widehat{\boldsymbol{\chi}^{ij}}(0)\right)\right) = \nabla\widehat{\eta^{ij}}(0) \qquad \text{in } \mathcal{Y}_S,$$

and it is immediate from (5.24) that $\sigma^{ij}(t) = -g(t)\widehat{\eta^{ij}}(0)$ for all times. Hence, the effective memory function is

$$G^{hom}(t) = \left(E_\infty^{hom} - \frac{|\mathcal{Y}|\gamma p_a}{|\mathcal{Y}_S|}\mathrm{Id}\right) g(t).$$

As a consequence, when the relaxation function is separable it is enough to solve the local problem only once. The only new memory effect to appear is due to the coupling with the gas in the pores, which increases the elastic bulk modulus but not its viscous counterpart.

On the other hand, if the dependance on space and time is not separable, it is necessary to compute the effective relaxation function for all times or, equivalently, in the Laplace or Fourier transformed domain.

5.3 Numerical offline/online strategy for the global dispersive problem

To further improve our understanding of the mechanics of the lungs, we now consider the numerical solution of the effective equation (5.23). Our objective is to obtain a fast numerical method for the computation of the solutions to the homogenized wave propagation problem (5.23). The strategy we propose consists in two distinct parts:

- Computing the homogenized material parameters, based on a choice of parameters describing the material at the microscopic level. This is a preliminary, *offline* step, independent of the macroscale geometry or source data, and is described in Section 5.3.2.
- Integrating in time the propagation of the viscoelastic wave on a given macroscale geometry by an efficient Discontinuous Galerkin method, presented in Section 5.3.3 and 5.3.4.

5.3.1 Evaluation of the convolution integral

Several numerical methods have been developed to solve the initial boundary problem associated with the equations of elasticity or viscoelasticity, with notable applications to propagation of seismic waves or to the determination of the elastic parameters of soft tissue by MRI measurements. The treatment of the convolution term in (5.23) is an important factor in the choice of the method. One

specific model and widely used model is the Zener or Standard Linear Solid model, for which the complex modulus is represented with a Debye–type relaxation function:

$$\widehat{E}(\omega) = E_0 + \frac{E_\infty - E_0}{1 + i\omega\tau_0}, \tag{5.25}$$

where E_∞ is the relaxed elastic modulus, E_0 is the instantaneous elastic modulus and τ_0 is the relaxation time. If E_∞ reduces to zero we obtain the popular Maxwell model. The inverse Fourier transform of (5.25) is an exponential function

$$E(t) = E_0 + (E_\infty - E_0)\left(1 - \exp\left(-\frac{t}{\tau_0}\right)\right),$$

and this key characteristic has led to the development of several computationally efficient algorithms for incorporating Standard Linear Solids into Finite Element or Finite Difference codes [SH10]. The algorithms take the form of simple recursion relations, or auxiliary difference equations that are updated along with the standard elastic wave equation, by adding an additional internal variable.

The Zener model is a poor model of viscoelastic behavior for most materials over wide frequency ranges. However because the Fourier transform of most non–Zener models are not exponential functions, they cannot be incorporated directly into Finite Elements or Finite Difference codes using recursion relations or auxiliary difference equations. This is in particular the case of the homogenized model we have obtained. Historically, it was proposed that the integral may be simply discretized by a trapezoidal method. However, this proves too costly in practice since the convolution must be reevaluated at each time step, so the entire history of the deformation must be kept in memory.

Another possibility is to use the Laplace transform to change the numerical computation from solving the time evolution problem (5.23) to solving a series of independent elliptic problems for a number of well–chosen Laplace parameters (5.18). The solution in time is then obtained by performing an inverse Laplace transform. Such a scheme is particularly easy to implement for the homogenized material since the complex elastic modulus can be computed for each frequency of interest by solving the cell problem (5.16). This approach is detailed e.g. in [Bla11]. However, the computational and memory costs are significant for wave propagation computations since numerous large linear systems have to be solved to compute the solution of the complex elliptic problems associated with the Laplace transformed viscoelastic wave equation on a realistic 2D or 3D geometry, and their solutions have to be retained in memory until the inverse Laplace transform is performed to recover the time–dependent solution.

An approach used by many investigators is to approximate the complex relaxation modulus using a Prony series expansion of the form

$$E(t) \approx E_0 - \sum_{i=1}^{n} E_i\left(1 - e^{-t/\tau_i}\right) = E_\infty + \sum_{i=1}^{n} E_i e^{-t/\tau_p}, \tag{5.26}$$

where n is the total number of functions, E_i the relaxation modulus and τ_i the relaxation time of the i–th function. This model is called the Generalized Maxwell or Wiechert model. Most of the algorithms developed for Zener or Maxwell models can efficiently incorporate multiple relaxation mechanisms as a way to accomodate models with a non–exponential relaxation function. Indeed, in this case, we may transform the convolution integral appearing in the evolution equation (5.23) by introducing additional internal variables to the original set of unkowns. Denoting by $e(t)$ the strain tensor $e(\mathbf{u})$, we have the relation:

$$\int_0^t E(t-\tau)\partial_t e(\tau)\mathrm{d}\tau = E_0 e(t) - E_i e_i, \tag{5.27}$$

where we have introduced n internal variables e_i, defined by

$$e_i = \int_0^t \partial_t e(\tau) \left(1 - e^{(\tau - t)/\tau_i}\right) \mathrm{d}\tau \qquad \text{for } i = 1, \dots, n,$$

or alternatively satisfying $e_i(0) = 0$ and the additional ordinary differential equation

$$\tau_i \partial_t e_i + e_i = e.$$

Hence, the use of the Wiechert model to describe the homogenized material enables us to replace the expensive computation of the convolution, at the cost of introducing additional internal variables.

5.3.2 Computation and fitting of the dispersive curve

Next, we present a method for computing the viscoelastic complex modulus of the homogenized material and its Prony series representation (5.26). This is the first, *offline* step of the numerical method and can be done ahead of the time–domain computation, with no knowledge of the macroscopic geometry or of the wave data. This computation of the homogenized parameters can be quite expensive, but it has to be done only once for each set of micro–scale parameters.

In this paper, we chose to obtain the coefficients of the Prony series approximating the homogenized relaxation function using the method of nonlinear least–squares. This approach yields good results and can be implemented using standard routines. The approach is to sample the homogenized coefficients and fit the complex modulus with a Prony series by fitting both real and imaginary parts at the same time:

$$\mathrm{Re}\left(\widehat{E}^{hom}(\omega)\right) = E_\infty^{hom} + \sum_{p=1}^{N_p} E_p \left(\frac{1}{1 + \omega^2 \tau_p^2}\right), \tag{5.28}$$

$$\mathrm{Im}\left(\widehat{E}^{hom}(\omega)\right)/\omega = \mathrm{Re}\left(\widehat{G}^{hom}(\omega)\right) = \sum_{p=1}^{N_p} E_p \left(\frac{\tau_p}{1 + \omega^2 \tau_p^2}\right). \tag{5.29}$$

Remark 5.3.1. *We note that a similar problem arises in the modeling of electromagnetic waves in dispersive media. In this case, the model corresponding to the frequency dependence in (5.25) is called the Debye equation.*

Remark 5.3.2. *In [YPY98], it was proposed to fit the modulus in the (real) Laplace transformed domain, but the results were found not to be very stable when comparing the complex moduli in the Fourier frequency domain.*

Solution of the cell problems. To implement the least-squares method, we sample the complex modulus at a large number of frequencies covering the range of interest. This is achieved by solving the complex elliptic problems (5.16) to compute the frequency–dependent complex correctors $\widehat{\boldsymbol{\chi}^{ij}}(\mathbf{y}, \omega)$. The numerical solution of the cell problems (5.16) is obtained by standard Finite Element methods for a given set of parameters modeling the microscale parenchyma tissue.

Remark 5.3.3. *Note that this step can be quite costly, as it potentially requires solving a large number of independent highly resolved cell problem. However, this work is done offline, and can be trivially parallelelized.*

If the cell problems are further parameterized by another parameter, for example by dependence of the coefficients or the cell geometry on the slow variable $\mathbf{x}$*, then this computation has also to be done for every point in the macroscopic domain. In this case it would be interesting to consider methods of reduced complexity for solving repeatedly the parameterized cell problems (5.16), e.g. the reduced order basis method as proposed in [Boy08]. The reduced basis method has been applied for such computations e.g. in [Mor11, MMS12].*

5.3.3 Discontinuous Galerkin discretization

Assume now that we have a distribution (E_i, τ_i) of relaxation mechanisms describing the viscoelastic complex modulus of the homogenized medium as in (5.26). To solve the problem (5.23), we express the equation system in the first–order velocity–strain formulation. To this end, we introduce the velocity vector $\mathbf{v} = \partial_t \mathbf{u}$, and denote the tensorial product of two vectors $\mathbf{a}$, $\mathbf{b}$ in $\mathbb{R}^d$ as $\mathbf{a} \otimes \mathbf{b}$ in $\mathbb{R}^{d\times d}$ with

$$(\mathbf{a} \otimes \mathbf{b})_{ij} = a_i b_j.$$

Then, using the equation of motion (5.23) and the relation (5.27), we formulate the pseudo–conservative system of viscoelastic wave equations in the form of a multi–dimensional conservation law complemented with n relaxation laws on Ω, for $t \geq 0$:

$$\begin{cases} \rho_S |Y_S| \partial_t \mathbf{v} - \mathbf{div}\left(E_0^{hom} e - E_i^{hom} e_i\right) = \mathbf{f}, \\ \partial_t e - \operatorname{div}\left(\dfrac{\mathbf{v} \otimes \mathbf{e}_j + \mathbf{e}_j \otimes \mathbf{v}}{2}\right) = 0, \\ \tau_1 \partial_t e_1 + e_1 = e, \\ \vdots \quad \vdots \\ \tau_n \partial_t e_n + e_n = e, \end{cases} \tag{5.30}$$

with zero initial and boundary conditions.

Note that each additional relaxation mechanism adds a further 3 variables in dimension two and 6 in dimension three, one for each strain component of the additional internal variable. Therefore, the system consisting of 5 or 9 equations in the purely elastic case is complemented by an additional $3n$ or $6n$ equations (depending on the dimension) in the viscoelastic case when we use n relaxation mechanisms.

We denote $\mathbf{W} = (\mathbf{v}, e)$ as the vector composed by the velocity and the strain components and $\mathbf{M} = (e_1, \ldots, e_n)$ as the vector composed by the internal strain variable components. The system (5.30) can be rewritten in compact form

$$\begin{cases} \partial_t \mathbf{W} - \mathbf{div}\left(\mathcal{A}_1 \mathbf{W} - \mathcal{A}_2 \mathbf{M}\right) = \mathbf{f}, \\ \mathcal{T} \partial_t \mathbf{M} + \mathbf{M} = \mathcal{B} \mathbf{W}, \end{cases} \tag{5.31}$$

where we define, using the block–matrix notation, the matrices

$$\mathcal{A}_1 = (\rho_S |Y_S|)^{-1} \begin{bmatrix} 0 & \dfrac{\mathbf{e}_i \otimes \mathbf{e}_j + \mathbf{e}_j \otimes \mathbf{e}_i}{2} \\ E_0^{hom} & 0 \end{bmatrix}, \qquad \mathcal{A}_2 = (\rho_S |Y_S|)^{-1} \begin{bmatrix} E_1^{hom} & \ldots & E_n^{hom} \end{bmatrix},$$

$$\mathcal{T} = \begin{bmatrix} \tau_1 \mathrm{Id} & \ldots & \tau_n \mathrm{Id} \end{bmatrix}, \qquad \mathcal{B} = \begin{bmatrix} \begin{bmatrix} 0 \\ \mathrm{Id} \end{bmatrix} & \ldots & \begin{bmatrix} 0 \\ \mathrm{Id} \end{bmatrix} \end{bmatrix}^T.$$

Note that the dimension of the vector $\mathbf{M}$ and of the matrices $\mathcal{A}_2$, $\mathcal{T}$ and $\mathcal{B}$ depends on the chosen number n of the relaxation mechanisms.

We assume that the computational domain Ω is composed of K non–overlapping elements (e.g. triangles in dimension two, tetrahedra in dimension three)

$$\Omega = \bigcup_{k=1}^{K} \mathcal{D}_k,$$

and that the solution in each subdomain $\mathcal{D}_k$ is well approximated by the local polynomial of degree p

$$\mathbf{W}^k(\mathbf{x},t) = \mathbf{W}^k(\mathbf{x}_i^k,t)L_i^k(\mathbf{x}) = \mathbf{W}_i^k(t)L_i^k(\mathbf{x}),$$
$$\mathbf{M}^k(\mathbf{x},t) = \mathbf{M}^k(\mathbf{x}_i^k,t)L_i^k(\mathbf{x}) = \mathbf{M}_i^k(t)L_i^k(\mathbf{x}),$$

where $\mathbf{x}_i^k$ are the N grid points in the k–th element and $L_i^k(\mathbf{x})$ is the two– or three–dimensional multivariate Lagrange polynomial based on these points (we refer to [HW08] for a detailed account of the nodal spatial discretization). Note that

$$N = \frac{(p+1)(p+2)}{2} \text{ in 2D}, \quad N = \frac{(p+1)(p+2)(p+3)}{6} \text{ in 3D}.$$

The physical flux is approximated locally as

$$\mathcal{F}^k\left(\mathbf{W}^k,\mathbf{M}^k\right) = \left(\mathcal{A}_1\mathbf{W}_i^k - \mathcal{A}_2\mathbf{M}_i^k\right)L_i^k(\mathbf{x}). \tag{5.32}$$

We implement a Galerkin projection approach and integrate (5.30) against the N local test functions $L_i^k(\mathbf{x})$ for each element. After integration by parts, we obtain the semi–discrete form of the scheme

$$\begin{cases} \displaystyle\int_{\mathcal{D}_k}\left(\partial_t\mathbf{W}^k - \mathbf{div}\mathcal{F}^k\right)L_i^k(\mathbf{x}) = \int_{\partial\mathcal{D}_k}\left(\mathcal{F}^k - \mathcal{F}^*\right)L_i^k(\mathbf{x})\mathbf{n} + \int_{\mathcal{D}_k}\mathbf{f}(\mathbf{x},t)L_i^k(\mathbf{x}), \\ \mathcal{T}\partial_t\mathbf{M}^k + \mathbf{M}^k = \mathcal{B}\mathbf{W}^k. \end{cases} \tag{5.33}$$

As numerical flux we use the local Lax–Friedrichs flux [LeV90]

$$\mathcal{F}^* = \mathcal{F}^*\left(\mathbf{W}^+,\mathbf{M}^+,\mathbf{W}^-,\mathbf{M}^-\right) = \mathcal{A}_1\frac{\mathbf{W}^+ + \mathbf{W}^-}{2} - \mathcal{A}_2\frac{\mathbf{M}^+ + \mathbf{M}^-}{2} - \frac{c}{2}\left(\mathbf{W}^+ - \mathbf{W}^-\right),$$

where $\mathbf{W}^-$, $\mathbf{M}^-$ refers to the local solution, $\mathbf{W}^+$, $\mathbf{M}^+$ refers to the neighboring solutions, and c is the maximum eigenvalue of the flux Jacobian $\mathcal{A}_1$, which here is the maximum wave speed in the unrelaxed elastic medium.

5.3.4 Implicit–explicit time–stepping scheme

We will integrate in time using a high–order Runge–Kutta scheme. It is possible to use a fully explicit time–integration scheme, which is simple to implement and the most efficient for low levels of stiffness, but imposes a stability–based time–step restriction. Considering the scheme (5.33), we note that there are two different mechanisms potentially controlling the maximum possible time–step:

- the usual Courant–Friedrichs–Levy condition, induced by the discretization of a first–order operator and which is controlled by the geometry of the spatial discretization and the wave speed,
- the characteristic times τ_i associated with the relaxation mechanisms, which *a priori* may be arbitrarily small. Indeed the range of relaxation times can be very wide, even as large as 10^{10} for a Maxwell system [SH10], and a suitable time integrator shoud be both stable and accurate for small and large values of the relaxation time.

To adress this second limitation, we implement an implicit–explicit Runge–Kutta method proposed by Kennedy and Carpenter [KC03], see also [KCGH07]. This allows us to keep the efficiency of the explicit approach and avoid solving the large, non–stiff linear system associated with the wave equation discretized by the first equation in (5.33). At the same time, it integrates implicitly and

accurately the system of ODEs formed by the second equation of the problem, which effectively forms a diagonal linear system which is trivial to solve. Let us write the system (5.33) as

$$\frac{\mathrm{d}}{\mathrm{d}t}\mathbf{W} = \mathbf{F}^{ex}\left(\mathbf{W}, \mathbf{M}, t\right),$$
$$\frac{\mathrm{d}}{\mathrm{d}t}\mathbf{M} = \mathbf{F}^{im}\left(\mathbf{W}, \mathbf{M}, t\right).$$

Then the time–stepping scheme writes as follows. To compute $\mathbf{W}(t+\Delta t) = \mathbf{W}^{(n+1)}$ with an s–stage IMEX–RK method,

$$\begin{cases} \mathbf{W}^{(i)} &= \mathbf{W}^{(n)} + \Delta t \sum_{j=1}^{s} a_{ij}^{ex} \mathbf{F}^{ex}\left(\mathbf{W}^{(j)}, \mathbf{M}^{(j)}, t^{(n)} + c_j \Delta t\right), \\ \mathbf{M}^{(i)} &= \mathbf{M}^{(n)} + \Delta t \sum_{j=1}^{s} a_{ij}^{im} \mathbf{F}^{im}\left(\mathbf{W}^{(j)}, \mathbf{M}^{(j)}, t^{(n)} + c_j \Delta t\right), \end{cases}$$
$$\begin{cases} \mathbf{W}^{(n+1)} &= \mathbf{W}^{(n)} + \Delta t \sum_{j=1}^{s} b_i \mathbf{F}^{ex}\left(\mathbf{W}^{(i)}, \mathbf{M}^{(j)}, t^{(n)} + c_i \Delta t\right), \\ \mathbf{M}^{(n+1)} &= \mathbf{M}^{(n)} + \Delta t \sum_{j=1}^{s} b_i \mathbf{F}^{im}\left(\mathbf{W}^{(i)}, \mathbf{M}^{(j)}, t^{(n)} + c_i \Delta t\right), \end{cases}$$

where $\mathbf{W}^{(i)} = \mathbf{W}\left(t^{(n)} + c_i \Delta t\right)$, and the fixed scalar coefficients a_{ij}^{ex}, a_{ij}^{im}, b_j and c_i determine the accuracy and stability of the given RK scheme.

The matrix A^{ex} is characteristic of a fully explicit Runge–Kutta scheme, usually referred to as an ERK scheme. The matrix A^{im} is associated with a singly diagonally implicit Runge–Kutta scheme, or ESDIRK scheme. Note that the two schemes are coupled through the nodes c_i and the weights b_j. The precise values of the coefficients for different IMEX schemes can be found e.g. in [KC03, Bos09].

Coupling the two parts of the scheme is straightforward: at each stage of the RK computation, the explicit variable $\mathbf{W}$ (displacement and stress) is integrated to obtain $\mathbf{W}^{(i)}$, and then the implicit variable $\mathbf{M}$ (internal variables) are integrated using the explicitly computed stress as a source term.

5.4 Numerical results

In this section, we present the results of numerical experiments in a two–dimensional setting. First, we solve the cell problems (5.16) on a few examples of cell geometries and parameters using the Finite Elements software FreeFem++ [Hec12]. Then, we use the C++ Least–Squares library levmar [Lou04] to fit the computed dispersion curve to a Prony series. Finally, we implement the numerical scheme (5.33) using the Discontinuous Galerkin solver Hedge [Klo10].

5.4.1 Effective viscoelastic modulus computation

To show that the inhomogeneity of the material at the microscale results in interesting effects, we compute the effective viscoelastic complex modulus for a two–dimensional test micro–scale geometry. The chosen periodicity cell is the unit square. Note that this choice has significant effects on the resulting properties of the homogenized material, as will become clear from the wave propagation simulations.To model the connective tissue of the parenchyma, we propose to study a periodic, connected, elastic skeleton presenting inclusions filled with a viscous material, modeling respectively the network of elastic fibers sustaining the lungs and the ground substance and fluids contained in the parenchyma.

Remark 5.4.1. *It is not possible in this two–dimensional setting to model both phases of the material as connected, even though both the elastic fiber network and the blood capillary network are connected in the real lung parenchyma.*

In our model, the domain $\mathcal{Y}_S$ is divided into two distinct parts, noted $\mathcal{Y}_S^f$ and $\mathcal{Y}_S^v$, on which the material's parameters $E_\infty(\mathbf{y})$ (relaxed elastic modulus) and $G(\mathbf{y}, t)$ (memory function), defined by (5.7), are constant with respect to the space variable, see Figure 5.2. We further assume that $\mathcal{Y}_S^f$ is connected. Assuming that the material is locally isotropic, the mechanical properties of the elastic substance, dominated by the purely elastic reponse, are given by the relations

$$E_\infty = \mu \mathrm{Id} \quad \text{and} \quad G \approx 0, \tag{5.34}$$

where μ is the shear modulus of the elastic substance. Several choices are possible for the viscous filling, and we show results for a Kelvin–Voigt body, satisfying the relations

$$E_\infty \approx 0 \quad \text{and} \quad G = \nu\delta(t), \tag{5.35}$$

where ν is an effective viscosity and δ the Dirac distribution. We consider physiologically relevant values for the parameters, as discussed e.g. in [OL01]. Let us note that there are very few available studies of the detailed mechanics of the constituents of the alveolar wall, see e.g. [CIB+05, RW11].

Parameter	Description	Estimate
μ	Shear Modulus of the Elastic Fibers	$10^5\ Pa$
ν	Shear viscosity of the Ground Substance	$10^3\ Pa \cdot s$
ρ_s	Density of the Alveolar Wall	$10^3\ Kg \cdot m^{-3}$
p_a	Atmospheric pressure	$10^5\ Pa$

Table 5.1 – Parameter estimates for the fluid–structure model (5.5)

Remark 5.4.2. *We consider a domain $\mathcal{Y}_S$ symmetric with respect to the axis OX and OY, so it is possible to use only a quarter of the cell as the computational domain. Moreover, the six values in $\widehat{E}^{hom}$ reduces to three different values in this case.*

Figure 5.3 shows the results. We observe that the homogenized viscoelastic properties of the material are very different from the behavior of either the elastic, viscous or gas component. In particular, the behavior of pressure waves can be predicted by analyzing the diagonal components of the viscoelastic tensor $\mathcal{G}^{hom}_{1111}$ and $\mathcal{G}^{hom}_{1122}$. One observation is that the effective stiffness of the homogenized material goes from the value of the gas compressibility at low frequencies, equal to $\gamma p_a \approx 1.4 \cdot 10^5 Pa$, as predicted by the Rice model [Ric83], to a much higher value for frequencies above 10 kHz. This result is consistent with experimental observations [RHD+10], although it would be necessary to study numerically more realistic 3D geometries to quantitatively verify this assertion. Hence, it seems that the low–frequency limit is not very dependent on the microstructure, as it depends mainly on the compressibility of the gas content. On the other hand, the high–frequency behavior of the homogenized material is significantly affected by the geometric configuration of the microstructure as well as the relaxation moduli of the various components of the parenchyma. Another observation is that the loss factor, defined as the ratio between the imaginary part and the real part of the compressibility, peaks at a frequency of a few kHz, which indicates a very high attenuation of the pressure waves in the medium in a band of frequencies around this peak. Again, this is consistent with the experimental observation that there is extreme attenuation of sound waves in the audible range through the lungs' parenchyma above 1.5 kHz.

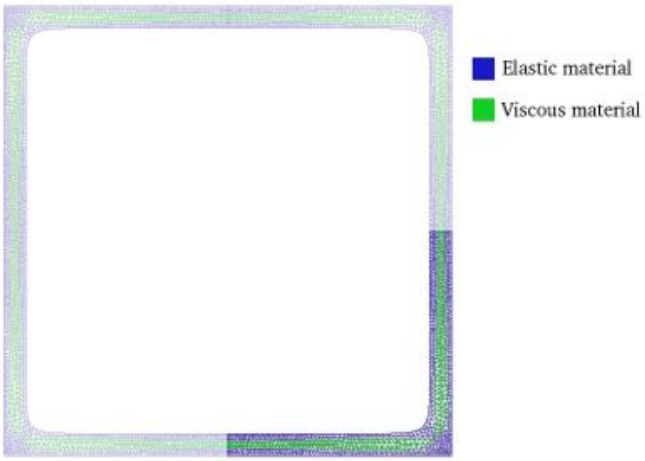

Figure 5.2 – Computational mesh representing the test geometry

5.4.2 Fitting the dispersion curve

The next step consists in the fitting of the curve obtained by a Prony series using the Least–Squares method. We adjust the coefficients (E_p, τ_p) in the expansion (5.26) using a nonlinear least–squares procedure as discussed in [BW89]. Note that for the stability of the time–domain integration method, the coefficients τ_p and E_p should be positive, and this must be incorporated as a constraint in the least–squares algorithm. To show the effect of the number of terms in the Prony series approximation, the number n of relaxation mechanisms is varied by 1, 2, 5 and 9 and the best results are shown in Figure 5.4 for the first coefficient $\mathcal{G}^{hom}_{1111}$. The choice of the number of relaxation modes is important. We have seen that each additional relaxation mode increases significantly the number of degrees of freedom involved for solving the homogenized problem (5.23) in the time domain and hence the associated memory cost, since we need $5+3n$ degrees of freedom in 2D and $9+6n$ in 3D for each grid point in the mesh. Hence, it is highly desirable to keep the number of relaxation modes as low as possible to ensure both reasonable memory costs and an acceptable error level. To achieve this, it is best not to preset the relaxation times τ_p, as proposed in [Sch61], but to optimize their distribution.

The frequency range considered covers 8 orders of magnitude, and we see that 9 relaxation mechanisms are necessary to capture precisely the behavior of the homogenized material. Note that above this number, the residual error levels off. For practical purposes, it may be necessary to reduce the frequency range of the optimization procedure and hence the number of relaxation frequencies to avoid using excessive computer memory.

While a good fit can be obtained by a simple Least–Square approach, our experiences shows that the results depend considerably on the chosen initial distribution of relaxation times. To show the effect of the initial distribution, we have computed the Least–Squares fit obtained for 500 initial random distributions of relaxation times for values of n between 0 and 15. The results are shown in Figure 5.5. In particular, it appears that the best possible fit can be obtained with $n = 9$. Using more relaxation mechanisms makes it easier to find the correct fit but does not increase the precision of the method.

Remark 5.4.3. *It may be interesting, in order to obtain a fully automated computational method, to use more advanced fitting techniques. For example, genetic algorithms have been proposed e.g. in [CR10], as well as hybrid particle swarm–least squares optimization in [KDL07], for the similar*

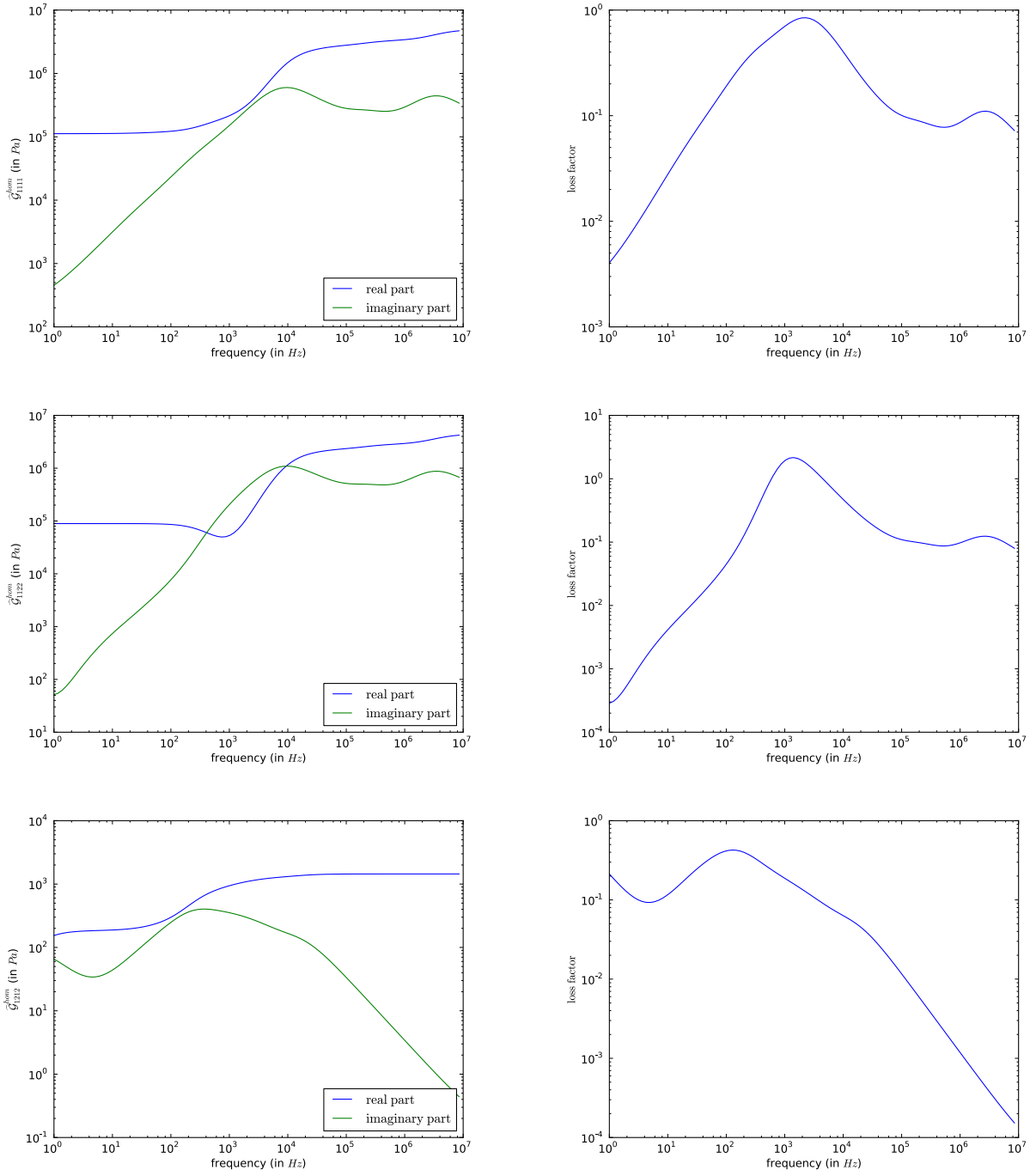

Figure 5.3 – The three nonzero complex coefficients of the viscoelastic homogenized tensor (in Pa) as a function of frequency (in Hz) obtained by the formula (5.19). On the left we plot the real and imaginary parts, and on the right the loss factor which is the quotient of the imaginary over the real part of the coefficient.

a)

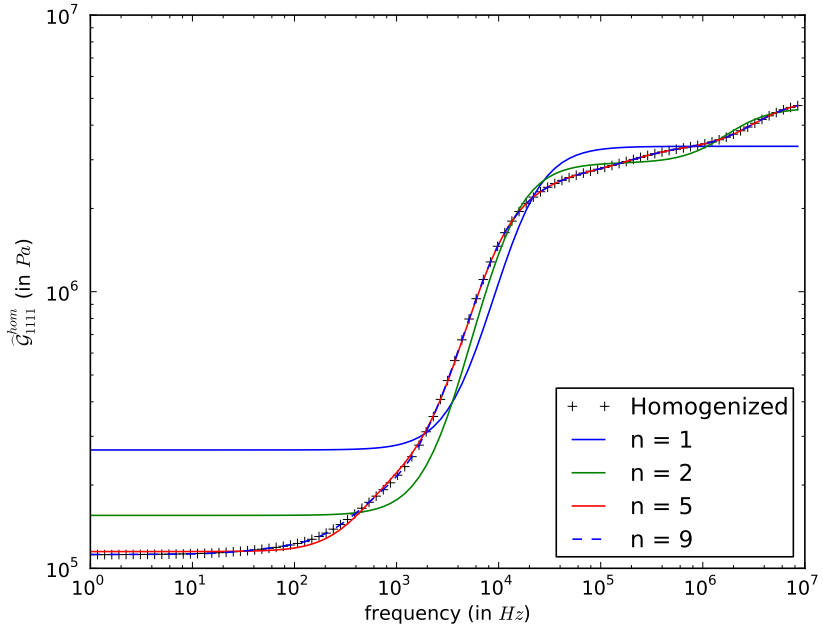

b)

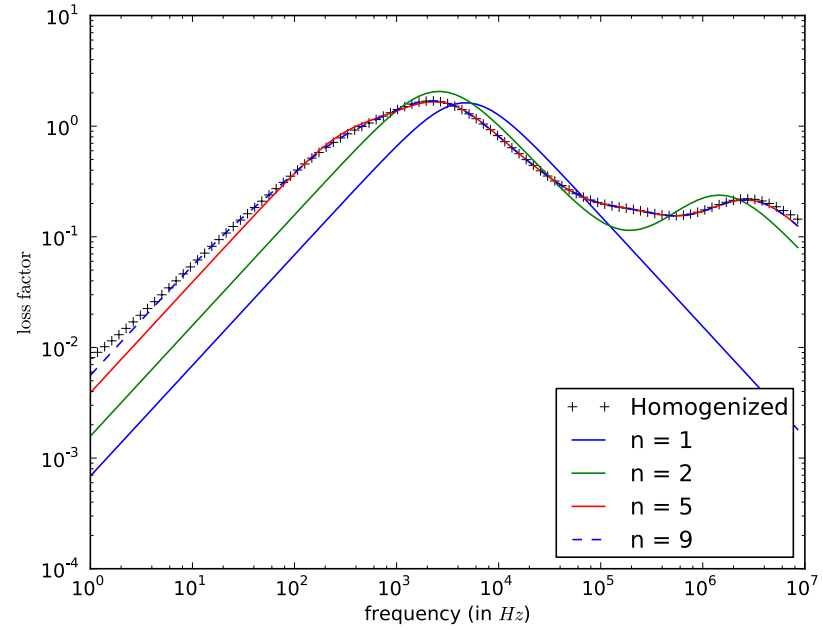

Figure 5.4 – Effect of the number of fitting terms: (a) Effective modulus, and (b) effective loss factor as a function of frequency.

a)

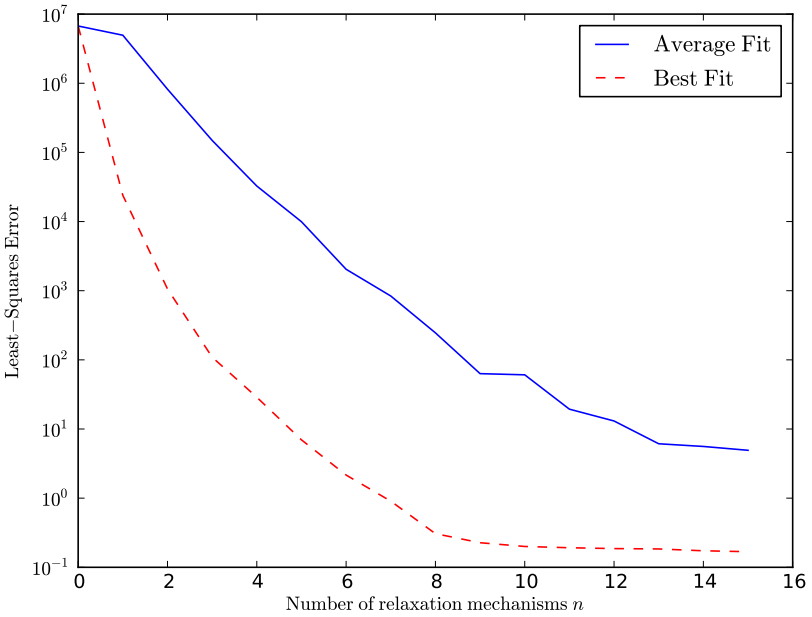

b)

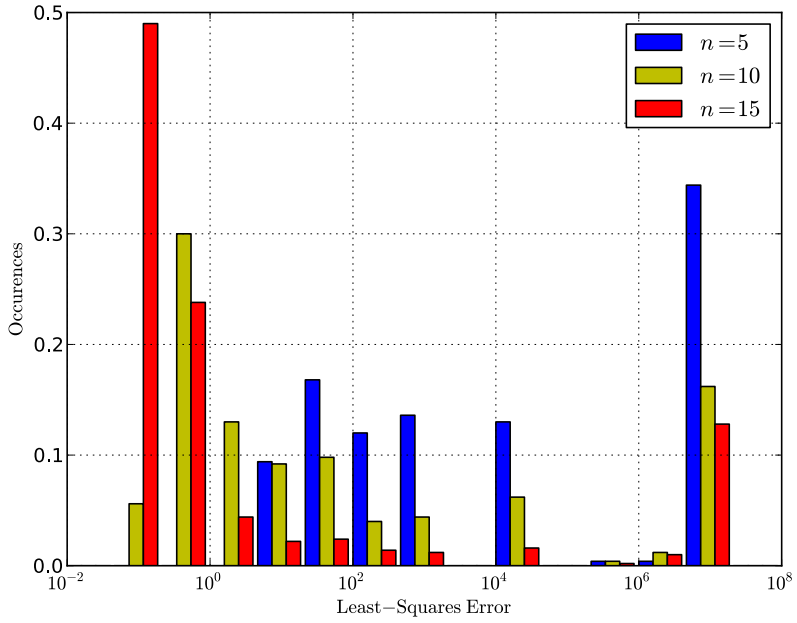

Figure 5.5 – Effect of the number of fitting terms: (a) best and average fit obtained, and (b) distribution of the error for a few values of n.

problem of fitting the frequency–dependent permittivity of a dielectric material to a Debye series.

5.4.3 Wave propagation computations

Finally, we have implemented the Discontinuous Galerkin numerical scheme for the time–dependent homogenized problem (5.23) described in Sections 5.3.3 and 5.3.4. To probe the frequency–dependent attenuation of the homogenized material, we have computed the propagation of a two–dimensional pulse in the disk–shaped domain at various frequencies. We introduce a small volumic source at the center of the disk by setting $\mathbf{f} = s(t)e^{-|\mathbf{x}|^2/\delta^2}\mathbf{x}$, where δ is a small parameter and $s(t)$ is a Ricker function given by $s(t) = \left(1 - (\omega_0 t - \beta)^2\right) \exp\left((\omega_0 t - \beta)^2\right)$ with $\beta = 3$ as a phase delay parameter and ω_0 the dominant frequency of the pulse. Initial conditions for the system are $\mathbf{v} = \mathbf{0}$ and $e, e_1, \ldots, e_n = 0$. We compare the behavior of the viscoelastic medium obtained by homogenization, and approximated by the Prony series, to that of a purely elastic medium presenting the same instantaneous elastic coefficients at the chosen frequency.

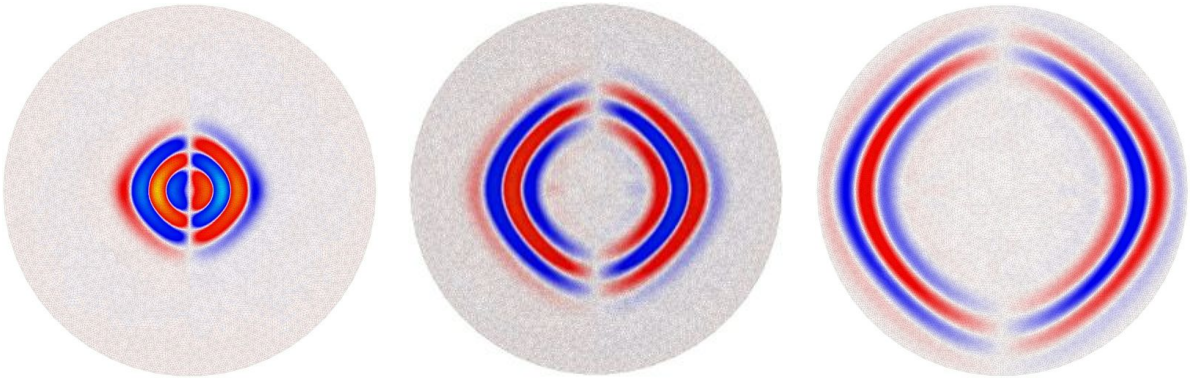

$t = .15$ s $\quad$ $t = .28$ s $\quad$ $t = .4$ s

(a) Propagation in the viscoelastic homogenized medium with coefficients as in Figure 5.3.

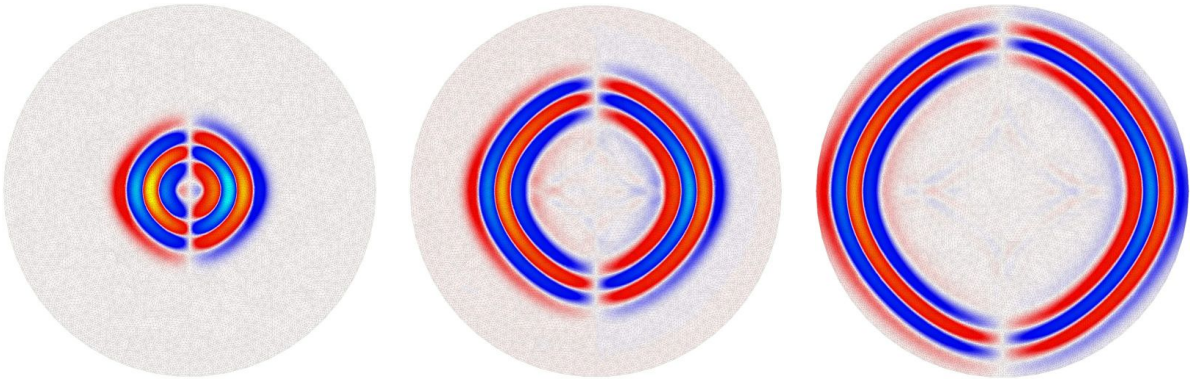

$t = .15$ s $\quad$ $t = .28$ s $\quad$ $t = .4$ s

(b) Propagation in a purely elastic reference medium with the same elastic coefficients at frequency 10 Hz.

Figure 5.6 – Instantaneous snapshots of the propagation of a wave of frequency 10 Hz as described in Section 5.4.3. The plots present the first component of the velocity at three different instants. The same color scale is used for all six snapshots.

Figure 5.6 shows three wavefield snapshots at increasing times of the simulation for $\omega_0 = 10$ Hz, which corresponds to a low–frequency regime. There is a slight decrease in amplitude in the

viscoelastic medium compared to the purely elastic medium, due to absorption, but the signal is shown to propagate without significant distortion.

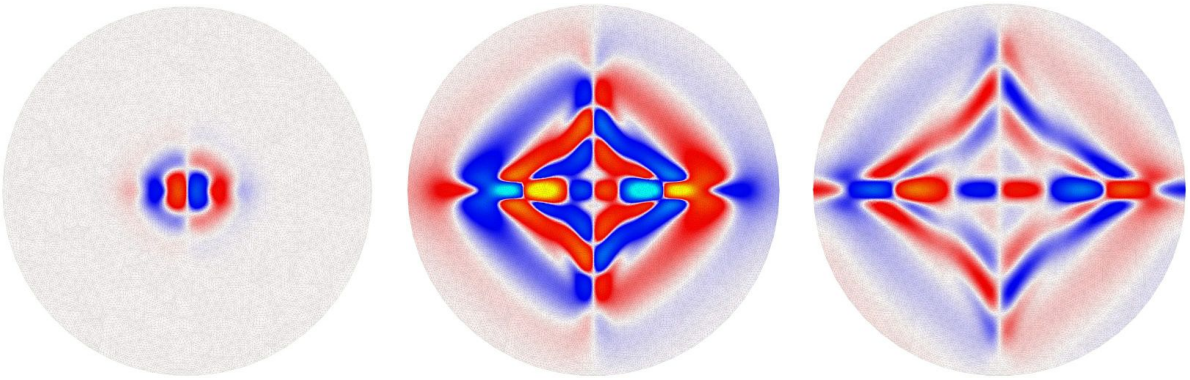

$t = .6$ ms | color scale upscaled by 200 $t = 1.4$ ms | color scale upscaled by 200 $t = 2$ ms

(a) Propagation in the viscoelastic homogenized medium with coefficients as in Figure 5.3.

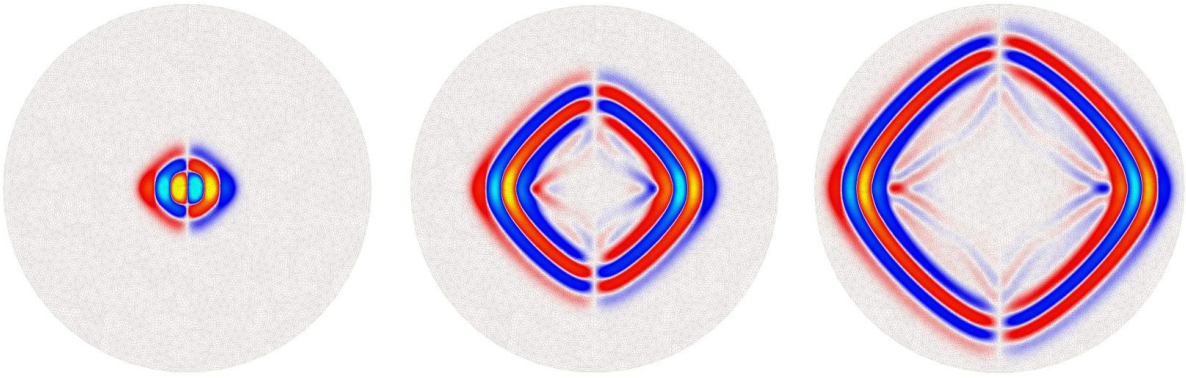

$t = .6$ ms | $t = 1.4$ ms | $t = 2$ ms

(b) Propagation in a purely elastic reference medium with the same elastic coefficients at frequency 2000 Hz.

Figure 5.7 – Instantaneous snapshots of the propagation of a wave of frequency 2000 Hz as described in Section 5.4.3. The plots present the first component of the velocity at three different instants. In the two last frames of the first row, the color scale for the velocity has been upscaled by a factor of 200 because the signal has been almost completely dissipated in the viscoelastic homogenized medium, especially the high frequency components.

Figure 5.7 also shows three snapshots at increasing times of the simulation for $\omega_0 = 2000$ Hz, which corresponds to a mid–frequency regime. Now there is a significant difference in the wave propagation in the homogenized medium compared to the reference elastic medium. In the former, the higher frequency content of the pulse is dissipated almost immediately, leading to a drop in amplitude of the signal by a factor of 200 after just a few wavelengths. In this range of frequencies, the homogenized medium does not propagate the signal which is absorbed extremely quickly. We note also that the behavior is markedly anisotropic in both the viscoelastic and elastic media.

5.4.4 Orthotropic and isotropic behavior

An important observation is that the homogenized behavior is highly anisotropic at higher frequencies, with waves propagating almost exclusively along the axis OX and OY. This results from the symmetry properties of the square periodicity cell, which ensure that the homogenized material is *orthotropic*, but not necessarily invariant with respect to rotations. Hence, this is an artefact of the periodicity we have imposed on the material, whereas the real parenchyma does not have preferred directions for sound propagation.

To recover a more realistic isotropic behavior, several options are possible. In 2D, we can recover isotropic behavior by using a hexagonal periodicity cell instead of a square cell. However, this results from a very particular choice of microstructure model, and there is no equivalent result in 3D. In [OL01], the homogenized coefficients were averaged directly under an assumption of macroscopic isotropy of the homogenized material, while in [SJTL08], the authors used experimental values of Young's modulus and Poisson's ratio for the elastic part of their homogenized parenchyma model.

We show here the effect of introducing random rotations inside each element of the discretization, mimicking the random arrangement of the alveoli in the real tissue. This has the effect of a global numerical averaging of the preferred directions of the homogenized material as the preferred axis now have a random orientation inside each element. The results are shown in Figure 5.8. Although a significant scattering of the wavefield is induced by the randomness of the media, we observe that the behavior is now isotropic, and the signal propagates with no preferred direction. Moreover, note that the artificial randomness does not induce much more dissipation than in the reference homogenized case.

Conclusion

We have presented a homogenized model for viscoelastic porous media such as the lung. This model has enabled us to investigate theoretically and numerically some macroscopic properties of the tissue resulting from the alveolar structure at the microscopic level. The resulting homogenized material has a viscoelastic behavior with new memory effects which have been discussed in detail. Numerical results in 2D show that the material has a band–pass filter behavior. This is in line with recent physiological observations [RHD+10], which is interesting given the serious simplifications our model is based on.

Subsequently, a new Discontinuous Galerkin method was developed to deal with the specific numerical issues associated with the presence of the memory effects. We have shown the effectiveness and robustness of this method in 2D wave propagation simulations.

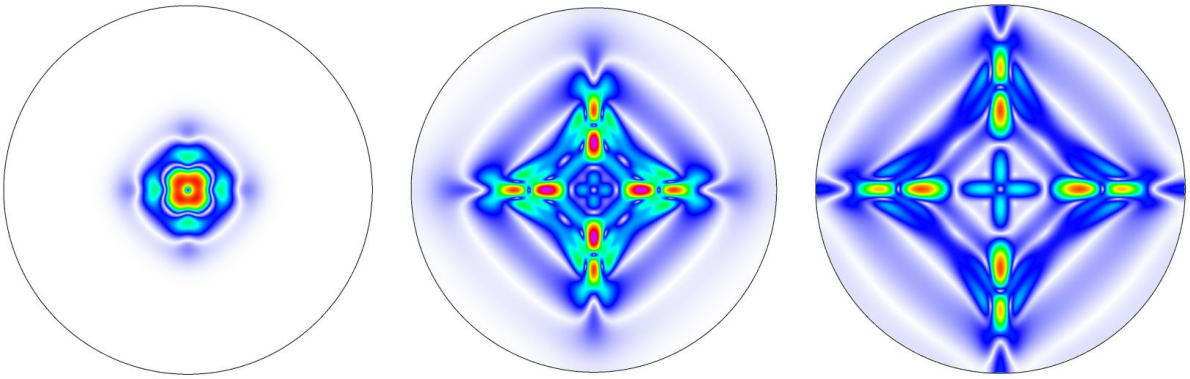

$t = .6$ ms | color scale upscaled by 50, $t = 1.4$ ms | color scale upscaled by 100, $t = 2$ ms

(a) Propagation in the anistropic homogenized medium.

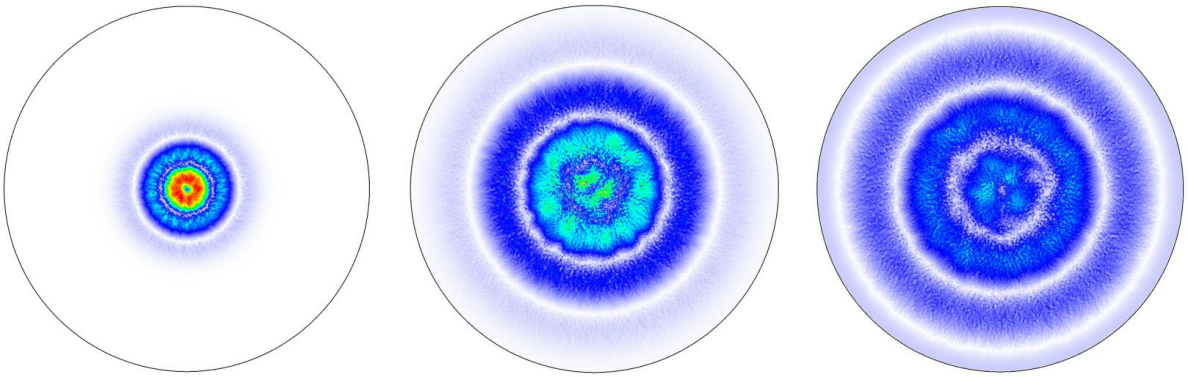

$t = .6$ ms | color scale upscaled by 50, $t = 1.4$ ms | color scale upscaled by 100, $t = 2$ ms

(b) Propagation in the same homogenized medium with random local rotations of the reference frame.

Figure 5.8 – Instantaneous snapshots of the propagation of a wave of frequency 2000 Hz with and without local random rotations of the reference frame as described in Section 5.4.3. The plots present the magnitude of the velocity at three different instants. The color scale for the velocity has been upscaled by a factor of 50 and 100 respectively in the two frames to the right because the signal has been almost completely dissipated in the viscoelastic homogenized medium, especially the high frequency components.

Bibliographie

[AAGM12] F. Alouges, A. Augier, B. Graille, and B. Merlet. Homogenization of coupled equations for sound propagation in porous media. Accepted for publication in Adv. Diff. Eq., 2012.

[AC96] G. Allaire and C. Conca. Bloch–wave homogenization for a spectral problem in fluid–solid structures. *Arch. Rational Mech. Anal.*, 135 :197–257, 1996.

[AGMR08] A. Ávila, G. Griso, B. Miara, and E. Rohan. Multiscale modeling of elastic waves : Theoretical justification and numerical simulation of band gaps. *Multiscale Modeling & Simulation*, 7(1) :1–21, 2008.

[All89] G. Allaire. Homogenization of the Stokes flow in a connected porous medium. *Asymptotic Anal.*, 2(3) :203–222, 1989.

[All92] G. Allaire. Homogenization and two–scale convergence. *SIAM J. Math. Anal.*, 23(6) :1482–1518, 1992.

[Ans71] P. M. Anselone. *Collectively compact operator approximation theory and applications to integral equations*. Prentice-Hall Inc., Englewood Cliffs, N. J., 1971. With an appendix by Joel Davis, Prentice-Hall Series in Automatic Computation.

[Aug10] A. Augier. *Modélisation et simulation numérique de matériaux microstructurés pour l'isolation acoustique des cabines d'avion*. PhD thesis, Université Paris–Sud (Orsay), 2010.

[Aur80] J. L. Auriault. Dynamic behaviour of a porous medium saturated by a newtonian fluid. *Int. Journ. Engrg. Sci.*, 18(6) :775 – 785, 1980.

[Ban91] C. Bandt. Self-similar sets. V. Integer matrices and fractal tilings of $\mathbf{R}^n$. *Proc. Amer. Math. Soc.*, 112(2) :549–562, 1991.

[Bat09] J. H. T. Bates. *Lung Mechanics, An Inverse Modeling Approach*. Cambridge University Press, 2009.

[BBDDG05] A. S. Bonnet-Ben Dhia, D. Drissi, and N. Gmati. Mathematical analysis of the acoustic diffraction by a muffler containing perforated ducts. *Math. Models Methods Appl. Sci.*, 15(7) :1059–1090, 2005.

[BBJM05] C. Baranger, L. Boudin, P.-E. Jabin, and S. Mancini. A modeling of biospray for the upper airways. *ESAIM : Proc.*, 14 :41–47, 2005.

[BF04] G. Bouchitte and D. Felbacq. Homogenization near resonances and artificial magnetism from dielectrics. *C. R. Math.*, 339(5) :377 – 382, 2004.

[BG11] A. Blasselle and G. Griso. Mechanical modeling of the skin. *Asymptotic Analysis*, 74(3) :167–198, January 2011.

[BGM10] L. Baffico, C. Grandmont, and B. Maury. Multiscale modeling of the respiratory tract. *Math. Models Methods Appl. Sci.*, 20(1) :59–93, 2010.

[BGMO08] L. Baffico, C. Grandmont, Y. Maday, and A. Osses. Homogenization of elastic media with gaseous inclusions. *Multiscale Model. Simul.*, 7(1) :432–465, 2008.

[Bio56a] M. A. Biot. Theory of propagation of elastic waves in a fluid-saturated porous solid. I. Low-frequency range. *J. Acoust. Soc. Amer.*, 28 :168–178, 1956.

[Bio56b] M. A. Biot. Theory of propagation of elastic waves in a fluid-saturated porous solid. II. Higher frequency range. *J. Acoust. Soc. Amer.*, 28 :179–191, 1956.

[Bio62] M. A. Biot. Mechanics of deformation and acoustic propagation in porous media. *J. Appl. Phys.*, 33 :1482–1498, 1962.

[BK82] R. Burridge and J. Keller. Biot's poroelasticity equations by homogenization. In *Macroscopic Properties of Disordered Media*, volume 154 of *Lecture Notes in Physics*, pages 51–57. Springer, 1982.

[Bla11] A. Blasselle. *Modélisation mathématique de la peau*. PhD thesis, Université Pierre et Marie Curie, Nov 2011.

[BLD87] J. P. Butler, J. L. Lehr, and J. M. Drazen. Longitudinal elastic wave propagation in pulmonary parenchyma. *J. Appl. Phys.*, 62(4) :1349–1355, 1987.

[BLP78] A. Bensoussan, J.-L. Lions, and G. Papanicolaou. *Asymptotic analysis for periodic structures*, volume 5 of *Studies in Mathematics and its Applications*. North-Holland Publishing Co., Amsterdam, 1978.

[Bos09] S. Boscarino. On an accurate third order implicit-explicit Runge–Kutta method for stiff problems. *Applied Numerical Mathematics*, 59(7) :1515–1528, 2009.

[Boy08] S. Boyaval. Reduced–basis approach for homogenization beyond the periodic setting. *Multiscale Modeling & Simulation*, 7(1) :466–494, 2008.

[BW89] M. Baumgaertel and H. H. Winter. Determination of discrete relaxation and retardation time spectra from dynamic mechanical data. *Rheologica Acta*, 28 :511–519, 1989.

[CD89] D. Cioranescu and P. Donato. Exact internal controllability in perforated domains. *J. Math. Pures Appl. (9)*, 68(2) :185–213, 1989.

[CDG08] D. Cioranescu, A. Damlamian, and G. Griso. The periodic unfolding method in homogenization. *SIAM J. Math. Anal.*, 40(4) :1585–1620, 2008.

[CFGM01] T. Clopeau, J. L. Ferrin, R. P. Gilbert, and A. Mikelic. Homogenizing the acoustic properties of the seabed, part ii. *Math. Comp. Model.*, 33 :821–841, 2001.

[Cia88] P. G. Ciarlet. *Mathematical elasticity. Vol. I. Three-dimensional elasticity*, volume 20 of *Studies in Mathematics and its Applications*. North-Holland Publishing Co., Amsterdam, 1988.

[CIB+05] F. S. A. Calvancante, S. Ito, K. Brewer, H. Sakai, A. M. Alencar, M. P. Almeida, J. S. Adrade Jr., A. Majumdar, E. P. Ingenito, and B. Suki. Mechanical interactions between collagen and proteoglycans : implications for the stability of lung tissue. *J. Appl. Phys.*, 98 :672–679, 2005.

[Con85] C. Conca. On the application of the homogenization theory to a class of problems arising in fluid mechanics. *J. Math. Pures Appl. (9)*, 64(1) :31–75, 1985.

[CR10] J. Clegg and M. P. Robinson. A genetic algorithm used to fit Debye functions to the dielectric properties of tissues. *2010 IEEE Congress on Evolutionary Computation (CEC)*, pages 1–8, 2010.

[CS04] J. R. Cebral and R. M. Summers. Tracheal and central bronchial aerodynamics using virtual bronchoscopy and computational fluid dynamics. *IEEE Trans. Med. Imaging*, 23(8) :1021–1033, 2004.

[Cum01] P Cummings. *Analysis of Finite Element Based Numerical Methods for Acoustic Waves, Elastic Waves, and Fluid-Solid Interactions in the Frequency Domain.* PhD thesis, University of Tennessee, May 2001.

[Das95] S. Dasser. Méthode de péenalisation pour l'homogénéisation d'un problème de couplage fluide–structure. *C. R. Acad. Sci. Paris*, 320(6) :759–764, 1995.

[DL72] G. Duvaut and J.-L. Lions. *Les inéquations en mécanique et en physique.* Dunod, Paris, 1972. Travaux et Recherches Mathématiques, No. 21.

[DMS80] P. J. Dale, F. L. Matthews, and R. C. Schroter. Finite element analysis of lung alveolus. *Journal of Biomechanics*, 13(10) :865–873, 1980.

[DS06] E. Denny and R. C. Schroter. A model of non-uniform lung parenchyma distortion. *Journal of Biomechanics*, 39(4) :652 – 663, 2006.

[Dun86] F. Dunn. Attenuation and speed of ultrasound in lung : Dependence upon frequency and inflation. *J. Acoust. Soc. Am.*, 80 :1248–1250, 1986.

[ESJP95] I. A. Ene and J. Saint-Jean Paulin. Homogénéisation et convergence double échelle pour un écoulement de Stokes dans un milieu poreux élastique de faible épaisseur. *C. R. Acad. Sci. Paris*, 321(6) :211–216, 1995.

[ESP75] H.I. Ene and E. Sanchez-Palencia. Équations et phénomènes de surface pour l'écoulement dans un modèle de milieu poreux. *J. Mecan.*, 14 :73–108, 1975.

[FGX05] M. Fang, R. P. Gilbert, and X. Xie. Deriving the effective ultrasound equations for soft tissue interrogation. *Comput. Math. Appl.*, 49(7-8) :1069–1080, 2005.

[FM92] M. Fabrizio and A. Morro. *Mathematical problems in linear viscoelasticity*, volume 12 of *SIAM Studies in Applied Mathematics.* Society for Industrial and Applied Mathematics (SIAM), Philadelphia, PA, 1992.

[FM03] J. L. Ferrín and A. Mikelić. Homogenizing the acoustic properties of a porous matrix containing an incompressible inviscid fluid. *Math. Methods Appl. Sci.*, 26(10) :831–859, 2003.

[FMP+05] C. Fetita, S. Mancini, D. Perchet, F. Prêteux, M. Thiriet, and L. Vial. An image–based computational model of oscillatory flow in the proximal part of tracheobronchial trees. *Computer Methods in Biomechanics and Biomedical Engineering*, 8(4) :279–293, 2005.

[Fri69] A. Friedman. *Partial differential equations.* Holt, Rinehart and Winston, Inc., New York, 1969.

[FSF11] M. Florens, B. Sapoval, and M. Filoche. The optimal branching asymmetry of a bidirectional distribution tree. *Computer Physics Communications*, 182(9) :1932 – 1936, 2011.

[Fun88] Y. C. Fung. A model of the lung structure and its validation. *J. Appl. Phys.*, 64(5) :2132–2141, 1988.

[GM00] R. P. Gilbert and A. Mikelić. Homogenizing the acoustic properties of the seabed. I. *Nonlinear Anal.*, 40(1-8, Ser. A : Theory, Methods) :185–212, 2000.

[GMM06] C. Grandmont, B. Maury, and N. Meunier. A viscoelastic model with non–local damping, application to the human lungs. *Mathematical Modelling and Numerical Analysis*, 40(1) :201–224, 2006.

[GR86] V. Girault and P.-A. Raviart. *Finite element methods for Navier-Stokes equations*, volume 5 of *Springer Series in Computational Mathematics.* Springer, Berlin, 1986. Theory and algorithms.

[GWN02] Q. Grimal, A. Watzky, and S. Naili. A one–dimensional model for the propagation of transient pressure waves through the lung. *Journal of Biomechanics*, 35(8) :1081–1089, 2002.

[Han05] A. Hanyga. Viscous dissipation and completely monotonic relaxation moduli. *Rheologica Acta*, 44 :614–621, 2005.

[Hec12] F. Hecht. *FreeFem++ manual*, 2012.

[HKR00] G. C. Hsiao, R. E. Kleinman, and G. F. Roach. Weak solutions of fluid-solid interaction problems. *Math. Nachr.*, 218 :139–163, 2000.

[HS78] P. R. Halmos and V. S. Sunder. *Bounded integral operators on L^2 spaces*, volume 96 of *Ergebnisse der Mathematik und ihrer Grenzgebiete [Results in Mathematics and Related Areas]*. Springer, Berlin, 1978.

[HW08] J. S. Hesthaven and T. Warburton. *Nodal discontinuous Galerkin methods*, volume 54 of *Texts in Applied Mathematics*. Springer, New York, 2008.

[KC03] C. A. Kennedy and M. H. Carpenter. Additive Runge-Kutta schemes for convection-diffusion-reaction equations. *Appl. Numer. Math.*, 44(1-2) :139–181, 2003.

[KCGH07] A. Kanevsky, M. H. Carpenter, D. Gottlieb, and J. S. Hesthaven. Application of implicit-explicit high order Runge-Kutta methods to discontinuous-Galerkin schemes. *J. Comput. Phys.*, 225(2) :1753–1781, 2007.

[KDL07] D. F. Kelley, T. J. Destan, and R. J. Luebbers. Debye function expansions of complex permittivity using a hybrid particle swarm-least squares optimization approach. *Antennas and Propagation, IEEE Transactions on*, 55(7) :1999–2005, 2007.

[Klo10] A. Kloeckner. Hedge : Hybrid and Easy Discontinuous Galerkin Environment. `http://www.cims.nyu.edu/~kloeckner/`, 2010.

[KLS12] C. E. Kenig, F. Lin, and Z. Shen. Convergence rates in l2 for elliptic homogenization problems. *Archive for Rational Mechanics and Analysis*, 203 :1009–1036, 2012.

[Kra83] S. S. Kraman. Speed of low-frequency sound through lungs of normal men. *J. Appl. Phys.*, pages 1862–1867, 1983.

[KSMH86] R. Kowe, R. C. Schroter, F. L. Matthews, and D. Hitchings. Analysis of elastic and surface tension effects in the lung alveolus using finite element methods. *Journal of Biomechanics*, 19(7) :541–549, 1986.

[KTS99] H. Kitaoka, R. Takaki, and B. Suki. A three-dimensional model of the human airway tree. *J. Appl. Phys.*, 87(6) :2207–2217, 1999.

[KTT00] H. Kitaoka, S. Tamura, and R. Takaki. A three-dimensional model of the human pulmonary acinus. *J. Appl. Phys.*, 88(6) :2260–2268, 2000.

[L$\acute{7}$7] T. Lévy. Acoustic phenomena in elastic porous media. *Mech. Res. Comm.*, 4(4) :253–257, 1977.

[L$\acute{7}$9] T. Lévy. Propagation of waves in a fluid-saturated porous elastic solid. *Intern. J. of Eng. Sci.*, 17(9) :1005–1014, 1979.

[Lan83] Y. Lanir. Constitutive equations for the lung tissue. *J Biomech Eng*, 105(4) :374–380, Nov 1983.

[LeV90] R. J. LeVeque. *Numerical methods for conservation laws*. Lectures in Mathematics ETH Zürich. Birkhäuser Verlag, Basel, 1990.

[Lio69] J.-L. Lions. *Quelques méthodes de résolution des problèmes aux limites non linéaires*. Dunod, 1969.

[LM68] J.-L. Lions and E. Magenes. *Problèmes aux limites non homogènes et applications. Vol. 1.* Travaux et Recherches Mathématiques, No. 17. Dunod, Paris, 1968.

[LM05] P. L. Lions and N. Masmoudi. Homogenization of the Euler system in a 2D porous medium. *J. Math. Pures Appl.*, 84 :1–20, 2005.

[LMB+02] S. Ley, D. Mayer, B. S. Brook, E. J. Van Beek, C. P. Heussel, D. Rink, R. Hose, K. Markstaller, and H. U. Kauczor. Radiological imaging as the basis for a simulation software of ventilation in the tracheo–bronchial tree. *Eur. Radio.*, 12(9) :2218–2228, 2002.

[LNW02] D. Lukkassen, G. Nguetseng, and P. Wall. Two-scale convergence. *Int. J. Pure Appl. Math.*, 2(1) :35–86, 2002.

[Lou04] M. Lourakis. levmar : Levenberg-Marquardt nonlinear least squares algorithms in C/C++. `http://www.ics.forth.gr/~lourakis/levmar/`, 2004.

[LSP77] T. Lévy and E. Sanchez-Palencia. Equations and interface conditiosn for acoustic phenomena in porous media. *Journ. Math. Anal. and Appl.*, 61 :813–834, 1977.

[MAB+05] A. Majumdar, A. M. Alencar, S. V. Buldyrev, Z. Hantos, K. R. Lutchen, H. E. Stanley, and B. Suki. Relating airway diameter distributions to regular branching asymmetry in the lung. *Phys. Rev. Lett.*, 95 :168101, Oct 2005.

[Man82] B. B. Mandelbrot. *The fractal geometry of nature.* W. H. Freeman and Co., San Francisco, Calif., 1982.

[Mau05] B. Mauroy. 3D hydrodynamics in the upper human bronchial tree : Interplay between geometry and flow distribution. In *Fractals in Biology and Medicine*, Mathematics and Biosciences in Interaction, pages 43–53. Birkhäuser Basel, 2005.

[MBW+12] K. Morenz, H. Biller, F. Wolfram, S. Leonhadt, D. Ruter, T. Glaab, S. Uhlig, and J. Hohlfeld. Detection of air trapping in chronic obstructive pulmonary disease by low frequency ultrasound. *BMC Pulmonary Medicine*, 12(1) :8, 2012.

[Mei08a] A. M. Meirmanov. Acoustic and filtration properties of a thermoelastic porous medium : Biot's equation of thermo–poroelasticity. *Sb. Math.*, 199(3) :361–384, 2008.

[Mei08b] A. M. Meirmanov. Darcy's law for a compressible thermofluid. *Asymptotic Analysis*, 58(4) :191–209, 2008.

[Mei08c] A. M. Meirmanov. Homogenized models for a short–time filtration in elastic porous media. *Elec. Journ. Diff. Eq.*, 2008(14) :1–18, 2008.

[MFAS03] B. Mauroy, M. Filoche, J. Andrade, and B. Sapoval. Interplay between geometry and flow distribution in an airway tree. *Phys. Rev. Lett.*, 90(14), Apr 2003.

[MFWS04] B. Mauroy, M. Filoche, E. Weibel, and B. Sapoval. An optimal bronchial tree may be dangerous. *Nature*, pages 633–636, Jan 2004.

[Mil95] R. E. Miller. Homogenization of time–dependent systems with Kelvin–Voigt damping by two-scale convergence. *Discrete Contin. Dynam. Systems*, 1(4) :485–502, 1995.

[MMS12] Y. Maday, N. Morcos, and T. Sayah. Reduced basis numerical homogenization for scalar elliptic equations with random coefficients : application to blood micro-circulation. Submitted to SIAM J. Appl Math., 2012.

[Mor11] N. Morcos. *Modélisation mathématique et simulation de systèmes microvasculaires.* PhD thesis, Université Pierre et Marie Curie, June 2011.

[Mou09] A. Moussa. *Étude mathématique et numérique du transport d'aérosols dans le poumon humain.* PhD thesis, École normale supérieure de Cachan, December 2009.

[MP02] Z. Mikhak and P. C. Pedersen. Acoustic attenuation properties of the lung : an open question. *Ultrasound in Medicine and Biology*, 28(9) :1209 –1216, 2002.

[MSSM08] S. Martin, T. Similowski, C. Straus, and B. Maury. Impact of respiratory mechanics model parameters on gas exchange efficiency. In *Mathematical and numerical modelling of the human lung*, volume 23 of *ESAIM Proc.*, pages 30–47. EDP Sci., Les Ulis, 2008.

[Ngu89] G. Nguetseng. A general convergence result for a functional related to the theory of homogenization. *SIAM J. Math. Anal.*, 20(3) :608–623, 1989.

[Ngu90] G. Nguetseng. Asymptotic analysis for a stiff variational problem arising in mechanics. *SIAM J. Math. Anal.*, 21(6) :1394–1414, 1990.

[OL01] M. R. Owen and M. A. Lewis. The mechanics of lung tissue under high-frequency ventilation. *SIAM J. Appl. Math.*, 61(5) :pp. 1731–1761, 2001.

[OS95] B. Owren and H. H. Simonsen. Alternative integration methods for problems in structural dynamics. *Comput. Methods Appl. Mech. Engrg.*, 122(1-2) :1–10, 1995.

[Pea90] G. Peano. Sur une courbe, qui remplit toute une aire plane. *Math. Ann.*, 36(1) :157–160, 1890.

[PKW97] H. Pasterkamp, S. S. Kraman, and G. R. Wodicka. Respiratory sounds. advances beyond the stethoscope. *American journal of respiratory and critical care medicine*, 156(3) :974, 1997.

[PSP+96] M. A. Perzl, H. Schulz, H. G. Paretzke, K.H. Englemeier, and J. Heyder. Reconstruction of the lung geometry for the simulation of aerosol transport. *Journal of Aerosol Medicine*, 9(3) :409–418, 1996.

[Rao03] M. D. Rao. Recent applications of viscoelastic damping for noise control in automobiles and commercial airplanes. *Journal of Sound and Vibration*, 262(3) :457–474, 2003.

[RHD+10] D. Rueter, H. P. Hauber, D Droeman, P. Zabel, and S. Uhlig. Low-frequency ultrasound permeates the human thorax and lung : a novel approach to non-invasive monitoring. *Ultraschall Med.*, 31(1) :53–62, 2010.

[Ric83] D. A. Rice. Sound speed in pulmonary parenchyma. *J. Appl. Physiol.*, 54(1) :304–308, 1983.

[RW10] J. Rataj and S. Winter. On volume and surface area of parallel sets. *Indiana Univ. Math. J.*, 59(5) :1661–1685, 2010.

[RW11] E. Roan and M. W. Waters. What do we know about mechanical strain in lung alveoli ? *Am. J. Physiol. Lung Cell Mol. Physiol.*, 301(5) :625–635, 2011.

[SB11] B. Suki and J. H. T. Bates. Lung tissue mechanics as an emergent phenomenon. *J. Appl. Phys.*, 110(4) :1111–1118, 2011.

[Sch61] R. A. Schapery. A simple collocation method for fitting viscoelastic models to experimental data. *GALCIT SM*, 63 :23, 1961.

[SH79] J. Sanchez-Hubert. Etude de certaines équations intégrodifférentielles issues de la théorie de l'homogénéisation. *Bull. Un. Math. Ital.*, 16–B :857–875, 1979.

[SH10] J. Sorvari and J. Hämäläinen. Time integration in linear viscoelasticity—a comparative study. *Mechanics of Time-Dependent Materials*, 14 :307–328, 2010.

[Sim87] J. Simon. Compact sets in the space $L^p(0,T;B)$. *Ann. Mat. Pura Appl. (4)*, 146 :65–96, 1987.

[SIS+05] B. Suki, S. Ito, D. Stamenović, K. R. Lutchen, and E. P. Ingenito. Biomechanics of the lung parenchyma : critical roles of collagen and mechanical forces. *J. Appl. Physiol.*, 98(5) :1892–1899, 2005.

[SJTL08] M. Siklosi, O. E. Jensen, R. H. Tew, and A. Logg. Multiscale modeling of the acoustic properties of lung parenchyma. *ESAIM : Proc.*, 23 :78–97, 2008.

[SN59] B. Sz.-Nagy. Über Parallelmengen nichtkonvexer ebener Bereiche. *Acta Sci. Math. Szeged*, 20 :36–47, 1959.

[Sni08] J. Snitzman. *Respiratory Flows in the Pulmonary Acinus and Insights on the Control of Alveolar Flows*. PhD thesis, Swiss Federal Institute of Technology, Zürich, 2008.

[Sol64] W. G. Solomon. Replicating figures in the plane. *The Mathematical Gazette*, 48(366) :pp. 403–412, 1964.

[Sou07] A. Soualah. *Modélisation mathématique et numérique du poumon humain*. PhD thesis, Université Paris-Sud (Orsay), December 2007.

[SP80] E. Sanchez-Palencia. Vibration of mixtures of solids and fluids. In *Non-Homogeneous Media and Vibration Theory*, volume 127 of *Lecture Notes in Physics*, pages 158–190. Springer, 1980.

[SP86] E. Sanchez-Palencia. Homogenization in mechanics. a survey of solved and open problems. *Rend. Sem. Mat. Univers. Politecn. Torino*, 44(1), 1986.

[SS11] A. Shamaev and V. Shumilova. Homogenization of acoustic equations for a partially perforated viscoelastic solid with viscous liquid. *Doklady Physics*, 56 :43–46, 2011.

[Sta76] L. L. Stachó. On the volume function of parallel sets. *Acta Sci. Math. (Szeged)*, 38(3–4) :365–374, 1976.

[Str83] J.W. Strutt, Baron Rayleigh. On porous bodies in relation to sound. *Phil. Mag.*, 16 :181–186, 1883.

[Suq87] P. Suquet. Linear problems. In Enrique Sanchez-Palencia and André Zaoui, editors, *Homogenization Techniques for Composite Media*, volume 272 of *Lecture Notes in Physics*, pages 209–230. Springer, 1987.

[Tar80] L. Tartar. *Incompressible fluid flow through porous media—Convergence of the homogenization process. Appendix of [SP80]*, pages 368–380. Springer, 1980.

[Tar09] L. Tartar. *The general theory of homogenization*, volume 7 of *Lecture Notes of the Unione Matematica Italiana*. Springer, 2009. A personalized introduction.

[TPH00] M. H. Tawhai, A. J. Pullan, and P. J. Hunter. Generation of an anatomically based three-dimensional model of the conducting airways. *Annals of Biomedical Engineering*, 28 :793–802, 2000.

[Van09] C. Vannier. *Modélisation mathématique du poumon humain*. PhD thesis, Université Paris–Sud (Orsay), Jul 2009.

[VSM09] C. Vannier, D. Salort, and B. Maury. Trace theorems for trees and application to the human lungs. *Networks and Heterogeneous Media*, 4(3) :469–500, Jul 2009.

[WCRW11] L. Wiechert, A. Comerford, S. Rausch, and W. Wall. Advanced multi–scale modelling of the respiratory system. In *Fundamental Medical and Engineering Investigations on Protective Artificial Respiration*, volume 116 of *Notes on Numerical Fluid Mechanics and Multidisciplinary Design*, pages 1–32. Springer, 2011.

[Wei63] E. R. Weibel. Morphometry of the human lung. *Springer*, page 151, Jan 1963.

[Wei84] E. R. Weibel. *The pathway for oxygen*. Harvard Press, Cambridge, Mass., Jan 1984.

[Wei09] E. R. Weibel. What makes a good lung. *Swiss Medical Weekly*, 139 :375–386, 2009.

[WWCR10] W. A. Wall, L. Wiechert, A. Comerford, and S. Rausch. Towards a comprehensive computational model for the respiratory system. *In. J. Num. Methods Biomed. Engrg.*, 26(7) :807–827, 2010.

[YPY98] Y.-M. Yi, S.-H. Park, and S.-K. Youn. Asymptotic homogenization of viscoelastic composites with periodic microstructures. *Internat. J. Solids Structures*, 35(17) :2039–2055, 1998.